



Aalborg Universitet

AALBORG UNIVERSITY  
DENMARK

## Nonlinear Multibody Dynamics of Wind Turbines

Holm-Jørgensen, Kristian

*Publication date:*  
2009

*Document Version*  
Publisher's PDF, also known as Version of record

[Link to publication from Aalborg University](#)

*Citation for published version (APA):*  
Holm-Jørgensen, K. (2009). *Nonlinear Multibody Dynamics of Wind Turbines*. Department of Civil Engineering, Aalborg University.

### General rights

Copyright and moral rights for the publications made accessible in the public portal are retained by the authors and/or other copyright owners and it is a condition of accessing publications that users recognise and abide by the legal requirements associated with these rights.

- Users may download and print one copy of any publication from the public portal for the purpose of private study or research.
- You may not further distribute the material or use it for any profit-making activity or commercial gain
- You may freely distribute the URL identifying the publication in the public portal -

### Take down policy

If you believe that this document breaches copyright please contact us at [vbn@aub.aau.dk](mailto:vbn@aub.aau.dk) providing details, and we will remove access to the work immediately and investigate your claim.

# Nonlinear Multibody Dynamics of Wind Turbines

**Kristian Holm-Jørgensen**

**PhD Thesis**

Division of Structural Mechanics  
Department of Civil Engineering  
Aalborg University 2009



Aalborg University  
Department of Civil Engineering  
Division of Structural Mechanics

**DCE Thesis No. 19**

# **Nonlinear Multibody Dynamics of Wind Turbines**

by

**Kristian Holm-Jørgensen**

Submitted for the degree of  
Doctor of Philosophy

June 2009

©Aalborg University



## Scientific Publications at the Department of Civil Engineering

**Technical Reports** are published for timely dissemination of research results and scientific work carried out at the Department of Civil Engineering (DCE) at Aalborg University. This medium allows publication of more detailed explanations and results than typically allowed in scientific journals.

**Technical Memoranda** are produced to enable the preliminary dissemination of scientific work by the personnel of the DCE where such release is deemed to be appropriate. Documents of this kind may be incomplete or temporary versions of papers-or part of continuing work. This should be kept in mind when references are given to publications of this kind.

**Contract Reports** are produced to report scientific work carried out under contract. Publications of this kind contain confidential matter and are reserved for the sponsors and the DCE. Therefore, Contract Reports are generally not available for public circulation.

**Lecture Notes** contain material produced by the lecturers at the DCE for educational purposes. This may be scientific notes, lecture books, example problems or manuals for laboratory work, or computer programs developed at the DCE.

**Theses** are monographs or collections of papers published to report the scientific work carried out at the DCE to obtain a degree as either PhD or Doctor of Technology. The thesis is publicly available after the defence of the degree.

**Latest News** is published to enable rapid communication of information about scientific work carried out at the DCE. This includes the status of research projects, developments in the laboratories, information about collaborative work and recent research results.

Published 2009 by  
Aalborg University  
Department of Civil Engineering  
Sohngaardsholmsvej 57,  
DK-9000 Aalborg, Denmark

Printed in Aalborg at Aalborg University

ISSN 1901-7294  
DCE Thesis No. 19

---

# Preface

---

The present thesis “Nonlinear Multibody Dynamics of Wind Turbines” has been prepared in connection with a Ph.D. study carried out in the period August 2005 to November 2008 at the Department of Civil Engineering, Aalborg University, Denmark. The Ph.D. project was part of a collaboration among Department of Civil Engineering at Aalborg University, Department of Mechanical Engineering at the Technical University of Denmark, and Siemens Wind Power A/S. The study was financial supported by the Danish Council for Strategic Research within the programme “Nonlinear Multibody Dynamics of Wind Turbines”. The support is duly acknowledged.

First of all, I wish to thank my supervisor, Søren R.K. Nielsen for always having time for counseling and his everlasting interest in this project. Especially, I am grateful for his encouragement after the project period ended, for finishing this project.

I also wish to thank the persons from the project collaboration for their support and assistance, Steen Krenk at the Technical University of Denmark, Jørgen Thirstrup Petersen and Rune Rubak at Siemens Wind Power A/S.

A special thank to my friends and colleagues at the Department of Civil Engineering. Especially, Jesper Winther Stærdahl, Lasse Gilling, Henrik Steensgaard Toft, and Filip Westarp for their support, discussions, and making the days pleasant.

Aalborg, June, 2009

Kristian Holm-Jørgensen



---

## Summary in English

The continuing development of wind turbines aim at higher effect production and reducing the purchase and maintenance costs for the customers. This demands that the components in the wind turbine are optimized closer to the limit than previously. In order to determine the design loads it is necessary with a numerical model, which represents the reality as good as possible. For this purpose a flexible multibody formulation is suitable because large nonlinear geometric deformations of e.g. the blades can be accounted for while still having the possibility of modelling the remaining components individually and next couple them by use of joints. This gives a high level of modelling flexibility, where parts of the structure with relative ease can be interchanged to analyze other possibilities in a design process, or if a higher detail level is wanted for some components. In a multibody formulation each substructure e.g. a part of the blade is modelled by use of Bernoulli-Euler beam elements with St. Venant torsion. For each substructure a belonging moving frame is present, where to the displacements of the substructure must be relative small, in order for the linear displacement assumption to be fulfilled inside the moving frame. By modelling e.g. the blades by use of several substructures it is possible to account for large nonlinear geometric deformations.

The multibody formulation focused on in this project is based on the Local Observer Frame formulation, where the parameters that determine the motion of the frames do not enter the state vector, like in the more standard Floating Frame of Reference formulation. Hereby, the otherwise mixed set of referential and elastic coordinates are avoided and thereby the highly nonlinear equations of motion. However, this demands that the parameters to define the motion of the moving frames are regularly updated so the relative motion of the substructure from the belonging moving frame is reduced. The update algorithm of these parameters is based on the motion of the belonging beam element substructure. Based on a number of static analyses for a wind turbine blade with large nonlinear displacements it has shown most favorable to use the end points in the substructure for updating the moving frames.

For speeding up dynamical simulations for use in e.g. active control or parameter studies, system reduction of substructures in the multibody formulation is investigated. The first method a Ritz basis is used, which contains rigid body modes and a number of elastic eigenmodes compatible to the kinematical boundary conditions. By use of very few elastic eigenmodes to model a blade it has shown convenient to use a quasi-static term for the truncated elastic eigenmodes. The second method is based on a Component Mode Synthesis method with constraint modes and fixed interface normal modes. Hereby, the coupling degrees of freedom between adjacent substructures are preserved for use in setting up the kinematical constraints which secure compatibility at the assembling point. This method is more general and can also be used to model the blade in e.g. two substructures or to model other components in the wind turbine.

To determine the structural properties of a blade for use in beam element models, a FE-model is implemented which besides the more common beam element parameters also can determine e.g. torsional stiffness and the position of the shear center. The method makes use of three node triangular elements where the different material layers in the blade profile are taken into consideration. The results are compared to a similar tool which makes use of straight elements of uniform thickness to discretize the cross section, where a mean value of the material layers over the thickness direction is used. Good correspondence is demonstrated between the used discretization methods.

---





---

## Summary in Danish

Den fortsatte udvikling af vindmøller tilstræber større effektproduktion til en mindre indkøbs- og vedligeholdelsespris for kunderne. Dette kræver, at komponenterne i en vindmølle optimeres tættere på grænsen end hidtil. For at kunne bestemme designlasterne er det nødvendigt med en numerisk model, der afspejler virkeligheden så godt som muligt. Til dette formål er en fleksibel multibody-formulering velegnet, da der både kan tages højde for store ikke-lineære geometriske deformationer af f.eks. vingerne samtidig med, at de øvrige dele af strukturen kan modelleres individuelt og efterfølgende kobles sammen med de tilhørende lejer. Dette giver en høj grad af modellerings-fleksibilitet, hvor dele af strukturen relativt nemt kan udskiftes for at undersøge andre muligheder i en udviklingsfase, eller hvis der er fokus på højere detaljering af enkelte komponenter. I en multibody-formulering er en substruktur f.eks. en del af vingen modelleret ved brug af Bernoulli-Euler bjælkeelementer med St. Venant torsion. Til hver substruktur er der et tilhørende bevægeligt koordinatsystem, hvortil flytningerne af substrukturen skal være relativ små, så den lineære antagelse af flytningerne indenfor det bevægelige koordinatsystem er opfyldt. Ved at modellere f.eks. vingen af flere substrukturer kan der tages højde for store ikke-lineære geometriske deformationer.

Den multibody-formulering, der er i fokus i dette projekt, er baseret på en Local Observer Frame formulering, hvor de parametre der fastlægger bevægelsen af koordinatsystemerne ikke indgår som en del af løsningsvektoren, som i den mere standardiserede Floating Frame of Reference formulering. Hermed undgås det ellers miksede sæt af reference og elastiske koordinater som medfører stærkt ikke-lineære bevægelsesligninger. Dette kræver dog, at parametrene til fastlæggelse af de bevægelige koordinatsystemer løbende opdateres, så den relative bevægelse af substrukturen fra det tilhørende bevægelige koordinatsystem reduceres. Opdateringen af disse parametre er bestemt udfra bevægelsen af den pågældende bjælkeelement-substruktur. Baseret på en række statiske analyser for en vinge med store ikke-lineære deformationer har det vist sig mest fordelagtigt at benytte endepunkterne i substrukturene til at opdatere de bevægelige koordinatsystemer.

Af hensyn til hurtige dynamiske simuleringer til brug for f.eks. aktiv kontrol eller parameterstudier er systemreduktion af substrukturer i den pågældende multibody-formulering undersøgt. I den første metode benyttes en Ritz-basis, der indeholder stivlegeme-modes samt elastiske egensvingsningsformer kompatible til de kinematiske randbetingelser. Ved brug af ganske få elastiske egensvingsningsformer til at modellere en vinge viser det sig belejligt at inddrage et kvasistatisk led for de trunkerede elastiske egensvingsningsformer. I den anden metode, der bygger på Component Mode Synthesis, benyttes constraint modes og fixed interface normal modes. Hermed bevares koblingsfrihedsgraderne imellem de tilstødende substrukturer til brug for opstilling af de kinematiske bindinger, der sikrer kompatibilitet i overgangene. Denne metode er mere generel, og kan også benyttes til at opdele vingen i f.eks. to substrukturer eller til at modellere andre komponenter i vindmøllen.

Til at fastlægge vingens strukturelle egenskaber for brug i bjælkemodeller, er der implementeret en FE-model, som udover de mere gængse bjælkeparametre kan fastlægge bl.a. torsionsstivheden samt placering af forskydningscentret. Metoden benytter treknudede trekantelementer, hvor der tages højde for materialelagene i profilet. Resultaterne er sammenlignet med et lignende analyseværktøj som benytter lige elementer med en konstant tykkelse til at diskretisere tværsnittet, hvor materialelagene over tykkelsesretningen er midlet til et lag. God overensstemmelse mellem de benyttede diskretiseringsmetoder er vist.

---



---

# Contents

---

<b>1</b>	<b>Introduction</b>	<b>1</b>
1.1	Background . . . . .	1
1.2	Presentation of the Problem . . . . .	3
1.3	Published Papers . . . . .	4
1.3.1	Conference Papers . . . . .	4
1.3.2	International Journal Papers . . . . .	4
1.4	Overview of the Thesis . . . . .	5
<b>2</b>	<b>Multibody Formulations with a Moving Frame of Reference</b>	<b>7</b>
2.1	Multibody Formulations Based on a Moving Frame of Reference . . . . .	7
2.1.1	Introduction . . . . .	7
2.1.2	Motion of a Deformable Substructure Relative to a Belonging Moving Frame of Reference . . . . .	8
2.2	Constraints to Model Joints . . . . .	9
2.3	Equations of Motion for a Constrained Substructure based on a Local Observer Frame Formulation . . . . .	12
2.4	Concluding Remarks . . . . .	14
<b>3</b>	<b>Update Algorithms of the Moving Frame of Reference</b>	<b>15</b>
3.1	Introduction . . . . .	15
3.2	Update Algorithm for Dynamic Simulations . . . . .	15
3.3	Update Algorithms for Static Simulations . . . . .	20
3.3.1	Procedure for the Static Updating Algorithms . . . . .	20
3.3.2	Update Based on the Node at the Origin . . . . .	21
3.3.3	Update Based on the Node at the Origin and an Arbitrary Node . . . . .	21
3.4	Concluding Remarks . . . . .	22
<b>4</b>	<b>Static Analysis of Nonlinear Displacements</b>	<b>23</b>
4.1	Co-rotating Formulation based on Beam Elements . . . . .	23
4.2	Large Deformation of a Cantilever Beam . . . . .	23
4.3	Tip Displacement of a Clamped Wind Turbine Blade . . . . .	26
4.3.1	Convergency of Updating Algorithms . . . . .	27
4.3.2	Wind Turbine Blade Modelled by One Substructure . . . . .	27
4.3.3	Wind Turbine Blade Modelled by Two Substructures . . . . .	28
4.4	Concluding Remarks . . . . .	30

<b>5</b>	<b>Eigenfrequencies and Eigenmodes for a Multibody System</b>	<b>31</b>
5.1	Linear Constraints and Generalized Eigenvalue Problem . . . . .	31
5.2	Undamped Eigenfrequencies for a Fixed-base Wind Turbine Blade . . . . .	32
5.3	Undamped Eigenfrequencies and Eigenmodes for a Wind Turbine . . . . .	33
5.4	Concluding Remarks . . . . .	35
<b>6</b>	<b>System Reduction in Multibody Dynamics</b>	<b>37</b>
6.1	System Reduction in Multibody Dynamics of Wind Turbines . . . . .	37
6.1.1	System Reduction Method . . . . .	37
6.1.2	Numerical example . . . . .	40
6.1.3	Conclusions . . . . .	42
6.2	A Component Mode Synthesis Algorithm for Multibody Dynamics of Wind Turbines . . . . .	43
6.2.1	System Reduction Method . . . . .	43
6.2.2	Numerical example . . . . .	45
6.2.3	Conclusions . . . . .	47
6.3	Concluding Remarks . . . . .	48
<b>7</b>	<b>Cross-section Parameters for a Blade Section</b>	<b>49</b>
7.1	Method to Determine Cross-section Parameters . . . . .	49
7.2	Cross-section Parameters for a Rectangular Box Profile . . . . .	50
7.3	Generate Geometry for a Blade Section . . . . .	51
7.4	Meshing of Blade Section . . . . .	53
7.5	Comparison of Results to BHawC_Crs . . . . .	55
7.6	Concluding Remarks . . . . .	56
<b>8</b>	<b>Conclusion and Further Work</b>	<b>57</b>
8.1	Conclusion . . . . .	57
8.2	Further Work . . . . .	59
	<b>References</b>	<b>61</b>
<b>A</b>	<b>Equations of Motion for a Constrained Substructure in a Moving Frame of Reference</b>	<b>63</b>
A.1	Motion of a Material Point Relative to a Moving Frame of Reference . . . . .	63
A.2	Lagrange's Equation . . . . .	66
A.3	Kinetic Energy . . . . .	66
A.4	Potential Energy . . . . .	69
A.5	Equations of Motion . . . . .	69
A.5.1	Terms from Kinetic Energy . . . . .	69
A.5.2	Terms from Potential Energy . . . . .	70
A.5.3	Combined Terms from Kinetic and Potential Energy . . . . .	70
A.6	Concluding Remarks . . . . .	70
<b>B</b>	<b>Cross Section Parameters for Wind Turbine Blade and Tower</b>	<b>71</b>
B.1	Cross Section Parameters for Wind Turbine Blade . . . . .	71
B.2	Cross Section Parameters for Tower . . . . .	72

---

<b>C</b>	<b>Paper: On the Nonlinear Structural Analysis of Wind Turbine Blades using Reduced Degree-of-Freedom Models</b>	<b>75</b>
<b>D</b>	<b>Paper: System Reduction in Multibody Dynamics of Wind Turbines</b>	<b>99</b>
<b>E</b>	<b>Paper: A Component Mode Synthesis Algorithm for Multibody Dynamics of Wind Turbines</b>	<b>121</b>

---





---

# CHAPTER 1

## Introduction

---

In this chapter a brief introduction is given of the key aspects in this project related to wind turbine dynamics. This project is based on the modelling and formulation of numerical models for structural analysis of wind turbine dynamics, and so the aerodynamic part of an aeroelastic code is not considered. The chapter contains a list of the published papers during this project together with an overview of the chapters and appendices included in the present thesis.

### 1.1 Background

With the increasing size of wind turbines and the demand for cost efficient turbines, the different components in the turbines are optimized more than previously. This calls for an accurate and flexible numerical model of the turbine dynamics which is able to model the different components more realistic and to take large nonlinear geometric deformations of especially the blades into consideration. Also, the increasing slender design of the blades makes the structural properties of the blades more important to determine with a high accuracy. Especially, the torsional behavior should be accounted for to capture eventually flutter instabilities.

In Figure 1.1 a classic three-bladed horizontal axis wind turbine is illustrated with the primary structural components i.e. blades, hub, nacelle, tower, and foundation. Inside the nacelle, several structural components exist counting the rotor shaft, main bearings, gearbox, generator shaft, brake, generator, and the support of these components and auxiliary equipment in the nacelle. Moreover, a number of bearings are used in the turbine e.g. to pitch the blades and to yaw the nacelle. With the aid of large computer clusters the resources exist to take more precise models of the structural components and mechanical interfaces into consideration. This could e.g. be the bearings, gear sets, friction, and modelling of the brake. To further develop and test new designs of the wind turbines, it is necessary to have the possibility of implementing new ideas with relative ease in the aeroelastic code for time simulation of the structural dynamics. This calls for a very general formulation where it is possible to make such modifications or interchange the substructures with other modules. For example, for offshore foundation several possibilities exist e.g. a mono pile, gravity, bucket, or jacket foundations. Lately, even the need to model floating foundations for use at large depths have drawn attention. Inside the nacelle, the need to model other drive trains exist e.g. without a gearbox also known as a direct drive. With such large modifications it is also necessary to remodel the remaining components in the nacelle.

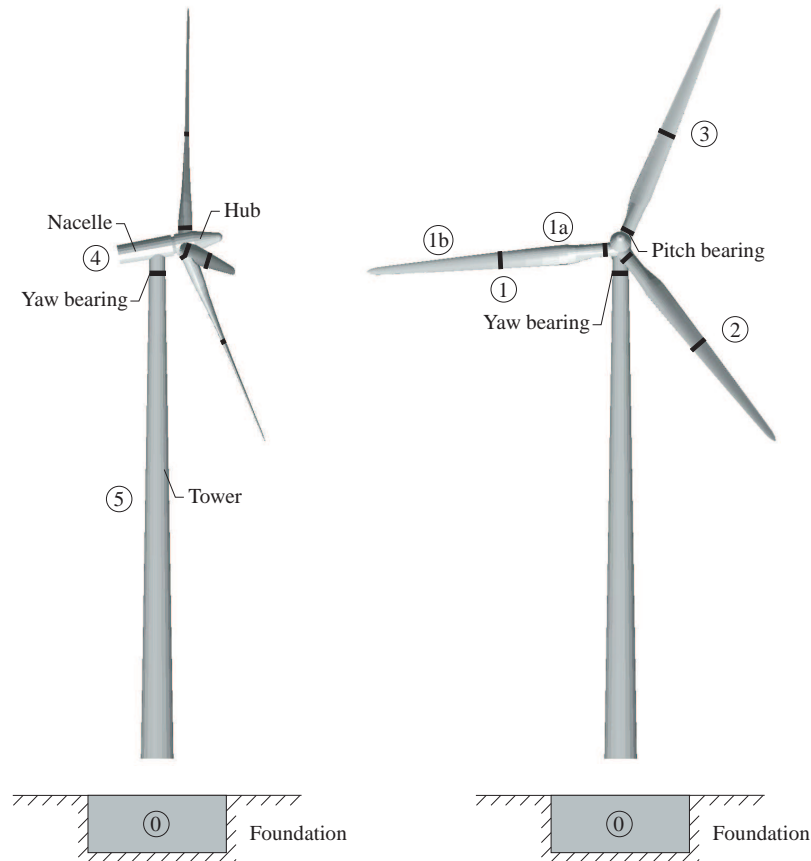


**Figure 1.1** A classic three-bladed horizontal axis wind turbine with the primary structural components i.e. blades, hub, nacelle, tower, and foundation.

For active control with state vector observation of the turbine to reduce loads and vibrations it is necessary with a numerical model that can be processed in real time to account for the changes in the global dynamics when an actuator is activated e.g. by pitching the blades or altering the generator torque. In such cases, the more detailed numerical models in the aeroelastic code consisting of hundreds of degrees of freedom can no longer be used. This calls for reduced models which account for the primary part of the turbine dynamics. In order not to operate two more or less independent numerical models it would be convenient if the reduced models were build directly based on the more detailed models and in the same code. This could e.g. be done by reducing the number of degrees of freedom to model the three blades and keeping the models of the remaining substructures with the original detail level. When the blade models are reduced it is necessary that they still describe the majority of the blade dynamics especially the nonlinear effects from the large geometric displacements. This is e.g. from the inertia and exterior loads, which are applied and follows the deformation of the blades. For parameters studies e.g. due to different site conditions it is also convenient with reduced models to speed up such analyses.

## 1.2 Presentation of the Problem

As described in the previous section, a wind turbine is a complex structure consisting of several rotating structural components, where especially the blades exhibit large geometrical deformations. In order to describe the global dynamics of such a system the focus in this project is drawn towards so-called flexible multibody formulations. In these formulations each structural component is modelled individually by means of a structural model forming a so-called substructure or super element. Next, the substructures are assembled by the use of joints or kinematical constraints. This makes a more general formulation where the different substructures with relative ease can be modelled and interchanged depending on the needs in the present wind turbine simulations.

The multibody formulation focused on in this project is based on the so-called Local Observer Frame formulation by Kawamoto et al. [1]. Kawamoto works at Toyota's research department, where they use this type of multibody formulation for simulating the dynamics in engines and the belonging car body.

In the present project, the use of such a multibody approach for wind turbines is investigated. With a high level of detail the structural components in a wind turbine can be modelled by use of FE beam elements. Therefore, such elements are in focus in the multibody formulation and updating algorithms of the moving frames, which are necessary in this approach. However, the used formulation is not restricted to beam elements, if e.g. solid or shell elements become relevant to model some of the components. Besides the structural modelling, relevant joints or kinematical constraints are necessary to assemble the different components. This is a subject which is not treated in Kawamoto et al. [1]. Often in multibody dynamics the constraint equations are differentiated twice with respect to time and incorporated in a system mass matrix, Shabana [2]. Next, constraint regularization is used to ensure that the constraints are satisfied on the displacement and velocity level. In the present project it is examined if such an approach can be avoided to eliminate the use of such fictitious terms. Further, for time integration of the equations of motion the use of Newmark methods are not widespread in the scientific community of multibody dynamics. Therefore, to facilitate the knowledge and experience from classic structural dynamics a Newmark method is investigated for use in the present multibody approach.

In order to model large nonlinear geometrical deformations of especially the blades, the results by use of the present multibody formulation are compared to a co-rotating beam element formulation. These results are based on static analysis to more easily include analytical results in the comparison. Moreover, a key point in the multibody formulation is the algorithm used to update the motion of the moving frame. Here, it is examined which approach that performs best to describe such large deformations.

In order to estimate the eigenfrequencies and mode shapes of the wind turbine it is necessary to investigate how the present multibody approach can be modified to perform such eigenvalue analysis. The eigenfrequencies of an assembled multibody system are necessary to determine if the exterior loading or the angular frequency of the rotor will excite such frequencies. Moreover, the eigenfrequencies are necessary with respect to controlling the wind turbine e.g. by changing the operating conditions to avoid resonances.

As mentioned in the previous section, system reduction is necessary for active control and convenient for parameter studies. Therefore, system reduction for use in the flexible multibody formulation is in focus in the present project. Hereby, it is possible to reduce the number of degrees of freedom in e.g. the blade structures and maintaining the remaining structures with the

---

original element discretization. The blades are the primary area for system reduction because they are the most complex structures and would otherwise require many degrees of freedom. However, the reduction should be more general than the one used for a blade in Appendix C, so the possibility exists of reducing other substructures as well. It is necessary for especially the blades that the reduced models still describe the majority of the blade dynamics especially the nonlinear effects from the large geometric displacements.

In order to describe the dynamics of the blades it is necessary that the cross sectional parameters for the beam elements are determined with a high accuracy. This is especially crucial when the used material in the blades is reduced to optimize the costs. In this project, the cross sectional parameters are determined for a composite blade section, but could be used for any cross section and material distribution. The main focus is to account for the different material layers where they are positioned instead of using average values of the materials in the different parts of the profile.

## 1.3 Published Papers

Below, the published papers during this Ph.D. project are listed. The international journal papers are enclosed in Appendix C, D, and E.

### 1.3.1 Conference Papers

- ◆ Kristian Holm-Jørgensen, Søren R.K. Nielsen, Rune Rubak.  
System Reduction in Nonlinear Multibody Dynamics of Wind Turbines.  
*Proceeding of the 14th International Congress on Sound and Vibration*, Cairns Australia  
9-12 July 2007. The International Institute of Acoustics and Vibration (IIAV), 2007.

### 1.3.2 International Journal Papers

- ◆ Kristian Holm-Jørgensen, Jesper Winther Stærdahl, Søren R.K. Nielsen.  
On the Nonlinear Structural Analysis of Wind Turbine Blades using Reduced Degree-of-Freedom Models.  
*Structural Engineering and Mechanics*, **28**(1), (2008), 107–127.
- ◆ Kristian Holm-Jørgensen, Søren R.K. Nielsen.  
System Reduction in Multibody Dynamics of Wind Turbines.  
*Multibody System Dynamics*. **21**(2), (2009), 147–165.
- ◆ Kristian Holm-Jørgensen, Søren R.K. Nielsen.  
A Component Mode Synthesis Algorithm for Multibody Dynamics of Wind Turbines.  
*Journal of Sound and Vibration*. (2009), to appear.

## 1.4 Overview of the Thesis

- ◆ Chapter 2. The used flexible multibody formulation based on a local observer frame formulation is introduced together with examples of how to specify displacement and rotation joints or constraints. The equations of motion are set up for a constrained multibody system.
  - ◆ Chapter 3. The updating algorithms for dynamic and static analysis are described for updating the moving frame parameters for use in the present multibody formulation. The implementation of the time integration algorithm together with iteration processes are described.
  - ◆ Chapter 4. Large static deformations of a cantilever beam and wind turbine blade are calculated and compared by use of the present multibody formulation and a co-rotating formulation. The effect of using different updating approaches in the static updating algorithm is examined together with convergency of the tip displacement for an increased number of substructures.
  - ◆ Chapter 5. Here, the equations of motion are modified in order to determine the undamped eigenfrequencies and belonging eigenmodes of a multibody system. The primary modification is in the constraint equations.
  - ◆ Chapter 6. A blade substructure in the present multibody formulation is modelled by FE beams and reduced by use of two approaches. In the first, a single substructure is used to model the blade, which is reduced by a proper Ritz basis. In the second, the blade is modelled by two substructures by use of a component mode synthesis method. This method is general for an arbitrary number of substructures and interface restrictions.
  - ◆ Chapter 7. A FE program is created to determine beam properties of an arbitrary cross section. The program is illustrated by the use of a wind turbine blade section and compared to the results of a program used in the wind turbine industry.
  - ◆ Chapter 8. A summary of the main conclusions and issues which need further investigations.
  - ◆ Appendix A. The equations of motion for a constrained substructure in the used multibody formulation are derived.
  - ◆ Appendix B. Cross section parameters for the used wind turbine blade and tower.
  - ◆ Appendix C. Enclosed journal paper: "On the Nonlinear Structural Analysis of Wind Turbine Blades using Reduced Degree-of-Freedom Models".
  - ◆ Appendix D. Enclosed journal paper: "System Reduction in Multibody Dynamics of Wind Turbines".
  - ◆ Appendix E. Enclosed journal paper: "A Component Mode Synthesis Algorithm for Multibody Dynamics of Wind Turbines".
-





---

## CHAPTER 2

# Multibody Formulations with a Moving Frame of Reference

---

In this chapter the multibody formulation in this project is introduced together with the belonging equations of motion. This multibody formulation is based on a Local Observer Frame of Reference formulations, where the rigid body motion relative to the floating frame is eliminated. However, because the moving frame parameters do not enter the system state vector successive update of the belonging moving frame parameters are required. Kinematical constraints are described together with different types of joints common for multibody systems. These displacement and rotation constraints are formulated as vector relations. Normally, constraint equations are differentiated twice with respect to time and solved at the acceleration level. In this project, constraint equations are solved at the displacement and rotation level, to eliminate the need for constraint regularization.

## 2.1 Multibody Formulations Based on a Moving Frame of Reference

### 2.1.1 Introduction

The basic idea of flexible multibody dynamics is to introduce a moving frame of reference to each substructure. Relative to the moving frame elastic displacements are relatively small, rendering linear analysis possible. Hence, nonlinearities are confined to the description of the moving frame. This is defined by a position vector and a parameter vector, also known as a pseudo vector, defining the origin and rotation of the moving frame relative to a fixed frame of reference. The standard formulation of multibody methods requires that there is no rigid body motion between the substructure and its moving frame. The position and orientation of the moving frame is defined by a set of coordinates that describe the rigid body translation and rotation of the substructure. These coordinates become a part of the degrees of freedom of the multibody system, see e.g. Nikraves [3], García and Bayo [4], G  radin and Cardona [5] and Shabana [2]. The use of such a mixed set of referential and elastic coordinates leads to highly non-linear system equations. Further, as a result of the inertial coupling between the said degrees of freedom the mass matrix depends on the referential coordinates, even when formulated in the moving frame. To circumvent these difficulties Kawamoto et al. [1, 6, 7, 8] suggested to let the moving frame of reference float in a controlled way relative to the moving substructure, so these are always

sufficiently close to each other, in order for the small displacement assumption to be fulfilled. In this approach they named the moving frame a Local Observer Frame. The main difference to the standard multibody formulations is that the parameters for the moving frame do not enter as degrees of freedom in the system vector and that it is possible for the substructure to have a small rigid body displacement relative to the moving frame. By explicitly predicting the motion of the moving frame the system matrices no longer depend on the generalized coordinates. To reduce or eliminate the gap between the predicted and actual motion, it is necessary to regularly update the motion of the moving frame of reference as demonstrated in e.g. Kawamoto et al. [8].

In this project the focus is to use this Local Observer Frame formulation for a multibody system. In this chapter the motion of a material point for a deformable substructure relative to a belonging moving frame of reference is described, which is essential for both multibody formulations. Moreover, the way of incorporating kinematical constraints is described. The derived equations of motion are based on a work note by Krenk [9] for an unconstrained substructure, which are extended to a constrained substructure in Appendix A. The chapter is also based on the journal paper attached in Appendix E.

### 2.1.2 Motion of a Deformable Substructure Relative to a Belonging Moving Frame of Reference

In this section the motion of a material point for a deformable substructure relative to a belonging moving frame of reference  $(x_1, x_2, x_3)$  is described. A fixed  $(\bar{x}_1, \bar{x}_2, \bar{x}_3)$ -coordinate system is introduced in order to describe the motion relative to a known fixed position. Accordingly, fixed frame and moving frame components of vectors and tensors will be indicated with and without a bar, respectively. The origin  $c$  of the moving frame of reference relative to the fixed frame is described by a position vector  $\bar{\mathbf{x}}_c$ , see Figure 2.1. Similarly, the rotation of the moving frame relative to the fixed frame is determined by the parameter vector (or pseudo vector)  $\boldsymbol{\theta}$ .

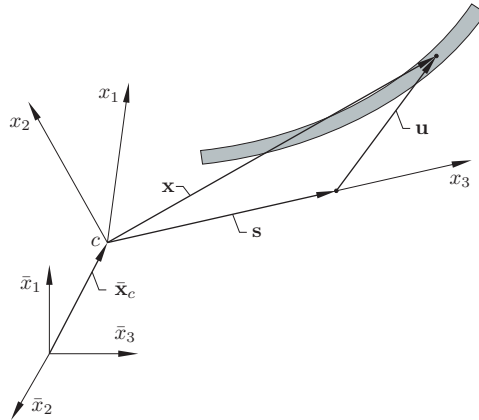


**Figure 2.1** Position of a material point relative to the moving frame of reference  $(x_1, x_2, x_3)$ .

In the following the derivations of the equations for the substructure will be illustrated for a straight Bernoulli-Euler beam structure. The position of a material point on the beam axis

relative to the moving frame of reference is given by

$$\mathbf{x}(\mathbf{s}, t) = \mathbf{s} + \mathbf{u}(\mathbf{s}, t) \quad (2.1)$$

$\mathbf{s}$  is a position vector from the origin of the moving  $(x_1, x_2, x_3)$ -coordinate system to the referential position of the bending center in a given cross-section of the beam.  $\mathbf{u}(\mathbf{s}, t)$  is the displacement of the said material point, see Figure 2.1. In an FE discretization  $\mathbf{u}(\mathbf{s}, t)$  within a beam element is interpolated in the form, see (A.2) in Appendix A.

$$\mathbf{u}(\mathbf{s}, t) = \mathbf{N}(\mathbf{s})\mathbf{y}(t) \quad (2.2)$$

$\mathbf{y}(t)$  contains the degrees of freedom of the element. In an FE beam model they represent the nodal displacements and rotations relative to the moving frame of reference. Next, the position vector of the material point is described in the fixed frame by use of the position vector  $\bar{\mathbf{x}}_c$  and a rotation matrix  $\mathbf{R}$  to rotate the moving frame components of  $\mathbf{x}$  into fixed frame components

$$\bar{\mathbf{x}}(\mathbf{s}, t) = \bar{\mathbf{x}}_c + \mathbf{R}(\mathbf{s} + \mathbf{u}(\mathbf{s}, t)) \quad (2.3)$$

where  $\mathbf{R}$  is defined by the pseudo vector  $\boldsymbol{\theta}$  as given by the Rodriguez formula, see e.g. Shabana [2]

$$\mathbf{R} = \cos \theta \mathbf{I} + (1 - \cos \theta) \mathbf{n} \mathbf{n}^T + \sin \theta \tilde{\mathbf{n}} \quad (2.4)$$

where  $\mathbf{n} = \boldsymbol{\theta}/\theta$  is the rotation unit vector and  $\theta = |\boldsymbol{\theta}|$ . The moving frame components of the velocity and acceleration vector of the material point become cf. (A.9) and (A.14), respectively, in Appendix A

$$\mathbf{v} = \mathbf{v}_c + \tilde{\boldsymbol{\omega}}(\mathbf{s} + \mathbf{u}) + \dot{\mathbf{u}} \quad (2.5)$$

$$\mathbf{a} = \mathbf{a}_c + (\tilde{\boldsymbol{\alpha}} + \tilde{\boldsymbol{\omega}}\tilde{\boldsymbol{\omega}})(\mathbf{s} + \mathbf{u}) + 2\tilde{\boldsymbol{\omega}}\dot{\mathbf{u}} + \ddot{\mathbf{u}} \quad (2.6)$$

where the angular velocity vector  $\boldsymbol{\omega}$  and angular acceleration vector  $\boldsymbol{\alpha}$  of the moving frame of reference have been introduced. The relation between these two moving frame parameters are given by  $\boldsymbol{\alpha} = \dot{\boldsymbol{\omega}}$ .  $\tilde{\boldsymbol{\omega}}$  and  $\tilde{\boldsymbol{\alpha}}$  denote the spin matrices in moving coordinates related to  $\boldsymbol{\omega}$  and  $\boldsymbol{\alpha}$ . The first term  $\mathbf{v}_c$  in (2.5) is the translational velocity of the moving frame, the second term  $\tilde{\boldsymbol{\omega}}(\mathbf{s} + \mathbf{u})$  is the rotational velocity, and the last term  $\dot{\mathbf{u}}$  stores the moving coordinates of the local velocity vector of the material point, i.e. the velocity vectors seen by an observer fixed to the moving frame. The first term  $\mathbf{a}_c$  in (2.6) denotes the translational acceleration of the moving frame origin. The term  $\tilde{\boldsymbol{\alpha}}(\mathbf{s} + \mathbf{u})$  is the angular acceleration which is orthogonal to  $\boldsymbol{\alpha}$  and  $(\mathbf{s} + \mathbf{u})$ . The next term  $\tilde{\boldsymbol{\omega}}\tilde{\boldsymbol{\omega}}(\mathbf{s} + \mathbf{u}) = \boldsymbol{\omega} \times (\boldsymbol{\omega} \times (\mathbf{s} + \mathbf{u}))$  describes the centrifugal acceleration. The Coriolis acceleration in moving coordinates is described by  $2\tilde{\boldsymbol{\omega}}\dot{\mathbf{u}}$  which is perpendicular to both the direction of the local velocity vector of the considered point and to the rotation axis. Finally, the term  $\ddot{\mathbf{u}}$  describes the moving frame components of the acceleration of the material point as seen by an observer in the moving frame.

## 2.2 Constraints to Model Joints

To set up the equations of motion for a multibody system it is necessary to introduce kinematical constraints in order to incorporate compatibility of the mutual displacements and rotations of the

substructures. Moreover, the kinematical constraints are also used to describe joints between the substructures. In relation to wind turbines, displacement constraints between the rotor shaft and the nacelle are specified at the bearings of the nacelle. Rotational constraints are e.g. prescribed between the rotor shaft and the blade substructure in terms of a controlled pitch angle. The kinematic constraints are vector relations with components, which need to be defined in a common coordinate system e.g. a global fixed coordinate system or the moving frame of reference of one of the substructures. In Figure 2.2 six different joints are sketched, redrawn from G  rardin and Cardona [5], which can be used to describe the physical connection between two substructures. The different types are shortly described in the list below:

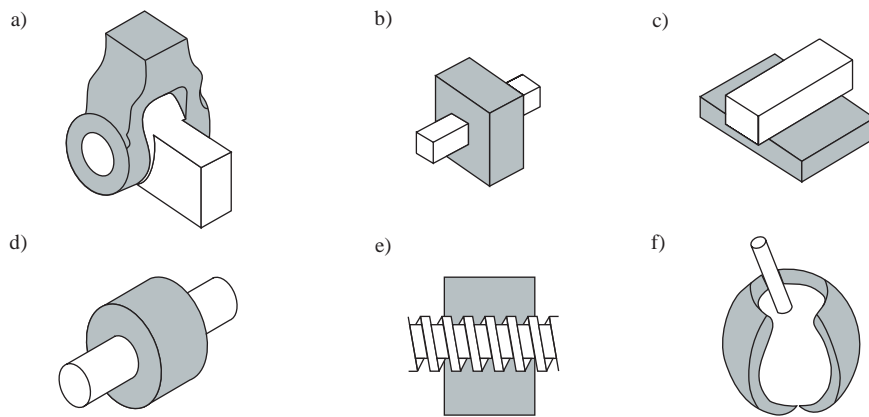


**Figure 2.2** Illustration of different joints between two substructures.

- ◆ a) The revolute or hinge joint: Rotation around one axis is allowed and the remaining three translations and two rotations are fixed.
- ◆ b) The prismatic joint: Translation along one axis is allowed and the remaining five motions are fixed.
- ◆ c) The planar joint: Translation along both axis in the plane and rotation around the direction normal to the plane. The remaining translation and two rotations are fixed.
- ◆ d) The cylindrical joint: Both translation and rotation about the same axis is allowed and the remaining four motions are fixed.
- ◆ e) The screw joint: A cylindrical joint where the translation along the axis is related to the rotation around it.
- ◆ f) A spherical joint: All rotations are free and all translations are fixed.

In the following, examples are given of how to set up kinematical displacement and rotation constraints between two flexible substructures, see Figure 2.3. In the present case it is chosen to fix the displacements and rotations at a common point to secure compatibility at the interface between the two substructures.  $s_{1,0}$  and  $s_{2,0}$  denote the referential position vectors in the respective

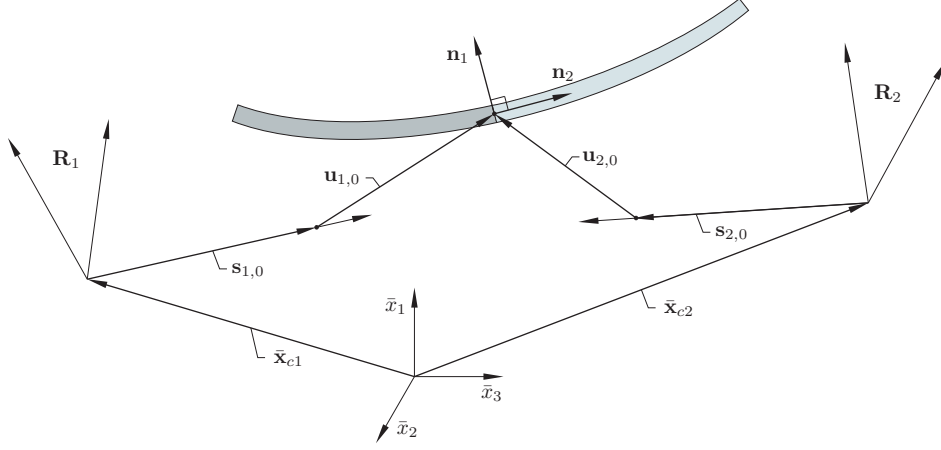


**Figure 2.3** Illustration of two substructures where the kinematical displacement and rotation constraints secure compatibility at the interface between the two substructures.

moving frames, defining a point in substructures 1 and 2 at which a kinematical displacement constraint is specified, and  $\mathbf{u}_{1,0}$  and  $\mathbf{u}_{2,0}$  are the corresponding displacement vectors. In the following a lower index  $i$  define one of the two substructures. A displacement constraint which fixes the position of two arbitrary points becomes, cf. (2.3)

$$\begin{aligned}
 \Phi_{dc} &= \bar{\mathbf{x}}_{c1} + \mathbf{R}_1(\mathbf{s}_{1,0} + \mathbf{u}_{1,0}) - (\bar{\mathbf{x}}_{c2} + \mathbf{R}_2(\mathbf{s}_{2,0} + \mathbf{u}_{2,0})) \\
 &= \bar{\mathbf{x}}_{c1} + \mathbf{R}_1(\mathbf{s}_{1,0} + \mathbf{N}_{1,0}\mathbf{y}_1) - (\bar{\mathbf{x}}_{c2} + \mathbf{R}_2(\mathbf{s}_{2,0} + \mathbf{N}_{2,0}\mathbf{y}_2)) \\
 &= \mathbf{B}_{d,1}\mathbf{y}_1 - \mathbf{B}_{d,2}\mathbf{y}_2 - \mathbf{b} = \mathbf{0} \\
 \mathbf{B}_{d,i} &= \mathbf{R}_i\mathbf{N}_{i,0} \quad , \quad \mathbf{b} = -(\bar{\mathbf{x}}_{c1} + \mathbf{R}_1\mathbf{s}_{1,0}) + (\bar{\mathbf{x}}_{c2} + \mathbf{R}_2\mathbf{s}_{2,0})
 \end{aligned} \tag{2.7}$$

In an FE formulation,  $\mathbf{u}_i(\mathbf{s}_i, t)$  is interpolated by a set of shape functions  $\mathbf{N}_i(\mathbf{s}_i)$  and degrees of freedom  $\mathbf{y}_i(t)$ ,  $\mathbf{u}_{i,0}(t) = \mathbf{N}_{i,0}\mathbf{y}_i(t)$ , where  $\mathbf{N}_{i,0} = \mathbf{N}_i(\mathbf{s}_{i,0})$ . Further,  $\mathbf{R}_1$  and  $\mathbf{R}_2$  represent the rotation tensors of the moving frames relative to the global coordinate system. Let  $\boldsymbol{\varphi}_{i,0}$  denote the parameter vector of the local rotation tensor of the interface node relative to the moving frame of substructure  $i$ . The rotation tensor of the said node relative to the global coordinate system is then given by

$$\mathbf{R}_i^* = \mathbf{R}_i\mathbf{R}(\boldsymbol{\varphi}_{i,0}) \simeq \mathbf{R}_i(\mathbf{I} + \tilde{\boldsymbol{\varphi}}_{i,0}) \tag{2.8}$$

where the indicated linearization presumes  $|\boldsymbol{\varphi}_{0,i}| \ll 1$ .  $\boldsymbol{\varphi}_{i,0}$  may then be interpreted as the components of the rotation vector relative to the moving frame of reference. Let  $\mathbf{n}_1$  and  $\mathbf{n}_2$  be the local components in the moving coordinate systems of unit vectors attached to the interface nodes in substructures 1 and 2. The rotation of these vectors is given as  $\mathbf{R}_1^*\mathbf{n}_1$  and  $\mathbf{R}_2^*\mathbf{n}_2$ , respectively. Assume, that the vectors before and during the elastic deformation of the interface nodes remain orthogonal. Then the rotational constraint can be specified as

$$\Phi_{rc} = (\mathbf{R}_1^*\mathbf{n}_1)^T \mathbf{R}_2^*\mathbf{n}_2 = 0 \tag{2.9}$$

A total of three scalar products are necessary to fix the rotations in the joint. By insertion of (2.8) in (2.9) the rotational constraint becomes

$$\begin{aligned}\Phi_{rc} &= \mathbf{n}_2^T \mathbf{R}_2^T \mathbf{R}_1 \tilde{\mathbf{n}}_1 \varphi_{1,0} + \mathbf{n}_1^T \mathbf{R}_1^T \mathbf{R}_2 \tilde{\mathbf{n}}_2 \varphi_{2,0} - \mathbf{n}_1^T \mathbf{R}_1^T \mathbf{R}_2 \mathbf{n}_2 + \varphi_{1,0}^T \tilde{\mathbf{n}}_1 \mathbf{R}_1^T \mathbf{R}_2 \tilde{\mathbf{n}}_2 \varphi_{2,0} \\ &= \mathbf{n}_2^T \mathbf{R}_2^T \mathbf{R}_1 \tilde{\mathbf{n}}_1 \mathbf{P}_{1,0} \mathbf{y}_1 + \mathbf{n}_1^T \mathbf{R}_1^T \mathbf{R}_2 \tilde{\mathbf{n}}_2 \mathbf{P}_{2,0} \mathbf{y}_2 \\ &\quad - \mathbf{n}_1^T \mathbf{R}_1^T \mathbf{R}_2 \mathbf{n}_2 + (\mathbf{P}_{1,0} \mathbf{y}_1)^T \tilde{\mathbf{n}}_1 \mathbf{R}_1^T \mathbf{R}_2 \tilde{\mathbf{n}}_2 \mathbf{P}_{2,0} \mathbf{y}_2\end{aligned}\quad (2.10)$$

$$= \mathbf{B}_{r,1} \mathbf{y}_1 + \mathbf{B}_{r,2} \mathbf{y}_2 - \mathbf{b} = 0 \quad (2.11)$$

$$\begin{aligned}\mathbf{B}_{r,1} &= \mathbf{n}_2^T \mathbf{R}_2^T \mathbf{R}_1 \tilde{\mathbf{n}}_1 \mathbf{P}_{1,0} \quad , \quad \mathbf{b} = \mathbf{n}_1^T \mathbf{R}_1^T \mathbf{R}_2 \mathbf{n}_2 - (\mathbf{P}_{1,0} \mathbf{y}_1)^T \tilde{\mathbf{n}}_1 \mathbf{R}_1^T \mathbf{R}_2 \tilde{\mathbf{n}}_2 \mathbf{P}_{2,0} \mathbf{y}_2 \quad , \\ \mathbf{B}_{r,2} &= \mathbf{n}_1^T \mathbf{R}_1^T \mathbf{R}_2 \tilde{\mathbf{n}}_2 \mathbf{P}_{2,0}\end{aligned}\quad (2.12)$$

The components of the local rotation vectors are determined by  $\varphi_{i,0} = \mathbf{P}_{i,0} \mathbf{y}_i$ , where  $\mathbf{P}_i(\mathbf{s}_i)$  represents the compatible rotations derived from the shape functions. Hereby, (2.7) becomes linear in  $\mathbf{y}_i$  whereas quadratic nonlinearities appear in (2.11) via the term  $\mathbf{b}$ . This necessitates an iteration approach, where predicted values of  $\mathbf{y}_1$  and  $\mathbf{y}_2$  are inserted.

Another possibility is to use the following Cayley approach [5], instead of the approximation in (2.8).

$$\mathbf{R}_i^* = \mathbf{R}_i \mathbf{R}(\varphi_{i,0}) \simeq \mathbf{R}_i \left( (\mathbf{I} - \frac{1}{2} \tilde{\varphi}_{i,0})^{-1} (\mathbf{I} - \frac{1}{2} \tilde{\varphi}_{i,0}) \right) \quad (2.13)$$

The advantage of this approximation is that the unit vectors in  $\mathbf{R}_i^*$  remain unit vectors which is not the case in (2.8). The rotation tensor (2.13) of the node can be implemented similarly to (2.8) where the term  $(\mathbf{I} - \frac{1}{2} \tilde{\varphi}_{i,0})^{-1}$  is evaluated based on the predicted values of  $\mathbf{y}_1$  and  $\mathbf{y}_2$ . However, it has not been possible to get this approach to converge. A possibility could be to use (2.8) in the initial iteration and then switch to (2.13), but this has not been examined.

## 2.3 Equations of Motion for a Constrained Substructure based on a Local Observer Frame Formulation

In this section the equations of motion for a constrained substructure based on the Local Observer Frame formulation are described. The equations of motion of the substructure  $i$  are conveniently derived by analytical mechanics using an extended Lagrangian to account for the kinematic constraints, in combination to the kinetic energy  $T = T(\mathbf{y}_i, \dot{\mathbf{y}}_i)$  and the potential energy  $U = U(\mathbf{y}_i)$  from all substructures. The latter contains contribution from the strain energy and conservative external loads  $\mathbf{Q}_{c,i}(\mathbf{y}_i)$  such as gravity, in addition to vectorial quantities as the non-conservative loads  $\mathbf{Q}_{nc,i}(\mathbf{y}_i)$ . In principle, these loads may be linearized in the applied moving frame of reference. The non-conservative loads are caused by the follower character of the aerodynamic loads. The kinetic energy is most convenient determined by use of the moving frame components of the velocity vector  $\mathbf{v}$  from (2.5). In a slightly modified version of those given by Kawamoto et al. [6] the resulting equations become

$$\begin{aligned}\mathbf{M}_i \ddot{\mathbf{y}}_i + \left( \mathbf{C}_{0,i} + 2\mathbf{G}_i \right) \dot{\mathbf{y}}_i + \left( \mathbf{K}_{e,i} + \dot{\mathbf{G}}_i + \mathbf{D}_i + \mathbf{K}_{g,i} \right) \mathbf{y}_i + \mathbf{B}_i^T(\mathbf{y}_i) \bar{\boldsymbol{\lambda}}_i = \\ -\mathbf{M}_{0,i}^T \mathbf{a}_{c,i} - \dot{\mathbf{J}}_{0,i}^T + \mathbf{J}_{2,i}^T + \mathbf{Q}_{c,i}(\mathbf{y}_i) + \mathbf{Q}_{nc,i}(\mathbf{y}_i)\end{aligned}\quad (2.14)$$

where the Lagrange multipliers  $\bar{\boldsymbol{\lambda}}_i$  contain the global components of the reaction forces and moments conjugated to the kinematic constraints and  $\mathbf{B}_i^T(\mathbf{y}_i)$  is the constraint matrix. Because



the constraints have been formulated in the fixed frame of reference the vector of Lagrange multipliers  $\bar{\lambda}$  is also specified in the fixed frame. The symmetric matrices  $\mathbf{C}_{0,i}$  and  $\mathbf{K}_{e,i}$  denote the structural damping and elastic stiffness matrix, respectively. The latter includes bending, torsional, and axial stiffnesses.  $\mathbf{K}_{g,i}$  denotes the geometrical stiffness matrix. For a beam-like substructure of the length  $L$  this may be written as

$$\mathbf{K}_{g,i} = \Omega^2(t) \int_L Q_3(x_3, t) \frac{d\mathbf{N}_{g,i}^T}{dx_3} \frac{d\mathbf{N}_{g,i}}{dx_3} dx_3 \quad (2.15)$$

where  $Q_3(x_3, t)$  represents the distribution of the centrifugal axial force for  $\Omega = 1$ , so  $\Omega^2(t)Q_3(x_3, t)$  denotes the axial force at the position  $x_3$ .  $\mathbf{N}_{g,i}$  includes the two first rows in  $\mathbf{N}_i$  which represent the two displacement components orthogonal to the beam axis. For a wind turbine blade the axial load is caused by the centrifugal and gravity forces. During operation the geometric stiffness from the centrifugal axial force will assist to stretch out the blade corresponding to an increased stiffness and thereby reduce the displacements in the flap direction. Moreover, this term has shown to increase the stability of the numerical model. The other matrices and vectors are defined as

$$\mathbf{M}_i = \int_L \mathbf{N}_i^T \mathbf{N}_i \mu dx_3 \quad , \quad \mathbf{M}_{0,i} = \int_L \mathbf{N}_i \mu dx_3 \quad , \quad \mathbf{D}_i = \int_L \mathbf{N}_i^T \tilde{\omega}_i \tilde{\omega}_i \mathbf{N}_i \mu dx_3 \quad (2.16)$$

$$\mathbf{G}_i = \int_L \mathbf{N}_i^T \tilde{\omega}_i \mathbf{N}_i \mu dx_3 \quad , \quad \mathbf{J}_{0,i} = \omega_i^T \int_L \tilde{\mathbf{s}} \mathbf{N}_i \mu dx_3 \quad , \quad \mathbf{J}_{2,i} = \omega_i^T \int_L \tilde{\omega}_i \mathbf{N}_i \mu dx_3 \quad (2.17)$$

$$\dot{\mathbf{G}}_i = \int_L \mathbf{N}_i^T \tilde{\alpha}_i \mathbf{N}_i \mu dx_3 \quad , \quad \dot{\mathbf{J}}_{0,i} = \alpha_i^T \int_L \tilde{\mathbf{s}} \mathbf{N}_i \mu dx_3 \quad (2.18)$$

$\mathbf{M}_i$  is the conventional symmetric mass matrix of the substructure in the moving frame of reference, which in the present formulation is independent of the moving frame of reference parameters.  $\mu = \mu(s)$  denotes the mass per unit length.  $\mathbf{M}_{0,i}$  is a matrix representing the inertial effect of uniform translation. The effect of centrifugal forces due to elastic deformations is contained in the symmetric matrix  $\mathbf{D}_i$  and the gyroscopic forces are represented by the skew symmetric matrix  $\mathbf{G}_i$ . The remaining  $\mathbf{J}_{0,i}$  and  $\mathbf{J}_{2,i}$  terms are couplings between the reference position and the shape functions. In Kawamoto et al. [8] it is shown how  $\mathbf{D}_i$ ,  $\mathbf{G}_i$ , and  $\dot{\mathbf{G}}_i$  can be simplified by extracting  $\tilde{\omega}_i$  and  $\tilde{\alpha}_i$  outside the integration for isoparametric volume elements. For ease the non-linearity displayed by the dependency of  $\mathbf{y}_i$  in the load vector is neglected, whereby the equations of motion conveniently are written in the form

$$\mathbf{M}_i \ddot{\mathbf{y}}_i + \mathbf{C}_i \dot{\mathbf{y}}_i + \mathbf{K}_i \mathbf{y}_i + \mathbf{B}_i^T(\mathbf{y}_i) \bar{\lambda}_i = \mathbf{f}_i(t) \quad (2.19)$$

where

$$\mathbf{C}_i = \mathbf{C}_{0,i} + 2\mathbf{G}_i \quad , \quad \mathbf{K}_i = \mathbf{K}_{e,i} + \dot{\mathbf{G}}_i + \mathbf{D}_i + \mathbf{K}_{g,i} \quad (2.20)$$

$$\mathbf{f}_i(t) = -\mathbf{M}_{0,i}^T \mathbf{a}_{c,i} - \dot{\mathbf{J}}_{0,i}^T + \mathbf{J}_{2,i}^T + \mathbf{Q}_{c,i} + \mathbf{Q}_{nc,i} \quad (2.21)$$

$\mathbf{C}_i$  and  $\mathbf{K}_i$  may be interpreted as resulting non-symmetric damping and stiffness matrices for the unconstrained substructure.

Next, the global equations of motion are formulated by combining the equation of motion (2.19) for each substructure with the kinematical constraints (2.7) and (2.11). From the structure

of these kinematical constraints it can be seen that they can be included in the system stiffness matrix. Often in multibody dynamics the constraints are differentiated twice with respect to time and inserted in the system mass matrix. Next, constraint regularization is used to ensure that the constraints are satisfied on the displacement and velocity level. In the present approach the constraints are solved as they originally are formulated i.e. as actual displacements and rotations, and it is therefore not necessary with constraint regularization. For ease the equations of motion is only demonstrated for a multibody system consisting of 2 substructures where the equations attain the form

$$\begin{bmatrix} \mathbf{M}_1 & \mathbf{0} & \mathbf{0} \\ \mathbf{0} & \mathbf{M}_2 & \mathbf{0} \\ \mathbf{0} & \mathbf{0} & \mathbf{0} \end{bmatrix} \begin{bmatrix} \ddot{\mathbf{y}}_1 \\ \ddot{\mathbf{y}}_2 \\ \ddot{\bar{\lambda}} \end{bmatrix} + \begin{bmatrix} \mathbf{C}_1 & \mathbf{0} & \mathbf{0} \\ \mathbf{0} & \mathbf{C}_2 & \mathbf{0} \\ \mathbf{0} & \mathbf{0} & \mathbf{0} \end{bmatrix} \begin{bmatrix} \dot{\mathbf{y}}_1 \\ \dot{\mathbf{y}}_2 \\ \dot{\bar{\lambda}} \end{bmatrix} + \begin{bmatrix} \mathbf{K}_1 & \mathbf{0} & \mathbf{B}_1^T \\ \mathbf{0} & \mathbf{K}_2 & \mathbf{B}_2^T \\ \mathbf{B}_1 & \mathbf{B}_2 & \mathbf{0} \end{bmatrix} \begin{bmatrix} \mathbf{y}_1 \\ \mathbf{y}_2 \\ \bar{\lambda} \end{bmatrix} = \begin{bmatrix} \mathbf{f}_1 \\ \mathbf{f}_2 \\ \mathbf{b} \end{bmatrix} \Rightarrow$$

$$\mathbf{M}\ddot{\mathbf{z}} + \mathbf{C}\dot{\mathbf{z}} + \mathbf{K}\mathbf{z} = \mathbf{f}(t) \quad (2.22)$$

where  $\bar{\lambda} = \bar{\lambda}_1 = -\bar{\lambda}_2$ . It should be noted that the constraints in principle can be set up in a arbitrary coordinate system, whereby the components of  $\bar{\lambda}$  will be in that chosen coordinate system.

Because the constraints in principle introduce infinite stiffness into the global system it becomes necessary to apply unconditional stable time integrators. In the present case this is achieved by means of a non-linear Newmark algorithm. The use of Newmark methods is not widespread in the scientific community of multibody dynamics. However, according to G  radin and Cardona [5], fully implicit algorithms such as the Newmark algorithm are very useful when dealing specifically with flexible multibody dynamics. In the aeroelastic multibody wind turbine code HawC2 a Newmark algorithm is also used according to Hansen [10]. The implementation of the non-linear Newmark algorithm and the updating algorithm of the moving frame parameters are described in the next chapter.

## 2.4 Concluding Remarks

In this chapter the multibody formulation based on a Local Observer Frame has been described with the equations of motion for a multibody system consisting of substructures and a number of kinematical constraints. The used method of implementing kinematical constraints is described for both displacements and rotations based on vector relations. These constraints are solved as they originally are formulated i.e. as actual displacements and rotations, and the constraint matrix hereby enters the system stiffness matrix. By use of the present multibody approach it is necessary to update the moving frame parameters by an algorithm because they are not included in the system vector as in the standard multibody formulation. This will be described in the following chapter.

---

## CHAPTER 3

# Update Algorithms of the Moving Frame of Reference

---

In this chapter it is described how the moving frame of reference and the belonging substructure are updated for dynamic and static analysis. The presented algorithms are constructed with a beam element model in focus but could be used for other kinds of elements. The algorithm for dynamic simulations makes use of the motion of the two boundary nodes in the substructure to update the belonging moving frame to ensure this frame is close to the actual deformed structure. Finally, two updating methods are described for static analysis, where one makes use of the motion at the origin of the substructure to update the moving frame. In the other method the moving frame is updated based on the motion of both boundary nodes.

### 3.1 Introduction

In the standard floating frame of reference formulation see e.g. Nikravesh [3], García and Bayo [4], G  radin and Cardona [5] and Shabana [2], the coordinates describing the motion of the moving frame of reference are a part of the system state vector, and thereby automatically updated when the equations of motion are solved. In the present multibody formulation where the motion of the moving frame is predicted and these coordinates do not enter the system state vector, it is necessary to regularly update the motion of the moving frame of reference as demonstrated in Kawamoto et al. [8] to reduce or eliminate the gap between the predicted and actual motion. In Kawamoto et al. [1] the updating scheme is originally described, where the orientation, angular velocity, and angular acceleration of the moving frame are updated based on a local triad linked to four nodes in the substructure. In Kawamoto et al. [6] the local triad is updated based on a polar decomposition. In Kawamoto et al. [7, 8] rigid body modes are used to update the motion of the moving frame. The updating scheme of the moving frame of reference in this chapter follows the same principles as described in Kawamoto et al. [6]. A small change when updating the moving frame is presented, where the orientation of the moving frame is updated based on the motion of two boundary nodes. It is possible to use other nodes than the boundary nodes in the updating procedure.

### 3.2 Update Algorithm for Dynamic Simulations

In this section the update algorithm of the moving frame of reference for dynamic simulations is described. This algorithm is based on the description in the enclosed paper in Appendix E.

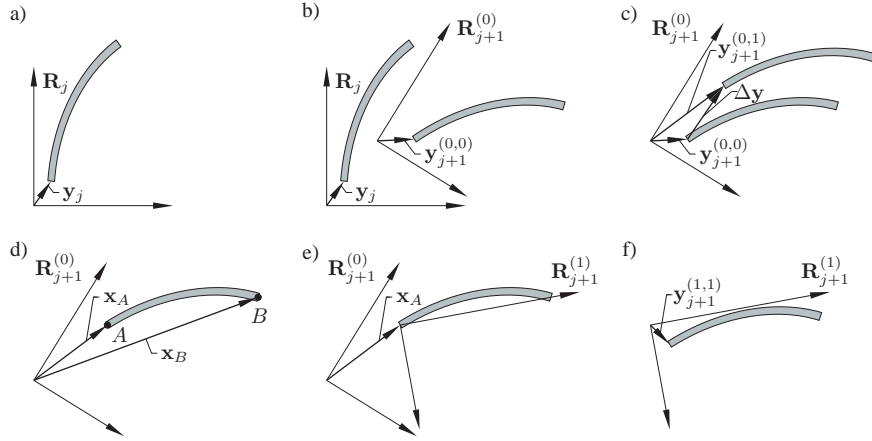


**Figure 3.1** a) Moving frame and substructure at the initial situation at time  $t = t_j$ . b) Prediction of moving frame and system state vector at time  $t_{j+1} = t_j + \Delta t$ . c) Determination of the system state vector for the first iteration step. d) Updating of the moving frame based on the converged motion of two boundary nodes. e) Updated position and orientation of the moving frame. f) Determination of the system state vector referring the motion of the substructure to the updated moving frame of reference.

At first an introductory overview of the following updating algorithm will be given based on a number of 2D illustrations depicted in Figure 3.1. The orientation of the moving frame of reference defined by the related rotation tensor  $\mathbf{R}(t)$  has been indicated at various levels of the updating procedure.  $\mathbf{y}(t)$  contains all the interior and boundary degrees of freedom of the moving substructure relative to the origin of the belonging moving frame.  $\mathbf{y}(t)$  is a part of the state vector  $\mathbf{z}(t)$  in (2.22), which is the variable actually solved for. However, for the purpose of illustrating the steps in the updating process,  $\mathbf{y}(t)$  is used to symbolically indicate the position vector of the interface node, see Figure 3.1a. At the time  $t = t_j$  the system state vector  $\mathbf{z}_j = \mathbf{z}(t_j)$  along with its time derivatives  $\dot{\mathbf{z}}_j = \dot{\mathbf{z}}(t_j)$  and  $\ddot{\mathbf{z}}_j = \ddot{\mathbf{z}}(t_j)$  are known. Additionally, several parameters describing the motion of the moving frame of reference for the substructure are known. These are the global components of the position vector of the origin  $\bar{\mathbf{x}}_{c,j} = \bar{\mathbf{x}}_c(t_j)$ , the related velocity vector  $\bar{\mathbf{v}}_{c,j} = \bar{\mathbf{v}}_c(t_j)$ , and acceleration vector  $\bar{\mathbf{a}}_{c,j} = \bar{\mathbf{a}}_c(t_j)$ , as well as the components of the rotation tensor  $\mathbf{R}_j = \mathbf{R}(t_j)$  and the moving frame components of the angular velocity and angular acceleration vectors  $\boldsymbol{\omega}_j = \boldsymbol{\omega}(t_j)$ , and  $\boldsymbol{\alpha}_j = \boldsymbol{\alpha}(t_j)$ , respectively. All these known parameters and system vectors make the starting point at the determination of the corresponding quantities at the new time  $t_{j+1} = t_j + \Delta t$ , on condition that the new load vector  $\mathbf{f}_{j+1} = \mathbf{f}(t_{j+1})$  can be calculated. In what follows an upper index ( $k_1$ ) is used to specify the updating step of the moving frame of reference parameters within the time step. Similarly, an upper index ( $k_1, k_2$ ) is used for the system state vector, where  $k_2$  indicates the iteration step of the system state vector within the present updating step  $k_1$  of the moving frame of reference. When determining the motion of the multibody system it is necessary that both the moving frame parameters and system state vector have the same upper index  $k_1$ . Initially, predicted values based on simple Taylor expansions for the vectors related to the moving frame and the moving substructure at the time  $t_{j+1}$  are determined from the corresponding values at time  $t_j$ . Predicted values are denoted with an upper index  $k_1 = k_2 = 0$ , and the prediction step has been sketched in Figure 3.1b. Next, the equations of motion (2.22) are solved with the predicted values entering the system matrices

and vectors. Hereby, the nodal displacement vector for the first iteration  $\mathbf{y}_{j+1}^{(0,1)}$  together with its time derivatives are determined, see Figure 3.1c.  $\Delta\mathbf{y}$  indicates the displacement difference between predicted and corrected estimates, which should be below a chosen convergency limit for the nonlinear constraints to be converged. This is where the upper index  $k_2$  is increased for each iteration until the substructure motion relative to the present moving frame parameters is converged. When the system state vector has converged it may be necessary to update as well the moving frame of reference. The position of the moving frame origin together with its time derivatives are updated based on the motion of the belonging boundary node of the substructure. The orientation together with angular velocity and angular acceleration are updated by use of the motion of two boundary nodes. In Figure 3.1d both nodes are sketched, where they have been labelled  $A$  and  $B$  and the position vector in (2.1) from the origin of the moving frame to these nodes is denoted  $\mathbf{x}_A$  and  $\mathbf{x}_B$ , respectively. In Figure 3.1e the updated position and orientation of the moving frame of reference are illustrated. In order to specify the substructure motion relative to the new updated moving frame it is necessary to solve the equations of motion with updated system matrices and vectors. Hereby, a new nodal displacement vector  $\mathbf{y}_{j+1}^{(1,1)}$  is determined referring the motion of the substructure to the updated moving frame of reference given by the rotation tensor  $\mathbf{R}_{j+1}^{(1)}$ , see Figure 3.1f. This updating of the moving frame of reference within the time step continues a predefined number of times. For each update it is necessary to iterate the belonging substructure motion.

Next, the indicated updating algorithm is described in a formal way. At the instant of time  $t = t_{j+1}$  the vectors related to the origin of the moving frame of reference are predicted by the truncated Taylor expansions of the solution from the previous time step

$$\bar{\mathbf{x}}_{c,j+1}^{(0)} = \bar{\mathbf{x}}_{c,j} + \bar{\mathbf{v}}_{c,j}\Delta t + \frac{1}{2}\bar{\mathbf{a}}_{c,j}\Delta t^2, \quad \bar{\mathbf{v}}_{c,j+1}^{(0)} = \bar{\mathbf{v}}_{c,j} + \bar{\mathbf{a}}_{c,j}\Delta t, \quad \bar{\mathbf{a}}_{c,j+1}^{(0)} = \bar{\mathbf{a}}_{c,j} \quad (3.1)$$

$\bar{\mathbf{x}}_{c,j+1}^{(0)}$  is used in the displacement constraints (2.7). The moving frame components of the vectors defining the rotation of the moving frame of reference are similarly predicted by the Taylor expansions

$$\Delta\boldsymbol{\psi}_{j+1}^{(0)} = \boldsymbol{\omega}_j\Delta t + \frac{1}{2}\boldsymbol{\alpha}_j\Delta t^2, \quad \boldsymbol{\omega}_{j+1}^{(0)} = \boldsymbol{\omega}_j + \boldsymbol{\alpha}_j\Delta t, \quad \boldsymbol{\alpha}_{j+1}^{(0)} = \boldsymbol{\alpha}_j \quad (3.2)$$

$\Delta\boldsymbol{\psi}_{j+1}^{(0)}$  denotes the moving frame components of the predicted rotation vector of the moving frame during the interval  $\Delta t$ . The rotation tensor  $\mathbf{R}_{j+1}^{(0)}$ , corresponding to the moving frame orientation after the rotation  $\Delta\boldsymbol{\psi}_{j+1}^{(0)}$ , is next determined by use of Rodriguez formula (A.4)

$$\mathbf{R}_{j+1}^{(0)} = \mathbf{R}_j\mathbf{R}(\Delta\boldsymbol{\psi}_{j+1}^{(0)}) \quad (3.3)$$

In (2.21) the moving frame components of the acceleration of the origin are needed. These are determined from the corresponding global components via the transformation

$$\mathbf{a}_{c,j+1}^{(0)} = \mathbf{R}_{j+1}^{(0)T}\bar{\mathbf{a}}_{c,j+1}^{(0)} \quad (3.4)$$

Next, the system state vector are predicted based on the truncated Taylor expansions

$$\mathbf{z}_{j+1}^{(0,0)} = \mathbf{z}_j + \dot{\mathbf{z}}_j\Delta t + \frac{1}{2}\ddot{\mathbf{z}}_j\Delta t^2, \quad \dot{\mathbf{z}}_{j+1}^{(0,0)} = \dot{\mathbf{z}}_j + \ddot{\mathbf{z}}_j\Delta t, \quad \ddot{\mathbf{z}}_{j+1}^{(0,0)} = \ddot{\mathbf{z}}_j \quad (3.5)$$

Hereby, all predicted parameters for the moving frame of reference together with the predicted system state vector are determined. The damping matrix  $\mathbf{C}^{(0)}$ , stiffness matrix  $\mathbf{K}^{(0)}$ , and mass matrix  $\mathbf{M}$  from (2.22) are next determined. Here, it should be noted that the mass matrix is independent of the moving frame parameters and thereby constant. In order to solve (2.22) the residual  $\mathbf{r}$  and equivalent system stiffness matrix  $\hat{\mathbf{K}}$  are determined by use of the nonlinear Newmark algorithm, G radin and Rixen [11]

$$\mathbf{r} = -\mathbf{M}\ddot{\mathbf{z}}_{j+1}^{(0,0)} - \mathbf{C}^{(0)}\dot{\mathbf{z}}_{j+1}^{(0,0)} - \mathbf{K}^{(0)}\mathbf{z}_{j+1}^{(0,0)} + \mathbf{f}_{j+1}^{(0)}, \quad \hat{\mathbf{K}} = \frac{1}{\beta\Delta t^2}\mathbf{M} + \frac{\gamma}{\beta\Delta t}\mathbf{C}^{(0)} + \mathbf{K}^{(0)} \quad (3.6)$$

where  $\gamma = \frac{1}{2} + \alpha$ ,  $\beta = \frac{1}{4}(1 + \alpha)^2$ , and  $\alpha$  is used to incorporate numerical damping. Newmark integration by use of  $(\beta, \gamma = \frac{1}{4}, \frac{1}{2})$  does not guarantee unconditional stability for nonlinear systems. By solving  $\hat{\mathbf{K}}\Delta\mathbf{z} = \mathbf{r}$  for the unknowns  $\Delta\mathbf{z}$ , the following corrected values of the system state vector are determined

$$\mathbf{z}_{j+1}^{(0,1)} = \mathbf{z}_{j+1}^{(0,0)} + \Delta\mathbf{z}, \quad \dot{\mathbf{z}}_{j+1}^{(0,1)} = \dot{\mathbf{z}}_{j+1}^{(0,0)} + \frac{\gamma}{\beta\Delta t}\Delta\mathbf{z}, \quad \ddot{\mathbf{z}}_{j+1}^{(0,1)} = \ddot{\mathbf{z}}_{j+1}^{(0,0)} + \frac{1}{\beta\Delta t^2}\Delta\mathbf{z} \quad (3.7)$$

Hereby the displacement and rotation degrees of freedom of the substructure referred to the moving frame of reference can be determined together with their time derivatives. The converged substructure displacements and rotations at the boundaries are referred to as  $\mathbf{u}_A$ ,  $\varphi_A$ , and  $\mathbf{u}_B$ ,  $\varphi_B$ . The same notation follows for the time derivatives of the displacements and rotations. The position, velocity and acceleration of the origin of the moving frame of reference are updated by use of (2.3), (2.5) and (2.6)

$$\bar{\mathbf{x}}_{c,j+1}^{(k+1)} = \bar{\mathbf{x}}_{c,j+1}^{(k)} + \mathbf{R}_{j+1}^{(k)}\mathbf{u}_A \quad (3.8)$$

$$\bar{\mathbf{v}}_{c,j+1}^{(k+1)} = \bar{\mathbf{v}}_{c,j+1}^{(k)} + \mathbf{R}_{j+1}^{(k)}\left(\tilde{\boldsymbol{\omega}}_{j+1}^{(k)}(\mathbf{s} + \mathbf{u}_A) + \dot{\mathbf{u}}_A\right) \quad (3.9)$$

$$\bar{\mathbf{a}}_{c,j+1}^{(k+1)} = \bar{\mathbf{a}}_{c,j+1}^{(k)} + \mathbf{R}_{j+1}^{(k)}\left((\tilde{\boldsymbol{\alpha}}_{j+1}^{(k)} + \tilde{\boldsymbol{\omega}}_{j+1}^{(k)}\tilde{\boldsymbol{\omega}}_{j+1}^{(k)})(\mathbf{s} + \mathbf{u}_A) + 2\tilde{\boldsymbol{\omega}}_{j+1}^{(k)}\dot{\mathbf{u}}_A + \ddot{\mathbf{u}}_A\right) \quad (3.10)$$

In the following, the update of the orientation, angular velocity and angular acceleration of the moving frame of reference is described, which is based on the motion of both boundary nodes  $A$  and  $B$ . The purpose of the present update is to align the beam axis and thereby the  $x_3$ -axis so it passes through both nodes. In order to determine the orientation of the remaining  $x_1$ - and  $x_2$ -axes the average rotation  $\varphi_3$  around the beam axis is used, which is given by the third rotation component at the two nodes

$$\varphi_3 = \frac{1}{2}(\varphi_{B,3} + \varphi_{A,3}) \quad (3.11)$$

Then, the two basis vectors  $\mathbf{n}_1$  and  $\mathbf{n}_2$  for the  $x_1$ - and  $x_2$ -axis are given as

$$\begin{bmatrix} \mathbf{n}_1 & \mathbf{n}_2 & \mathbf{n}_3 \end{bmatrix} = \begin{bmatrix} \cos \varphi_3 & -\sin \varphi_3 & 0 \\ \sin \varphi_3 & \cos \varphi_3 & 0 \\ 0 & 0 & 1 \end{bmatrix} \quad (3.12)$$

The purpose is to rotate the full basis through the minimum angle bringing one of the vectors into a given new direction. In the present case the vector  $\mathbf{n}_3$  is to be rotated into the direction of the beam axis defined by the unit vector  $(\mathbf{x}_B - \mathbf{x}_A)/|\mathbf{x}_B - \mathbf{x}_A|$ , where  $\mathbf{x}_A$  and  $\mathbf{x}_B$  are the

position vectors of the end nodes relative to the moving frame origin cf. Figure 3.1d. First, the mean direction is defined by the unit vector  $\mathbf{n}$

$$\mathbf{n} = \mathbf{n}_3 + \frac{\mathbf{x}_B - \mathbf{x}_A}{|\mathbf{x}_B - \mathbf{x}_A|}, \quad \mathbf{n} := \mathbf{n}/|\mathbf{n}| \quad (3.13)$$

Next, a Householder transformation is used, which corresponds to a reflection in the plane orthogonal to the unit vector  $\mathbf{n}$ , Krenk [12]

$$\Delta \mathbf{R} = (\mathbf{I} - 2\mathbf{n}\mathbf{n}^T) \begin{bmatrix} \mathbf{n}_1 & \mathbf{n}_2 & -\mathbf{n}_3 \end{bmatrix} \quad (3.14)$$

Hereby, a new set of unit vectors contained in  $\Delta \mathbf{R}$  are determined, which describe the updated orientation seen from the present orientation of the moving frame of reference. The updated rotation tensor is given by

$$\mathbf{R}_{j+1}^{(k+1)} = \mathbf{R}_{j+1}^{(k)} \Delta \mathbf{R} \quad (3.15)$$

In order to update the angular velocity it is used that the global components of the velocity at node  $B$  should be the same in the present known configuration of the moving frame and in the updated one. The global components of the velocity at node  $B$  are determined by use of (2.5)

$$\bar{\mathbf{v}}_B = \bar{\mathbf{v}}_{c,j+1}^{(k)} + \mathbf{R}_{j+1}^{(k)} \left( \tilde{\boldsymbol{\omega}}_{j+1}^{(k)} (\mathbf{s}_B + \mathbf{u}_B) + \dot{\mathbf{u}}_B \right) \quad (3.16)$$

where  $\mathbf{s}_B$  given in the updated moving frame of reference marks the node  $B$ . The updating strategy presumes that the local displacement and velocity at  $B$  vanish. Hereby, by use of (2.5) and the results from (3.16) the following relation is obtained for the updated angular velocity

$$\mathbf{R}_{j+1}^{(k+1)T} \left( \bar{\mathbf{v}}_B - \bar{\mathbf{v}}_{c,j+1}^{(k+1)} \right) = \tilde{\boldsymbol{\omega}}_{j+1}^{(k+1)} \mathbf{s}_B \quad (3.17)$$

The two first rows give a solution for the two first components of the angular velocity  $\omega_{1,j+1}^{(k+1)}$  and  $\omega_{2,j+1}^{(k+1)}$ . The third component is determined from the previous known value and the average of the belonging angular velocity component of the two nodes

$$\omega_{3,j+1}^{(k+1)} = \omega_{3,j+1}^{(k)} + \frac{1}{2} (\dot{\varphi}_{B,3} + \dot{\varphi}_{A,3}) \quad (3.18)$$

Similarly, the angular acceleration is determined by use of (2.6)

$$\bar{\mathbf{a}}_B = \bar{\mathbf{a}}_{c,j+1}^{(k)} + \mathbf{R}_{j+1}^{(k)} \left( (\tilde{\boldsymbol{\alpha}}_{j+1}^{(k)} + \tilde{\boldsymbol{\omega}}_{j+1}^{(k)} \tilde{\boldsymbol{\omega}}_{j+1}^{(k)}) (\mathbf{s}_B + \mathbf{u}_B) + 2\tilde{\boldsymbol{\omega}}_{j+1}^{(k)} \dot{\mathbf{u}}_B + \ddot{\mathbf{u}}_B \right) \quad (3.19)$$

$$\mathbf{R}_{j+1}^{(k+1)T} \left( \bar{\mathbf{a}}_B - \bar{\mathbf{a}}_{c,j+1}^{(k+1)} \right) - \tilde{\boldsymbol{\omega}}_{j+1}^{(k+1)} \tilde{\boldsymbol{\omega}}_{j+1}^{(k+1)} \mathbf{s}_B = \tilde{\boldsymbol{\alpha}}_{j+1}^{(k+1)} \mathbf{s}_B \quad (3.20)$$

$$\alpha_{3,j+1}^{(k+1)} = \alpha_{3,j+1}^{(k)} + \frac{1}{2} (\ddot{\varphi}_{B,3} + \ddot{\varphi}_{A,3}) \quad (3.21)$$

Hereby, all moving frame parameters have been updated and it is now necessary to solve (3.6) with updated system matrices and vectors to determine the substructure motion relative to this new frame.

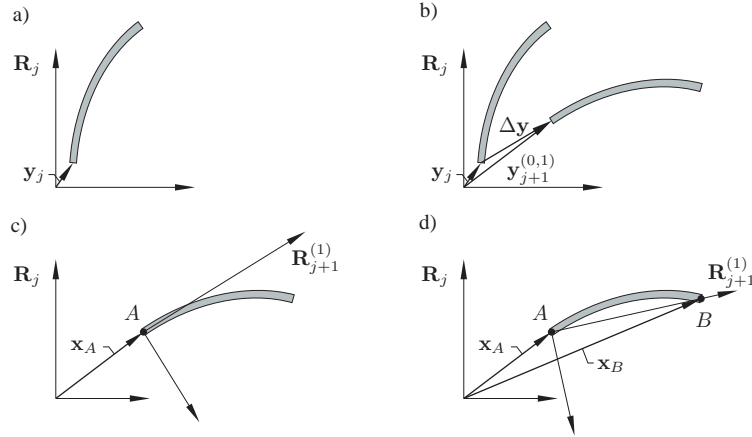


**Figure 3.2** a) Moving frame and substructure at the load step  $j$ . b) Iterate the system state vector for the load step  $j + 1$ . c) Updating of the moving frame based on the motion of the node at the origin. d) Updating of the moving frame based on the motion of two boundary nodes.

### 3.3 Update Algorithms for Static Simulations

In this section it is described how the moving frames are updated for use in static simulations. Compared to the procedure for updating the moving frame in a dynamic analysis as illustrated in Figure 3.1, the major difference is that no prediction step is used in these static analysis. An advantage of the present multibody formulation when performing static analysis is that very few changes of the equations of equilibrium are necessary. Because the constraints are formulated so they enter the system stiffness matrix in (2.22), they can be reused for static analysis. In the standard Floating Frame of Reference formulation the constraints are formulated so they enter the system mass matrix and therefore need further modification if used in static analysis. The reason for updating the moving frames in static analysis is to get more correct results when the structure exhibits large nonlinear displacements. In Chapter 4 such nonlinear displacements are further examined by use of the two updating algorithms described in this section. In the first method, the motion of the node at the origin of the substructure is used to update the belonging moving frame. The second method corresponds to a static version of the updating algorithm for dynamic simulations in section 3.2. Here, the motion of the node at the origin of the substructure is used together with the motion of an arbitrary point in the substructure to update the moving frame.

#### 3.3.1 Procedure for the Static Updating Algorithms

In Figure 3.2 a series of sketches are shown to illustrate the procedure when updating the moving frames in a static simulation. The lower index ' $j$ ' now indicates a load step, otherwise the same notation is used for the upper indices as in section 3.2. In Figure 3.2a the moving frame and substructure are shown for the converged solution at load step  $j$ . In the next load step  $j + 1$  the exterior load is changed, and the substructure is iterated to a new position within the moving frame, see Figure 3.2b. Due to the nonlinear constraints several iterations may be necessary



to obtain a residual which is within the specified convergency limits. When the solution has converged it is chosen to update the moving frame. In the present situation two methods are possible. In Figure 3.2c the node at the origin of the substructure is used to update the moving frame. Hereby, the moving frame obtains the same position and orientation as this node. Another possibility is demonstrated in Figure 3.2d, where the motion of the node at the origin and an arbitrary point, here the end node, are used to update the moving frame. At this point the updated moving frame and displacement vector do not correspond and it is therefore necessary to iterate the position of the substructure within the updated frame, similarly to Figure 3.2b. This updating procedure of the moving frame within each load step is performed a predefined number of times. More ideally, a convergency criteria should be set up for when to update the moving frame. Hereby, fewer updates would be necessary within each load step and in some cases it would not even be necessary to update the moving frame.

### 3.3.2 Update Based on the Node at the Origin

This updating algorithm follows the illustrations in Figure 3.2a-b-c, where the node at the origin of the substructure labeled node  $A$  is used to update the moving frame. The position of the moving frame is update by use of the displacement  $\mathbf{u}_A$  of node  $A$

$$\bar{\mathbf{x}}_{c,j+1}^{(k+1)} = \bar{\mathbf{x}}_{c,j+1}^{(k)} + \mathbf{R}_{j+1}^{(k)} \mathbf{u}_A \quad (3.22)$$

Similarly, the small rotation  $\varphi_A$  of node  $A$  is used to determine the increment of the rotation tensor

$$\Delta \mathbf{R} = \mathbf{R}(\varphi_A) \quad (3.23)$$

which is used to updated the orientation of the moving frame

$$\mathbf{R}_{j+1}^{(k+1)} = \mathbf{R}_{j+1}^{(k)} \Delta \mathbf{R} \quad (3.24)$$

### 3.3.3 Update Based on the Node at the Origin and an Arbitrary Node

This updating algorithm is based on the updating algorithm for dynamic simulations in section 3.2, where the motion of a node at the origin of the substructure and an arbitrary node are used to update the moving frame. It is not necessary that the arbitrary point is a node, an interior point could also be used but then it is necessary to determine the motion at this point by use of shape functions. The position of the origin of the moving frame is determined similarly to (3.8)

$$\bar{\mathbf{x}}_{c,j+1}^{(k+1)} = \bar{\mathbf{x}}_{c,j+1}^{(k)} + \mathbf{R}_{j+1}^{(k)} \mathbf{u}_A \quad (3.25)$$

The orientation of the moving frame follows the same description as related to (3.11)–(3.15). These equations are repeated below for completeness.

$$\varphi_3 = \frac{1}{2}(\varphi_{B,3} + \varphi_{A,3}) \quad (3.26)$$

$$\begin{bmatrix} \mathbf{n}_1 & \mathbf{n}_2 & \mathbf{n}_3 \end{bmatrix} = \begin{bmatrix} \cos \varphi_3 & -\sin \varphi_3 & 0 \\ \sin \varphi_3 & \cos \varphi_3 & 0 \\ 0 & 0 & 1 \end{bmatrix} \quad (3.27)$$

$$\mathbf{n} = \mathbf{n}_3 + \frac{\mathbf{x}_B - \mathbf{x}_A}{|\mathbf{x}_B - \mathbf{x}_A|}, \quad \mathbf{n} := \mathbf{n}/|\mathbf{n}| \quad (3.28)$$

$$\Delta \mathbf{R} = (\mathbf{I} - 2\mathbf{n}\mathbf{n}^T) \begin{bmatrix} \mathbf{n}_1 & \mathbf{n}_2 & -\mathbf{n}_3 \end{bmatrix} \quad (3.29)$$

$$\mathbf{R}_{j+1}^{(k+1)} = \mathbf{R}_{j+1}^{(k)} \Delta \mathbf{R} \quad (3.30)$$

### 3.4 Concluding Remarks

In this chapter it is described how the moving frame of reference is updated for dynamic and static analysis for use in the present multibody formulation. The update algorithm for the dynamic simulations is based on the motion of the boundary nodes in the substructures. In the static update algorithm two methods are described, one which uses the motion of the node at the origin to update the moving frame. In the other case the motion at the origin together with an arbitrary point in the substructure is used to update the frame. Very few modifications of the equations of motion are necessary to change between static and dynamic analysis. Especially the constraints can be used in both cases without any modification.

---

## CHAPTER 4

# Static Analysis of Nonlinear Displacements

---

In this chapter large static nonlinear geometric displacements are analyzed by use of the multibody formulation. The results are based on the extensible elastica and a clamped wind turbine blade. Different update approaches of the moving frame and the convergency of the displacements by increasing the number of substructures are analyzed. The results are compared to a co-rotating beam formulation, where good correspondence is observed. By dividing the blade into just two substructures of unequal reference length makes it possible to absorb the non-linearities in an efficient way, which otherwise would require four substructures of equal reference length.

### 4.1 Co-rotating Formulation based on Beam Elements

To determine the accuracy of the multibody model a nonlinear co-rotating beam formulation is implemented. The model is based on Krenk [12], where a detailed derivation of the tangent stiffness matrix is given.

The idea of a co-rotating formulation is to separate the deformation of each element into a rigid body motion i.e. a translation and rotation of each element with respect to a fixed coordinate system, and an elastic deformation within the local coordinate system fixed to the element. Because the elastic deformations are moderate linear Timoshenko beam theory is adequate. Inside the local coordinate system the beam is able to deform in the longitudinal direction, rotate around the beam axis, and may undergo bending deformations and shear deformations. No coupling between warping and axial elongation is used i.e. only St. Venant torsion (homogeneous torsion) is used. The orientation of the local coordinate system is defined by the base unit vectors  $\mathbf{i}_1, \mathbf{i}_2, \mathbf{i}_3$  shown in Figure 4.1a. The  $x_3$ -axis is chosen along the deformed beam through the end points  $A$  and  $B$  of the element, and the  $x_1$ - and  $x_2$ -axis are defined by the mean rotation at  $A$  and  $B$ . The angle  $\varphi$  around the  $x_3$ -axis to the principal axis is taken into consideration as shown in Figure 4.1b.

### 4.2 Large Deformation of a Cantilever Beam

In this section the possibility of describing a highly nonlinear static deformation by use of the multibody formulation in chapter 2 is examined. Both of the two static updating algorithms described in section 3.3 for the moving frame of reference are used to determine the most favorable

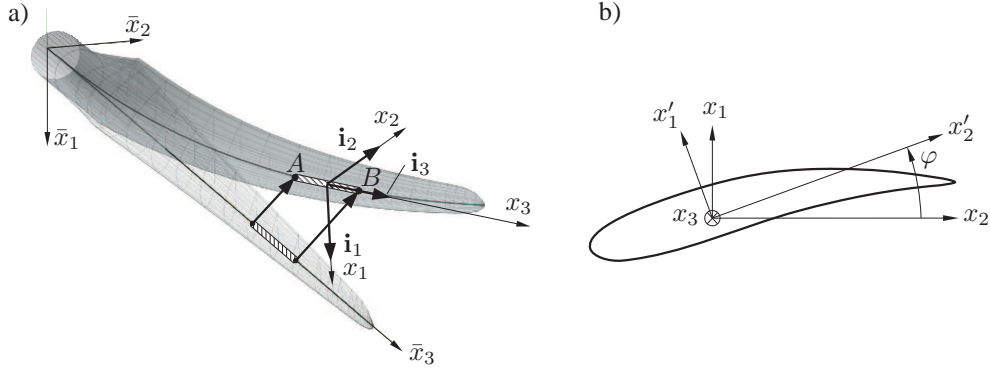


**Figure 4.1** a) An element in the co-rotating formulation. b) Rotation into principal axes based on the initial pretwist of the profile and the angle to the principal axes.

one. Moreover, the convergency by using more substructures for a better description of the non-linear deformation is demonstrated. Convergency of the co-rotating formulation is performed and all results are compared to the results of the extensible elastica theory for Bernoulli-Euler beams as e.g. given by Magnusson et al. [13] and reproduced in Gerstmayr and Irschik [14]. The implementation of the multibody formulation and the co-rotating formulation are both in 3D, but the following tests are in 2D. The setup consists of a cantilever beam with length  $L$  where an exterior tip load  $P = 3EI_2/L^2$  is applied with constant orientation in the positive  $\bar{x}_1$ -direction, see Figure 4.2a. The cross section is quadratic with a width of 0.1 m. The cross section parameters together with the size of the tip load are listed in Table 4.1. In the co-rotating formulation it is possible to incorporate the effective shear area. However, in order to compare these results to the results by use of the multibody formulation with Bernoulli-Euler beam elements, the shear deformations are eliminated, so the beam elements in the co-rotating formulation correspond to Bernoulli-Euler beams. In Figure 4.2b. the beam has been discretized into 3 substructures of equal reference length. The initial orientation of the belonging moving frame of references are equal to the orientation of the fixed frame of reference  $(\bar{x}_1, \bar{x}_2, \bar{x}_3)$ , see Figure 4.2b.

In Figure 4.3 the deformation of the beam is shown for a tip load of  $\frac{1}{2}P$  and  $P$ , where the beam is modelled by use of 1 element in each of the 3 substructures. All elements have equal reference length. In Figure 4.3a the updating algorithm based on the motion of the node at the origin of the moving frame is used. In Figure 4.3b the updating algorithm based on the motion of the node at the origin and at the end of substructure is used. It is clearly visible in Figure 4.3a that large displacements of the beam from the moving frames are observed especially for the two first substructures. In Figure 4.3b the displacements of the beam from the moving frames are highly reduced. In order for the linear theory describing the deformation of the beam inside the moving frames to be valid it is desired to have as small local displacements as possible.

The two updating algorithms are further investigated by examining how the tip position of the beam converges by increasing the number of substructures. Two cases are used one with 1 element in each substructure and another with 2 elements in each substructure. In both cases the reference length of the elements are equal. The reason for using 2 elements in each substructure is to demonstrate that the best results in this example are obtained by using a higher number of substructures and not a higher number of elements inside each substructure. The results are

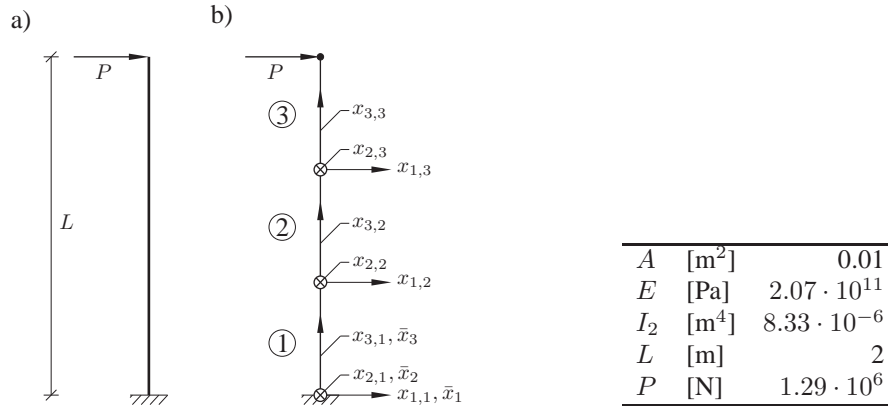


**Figure 4.2** a) Cantilever beam with a tip load. b) Discretization of beam into 3 substructures of equal reference length. Initial orientation of the belonging moving frames and the fixed frame of reference.

**Table 4.1** Cross section area  $A$ , Young's modulus  $E$ , moment of inertia  $I_2$ , length of beam  $L$ , and applied tip load  $P$ .

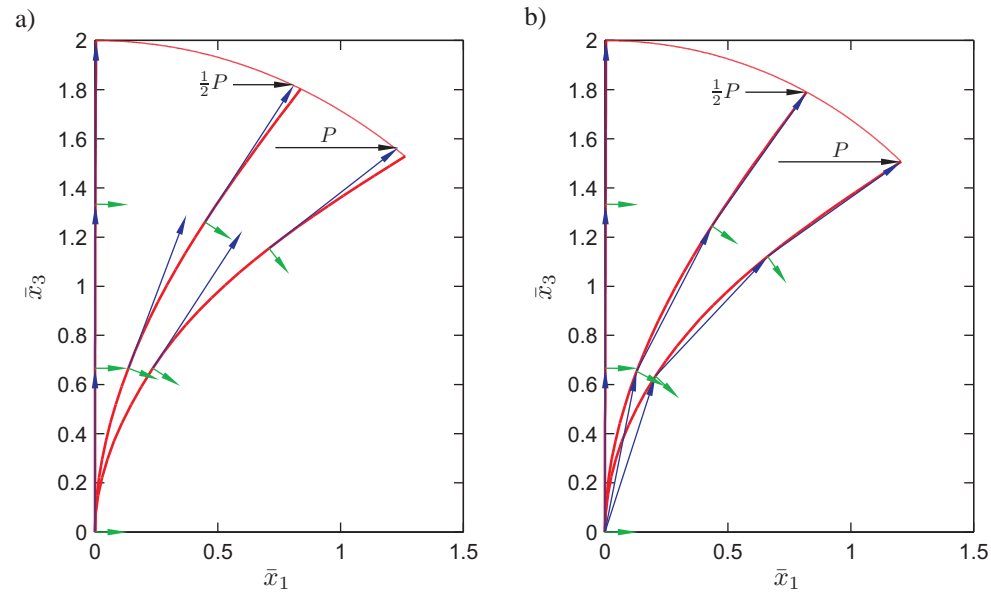


**Figure 4.3** Deformed beam when discretized into 3 substructures, each modelled by 1 element. a) Update based on node at origin. b) Update based on end nodes. ( — ) Tip position of beam. ( — ) Deformed beam. ( — )  $x_1$ -axis. ( — )  $x_3$ -axis.

compared to the results of the extensible elastica theory for Bernoulli-Euler beams, where the tip position is  $(\bar{x}_1; \bar{x}_3) = (1.207; 1.491)$ . This corresponds to a tip displacement of approximately 65% of the undeformed beam length. Convergency of the co-rotating formulation is also included as this model is used in a later example, where the deformation of a wind turbine blade

is examined. In Figure 4.4a and Figure 4.4b the tip position of the beam in  $\bar{x}_1$  and  $\bar{x}_3$ , is shown, respectively. The abscissa denotes the total number of elements  $n_{el}$ , which also is used to denote the total number of substructures. When e.g.  $n_{el} = 20$  and 1 or 2 elements are used in each substructure a total of 20 or 10 substructures, respectively, are used in the model.

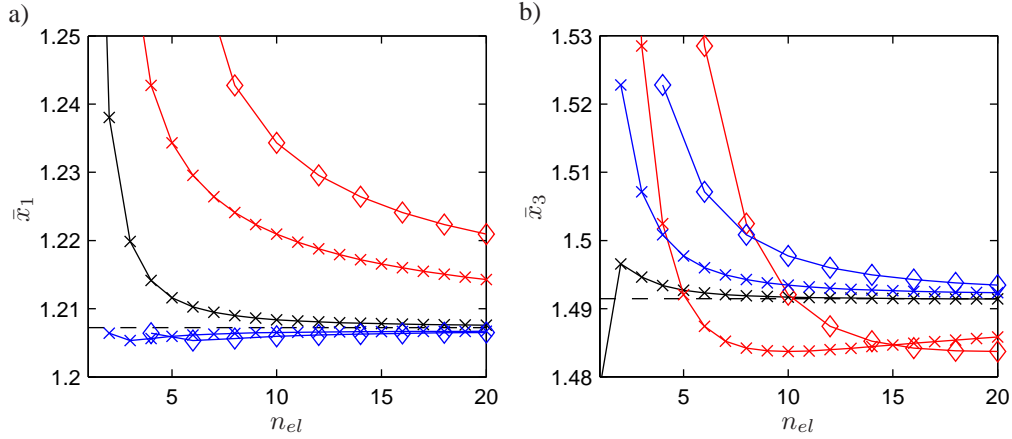


**Figure 4.4** Tip position of beam in the: a)  $\bar{x}_1$ -direction. b)  $\bar{x}_3$ -direction. (—) Update based on node at origin, (x) 1 element pr. substructure, (◊) 2 elements pr. substructure. (—) Update based on end nodes, (x) 1 element pr. substructure, (◊) 2 elements pr. substructure. (—) Co-rotating formulation. (—) Analytical solution.

It was not possible to get a stable solution by use of 1 substructure when using the updating algorithm based on both end nodes. This is probably due to the linearized rotational constraints. In Figure 4.4 it is demonstrated that it has little to none effect by using 2 elements compared to only using 1 element in each substructure, no matter which updating algorithm is used. This is also due to the constant cross section parameters throughout the beam. In Figure 4.4 it is shown that the updating algorithm based on both end nodes results in tip displacements which converge much faster than the updating algorithm where only the node at the origin is used. Overall, the multibody formulation, with the updating algorithm by use of the end nodes, converges faster for the  $\bar{x}_1$ -component but slower for the  $\bar{x}_3$ -component, compared to the co-rotating formulation and also towards the analytical solution. If a more precise description of the rotational constraint could be implemented, similar results as by use of the co-rotating formulation should be obtainable. It has been tried to implement rotational constraints based on the Cayley approach in (2.13), as described in section 2.2. However, this turned out to be instable i.e. it was not possible for the solution in the first load steps to converge.

### 4.3 Tip Displacement of a Clamped Wind Turbine Blade

In this section the accuracy of the updating methods for the multibody formulation are further investigated. The co-rotational formulation with 20 elements is used as the reference model. The examples are based on a clamped wind turbine blade where the variation of the cross section parameters throughout the blade are described in Appendix B. Prismatic elements are used based on the mean value of the cross section parameters at the end points in the respective beam

elements. The blade is discretized by a total of 20 elements with the same reference length. The total referential length of the blade is  $L = 44.8$  m. An exterior tip load with orientation in the  $\bar{x}_1$ -direction is applied so the tip displacement is approximately 20% of the undeformed blade length. The numeration of the substructures and the initial orientation of these are as described in Figure 4.2a.

### 4.3.1 Convergency of Updating Algorithms

In this section the convergency of the two updating algorithms from section 3.3 is investigated by increasing the number of substructures in the blade. It was shown in Figure 4.4 that the updating algorithm based on the motion of both end points is far superior to the one where only the node at the origin of the moving frame is used. However, this was based on a very large deformation which is reduced in the following examples. In this example a constant reference length is used for each substructure. Because a total of 20 elements of equal reference length are used in the discretization of the blade the number of substructures become  $n_{mb} = [1, 2, 4, 5, 10, 20]$ . The tip position of the blade after deformation is shown in Figure 4.5 based on the two updating algorithms and the different number of multibodies. In Figure 4.5 it is shown that the updating

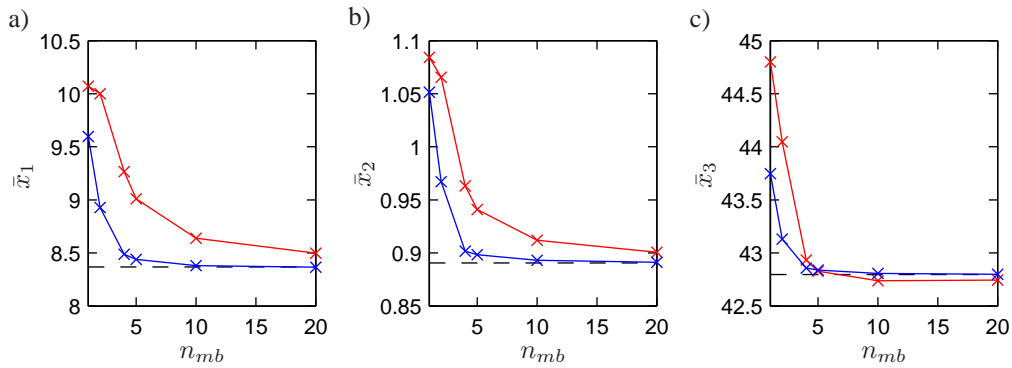


**Figure 4.5** Tip position of the blade by use of 20 elements of equal reference length which are divided into a number of substructures  $n_{mb}$  of equal reference length. a) Tip position in  $\bar{x}_1$ . b) Tip position in  $\bar{x}_2$ . c) Tip position in  $\bar{x}_3$ . ( — ) Update based on node at origin. ( — ) Update based on end nodes. ( — — ) Co-rotating formulation by use of 20 elements.

algorithm based on the motion of both end points in the substructure is the best of the two updating algorithms. 4 substructures updated based on the end points give similar results as by use of 20 substructures updated based on the motion of the node at the origin of the substructures. A total of 168 and 360 degrees of freedom, respectively, are used in these two cases. Moreover, far fewer moving frames need to be updated when only 4 substructures are present instead of 20 substructures.

### 4.3.2 Wind Turbine Blade Modelled by One Substructure

In order to reduce the number of degrees of freedom it is favourable with as few substructures as possible due to the constraints and the two extra nodes for each extra substructure. In this section it is further examined if it is possible to get satisfying results by use of one substructure based on

a two node updating scheme, where the one node is placed at the root, whereas the other node is varied throughout the blade. In Figure 4.8a the enumeration of the nodes throughout the blade is shown. In Figure 4.8b an example of the deformed blade is shown when the moving frame is updated based on node 1 and node 18. In Figure 4.6 the tip position is shown by use of the different nodes from the root of the blade where node 1 is placed, to the tip of the blade where node 21 is placed. In the case of using only node 1 the updating algorithm based on the node of the origin is used. It is shown in Figure 4.6 that the best results are obtained by updating the

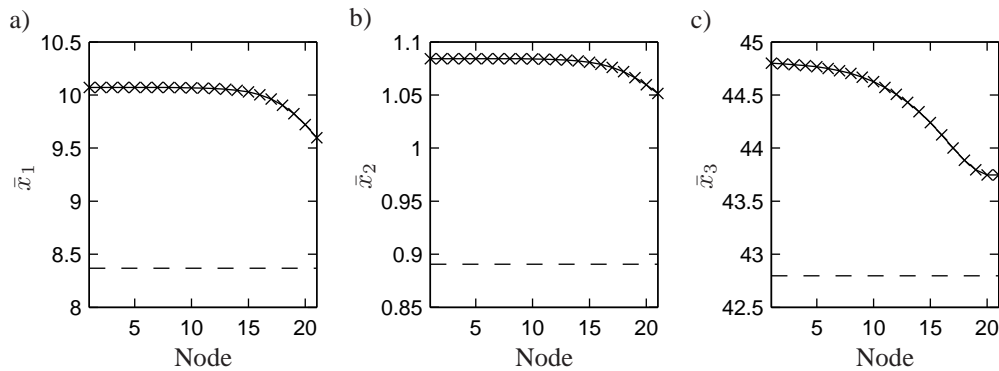


**Figure 4.6** Tip position of the blade by use of 20 elements of equal reference length and 1 substructure. The belonging moving frame is updated by use of the nodes from the root to the tip. a) Tip position in  $\bar{x}_1$ . b) Tip position in  $\bar{x}_2$ . c) Tip position in  $\bar{x}_3$ . ( — ) Update based on different element nodes of the blade. ( - - ) Co-rotating formulation by use of 20 elements.

moving frame based on the node at the tip of the blade. Hereby, the moving frame rotates as much as possible and thereby includes the largest non-linear effect. However, by comparison to the results of the co-rotating formulation it is shown that there are too large deviations for this magnitude of the tip displacement. Therefore, a single substructure is not enough to model the wind turbine blade.

### 4.3.3 Wind Turbine Blade Modelled by Two Substructures

In this section two substructures are used to model the blade. For both substructures the updating algorithm based on the position of the nodes at the ends of each substructure is used. It is examined how the best results are obtained by splitting the blade into the two substructures at different nodes throughout the blade. In Figure 4.8a the enumeration of the nodes throughout the blade is shown, which is used to identify where the blade is split into two substructures. Because at least one element is necessary in each substructure it can not be split at node 1 and node 21. In Figure 4.8c an example of the deformed blade is shown where it has been split into two substructures at node 16. Hereby 15 elements are used in the first substructure and 5 elements in the second substructure closest to the tip. The results of the tip position by splitting the blade into two substructures at different nodes are shown in Figure 4.7. Here, the best results are obtained by splitting the blade into two substructures at node 16. It is also shown that the results by use of these two substructures are almost identical to the co-rotating formulation and the case where four substructures of equal reference length are used. For a more realistic aerodynamic load the



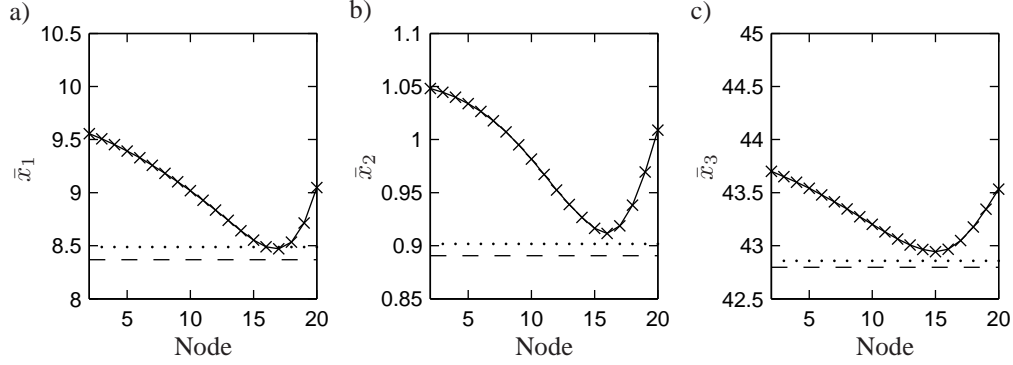


**Figure 4.7** Position of blade tip when split into 2 substructures at different nodes throughout the blade. Both moving frames are updated based on the end nodes in the respective substructure. a) Tip position in  $\bar{x}_1$ . b) Tip position in  $\bar{x}_2$ . c) Tip position in  $\bar{x}_3$ . ( — ) 2 substructures. ( ..... ) 4 substructures of equal reference length. ( — — ) Co-rotating formulation by use of 20 elements.

node number where the blade should be split into two substructures will most likely be different.

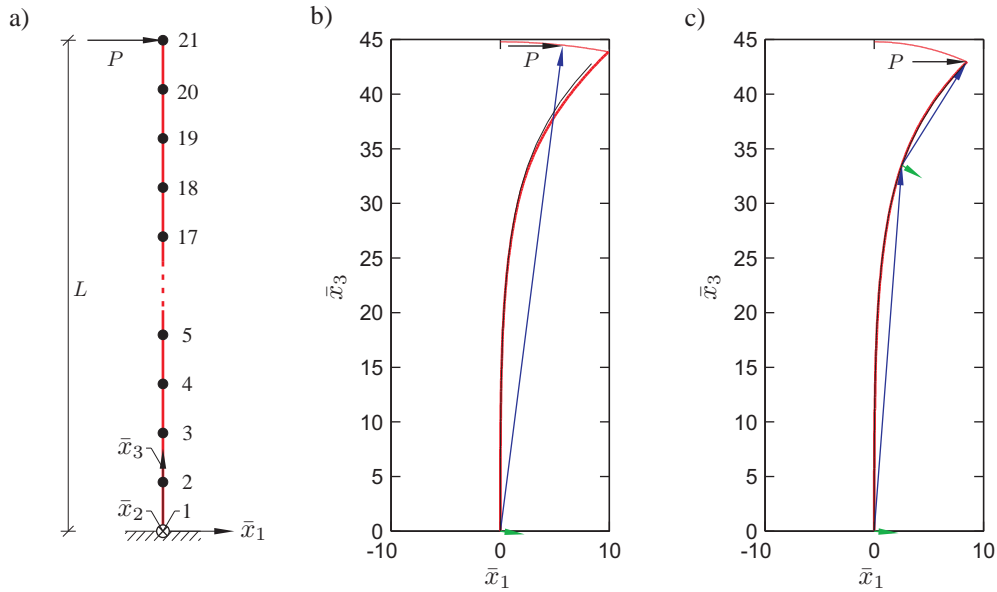


**Figure 4.8** a) Discretization of blade into 20 elements, where the node numbering is chronological from root to tip. b) Deformation of blade when divided into 1 substructure, where the moving frame is updated based on node 18. c) Blade divided into 2 substructures at node 16, where each moving frame is updated based on the end nodes in the respective substructure. ( — ) Tip position of blade. ( — ) Deformed blade. ( — )  $x_1$ -axis. ( — )  $x_3$ -axis. ( — ) Co-rotating formulation by use of 20 elements.

## 4.4 Concluding Remarks

Based on the analytical results for the extensible elastica theory for Bernoulli-Euler beams it can be concluded that the multibody model and the co-rotating formulation both converge towards the correct results. However, the co-rotating model converges fastest towards the correct results which is due to the linearized rotational constraints in the multibody model. It is demonstrated that by updating the moving frame based on the motion of the end nodes in the substructure is far superior to just using the node at the origin of the substructure. For the clamped wind turbine blade it is demonstrated that by use of two substructures of unequal reference length makes it possible to absorb the non-linearities in an efficient way, which otherwise would require four substructures of equal reference length.

---

# CHAPTER 5

## Eigenfrequencies and Eigenmodes for a Multibody System

---

In this chapter the undamped eigenfrequencies and mode shapes for a multibody model are determined. The purpose is to demonstrate that an existing multibody model, consisting of several substructures with ease can be modified to determine the eigenfrequencies and mode shapes. Due to the linear structure of the mass and stiffness matrix only the nonlinear constraints need to be modified. An example is demonstrated where the eigenfrequencies and mode shapes are determined for a multibody model of a simple wind turbine.

### 5.1 Linear Constraints and Generalized Eigenvalue Problem

In Chapter 3 it is described how the equations of motion are formulated for the used multibody formulation. It can be seen that because the motion of the belonging moving frames is assumed known, the only reason for the equations to become nonlinear is due to the rotational constraints, which enter the system stiffness matrix. When setting up the generalized eigenvalue problem the moving frames are fixed to their initial position and orientation. The mode shapes of the structure are then described relative to these fixed frames. The fixed frames must be initialized so the kinematical constraints at the interface to the adjacent substructure are satisfied. Hereby, it is possible to setup the rotational constraints at the interfaces as linear. In Figure 5.1a a sketch of two substructures is shown, which are assumed to be orthogonal in the referential state. The constraints at the interface between the substructures need to describe that the interface of the two substructures moves, so the substructures orthogonality at the point is preserved, see Figure 5.1b. In the following it is described how the original displacement and rotation constraints (2.7) and (2.11), respectively, are modified to become linear. First, the modified displacement constraints are described. Because the frames are fixed the modified displacement constraint become.

$$\begin{aligned}
 & \left. \begin{aligned} \bar{\mathbf{x}}_{c1} + \mathbf{R}_1(\mathbf{s}_{1,0} + \mathbf{u}_{1,0}) - (\bar{\mathbf{x}}_{c2} + \mathbf{R}_2(\mathbf{s}_{2,0} + \mathbf{u}_{2,0})) &= \mathbf{0} \\ \bar{\mathbf{x}}_{c1} + \mathbf{R}_1\mathbf{s}_{1,0} - (\bar{\mathbf{x}}_{c2} + \mathbf{R}_2\mathbf{s}_{2,0}) &= \mathbf{0} \end{aligned} \right\} \Rightarrow \\
 & \Phi_{dc} = \mathbf{R}_1\mathbf{u}_{1,0} - \mathbf{R}_2\mathbf{u}_{2,0} = \mathbf{0} \\
 & \Phi_{dc} = \mathbf{B}_{d,1}\mathbf{y}_1 + \mathbf{B}_{d,2}\mathbf{y}_2 = \mathbf{0} \quad , \quad \mathbf{B}_{d,1} = \mathbf{R}_1\mathbf{N}_{1,0} \quad , \quad \mathbf{B}_{d,2} = -\mathbf{R}_2\mathbf{N}_{2,0} \quad (5.1)
 \end{aligned}$$

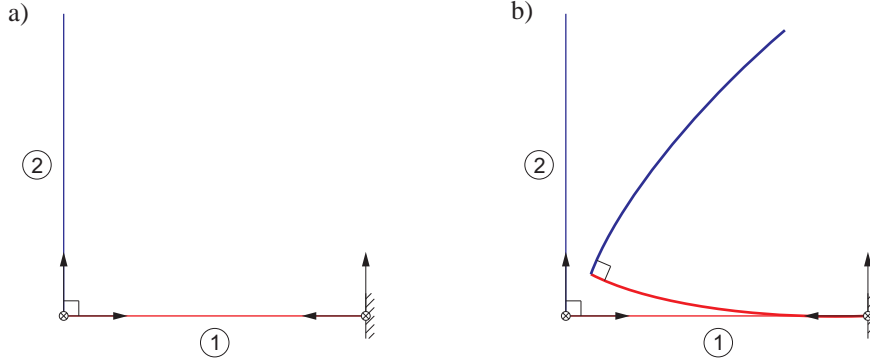


**Figure 5.1** a) A structure modelled by two substructures which are orthogonal to each other at the interface. b) Sketch where the orthogonality at the interface of the deformed structure is preserved.

The rotational constraints at the interface between the two substructures must be formulated such that this orthogonality is preserved.

$$\begin{aligned}\Phi_{rc} &= \mathbf{R}_1 \varphi_{1,0} - \mathbf{R}_2 \varphi_{2,0} = 0 \\ \Phi_{rc} &= \mathbf{B}_{r,1} \mathbf{y}_1 + \mathbf{B}_{r,2} \mathbf{y}_2 = 0 \quad , \quad \mathbf{B}_{r,1} = \mathbf{R}_1 \mathbf{P}_{1,0} \quad , \quad \mathbf{B}_{r,2} = -\mathbf{R}_2 \mathbf{P}_{2,0}\end{aligned}\quad (5.2)$$

The modified displacement and rotation constraints which now both are linear in  $\mathbf{y}_i$  and without terms in the load vector, are inserted in the system stiffness matrix (2.22) instead of (2.7) and (2.11), respectively. Hereby, the generalized eigenvalue problem for two substructures becomes.

$$(\mathbf{K} - \omega_j \mathbf{M}) \Phi_j = 0 \quad (5.3)$$

where

$$\mathbf{M} = \begin{bmatrix} \mathbf{M}_1 & 0 & 0 \\ 0 & \mathbf{M}_2 & 0 \\ 0 & 0 & 0 \end{bmatrix} \quad , \quad \mathbf{K} = \begin{bmatrix} \mathbf{K}_1 & 0 & \mathbf{B}_1^T \\ 0 & \mathbf{K}_2 & \mathbf{B}_2^T \\ \mathbf{B}_1 & \mathbf{B}_2 & 0 \end{bmatrix} \quad , \quad \mathbf{B}_i = \begin{bmatrix} \mathbf{B}_{d,i} \\ \mathbf{B}_{r,i} \end{bmatrix} \quad (5.4)$$

$\omega_j$  denotes the undamped eigenfrequency for mode  $j$ , and  $\Phi_j$  is the belonging eigenmodes. In the stiffness matrix  $\mathbf{K}_i$  only the elastic stiffness matrix  $\mathbf{K}_{e,i}$  from (2.20) is included. In this example, the fixed interface to the right of substructure 1 is not included but follows the same principles.

## 5.2 Undamped Eigenfrequencies for a Fixed-base Wind Turbine Blade

In this section the undamped eigenfrequencies and mode shapes are determined for a fixed-base wind turbine blade. The blade has been discretized by 20 beam elements of equal reference length. In Appendix B the used cross section parameters for the blade are listed. The purpose is to demonstrate that the eigenfrequencies and mode shapes do not change by use of 1, 2, 4, 5, and 10 substructures because the eigenvalue problem is linear. In each case an identical number of

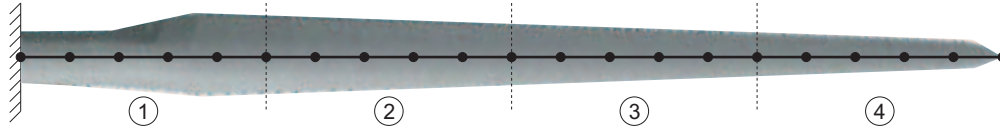


**Figure 5.2** Wind turbine blade discretized by 20 elements where 5 elements are used in each substructure.

Mode	Description of mode	1	2	4	5	10
1	1st flapwise	0.737	0.737	0.737	0.737	0.737
2	1st edgewise	1.498	1.498	1.498	1.498	1.498
3	2nd flapwise	2.179	2.179	2.179	2.179	2.179
4	3rd flapwise	4.663	4.663	4.663	4.663	4.663
5	2nd edgewise	5.472	5.472	5.472	5.472	5.472
6	4th flapwise	8.383	8.383	8.383	8.383	8.383
Degrees of freedom		132	144	168	180	240

**Table 5.1** 6 lowest undamped eigenfrequencies in Hz for a fixed-base wind turbine blade discretized by 20 elements in 1, 2, 4, 5, and 10 substructures.

elements are used in each substructure i.e. 5 elements are used in each substructure when 4 substructure are used to model the blade, see Figure 5.2. When solving the generalized eigenvalue problem 120 eigenfrequencies are real no-matter how many substructures used corresponding to the number of actual displacement and rotation degrees of freedom in the blade subtracted by the 6 degrees of freedom at the fixed base. The remaining number of eigenfrequencies correspond to twice the number of constraint equations. These eigenfrequencies attain 'Not a Number' due to no mass association to the constraint equations. In Table 5.1 the 6 lowest undamped eigenfrequencies are listed by use of 1, 2, 4, 5, and 10 substructures. Here, the number of degrees of freedom are shown based on the number of substructures used. The number of degrees of freedom increase heavily due to the extra nodes and constraints when increasing the number of substructures in the blade. It can be seen as anticipated that the eigenfrequencies are identical for all cases. In the six lowest eigenmodes the largest tip displacements are in the flapwise direction for 4 modes, whereas the largest tip displacement components are in the edgewise direction for the other modes. In Figure 5.3 the displacement components of the mode shapes are shown in the flapwise and edgewise directions for the first 6 eigenmodes. The largest displacement component in the tip has been normalized to 1. The mode shapes are illustrated by use of the results from 1 and 4 substructures. As anticipated the mode shapes are identical no-matter the number of used substructures.

### 5.3 Undamped Eigenfrequencies and Eigenmodes for a Wind Turbine

In this section the undamped eigenfrequencies and mode shapes are determined for a multibody model consisting of a simple wind turbine based on three blades, shaft, and tower. Each of the five structures are modelled by use of one substructure. The blades are 44.8m long and have

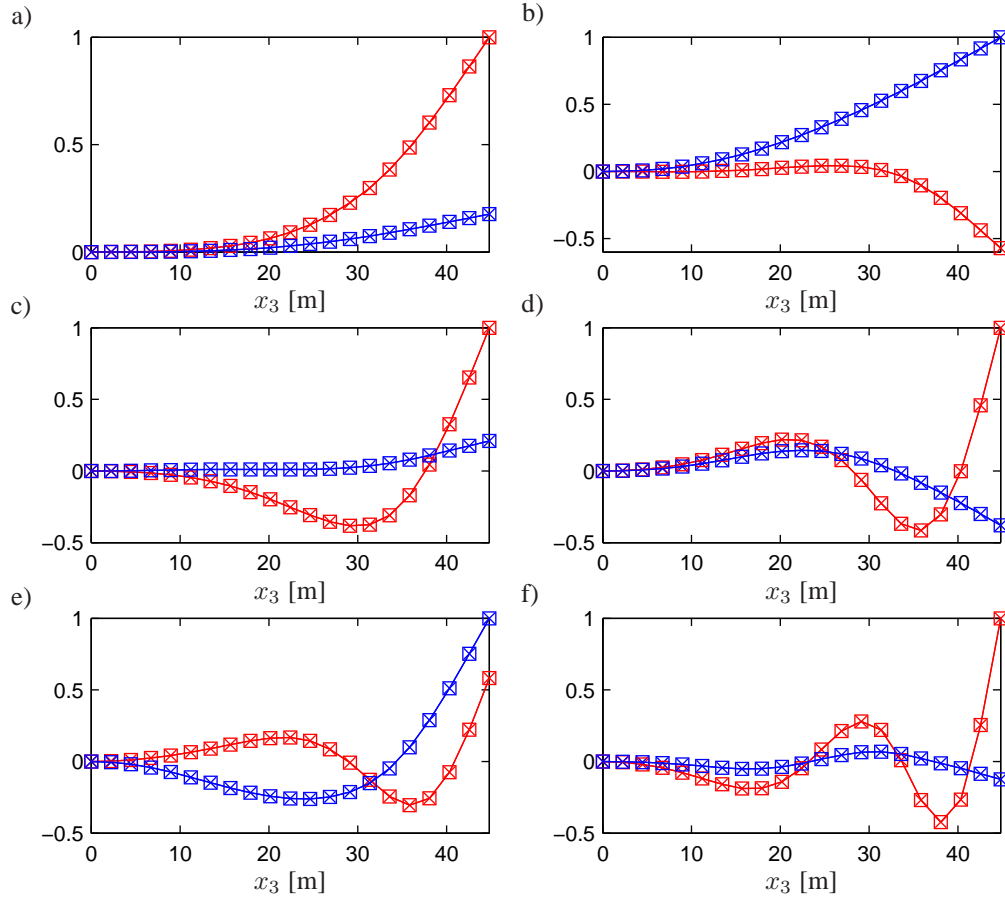


**Figure 5.3** a) 1st flapwise mode. b) 1st edgewise mode. c) 2nd flapwise mode. d) 3rd flapwise mode. e) 2nd edgewise mode. f) 4th flapwise mode. (— $\times$ ) Flapwise components. (— $\times$ ) Edgewise components. ( $\times$ ) 1 substructure used to model the blade. ( $\square$ ) 4 substructures used to model the blade.

each been discretized by 20 beam elements of equal reference length. The blades are not coned or pitched in this example and the shaft is not tilted. Each blade root is fixed to the shaft. The shaft is 4 m long and made highly stiff so it only works as a link between the blade roots and tower top. The rigid body rotation of the rotor related with the eigenfrequency of  $\omega_1 = 0$  is ignored. The elastic modes of the wind turbine is next analyzed by preventing the rotation of the rotor corresponding to the turbine is braked. The tower is 68.0 m high and modelled by use of 8 beam elements of equal reference length. A concentrated mass of 100 T has been added to the tower top to resemble the mass of the nacelle. The degrees of freedom at the tower bottom are fixed. In Appendix B the used cross section properties for the blades and tower are listed. In Table 5.2 the 11 lowest undamped eigenfrequencies for this wind turbine model are listed with a description of each turbine mode shape. It is observed that the two first eigenfrequencies are almost identical and dominated by the tower displacement. The reason for not being totally identical is because the turbine is not axis symmetric. The displacements of the tower in these

Mode	Eigenfrequency	Description of mode
1	0.446	1st tower, diagonal
2	0.448	1st tower, diagonal
3	0.690	1st rotor yaw
4	0.711	1st rotor tilt
5	0.756	1st blade flapwise
6	1.037	Blades in phase edgewise
7	1.486	1st blade edgewise, symmetric
8	1.514	1st blade edgewise, unsymmetric
9	1.820	2nd rotor yaw
10	1.920	2nd rotor tilt
11	2.195	2nd blade flapwise

**Table 5.2** 11 lowest undamped eigenfrequencies in Hz for the simple wind turbine multibody model.

two modes are in a plane  $\pm 45^\circ$  to the along wind direction. The eigenfrequencies for the 1st and 2nd blade mode in the flapwise direction from Table 5.1 are present in the full turbine model as mode 5 and 11, respectively. Similarly the 1st blade mode in the edgewise direction is present as mode 7. The eigenfrequencies have changed slightly due to the presence of the shaft and tower substructures. Besides a combination of primarily blade modes, the yaw and tilt modes of the rotor are also present. Figure 5.4a shows the turbine eigenmode number 1, which is dominated by the 1st tower mode. In Figure 5.4b the turbine eigenmode number 5 is shown, which is dominated by the 1st blade flapwise mode. In Figure 5.4c the turbine eigenmode number 9 is shown, which is the 2nd rotor yaw mode. In both cases the undeformed turbine is plotted with thin lines.

## 5.4 Concluding Remarks

In this chapter it is demonstrated that very few modifications of the existing multibody model are necessary in order to determine the eigenfrequencies and eigenmodes of the structure it models. The modifications are only related to the nonlinear constraints which are modified to become linear. These linear constraints are next inserted in the system stiffness matrix. An example of a simple wind turbine model consisting of three blades, shaft, and tower are used to demonstrate the facility of the method.

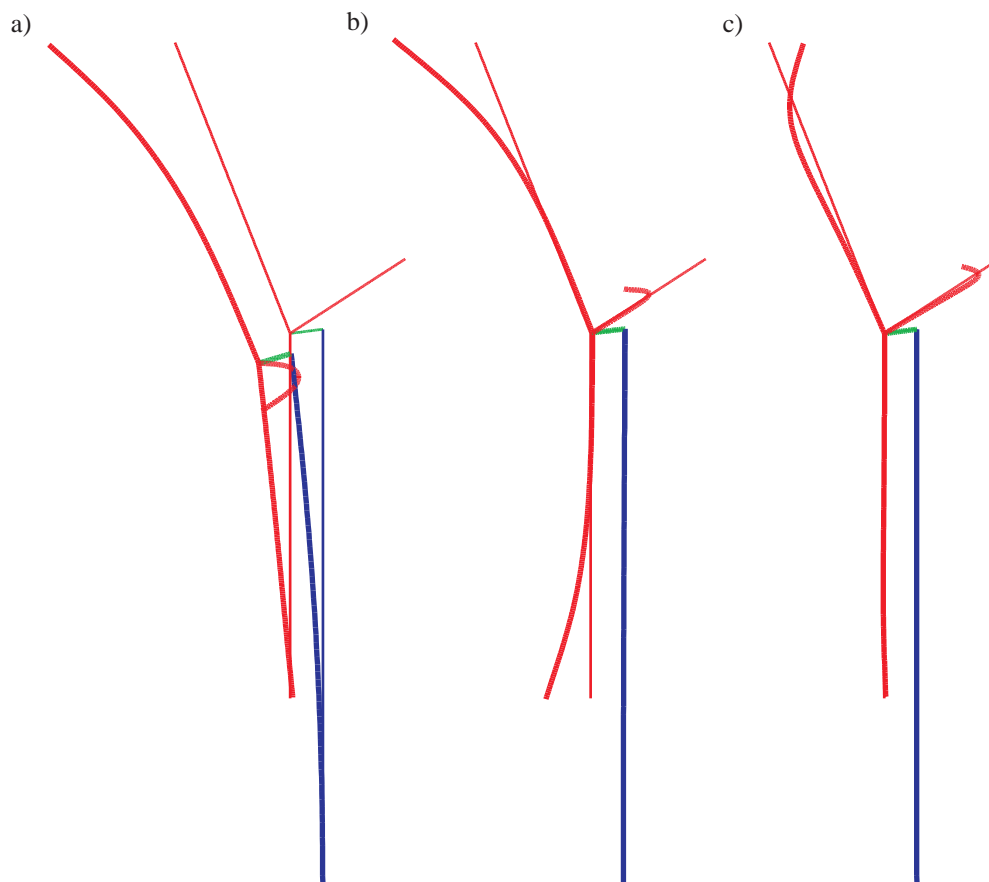


**Figure 5.4** Turbine mode: a) number 1 at 0.446 Hz which is the 1st tower mode. b) number 5 at 0.756 Hz which is dominated by the 1st blade flapwise mode . c) number 9 at 1.820 Hz which is the 2nd rotor yaw.



---

# CHAPTER 6

## System Reduction in Multibody Dynamics

---

In this chapter two system reduction methods are described for use in reducing the number of degrees of freedom in the multibody formulation. In the first method a Ritz basis is used consisting of rigid body modes and some dynamic low-frequency elastic eigenmodes compatible to the kinematic constraints at the interface of the substructure. Moreover, a quasi-static correction for the response of the high-frequency truncated eigenmodes are included. The second reduction method is based on a component mode synthesis method by the use of constraint modes and fixed interface normal modes. This makes a more general reduction of substructures possible, where the coupling degrees of freedom at the interface to adjacent substructures are included to secure compatibility at the interfaces. Both methods have been implemented in numerical examples and shown acceptable accuracy for the reduced models compared to the full FE-model.

### 6.1 System Reduction in Multibody Dynamics of Wind Turbines

In this section the system reduction method and numerical results from the enclosed paper in Appendix D are described. The reduction method is based on a Ritz basis consisting of rigid body modes and some dynamic low-frequency elastic eigenmodes compatible to the kinematic constraints of the related substructure. Concentrated forces within the substructure, e.g. due to actuator forces from tuned mass dampers or other vibration control devices, contain significant high frequency components, which cannot easily be decomposed into a limited number of modal loads. This is also the case for the aerodynamic load, which although continuous distributed is confined to the outer 30% of the blade. The high-frequency harmonics of these loads do not affect the dynamic response of the substructure, but do induce a quasi-static displacement component, which is included in the reduction method via a correction. In the present case a wind turbine blade modelled as one substructure is reduced by a Ritz basis consisting of rigid-body modes and fixed interface normal modes.

#### 6.1.1 System Reduction Method

The equations of motion for a substructure (2.19) are rewritten in the form

$$\mathbf{M}\ddot{\mathbf{y}} + \mathbf{C}\dot{\mathbf{y}} + \mathbf{K}\mathbf{y} = \mathbf{g}(t) = \mathbf{f}(t) - \mathbf{B}^T \bar{\lambda} \quad (6.1)$$

$\mathbf{g}(t)$  is a combined external load vector encompassing wind loads, inertial loads, and reaction forces from the kinematical constraints. The idea of the system reduction algorithm is to decompose the displacement vector  $\mathbf{y}(t)$  into a rigid body component  $\mathbf{y}_r(t)$  and an elastic component  $\mathbf{y}_e(t)$

$$\mathbf{y}(t) = \mathbf{y}_r(t) + \mathbf{y}_e(t) \quad (6.2)$$

These terms are next described by a Ritz basis and belonging generalized coordinates whereby the decompositions of  $\mathbf{y}_r(t)$  and  $\mathbf{y}_e(t)$  into rigid body  $\Phi_r$  and elastic mode shapes  $\Phi_e$ , respectively, become

$$\mathbf{y}_r(t) = \Phi_r \mathbf{q}_r(t) \quad (6.3)$$

$$\mathbf{y}_e(t) = \Phi_e \mathbf{q}_e(t) \quad (6.4)$$

where  $\mathbf{q}_r(t)$  and  $\mathbf{q}_e(t)$  store the rigid body and elastic generalized coordinates. The Ritz basis and generalized coordinates are assembled in the following form

$$\Phi = \begin{bmatrix} \Phi_r & \Phi_e \end{bmatrix}, \quad \mathbf{q}(t) = \begin{bmatrix} \mathbf{q}_r(t) \\ \mathbf{q}_e(t) \end{bmatrix} \quad (6.5)$$

The rigid body modes are described by e.g. 3 independent translation and 3 independent rotation modes to get a total of 6 independent rigid body modes.  $\Phi_r$  is not merely based on ones for the respective components in each mode but contains additional components, because a rotation around the  $x_1$ - and  $x_2$ -axis will give a displacement in the  $x_2$ - and  $x_1$ -direction, respectively. The elastic modes  $\Phi_e$  and thereby modal expansion of  $\mathbf{y}_e$  are compatible to the kinematical constraints. For a blade structure this corresponds to being fixed at the root. To incorporate the kinematical constraints on the elastic modes the rows and columns for the corresponding degrees of freedom in  $\mathbf{K}$  and  $\mathbf{M}$  are removed resulting in the following reduced generalized eigenvalue problem

$$\left( \tilde{\mathbf{K}}(\omega, \alpha, \Omega) - \tilde{\lambda}_j \tilde{\mathbf{M}} \right) \tilde{\Phi}_e^{(j)} = \mathbf{0}, \quad \tilde{\lambda}_j = \tilde{\omega}_j^2 \quad (6.6)$$

The eigenmodes are assumed to be constant in time, whereby it is necessary to select representative values of the angular velocity vector  $\omega$ , angular acceleration vector  $\alpha$ , and the operating angular frequency  $\Omega$ , at the evaluation of  $\tilde{\mathbf{K}}$  based on the stiffness matrix in (2.20). The vectors entering  $\tilde{\Phi}_e$  are ordered in ascending magnitude of the frequency  $\tilde{\omega}_j$ . Next,  $\tilde{\Phi}_e$  is expanded to full size  $\Phi_e$  by insertion of zeros for the degrees of freedom corresponding to the removed rows and columns. Insertion of (6.2)–(6.5) in (6.1) and premultiplication with  $\Phi^T$  provides the following reduced equations of motion

$$\mathbf{m}\ddot{\mathbf{q}} + \mathbf{c}\dot{\mathbf{q}} + \mathbf{k}\mathbf{q} = \Phi^T \mathbf{g}(t) \quad (6.7)$$

where

$$\left. \begin{aligned} \mathbf{m} &= \Phi^T \mathbf{M} \Phi \\ \mathbf{c} &= \Phi^T \mathbf{C} \Phi \\ \mathbf{k} &= \Phi^T \mathbf{K} \Phi \end{aligned} \right\} \quad (6.8)$$

Notice that none of the reduced matrices have a diagonal structure. Now, all the elastic modes with frequencies above a certain frequency  $\tilde{\omega}_0$  are assumed to respond quasi-static to the combined external load  $\mathbf{g}(t)$ , whereas the remaining elastic modes respond dynamically. Correspondingly, the partitioning of the elastic modes is subdivided into dynamic and quasi-static components. Then,  $\Phi_e$  and  $\mathbf{q}_e(t)$  in (6.5) are replaced by the following partitionings

$$\Phi_e = \begin{bmatrix} \Phi_d & \Phi_s \end{bmatrix}, \quad \mathbf{q}_e(t) = \begin{bmatrix} \mathbf{q}_d \\ \mathbf{q}_s \end{bmatrix} \quad (6.9)$$

The indices 'd' and 's' stand for dynamic and static components. Hereby, the displacement vector  $\mathbf{y}(t)$  in (6.2) is reformulated as

$$\mathbf{y}(t) = \mathbf{y}_r(t) + \mathbf{y}_d(t) + \mathbf{y}_s(t) \quad (6.10)$$

The static modes are not directly used, instead the quasi-static contribution is determined by the already included dynamical modes as follows, Preumont [15]

$$\tilde{\mathbf{y}}_s(t) = \left( \tilde{\mathbf{K}}^{-1} - \tilde{\Phi}_d \tilde{\mathbf{k}}_d^{-1} \tilde{\Phi}_d^T \right) \tilde{\mathbf{g}}(t) = \tilde{\mathbf{U}} \tilde{\mathbf{g}}(t) \quad (6.11)$$

where

$$\tilde{\mathbf{k}}_d = \tilde{\Phi}_d^T \tilde{\mathbf{K}} \tilde{\Phi}_d \quad (6.12)$$

It is therefore necessary that the kinematical supports eliminate any singularity of  $\tilde{\mathbf{K}}$ . The full vector  $\mathbf{y}_s(t)$  is obtained by reordering of the degrees of freedom in  $\tilde{\mathbf{U}}$  and  $\tilde{\mathbf{g}}(t)$  and insertion of zeros corresponding to the kinematical supports. Hereby,  $\tilde{\mathbf{U}}$  and  $\tilde{\mathbf{g}}(t)$  are transformed to full size  $\mathbf{U}$  and  $\mathbf{g}(t)$ , respectively. The displacement vector  $\mathbf{y}(t)$  is thereby determined from the linear transformation

$$\mathbf{y}(t) = \mathbf{A} \mathbf{w} + \mathbf{U} \mathbf{g}(t) \quad (6.13)$$

where

$$\mathbf{A} = \begin{bmatrix} \Phi_r & \Phi_d \end{bmatrix}, \quad \mathbf{w} = \begin{bmatrix} \mathbf{q}_r \\ \mathbf{q}_d \end{bmatrix} \quad (6.14)$$

Hereby the modal matrices from (6.8) are redefined as

$$\left. \begin{aligned} \mathbf{m} &= \mathbf{A}^T \mathbf{M} \mathbf{A} \\ \mathbf{c} &= \mathbf{A}^T \mathbf{C} \mathbf{A} \\ \mathbf{k} &= \mathbf{A}^T \mathbf{K} \mathbf{A} \end{aligned} \right\} \quad (6.15)$$

Based on the derived system reduction algorithm a structure in the original system of equations (2.22) can be reduced by insertion of (6.13) into (6.1). In the following numerical examples the blade structure has been reduced by using rigid body modes and elastic fixed-base eigenmodes.

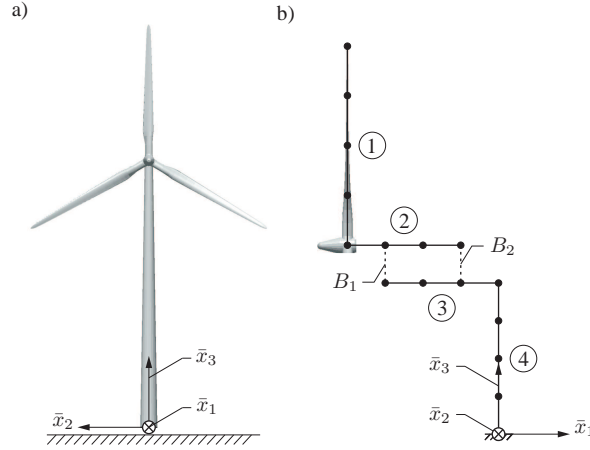


**Figure 6.1** a) Fixed frame of reference in the wind turbine. b) The numerical model consisting of four structures.

### 6.1.2 Numerical example

In this section the theory is illustrated with a simplified system consisting of four structures: one blade, rotor shaft, nacelle and tower, labelled 1, 2, 3, and 4, respectively, as shown in Figure 6.1b. The blade and shaft structures are fixed together and similarly with the nacelle and tower structures. Moreover, the tower structure is fixed to the ground. To connect the rotor and nacelle structures two main bearings  $B_1$  and  $B_2$  are introduced. The length  $L$  of the blade is 44.8 m with a total weight of 10 t and it is constructed by NACA 63-418 section profiles. The cross section parameters and the mass distribution throughout the blade are presented in Appendix B. The numerical FE-model of all structures is based on prismatic Bernoulli-Euler beam elements with St. Venant torsion and has 6 degrees of freedom for each node. In the numerical tests only the blade structure has been reduced because this is the most complex structure and undergoes the largest deformations which would otherwise require many degrees of freedom.

The numerical example consists of a start-up sequence and an operating sequence. In the start-up sequence the rotor speeds up from a stopped situation to the nominal angular velocity  $\Omega_n = 1.6$  rad/s and in the operating sequence the rotor rotates with the nominal angular velocity. Both sequences are modelled by prescribing the angular acceleration of the moving reference frame for the blade and rotor shaft structure. The following angular acceleration of each moving frame of reference is used during the two sequences where  $t_n$  defines the time where the nominal operating sequence starts

$$\alpha(t) = \begin{cases} \frac{\Omega_n}{t_n} \left( -\cos\left(\frac{2\pi t}{t_n}\right) + 1 \right) & , \quad 0 \leq t \leq t_n \\ 0 & , \quad t_n < t \end{cases} \quad (6.16)$$

In Figure 6.2a the angular acceleration and angular velocity are plotted for the two sequences where  $t_n = 10$  s and the simulation ends at  $t = 20$  s. To stress the reduction scheme a concentrated load  $P$  in the  $u_1$ -direction i.e. flap-direction is applied to the blade at  $x_3 \approx \frac{2}{3}L$ . The load

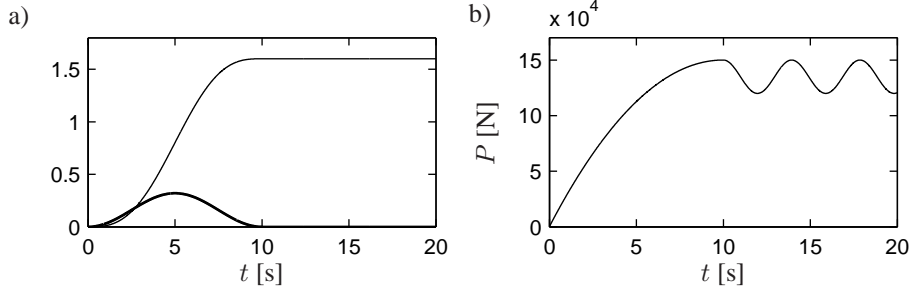


**Figure 6.2** Start-up sequence  $t = [0; 10]$  s and operating sequence  $t = ]10; 20]$  s. a) Angular acceleration ( — ) and belonging angular velocity ( - - - ) of the moving frame of reference. b) Magnitude of the concentrated load in the flap direction.

has the following characteristics during the start-up sequence and operating sequence

$$P(t) = \begin{cases} P_0 \left( -\left(\frac{t}{t_n}\right)^2 + \frac{2t}{t_n} \right) & , \quad 0 \leq t \leq t_n \\ P_0 \left( 1 + p_n \cos(\Omega_n(t - t_n)) \right) - p_n & , \quad t_n < t \end{cases} \quad (6.17)$$

In the start-up sequence the load is stepped up parabolically from  $P = 0$  at  $t = 0$  to a parabolic maximum of  $P = P_0$  at  $t_n$ . In the operating sequence the applied load is based on a constant load corresponding to a mean wind velocity and a harmonic component with amplitude  $p_n$  due to a variation in the shear wind field. In the simulations the following values have been used:  $P_0 = 1.5 \cdot 10^5$  N,  $p_n = 0.1$ ,  $\Omega_n = 1.6$  rad/s, and  $t_n = 10$  s. In Figure 6.2b the size of this concentrated load is illustrated throughout the simulation. The reason for applying the load at this point is because the majority of the wind load is concentrated around this position. A concentrated load will regularly require a lot of modes to discretize the response, which favors the reduction scheme when the quasi-static contribution from the truncated elastic modes is included.

When extracting the fixed base eigenmodes from (6.6) little differences are observed in the eigenfrequencies and mode shapes when using a stiffness matrix corresponding to a stopped situation ( $\alpha = 0$ ,  $\omega = 0$ ,  $\Omega = 0$ ) or nominal operation ( $\alpha = \alpha_n$ ,  $\omega = \omega_n$ ,  $\Omega = \Omega_n$ ). In the following results the mode shapes corresponding to nominal operation have been used throughout the simulation. In Figure 6.3 the tip displacement by using 1, 2 and 3 dynamical modes with and without the quasi-static contribution is compared to the FE-model. Here, it appears that by using 1 or 2 dynamical modes, Figure 6.3a and Figure 6.3b, respectively, without the quasi-static contribution results in considerably larger deflections compared to the FE-model. However, by inclusion of the quasi-static contribution the response is almost identical to that of the FE-model by using merely 1 dynamical mode. The reason for getting this good results by using only 1 dynamical mode is because the load applied is only in the blade direction. By using a detailed load model the number of necessary dynamical modes will probably rise to at least two. Using 3 dynamical modes, Figure 6.3c, it appears that the quasi-static contribution has very little influence.

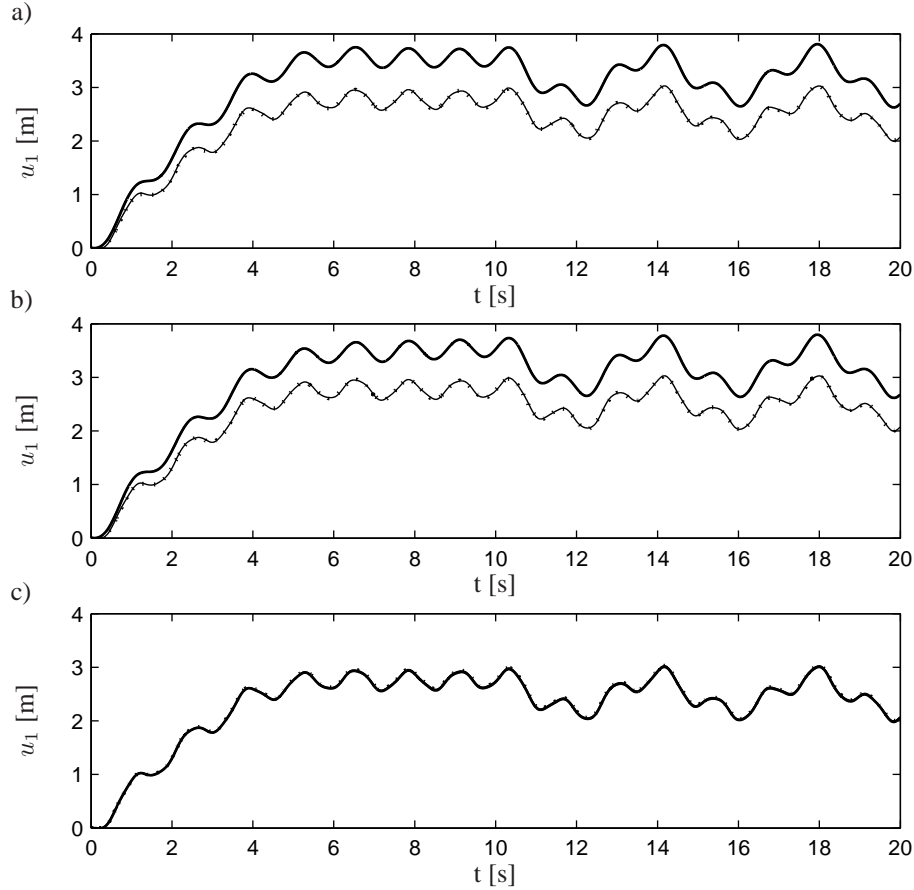


**Figure 6.3** Tip response with ( ····· ) and without ( — ) the quasi-static contribution compared to the FE-model ( — ). Number of dynamical modes: a) 1. b) 2. c) 3.

### 6.1.3 Conclusions

In the present system reduction method the displacement field is described by a Ritz basis consisting of rigid body and elastic fixed-base eigenmodes. Moreover, the quasi-static contribution from the truncated elastic modes is included in the formulation. Based on the numerical examples during start-up and nominal operation it is shown that it has little influence if the elastic modes included in the Ritz basis are obtained from a situation where the wind turbine is stopped or from a situation where the wind turbine operates at the nominal angular velocity. Hereby, the same mode shapes can be used for a wide operating area without losing much accuracy. By using a concentrated load almost an identical response is obtained by only using 1 dynamical mode with the quasi-static contribution compared to the full FE-model.

## 6.2 A Component Mode Synthesis Algorithm for Multibody Dynamics of Wind Turbines

In this section the system reduction method and numerical results from the enclosed paper in Appendix E are described. The system reduction method is based on a component mode synthesis method, where the response of the internal degrees of freedom of the substructure is described as the quasi-static response induced by the boundary degrees of freedom via the constraint modes superimposed in combination to a dynamic component induced by inertial effects and internal loads. The latter component is modelled by a truncated modal expansion in fixed interface undamped eigenmodes. The selected modal vector base for the internal dynamics ensures that the boundary degrees of freedom account for the rigid body dynamics of the substructure, and explicitly represent the coupling degrees of freedom at the interface to the adjacent substructures. In order to get a better description of the large nonlinear displacements of a wind turbine blade it is necessary to include more than one substructure in the blade. The purpose of the present system reduction method is to demonstrate a general approach for including an arbitrary number of reduced substructures to model e.g. a wind turbine blade.

### 6.2.1 System Reduction Method

The equations of motion for the substructure (2.19) are rewritten in the form

$$\mathbf{M}\ddot{\mathbf{y}} + \mathbf{C}\dot{\mathbf{y}} + \mathbf{K}\mathbf{y} = \mathbf{g}(t) = \mathbf{f}(t) - \mathbf{B}^T \bar{\lambda} \quad (6.18)$$

$\mathbf{g}(t)$  is a combined load vector encompassing wind loads, inertial loads, and reaction forces from the kinematical constraints.

At first, the displacement vector  $\mathbf{y}$  of dimension  $n$  is partitioned into boundary  $\mathbf{y}_b$  and interior  $\mathbf{y}_i$  degrees of freedom i.e.  $\mathbf{y}^T = [\mathbf{y}_b^T \quad \mathbf{y}_i^T]$ . The dimensions of  $\mathbf{y}_b$  and  $\mathbf{y}_i$  are  $n_b$  and  $n_i = n - n_b$ , respectively. The method will be illustrated with beam elements with 6 degrees of freedom for each node. Hereby  $n_b$  takes either the value 6 or 12 depending on the substructure has a free end or not. The two different sets of boundary conditions are sketched in Figure 6.4a and 6.4b. When a blade is modelled by two or more substructures the boundary conditions in Figure 6.4a and 6.4b are used for the innermost and outermost substructures, respectively. In Figure 6.4c and 6.4d constraint modes from a unit displacement for the two types of boundary conditions are sketched. Similarly, in Figure 6.4e and 6.4f constraint modes from a unit rotation are sketched. Obviously, the constraint modes account for the rigid body motion of the substructure. (6.18) takes the following form by use of the partitioning of  $\mathbf{y}$

$$\begin{bmatrix} \mathbf{M}_{bb} & \mathbf{M}_{bi} \\ \mathbf{M}_{ib} & \mathbf{M}_{ii} \end{bmatrix} \begin{bmatrix} \ddot{\mathbf{y}}_b \\ \ddot{\mathbf{y}}_i \end{bmatrix} + \begin{bmatrix} \mathbf{C}_{bb} & \mathbf{C}_{bi} \\ \mathbf{C}_{ib} & \mathbf{C}_{ii} \end{bmatrix} \begin{bmatrix} \dot{\mathbf{y}}_b \\ \dot{\mathbf{y}}_i \end{bmatrix} + \begin{bmatrix} \mathbf{K}_{bb} & \mathbf{K}_{bi} \\ \mathbf{K}_{ib} & \mathbf{K}_{ii} \end{bmatrix} \begin{bmatrix} \mathbf{y}_b \\ \mathbf{y}_i \end{bmatrix} = \begin{bmatrix} \mathbf{g}_b \\ \mathbf{g}_i \end{bmatrix} \quad (6.19)$$

Next, the interior degrees of freedom  $\mathbf{y}_i$  are written as a combination of the quasi-static response from the boundary degrees of freedom  $\mathbf{y}_b$  superposed with a modal representation of the remaining part of the internal response as follows

$$\mathbf{y}_i = -\mathbf{K}_{ii}^{-1} \mathbf{K}_{ib} \mathbf{y}_b + \Phi \mathbf{q} \quad (6.20)$$

$$\mathbf{q} = \begin{bmatrix} q_1(t) \\ \vdots \\ q_{n_i}(t) \end{bmatrix}, \quad \Phi = [\Phi_1 \quad \cdots \quad \Phi_{n_i}] \quad (6.21)$$

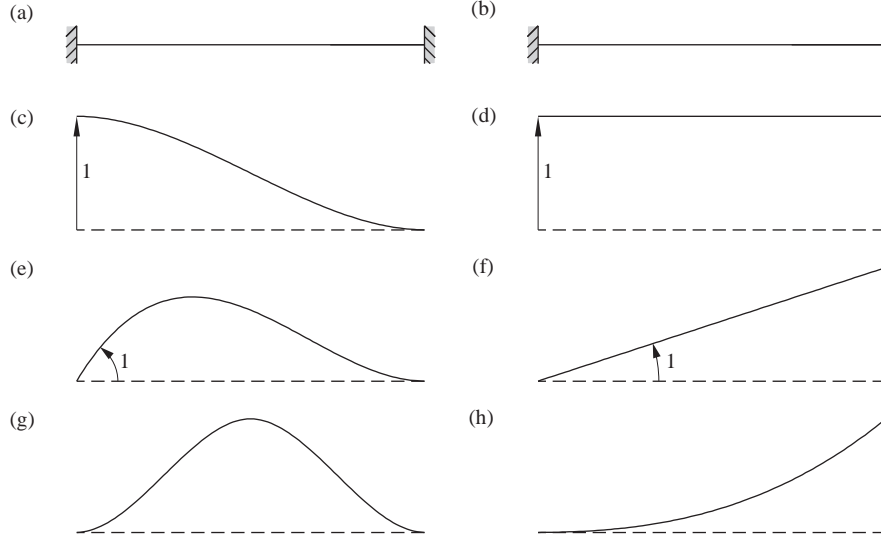


**Figure 6.4** (a) Boundary conditions for interior substructures. (b) Boundary conditions for substructure with a free end. (c)-(f) Constraint modes based on a unit displacement and unit rotation of the interface nodes. (g)-(h) Fixed interface normal modes.

$\Phi_j$  is the  $j$ 'th fixed interface normal mode and  $q_j$  is the related generalized coordinate. In Figure 6.4g and 6.4h an example of a fixed interface normal mode is sketched by use of the two types of boundary conditions. These eigenmodes are determined from the following generalized eigenvalue problem

$$\left( \mathbf{K}_{ii}(\omega, \alpha, \Omega) - \omega_j^2 \mathbf{M}_{ii} \right) \Phi_j = \mathbf{0} \quad (6.22)$$

It is intended that the eigenmodes are constant in time, whereby it is necessary to select the components of the angular velocity vector, angular acceleration vector, and the operating angular frequency, which all are used to set up the stiffness matrix in (2.20).  $\omega_j$  denotes the undamped angular eigenfrequencies of the substructure with fixed boundary degrees of freedom  $\mathbf{y}_b = \mathbf{0}$ . The eigenmodes are ordered in ascending magnitude of the frequency  $\omega_j$  and those with frequencies above a certain threshold frequency  $\omega_0$  are truncated without a quasi-static correction, whereas the remaining eigenmodes respond dynamically. Then, the dynamic degrees of freedom  $\mathbf{q}_d$  and dynamic eigenmodes  $\Phi_d$  become

$$\mathbf{q}_d = \begin{bmatrix} q_1(t) \\ \vdots \\ q_{n_d}(t) \end{bmatrix}, \quad \Phi_d = [ \Phi_1 \quad \cdots \quad \Phi_{n_d} ] \quad (6.23)$$

where  $\mathbf{q}_d$  has the dimensions  $n_d < n_i$ . The degrees of freedom  $\mathbf{y}(t)$  and its time derivatives defining the substructure can hereby be presented in the following reduced form

$$\mathbf{y}(t) = \mathbf{A}\mathbf{w}(t) \quad , \quad \dot{\mathbf{y}}(t) = \mathbf{A}\dot{\mathbf{w}}(t) \quad , \quad \ddot{\mathbf{y}}(t) = \mathbf{A}\ddot{\mathbf{w}}(t) \quad (6.24)$$



where

$$\mathbf{A} = \begin{bmatrix} \mathbf{I} & \mathbf{0} \\ \mathbf{V} & \mathbf{\Phi}_d \end{bmatrix}, \quad \mathbf{V} = -\mathbf{K}_{ii}^{-1} \mathbf{K}_{ib}, \quad \mathbf{w} = \begin{bmatrix} \mathbf{y}_b \\ \mathbf{q}_d \end{bmatrix} \quad (6.25)$$

Insertion of (6.24) in (6.18) and premultiplication with  $\mathbf{A}^T$  provide the following reduced equations of motion

$$\mathbf{m}\ddot{\mathbf{w}} + \mathbf{c}\dot{\mathbf{w}} + \mathbf{k}\mathbf{w} = \mathbf{A}^T \mathbf{g}(t) \quad (6.26)$$

where

$$\left. \begin{aligned} \mathbf{m} &= \mathbf{A}^T \mathbf{M} \mathbf{A} \\ \mathbf{c} &= \mathbf{A}^T \mathbf{C} \mathbf{A} \\ \mathbf{k} &= \mathbf{A}^T \mathbf{K} \mathbf{A} \end{aligned} \right\} \quad (6.27)$$

Notice that none of the reduced matrices have a diagonal structure. To set up the system equations of motion it is necessary to partition  $\mathbf{B}^T$  and  $\mathbf{f}$  in (6.18) consistently with the partition of  $\mathbf{y}$ .

To be used for later comparison an alternative variant is used to model the innermost substructures of the blade. This is done by the use of the same reduction scheme for these substructures as described above for the outermost substructure. Hereby, the innermost substructures are described by use of fixed-free eigenmodes and the dimension of the boundary degrees of freedom is  $n_b = 6$  corresponding to the fixed end. Hereby, the first six columns in  $\mathbf{A}$  correspond to rigid-body modes. This corresponds to the reduction scheme in section 6.1.1 without the quasi-static correction.

## 6.2.2 Numerical example

In this section the theory is illustrated with a simplified system consisting of a wind turbine blade divided into two substructures labelled 1 and 2, as shown in Figure 6.5b. The origin of the initial moving frame of reference  $(x_{1,1}, x_{2,1}, x_{3,1})$  belonging to substructure 1 is identical to the fixed frame of reference  $(\bar{x}_1, \bar{x}_2, \bar{x}_3)$  whereas the origin of the initial moving frame of reference  $(x_{1,2}, x_{2,2}, x_{3,2})$  belonging to substructure 2 is displaced half the blade length in the  $\bar{x}_3$ -direction. The initial orientation of the moving frames is identical to the fixed frame of reference, shown in Figure 6.5a. In total 11 constraints are introduced of which 6 fix the relative displacements and rotations at the assembling point of the two substructures. The remaining 5 constraints are used at the origin of substructure 1. Here, 3 constraints fix the displacements and 2 constraints fix the rotation around the  $\bar{x}_2$ - and  $\bar{x}_3$ -axes. I.e. at the root it is only possible for the blade to rotate around the  $\bar{x}_1$ -axis. The moving frame of reference for both substructures is updated based on the motion of the two end points in each substructure. The updating algorithm is described in Chapter 3 and the  $x_3$ -axis for the two moving frames are sketched in Figure 6.5c. The length of the blade is 44.8 m with a total mass of 10,000 kg and it is constructed by NACA 63-418 section profiles. The cross section parameters throughout the blade are presented in Appendix B.

The purpose of the numerical simulation is to verify that the results obtained from the reduced model based on fixed-fixed interface normal modes for substructure 1 are almost identical to the full FE model. Moreover, the importance of using compatible interface normal modes at the assembling point to substructure 2 is illustrated by the use of fixed-free interface normal

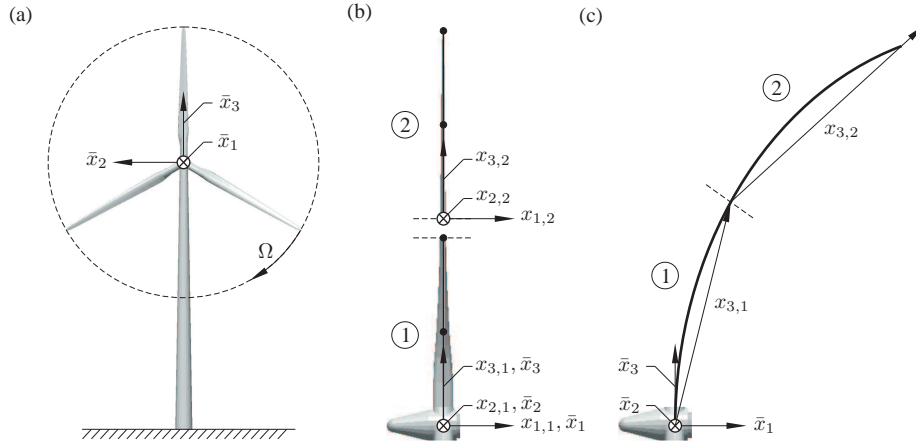


**Figure 6.5** (a) Fixed frame of reference in the wind turbine. (b) In the numerical model the blade is divided into two substructures labelled 1 and 2. (c) Illustration of the  $x_3$ -axis for the moving frame of reference belonging to substructure 1 and 2 denoted by  $x_{3,1}$  and  $x_{3,2}$ , respectively.

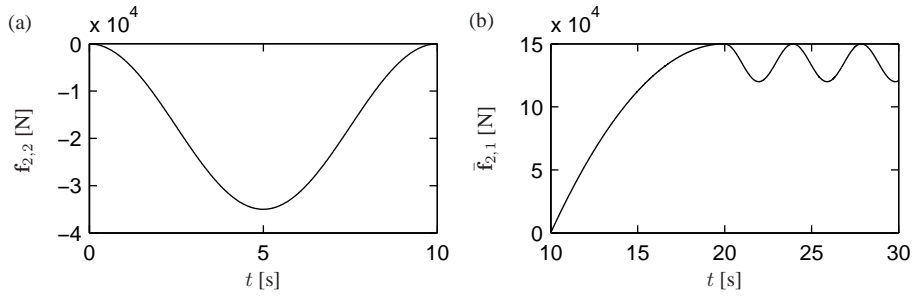


**Figure 6.6** (a) Load component in the  $x_2$ -direction. (b) Load component in the  $\bar{x}_1$ -direction.

modes for substructure 1, with the free end at the assembling point. For both reduced models, substructure 2 is modelled by the use of fixed-free interface normal modes. For comparison of the two reduced models it is chosen to keep the same number of degrees of freedom. The FE model has 132 degrees of freedom and the reduced models have 33 degrees of freedom.

The numerical simulation consists of a start-up sequence and an operating sequence. The start-up sequence is split in two where the first sequence  $0 \leq t \leq 10$  s speeds up the blade from a stopped situation at  $t = 0$  to the nominal angular velocity  $\Omega_n = 1.6 \text{ rad s}^{-1}$  of the rotor at  $t = 10$  s. In the second sequence  $10 \text{ s} < t \leq 20 \text{ s}$  an exterior load in the global  $\bar{x}_1$ -direction is stepped up. In the operating sequence  $t > 20$  s the exterior load is based on a constant load corresponding to a mean wind velocity and a harmonic component due to a variation in the shear wind field. The sequences are modelled by applying concentrated loads at a node in the beam model placed at the moving coordinate  $x_{3,2} = 6.72 \text{ m}$ . The reason for applying the load at this point is because the maximum intensity of the wind load is concentrated around this position. The applied load in the sequence  $0 \leq t \leq 10$  s is oriented in the edge direction in order to speed-up the blade with the time variation shown in Figure 6.6a. In the other two sequences the load

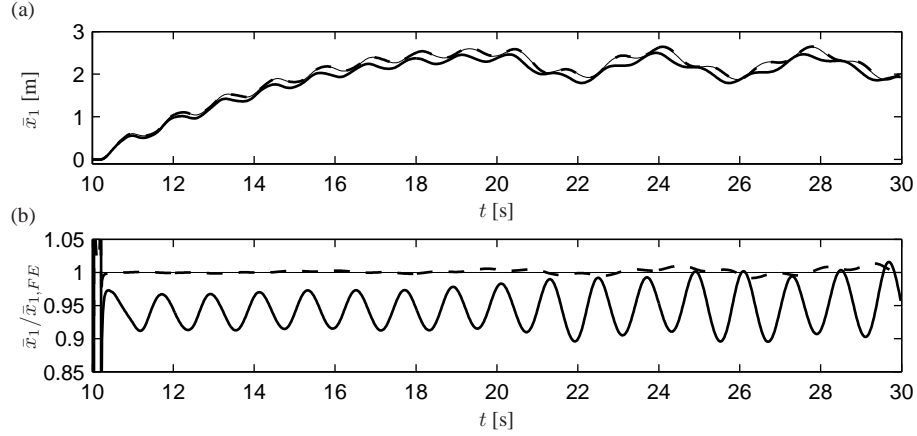


**Figure 6.7** (a) Tip position in  $\bar{x}_1$ . (b) Normalized tip position in  $\bar{x}_1$ . ( — ) FE model. ( - - ) Fixed-fixed modes. ( — ) Fixed-free modes.

is oriented in the  $\bar{x}_1$ -direction i.e. primarily in the flap direction with a time variation shown in Figure 6.6b.

When extracting the eigenmodes from (6.22) a stiffness matrix corresponding to nominal operation ( $\alpha = \alpha_n$ ,  $\omega = \omega_n$ ,  $\Omega = \Omega_n$ ) is used. Results for the tip position of the blade in the  $\bar{x}_1$ -direction during the time series  $10 \leq t \leq 30$  s are shown in Figure 6.7a for the FE model, and the two reduced models with fixed-fixed and fixed-free interface normal modes for substructure 1. The results from the FE model are used to normalize the results from the reduced models shown in Figure 6.7b. The reason for not displaying the first 10 s is because these displacements in  $\bar{x}_1$ -direction are small, and the normalized response of the reduced models is outside the area of interest. In Figure 6.7b the results by use of the fixed-fixed modes are very close to the full FE model, even though these modes are constant throughout the time series. Moreover, these modes are based on a constant angular velocity around just one axis, which is not the actual case, especially for substructure 2. By the use of the fixed-free modes the magnitude of the response is notably changed. The importance of using compatible interface normal modes at the assembling point between the substructures is hereby demonstrated.

### 6.2.3 Conclusions

It is demonstrated that an FE model of a wind turbine blade divided into two substructures in the used multibody formulation with completely freely moving frames of reference efficiently can be reduced by the use of constraint modes and fixed interface normal modes. Even by keeping these modes constant throughout the numerical simulations, where the blade goes from a stopped situation to the nominal operating situation, the results are almost identical to the full FE model. The importance of using compatible modes at the assembling point between the substructures of the blade is demonstrated.

### 6.3 Concluding Remarks

In this chapter it is demonstrated that the number of degrees of freedom in the used multibody formulation easily can be reduced by use of standard reduction methods for dynamical systems. The importance of including a quasi-static correction for the truncated high-frequency eigenmodes is demonstrated in which case only a few dynamically eigenmodes are needed to discretize the response. Moreover, the importance of using compatible modes at the interfaces of the substructures is demonstrated. In both system reduction methods sufficient accuracy has been obtained even though constant eigenmodes have been used throughout the simulation where the blade speeds up from a stopped situation to nominal angular velocity.

---

# CHAPTER 7

## Cross-section Parameters for a Blade Section

---

In this chapter the cross-section parameters for a composite blade section for use in beam elements are determined by use of a finite element procedure. The blade section is meshed in three node triangles based on the the outer profile geometry, the thickness of the material layers, and the internal webs. The determined cross-section parameters are compared to the corresponding results from the program BHawC\_Crs where the blade section has been discretized by use of straight line elements of uniform thickness. The results are almost identical by use of the created program and BHawC\_Crs.

### 7.1 Method to Determine Cross-section Parameters

The section describes an algorithm for determination of the cross-section parameters in beam elements based on a FE solution of the underlying Laplace and Poisson partial differential equations using triangular elements with emphasis on the devised geometry, implementation and mesh generation. The method is based on Krenk and Jeppesen [16] where all derivations are described and later implemented in the cross-section program CROSS SECTION by Jeppesen and Krenk [17]. The main difference is the element type, where straight elements of uniform thickness are used in Krenk and Jeppesen [16], triangular elements are used in the present implementation. This makes it possible to mesh e.g. a blade profile in the respective material layers instead of accounting for the different material layers over the thickness by a mean value. The main focus in the present chapter is to illustrate how the geometry of a blade section has been implemented in the present implementation and to compare the results to BHawC\_Crs which is the program used at Siemens Wind Power A/S for calculating the cross-section parameters for the beam elements in their aeroelastic code BHawC. The computer code implemented in BHawC\_Crs is originally a copy of CROSS SECTION, but some improvements have been performed by Jørgen Thirstrup Petersen [18] to take e.g. a more correct description of the actual geometry in the blade section into consideration. In BHawC\_Crs straight elements with uniform thickness are used to discretize the outer profile geometry and the internal webs in the blade section. In the present implementation three node triangles i.e. with linear shape functions are used to discretize the geometry and material layers in the blade section. The results obtained for the cross-section parameter by the use of triangular elements are compared to those obtained by the BHawC\_Crs implementation of straight line elements. There are two groups of cross-section parameters. The parameters in the first group are based on direct integration over the area and consist of e.g. the

cross section area, mass per unit length, center of gravity, effective moments of inertia, elastic center, and the angle to the principal axes. The second group of parameters include torsional stiffness, effective shear area, and the position of the shear center. The parameters in the second group are determined by a finite element method based on a variational formulation. The torsional stiffness and the position of the shear center are determined by first solving the unknown warping function in the Laplace equation with inhomogeneous Neumann conditions. Next, the Poisson equation with homogeneous Neumann conditions is solved twice with a shear force in each direction at the time, to determine the shear stresses and effective shear areas. The same stiffness matrices are used in both cases. Zienkiewicz and Taylor [19] has been used to setup the Laplace and Poisson equations with the respective boundary conditions by use of the present finite element triangles.

## 7.2 Cross-section Parameters for a Rectangular Box Profile

Before analysing a blade profile a more simple test consisting of a rectangular box profile is used to determine the cross-section parameters. The geometry of the box profile is described in Fig. 7.1a. The profile is homogeneous where the Young's modulus  $E$ , shear modulus  $G$ , and density  $\rho$  attain unit values. The cross-section parameters for this box profile are determined by use of three different programs: BHawC\_Crs, the present program, and the commercial program Ansys. Petersen [18] has made the analysis in BHawC\_Crs and he has also helped in setting up the Ansys model. In Ansys quadrilateral 8 node elements are used to mesh the profile. 8 elements are used in BHawC\_Crs, 3632 elements in the present program, and 716 elements are used in Ansys. The mesh used in the three different programs can be seen in Fig. 7.1b–d. In

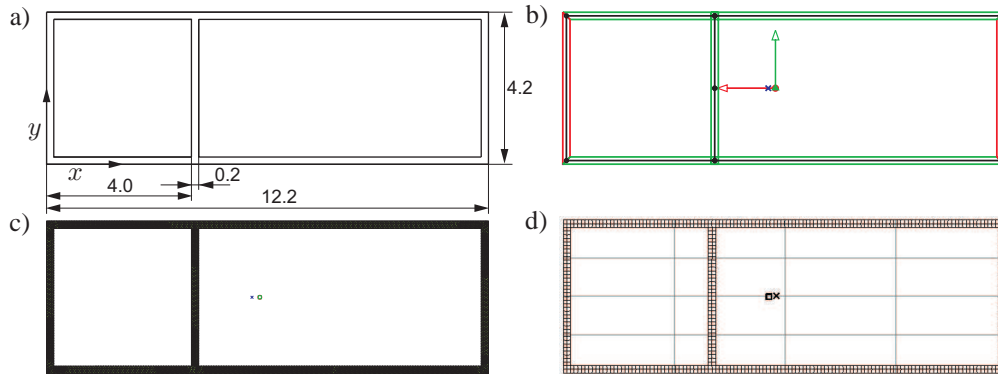


**Figure 7.1** a) Geometry of the rectangular box profile. b) Mesh in BHawC\_Crs. c) Mesh in present program. d) Mesh in Ansys.

Table 7.1 the cross-section parameters for the rectangular box profile are listed by use of the three programs. Here, it can be seen that very good correspondence between the three programs are obtained. Especially the cross-section parameters from the present program and Ansys are almost identical. BHawC\_Crs has slightly higher deviations which is due to overlapping areas at the intersections between the elements.

Description	Label	Unit	BHawC_Crs	Present program	Ansys
Mass	$m$	$[kg/m]$	7.240	7.160	7.160
Center of gravity	$x_{cg}$	$[m]$	5.880	5.888	5.888
Center of gravity	$y_{cg}$	$[m]$	2.100	2.100	2.100
Shear center	$x_{sh}$	$[m]$	5.680	5.672	5.672
Shear center	$y_{sh}$	$[m]$	2.100	2.100	2.100
Bending stiffness	$EI_x$	$[Nm^2]$	22.580	22.279	22.280
Bending stiffness	$EI_y$	$[Nm^2]$	117.900	117.972	117.973
Torsion stiffness	$GI_z$	$[Nm^2]$	57.850	58.759	58.673
Effective shear area	$k_x$	$[-]$	0.611	0.622	0.621
Effective shear area	$k_y$	$[-]$	0.237	0.241	0.240
Area	$A$	$[m^2]$	7.240	7.160	7.160
Angle to principal axis	$\varphi$	$[^\circ]$	-0.003	0.000	0.000
Elastic center	$x_{ea}$	$[m]$	5.880	5.888	5.888
Elastic center	$y_{ea}$	$[m]$	2.100	2.100	2.100

**Table 7.1** Comparison of cross-section parameters for a rectangular box profile by use of BHawC\_Crs, the present program, and Ansys.

## 7.3 Generate Geometry for a Blade Section

In this section the input geometry for a blade section is described and how this data is used to construct the contours between the different material layers and inner webs. Siemens Wind Power A/S has delivered the input for an arbitrary blade section for later comparison to BHawC\_Crs. The geometric input consists of:

- ◆ the outer profile geometry.
- ◆ two lines to define where the beam section is placed in the upper and lower part of the profile, see the lines  $b_1$  and  $b_2$  in Fig. 7.2a.
- ◆ two lines to define the center line of the front and rear web, see the lines  $w_1$  and  $w_2$  in Fig. 7.2a.
- ◆ five thicknesses for the profile: outer glass, beam, core, beam, inner glass.
- ◆ three thicknesses for each web: glass, core, glass.

The outer profile geometry, the two lines defining the beam section in the upper and lower part of the profile, and the two lines defining the webs are shown in Fig. 7.2a. In the two beam sections of the profile a total of five material layers are used in manufacturing the profile. Outside these sections only three material layers are used in manufacturing the profile corresponding to the thicknesses of the: the outer glass, core, inner glass. Similarly, the webs are based on three material layers. In the present program the beam sections are only described by three material layers: outer glass + beam, core, beam + inner glass. This makes a more simple geometry and more easy to mesh. Because the outer glass and inner glass have almost the same material properties as the beam, this restriction will have very little influence on the results. Moreover, the extra area in the interface between the beam section and regular section is small. In Fig. 7.3 the material layers in the profile are sketched for the manufactured profile and in the present numerical model. In Fig. 7.2b the thicknesses of the three material layers in the profile are shown where they have been offset inwards perpendicular to the outer geometry. A closer look on four areas in the blade section are shown in Fig. 7.4. In Fig. 7.4a the interface between the beam section and the regular

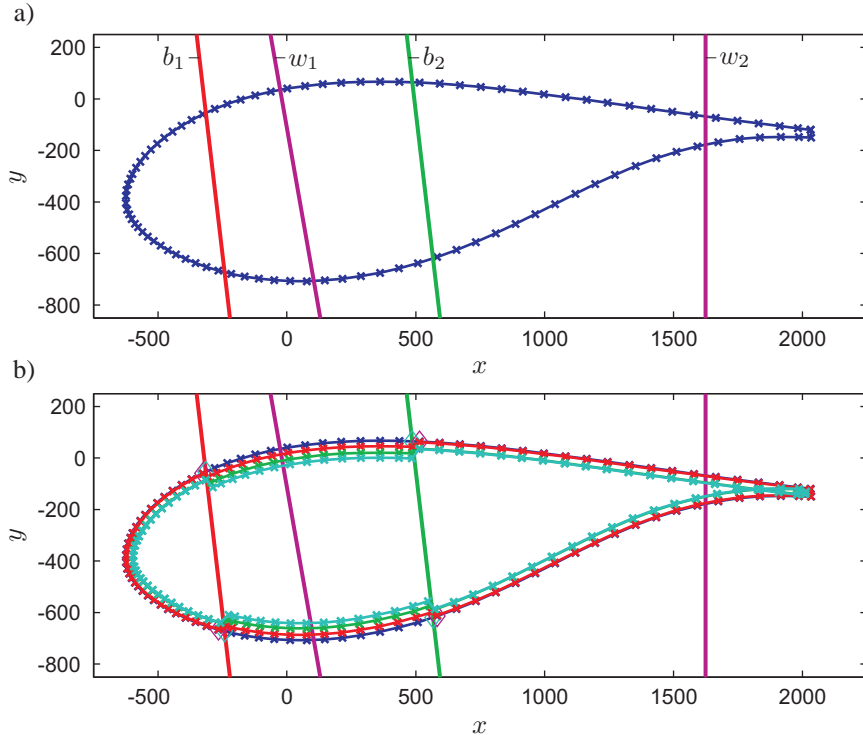


**Figure 7.2** a) Outer profile geometry and the four lines defining the two beam sections and two webs. b) The three material layers in the profile have been offset perpendicular inwards from the outer geometry.

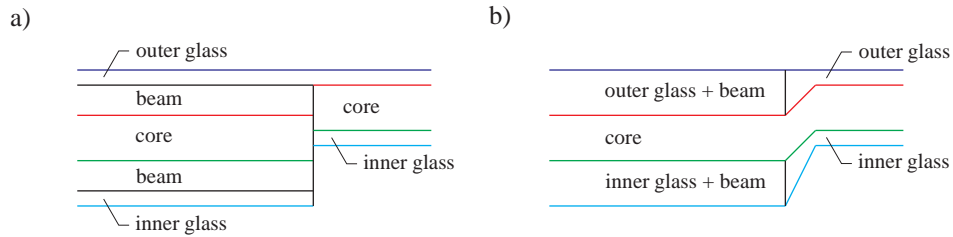


**Figure 7.3** Sketch of material layers in the beam section and the regular section. a) Manufactured profile. b) Present numerical model.

section of the profile is shown. In Fig. 7.4b the material layers at the trailing edge of the profile are overlapping due to offsetting from the outer geometry. This problem is solved in Fig. 7.4d by inserting nodes where the material layers intersect and removing the invalid nodes. In Fig. 7.4c the intersection of the front web with the inner profile is shown. The material layers in the webs are also defined by offsetting the thicknesses perpendicular to the center line. Hereby, all nodes defining the geometry in the blade section are specified and the next step is to mesh the profile.



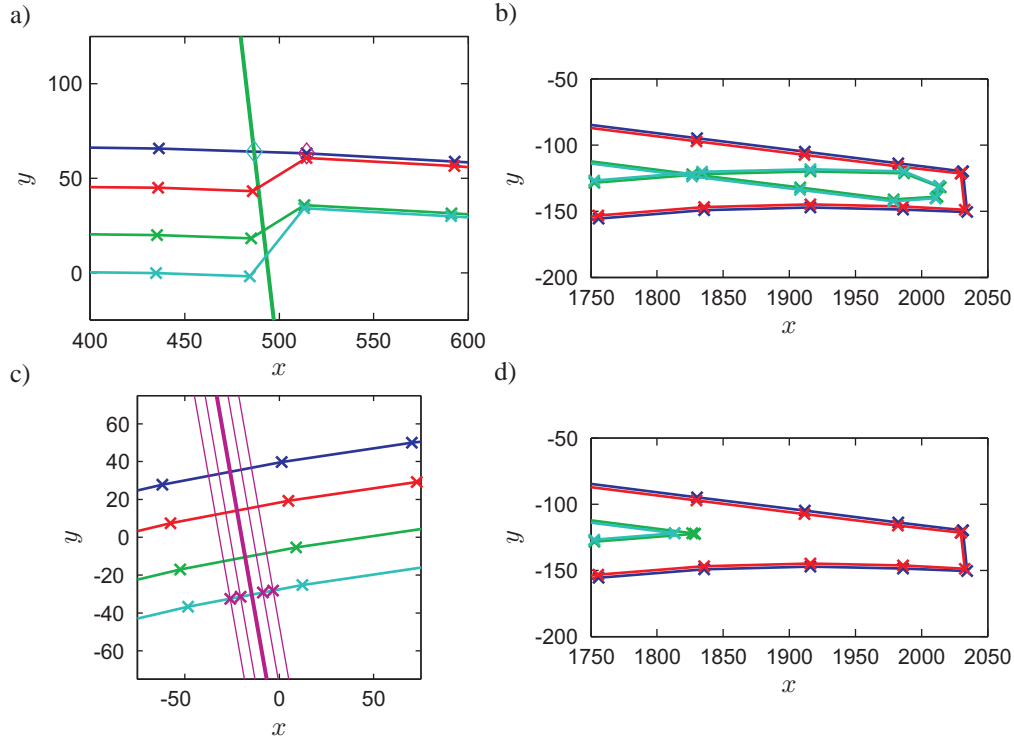


**Figure 7.4** a) Interface between beam and regular section of the profile. b) Overlapping material layers at the tail. c) Intersection of the material layers in the front web with the inner profile. d) The overlapping material layers have been removed.

## 7.4 Meshing of Blade Section

In the present implementation the freeware program EasyMesh [20] is used to mesh the cross-section into triangles. One of the advantages with this program is that it can mesh the cross-section into different material layers which is a necessity by use of the present approach. An input file for EasyMesh is constructed based on the positions of the nodes defining the geometry and contours between the different material layers. To get a regular mesh it is necessary to define a small reference length at the interface between the beam section and regular section of the profile but also at the interface between the webs and inner geometry. A total of 28506 triangles each with three nodes are generated in the six material layers. The profile is shown in Fig. 7.5 and the mesh in four areas is shown in Fig. 7.6. In Fig. 7.6a the mesh is shown at the interface between the beam section and regular section of the profile, where 5 different material layers are used. The small thickness of the inner glass layer and the small angle at the inner tail results in many elements in this region, see Fig. 7.6b. It can also be seen in this figure that only one element is used over the thickness for the outer and inner glass layer. In Fig. 7.6c many elements are necessary at the interface between the front web and the inner geometry. It was not possible by use of EasyMesh to define the material layers in the rear web, therefore this web is meshed in the same material layer as the inner glass, see Fig. 7.6d. The reason is the relatively small size of

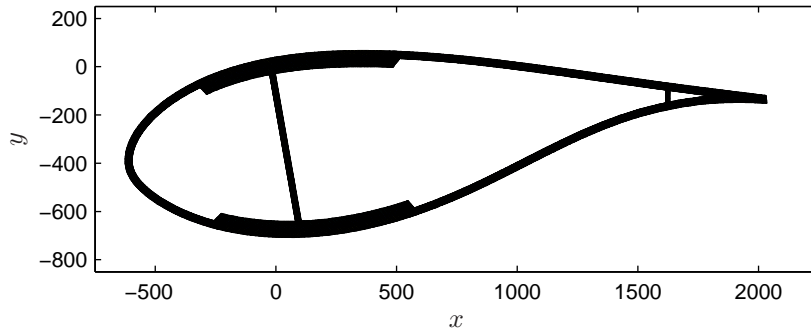


**Figure 7.5** A total of 28506 triangles define the six material layers in the profile.

the material layers in this web. Due to the small area of the rear web the results will not change notably. However, for the later comparison the material layers for the rear web in BHawC\_Crs are similarly changed to just one material layer corresponding to the inner glass.

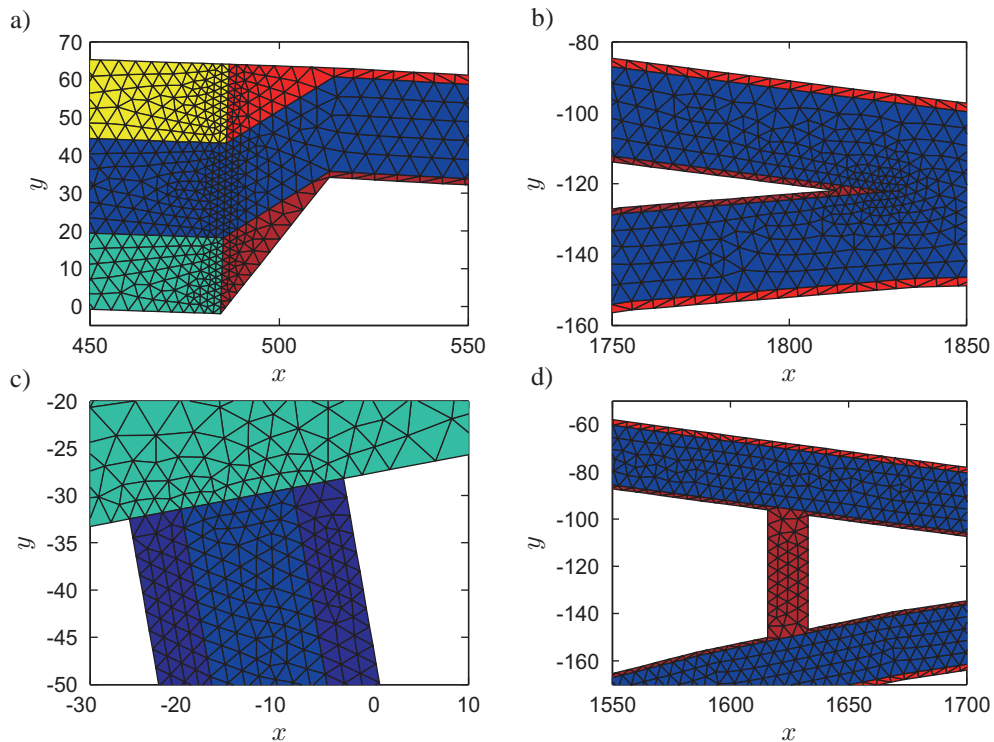


**Figure 7.6** a) Mesh at interface between the beam and regular section. b) High concentration of elements near the inner side of the trailing edge. c) Mesh at interface between the front web and the inner geometry. d) One material layer corresponding to the inner glass is used for the rear web.

Description	Label	Unit	BHawC_Crs	Present program	Difference [%]
Mass	$m$	$[kg/m]$	190.071	190.960	0.5
Center of gravity	$x_{cg}$	$[m]$	0.291	0.289	-0.7
Center of gravity	$y_{cg}$	$[m]$	-0.301	-0.301	0.0
Shear center	$x_{sh}$	$[m]$	-0.054	-0.054	0.0
Shear center	$y_{sh}$	$[m]$	-0.335	-0.337	0.6
Bending stiffness	$EI_x$	$[1E+08Nm^2]$	2.670	2.710	1.5
Bending stiffness	$EI_y$	$[1E+08Nm^2]$	6.476	6.618	2.2
Torsion stiffness	$GI_z$	$[1E+07Nm^2]$	3.492	3.661	4.8
Effective shear area	$k_x$	$[-]$	0.402	0.400	-0.5
Effective shear area	$k_y$	$[-]$	0.155	0.159	2.6
Area	$A$	$[m^2]$	0.241	0.237	-1.7
Angle to principal axis	$\varphi$	$[^\circ]$	7.249	7.570	4.4
Elastic center	$x_{ea}$	$[m]$	0.241	0.244	1.2
Elastic center	$y_{ea}$	$[m]$	-0.308	-0.307	-0.3

**Table 7.2** Comparison of cross-section parameters for a blade profile by use of BHawC\_Crs and the present program.

## 7.5 Comparison of Results to BHawC\_Crs

In this section the results from the present program are compared to the results from BHawC\_Crs. Petersen [18] has made the correction to the rear web in BHawC\_Crs and delivered the belonging results in Table 7.2. Here, it can be seen that there is a very good correspondence between the results from the two programs. Some deviations are present, but this was also the case with the rectangular box profile in section 7.2. The reasons for the deviations are different discretizations e.g. overlapping areas and the limitation with a constant shear stress over the thickness of the straight line elements. In Fig. 7.7 the warping function is plotted and in Fig. 7.8 the position of the gravity-, elastic-, shear-, and aerodynamic center are shown together with the orientation of the elastic axis. In Fig. 7.9 the mesh in BHawC\_Crs are shown together with the different centers and orientation of the principal axis. Here, it should be noted that the principal  $x$ -axis is plotted in the opposite direction for later use in BHawC.

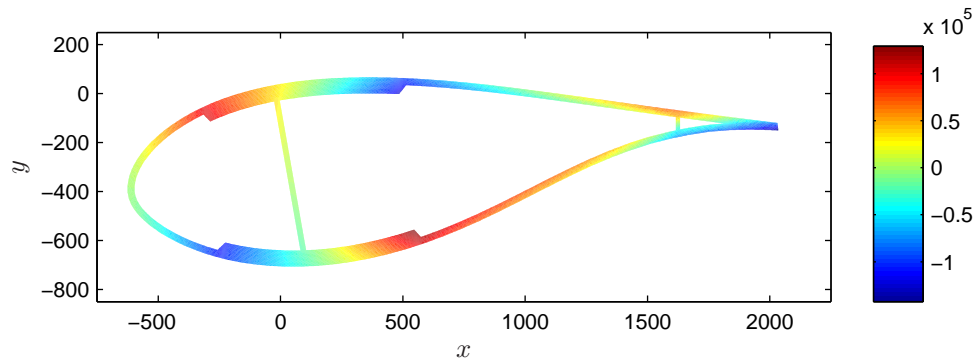


**Figure 7.7** Warping function in the blade section.

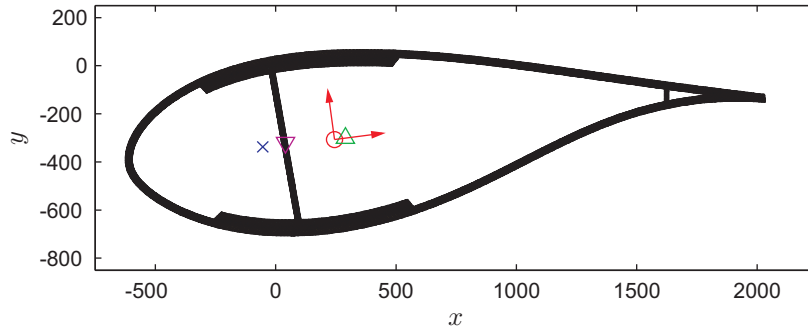


**Figure 7.8** Position of the gravity- ( $\triangle$ ), elastic- ( $\circ$ ), shear- ( $\times$ ), and aerodynamic center ( $\nabla$ ) are shown together with principal elastic axis (—).

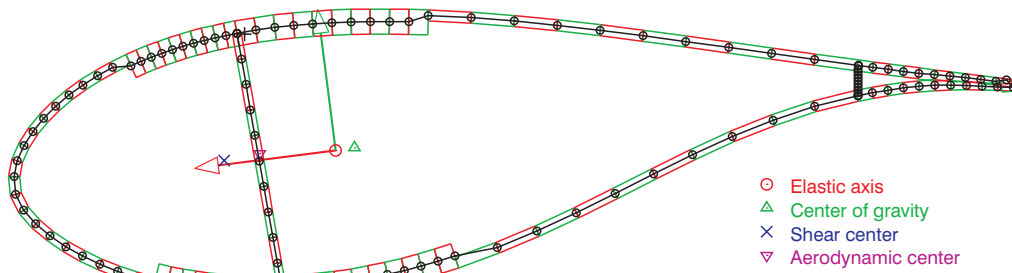


**Figure 7.9** Position of the gravity-, elastic-, shear-, and aerodynamic center are shown together with the principal elastic axis, by use of BHawC\_Crs.

## 7.6 Concluding Remarks

In this chapter it is demonstrated that by use of a finite element discretization based on triangles with linear shape functions do result in almost identical cross-section parameters as by use of a discretization consisting of rectangular line elements where the warping function is represented by a third-degree polynomial. The reason is that the blade profile has a moderate wall thickness where the line elements are sufficient. For further use of the present program with triangular elements another program for meshing is recommended due to the very sensitive and often uncontrollable behavior of EasyMesh.

---

## CHAPTER 8

# Conclusion and Further Work

---

In this chapter the conclusions throughout the thesis are summarized and suggestions for further work areas are listed.

### 8.1 Conclusion

In order to reduce the costs of wind turbines a key point is to optimize the structural components. This calls for an accurate numerical model which can represent the turbine dynamics with a high level of accuracy. In this thesis a flexible multibody formulation based on a Local Observer Frame formulation is in focus together with system reduction for use in analyzing the dynamics of a complex structure as a wind turbine. The use of a multibody formulation makes the modelling more flexible because each structure is modelled individually of the remaining and afterwards assembled to the full system model by use of joints and kinematical constraints. This is also facilitated when creating the reduced models, by only reducing the structures containing the most degrees of freedom.

**Chapter 2** The multibody formulation based on the Local Observer Frame formulation is introduced with emphasis on its differences to the more standard Floating Frame of Reference formulations. The primary difference is that the parameters describing the motion of the moving frame of reference are not part of the system state vector and thereby not updated automatically when solving the equations of motion. Moreover, small rigid body displacements are possible between the substructure and its belonging moving frame. The advantage is that the equations of motion become linear except for the rotation constraints by explicitly predicting the moving frame parameters. The constraint equations used to model e.g. joints, boundary conditions, and kinematical constraints for both displacements and rotations are based on vector relations and also described in this chapter in order to set up the equations of motion for a multibody system. The rotational constraints have been linearized i.e. they are only valid for small rotations of the substructure relative to the belonging moving frame. Next, constraint regularization is used to ensure that the constraints are satisfied on the displacement and velocity level. Often in multibody dynamics the constraint equations are differentiated twice with respect to time and enter the system mass matrix and load vector. In the present project, the approach has been to avoid the related fictitious terms used in the constraint regularization to stabilize the numerical scheme. This is done by solving the constraint equations at the original displacement level so they enter the system stiffness matrix and load vector. Moreover, solving the constraint equations at the displacement level instead of the acceleration level is also beneficial due to the omittance of the

often high frequency components of the accelerations. The equations of motion for a constrained multibody system are solved by use of the nonlinear Newmark time integration algorithm.

**Chapter 3** Because the parameters describing the motion of the moving frame of reference are not part of the system state vector it is necessary to update them in a separate algorithm, to secure that the displacements of the substructure relative to the moving frame remain small. The algorithm presented is primarily intended for beam element models, but can also be used for other types of models including reduced models. The update algorithm for the dynamic simulations is based on the motion of the two boundary nodes in the substructure, from which the moving frame is aligned. Existing updating algorithms which have been used for inspiration are based on the motion of three material points in the belonging substructure from which three independent base unit vectors can be extracted. These methods are primarily intended for solids, because the unit vectors to three material points in a beam model can be linearly dependent. However, the three unit vectors could probably be determined to three points in a fictitious triad placed in the substructure. By eliminating the velocity and acceleration terms, the updating algorithm for static simulations is devised. In the static update algorithm two methods are described, one which uses the motion of the node at the origin to update the moving frame. In the other case the motion at the origin together with an arbitrary point is used to update the frame.

**Chapter 4** Large nonlinear geometric displacements are examined by static analysis of a cantilever beam. The results from the flexible multibody model are compared to a co-rotating beam formulation and an analytical solution where good correspondence is obtained for an increased number of substructure. The update algorithm of the moving frame based on the position of the end nodes in each substructure shows most favorable. For a clamped wind turbine blade it is demonstrated that by use of two substructures of unequal reference length makes it possible to absorb the non-linearities in an efficient way, which otherwise would require four substructures of equal reference length. Very few modifications of the equations of motion are necessary to change from dynamic to static analysis. Especially the constraints can be used in both cases without any modification.

**Chapter 5** The system stiffness and mass matrix are used to determine the undamped eigenfrequencies and belonging eigenmodes of the full multibody model. This is possible by modifying the constraint equations for use in a generalized eigenvalue analysis. Especially the nonlinear terms in the rotational constraints are replaced by equivalent linear terms. The modified constraint equations are still inserted in the system stiffness matrix. An example of a simple wind turbine model consisting of three blades, shaft, and tower are used to demonstrate the facility of the method, where the undamped eigenfrequencies of the first 11 turbine modes are determined.

**Chapter 6** Here, two approaches are demonstrated on how to reduce the number of degrees of freedom of the blade structure in the multibody formulation. In the first approach a Ritz basis is used consisting of six rigid body modes and a number of dynamical fixed base eigenmodes. The importance of including a quasi-static correction for the truncated high-frequency eigenmodes is demonstrated when only a few dynamically eigenmodes are included to discretize the response. The second approach is based on a component mode synthesis method, based on constraint modes and fixed interface normal modes. This is a more general approach, which can be used for

other substructures of the wind turbine or when the blade is modelled by several substructures. In the case of just using a single substructure in the blade structure the method corresponds to the first approach with a Ritz basis. Moreover, the importance of using compatible modes at the interfaces of the substructures is demonstrated. In both system reduction methods sufficient accuracy has been obtained even though constant eigenmodes have been used throughout the simulation where the blade speeds up from a stopped situation to nominal angular velocity.

**Chapter 7** The cross sectional parameters for use in beam element models are determined for a composite blade section. The method is based on a finite element discretization by use of triangular elements with linear shape functions. The different material layers in the blade profile are taken into consideration at their actual position by meshing the profile in the respective material layers. The results are compared to BHawC\_Crs which uses straight line elements of uniform thickness, whereby the material properties over the thickness direction are determined by an average value. Overall, the results are almost identical besides the torsional stiffness which is approximately 5% larger by use of the present approach with a more detailed element type and where the material layers are taken into consideration at their correct position. The reason for the overall good agreement is because the blade profile has a moderate wall thickness where the line elements are sufficient.

## 8.2 Further Work

Below, a number of subjects and ideas are listed suitable for further investigations.

- ◆ Instead of using the linearized rotational constraints other options should be investigated to better describe rotations of the substructure relative to the moving frame. This is especially of interest if only a few substructures are used to model e.g. the blades. The suggested Cayley approach for rotational constraints would be of interest because it can be implemented in the present format.
  - ◆ A criteria should be made for when to update the moving frame parameters. This can be based on the motion of the substructure relative to the moving frame to secure the displacements are sufficiently small. Moreover, it would probably be possible to use the same parameters for the moving frame in several time steps, whereby the same system matrices can be used to speed up the simulation time.
  - ◆ Instead of choosing fixed material points to update the moving frame it would be interesting with a more flexible update approach where the moving frames automatically are updated to reduce the overall displacements of the substructure relative to the moving frame in the present time step.
  - ◆ A more optimal selection of both structural and numerical damping would probably stabilize the numerical models. Other time integration algorithms where especially the high frequency components are damped would be convenient to stabilize the numerical models.
-





---

# Bibliography

---

- [1] A. Kawamoto, M. Inagaki, T. Aoyama, K. Yasuda, Vibration of Moving Flexible Bodies (Formulation of Dynamics by using Normal Modes and a Local Observer Frame), *Proceeding of DETC99/VIB-8232* 1999.
- [2] A.A. Shabana, *Dynamics of Multibody Systems*, Third Edition, Cambridge University Press 2005.
- [3] P.E. Nikravesh, *Computer-aided Analysis of Mechanical Systems*, Prentice Hall 1988.
- [4] J.G. de Jalón & E. Bayo, *Kinematic and Dynamic Simulations of Multibody Systems - The Real-Time Challenge*, Springer-Verlag 1993.
- [5] M. Géradin & A. Cardona, *Flexible Multibody Dynamics - A Finite Element Approach*, John Wiley & Sons Ltd 2001.
- [6] A. Kawamoto, S. Krenk, A. Suzuki, Flexible body dynamics in a freely floating local frame, *ECCOMAS Conference on Multibody Dynamics 2007*, Milan, Italy, 25-28 June 2007.
- [7] A. Kawamoto, A. Suzuki, M. Inagaki, S. Krenk, Flexible-body dynamics in a floating frame with extraction of rigid body motion, *4th Asian Conference on Multibody Dynamics 2008*, ACMD, Jeju, Korea, August 20-23 2008.
- [8] A. Kawamoto, S. Krenk, A. Suzuki, M. Inagaki, Flexible body dynamics in a local frame of reference with explicitly predicted motion, *International Journal for Numerical Methods in Engineering*, (2009) to appear.
- [9] Steen Krenk, Department of Mechanical Engineering, Technical University of Denmark.
- [10] Anders Melchior Hansen, Risø DTU, Risø National Laboratory for Sustainable Energy, Wind Energy Division.
- [11] M. Géradin & D. Rixen, *Mechanical Vibrations: Theory and Application to Structural Dynamics*, Second Edition, John Wiley & Sons Ltd 1997.
- [12] S. Krenk, *Non-Linear Modeling and Analysis of Solids and Structures*, Cambridge University Press, Cambridge, 2009.
- [13] A. Magnusson, M. Ristinmaa, C. Ljung, Behavior of the extensible elastica solution, *International Journal of Solids and Structures*, 38 (2001) 8441–8457.

- 
- [14] J. Gerstmayr, H. Irschik On the correct representation of bending and axial deformation in the absolute nodal coordinate formulation with an elastic line approach, *Journal of Sound and Vibration*, 318 (2008) 461–487.
  - [15] A. Preumont: *Vibration Control of Active Structures, An Introduction* 2nd Edition, Kluwer Academic Publishers (2002).
  - [16] S. Krenk, B. Jeppesen, Finite Elements for Beam Cross-Sections of Moderate Wall Thickness, *Computers & Structures*, 32(5) (1989) 1035–1043.
  - [17] B. Jeppesen, S. Krenk, CROSS SECTION - Program Description and User Manual, *Risø National Laboratory*, Risø-M-2801 (1989).
  - [18] Jørgen Thirstrup Petersen, Siemens Wind Power A/S, Denmark.
  - [19] O.C. Zienkiewicz, R.L. Taylor, *The Finite Element Method, Volume 1: The Basis*, Fifth Edition, Butterworth-Heinemann 2000.
  - [20] B. Niceno, EasyMesh 1.4,  
<http://www-dinma.univ.trieste.it/nirftc/research/easymesh/>.
  - [21] K. Holm-Jørgensen, M.M. Jørgensen, *Modelling of generator failure of a wind turbine and active control of blade vibrations using smart materials*, Aalborg University, Department of Building Technology and Structural Engineering, 2004.

---

# APPENDIX A

## Equations of Motion for a Constrained Substructure in a Moving Frame of Reference

---

In this appendix the equations of motion for a substructure are derived based on Lagrange's equation. Bernoulli-Euler beam elements are used in the FE discretization of the displacement field of the substructure. Small displacements of the substructure within the moving frame are assumed whereby it is necessary that the moving frame is in the vicinity of the substructure. Reaction forces necessary to describe a constrained substructure are part of the equations of motion.

This chapter is based on a work note created by Steen Krenk [9]. This note was later modified and published in Kawamoto et al. [6], where volume elements were used in the FE discretization. Beam elements are used for the FE discretization of the displacement field in the present outline and the reaction forces necessary to describe kinematical constraints of the substructure are included.

### A.1 Motion of a Material Point Relative to a Moving Frame of Reference

In this section the motion of a material point for a deformable substructure relative to a belonging moving frame of reference  $(x_1, x_2, x_3)$  is derived. Additional, a fixed  $(\bar{x}_1, \bar{x}_2, \bar{x}_3)$ -coordinate system is introduced. Accordingly, fixed frame and moving frame components of vectors and tensors will be indicated with and without a bar, respectively. The moving frame of reference is moving in the vicinity of the substructure, and its origin relative to the fixed frame is described by a position vector  $\bar{\mathbf{x}}_c$ , see Fig. A.1. Similarly, the orientation of the moving frame relative to the fixed frame is determined by the parameter vector (or pseudo vector)  $\boldsymbol{\theta}$ . The position of a material point relative to the moving frame of reference is given by

$$\mathbf{x}(\mathbf{s}, t) = \mathbf{s} + \mathbf{u}(\mathbf{s}, t) \tag{A.1}$$

$\mathbf{s}$  is a position vector from the origin of the moving  $(x_1, x_2, x_3)$ -coordinate system to the referential position of the bending center in a given cross-section of the beam along the moving  $x_3$ -axis.  $\mathbf{u}(\mathbf{s}, t)$  is the displacement field relative to the referential position  $\mathbf{s}$ , see Fig A.1. In the present

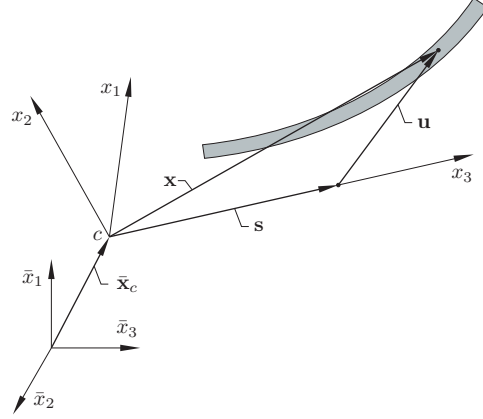


**Figure A.1** Position of a material point relative to the moving frame of reference  $(x_1, x_2, x_3)$ .

case Bernoulli-Euler beam elements are used in an FE discretization of the displacement field. Hereby, the displacement  $\mathbf{u}_{el}(\mathbf{s}_{el}, t)$  within a beam element is interpolated in the form

$$\mathbf{u}_{el}(\mathbf{s}_{el}, t) = \mathbf{N}_{el}(\mathbf{s}_{el})\mathbf{y}_{el}(t) \quad (\text{A.2})$$

$$\mathbf{N}_{el}(\mathbf{s}_{el}) = \begin{bmatrix} N_2 & 0 & 0 & 0 & N_3 & 0 & N_5 & 0 & 0 & 0 & N_6 & 0 \\ 0 & N_2 & 0 & -N_3 & 0 & 0 & 0 & N_5 & 0 & -N_6 & 0 & 0 \\ 0 & 0 & N_1 & 0 & 0 & 0 & 0 & 0 & N_4 & 0 & 0 & 0 \end{bmatrix}$$

$$\begin{aligned} N_1 &= 1 - \xi, & N_2 &= 2\xi^3 - 3\xi^2 + 1, & N_3 &= (\xi^3 - 2\xi^2 + \xi)L_{el} \\ N_4 &= \xi, & N_5 &= -2\xi^3 + 3\xi^2, & N_6 &= (\xi^3 - \xi^2)L_{el} \end{aligned}$$

$\xi = s_{el}/L_{el}$  is a dimensionless interpolation parameter where  $s_{el}$  is a local reference length from the beginning  $s_{el} = 0$  to the end  $s_{el} = L_{el}$  of the element and  $L_{el}$  is the reference length of the beam element.  $\mathbf{y}_{el}(t)$  contains the degrees of freedom of the element. In an FE beam model they represent the nodal displacements and rotations relative to the moving frame of reference and  $\mathbf{N}_{el}(\mathbf{s}_{el})$  is an interpolation matrix. In the following, the lower index 'el' is left out indicating that all element matrices and vectors have been assembled for the substructure. For convenience the time and spatial dependency of  $\mathbf{x}$  and  $\mathbf{u}$  are also left out. Next, the material point is described in the fixed frame by use of the position vector  $\bar{\mathbf{x}}_c$  and a rotation matrix  $\mathbf{R}$  to rotate the moving frame components of  $\mathbf{x}$  into fixed frame components

$$\bar{\mathbf{x}} = \bar{\mathbf{x}}_c + \mathbf{R}\mathbf{x} = \bar{\mathbf{x}}_c + \mathbf{R}(\mathbf{s} + \mathbf{u}) \quad (\text{A.3})$$

where  $\mathbf{R}$  stores the components of the rotation tensor related to the moving frame.  $\mathbf{R}$  is defined by the pseudo vector  $\boldsymbol{\theta}$  as given by Rodriguez formula, see e.g. Shabana [2]

$$\mathbf{R} = \cos \theta \mathbf{I} + (1 - \cos \theta) \mathbf{nn}^T + \sin \theta \tilde{\mathbf{n}} \quad (\text{A.4})$$

where  $\mathbf{n} = \boldsymbol{\theta}/\theta$  is the rotation unit vector,  $\theta = |\boldsymbol{\theta}|$ .  $\mathbf{nn}^T$  is the outer product of this vector with itself, and  $\tilde{\mathbf{n}}$  is the spin matrix related to  $\mathbf{n}$ .  $\tilde{\mathbf{n}}$  is given as

$$\tilde{\mathbf{n}} = \begin{bmatrix} 0 & -n_3 & n_2 \\ n_3 & 0 & -n_1 \\ -n_2 & n_1 & 0 \end{bmatrix} \quad (\text{A.5})$$

$[n_1, n_2, n_3]$  specify the components of  $\mathbf{n}$ , which are identical in the fixed and the moving frame. Time differentiation of the position vector (A.3) yields the velocity vector in fixed components

$$\bar{\mathbf{v}} = \dot{\mathbf{x}} = \dot{\mathbf{x}}_c + \dot{\mathbf{R}}(\mathbf{s} + \mathbf{u}) + \mathbf{R}\dot{\mathbf{u}} \quad (\text{A.6})$$

where the first term  $\dot{\mathbf{x}}_c$  is the translational velocity of the moving frame, the second term  $\dot{\mathbf{R}}(\mathbf{s} + \mathbf{u})$  is the rotational velocity and the last term  $\mathbf{R}\dot{\mathbf{u}}$  is the velocity from the local deformations of the material point inside the moving frame. Next, the fixed frame components of the velocity vector are transformed to moving frame components by pre-multiplication with  $\mathbf{R}^T$

$$\mathbf{v} = \mathbf{R}^T \dot{\mathbf{x}}_c + \mathbf{R}^T \dot{\mathbf{R}}(\mathbf{s} + \mathbf{u}) + \dot{\mathbf{u}} \quad (\text{A.7})$$

where it has been utilized that  $\mathbf{R}^T \mathbf{R} = \mathbf{I}$ . The product of the rotation matrices  $\mathbf{R}^T \dot{\mathbf{R}}$  can be expressed by the following spin matrix

$$\mathbf{R}^T \dot{\mathbf{R}} = \tilde{\boldsymbol{\omega}} = \begin{bmatrix} 0 & -\omega_3 & \omega_2 \\ \omega_3 & 0 & -\omega_1 \\ -\omega_2 & \omega_1 & 0 \end{bmatrix} \quad (\text{A.8})$$

where  $\boldsymbol{\omega}$  is the moving frame components of the angular velocity vector of the moving frame. The velocity of the origin of the moving frame  $\mathbf{v}_c$  is next introduced together with the spin matrix from (A.8) in (A.7)

$$\mathbf{v} = \mathbf{v}_c + \tilde{\boldsymbol{\omega}}(\mathbf{s} + \mathbf{u}) + \dot{\mathbf{u}} \quad (\text{A.9})$$

Next, the acceleration vector in fixed frame components is determined by time differentiation of the fixed frame velocity components in (A.6)

$$\bar{\mathbf{a}} = \ddot{\mathbf{x}} = \ddot{\mathbf{x}}_c + \ddot{\mathbf{R}}(\mathbf{s} + \mathbf{u}) + 2\dot{\mathbf{R}}\dot{\mathbf{u}} + \mathbf{R}\ddot{\mathbf{u}} \quad (\text{A.10})$$

The moving frame components are determined by pre-multiplication with  $\mathbf{R}^T$

$$\mathbf{a} = \mathbf{a}_c + \mathbf{R}^T \ddot{\mathbf{R}}(\mathbf{s} + \mathbf{u}) + 2\mathbf{R}^T \dot{\mathbf{R}}\dot{\mathbf{u}} + \ddot{\mathbf{u}} \quad (\text{A.11})$$

where the moving frame components of the acceleration of the moving frame origin in has been introduced as  $\mathbf{a}_c$ . The term  $\mathbf{R}^T \ddot{\mathbf{R}}$  can be determined from a time differentiation of  $\tilde{\boldsymbol{\omega}}$  in (A.8)

$$\dot{\tilde{\boldsymbol{\omega}}} = \dot{\mathbf{R}}^T \dot{\mathbf{R}} + \mathbf{R}^T \ddot{\mathbf{R}} \quad (\text{A.12})$$

This expression can be further simplified by use of the orthogonality condition  $\mathbf{R}\mathbf{R}^T = \mathbf{I}$ . Moreover,  $\boldsymbol{\alpha}$  is introduced as the angular acceleration vector determined from a time differentiation of the angular velocity vector  $\boldsymbol{\omega}$

$$\begin{aligned} \dot{\tilde{\boldsymbol{\omega}}} &= \tilde{\boldsymbol{\alpha}} = \dot{\mathbf{R}}^T \mathbf{R} \mathbf{R}^T \dot{\mathbf{R}} + \mathbf{R}^T \ddot{\mathbf{R}} \Rightarrow \\ \mathbf{R}^T \ddot{\mathbf{R}} &= \tilde{\boldsymbol{\alpha}} - \tilde{\boldsymbol{\omega}}^T \tilde{\boldsymbol{\omega}} = \tilde{\boldsymbol{\alpha}} + \tilde{\boldsymbol{\omega}} \tilde{\boldsymbol{\omega}} \end{aligned} \quad (\text{A.13})$$

where the skew-symmetric property of  $\tilde{\omega}$  has been used. The moving frame components of the acceleration vector are determined by substitution of (A.8) and (A.13) in (A.11)

$$\mathbf{a} = \mathbf{a}_c + (\tilde{\alpha} + \tilde{\omega}\tilde{\omega})(\mathbf{s} + \mathbf{u}) + 2\tilde{\omega}\dot{\mathbf{u}} + \ddot{\mathbf{u}} \quad (\text{A.14})$$

The first term  $\mathbf{a}_c$  denotes the moving frame components of the acceleration vector of the moving frame origin. The term  $\tilde{\alpha}(\mathbf{s} + \mathbf{u})$  is the angular acceleration which is tangential to the axis of rotation. The next term  $\tilde{\omega}\tilde{\omega}(\mathbf{s} + \mathbf{u})$  describes the centrifugal acceleration which acts in a plane tangent to  $\tilde{\omega}$  and directed away from the axis of rotation. The Coriolis acceleration is described by  $2\tilde{\omega}\dot{\mathbf{u}}$  which is perpendicular to both the direction of the local velocity vector of the moving substructure and to angular velocity vector. Finally, the term  $\ddot{\mathbf{u}}$  describes the moving frame components of the acceleration of the material point as seen by an observer fixed to the moving frame.

## A.2 Lagrange's Equation

The equations of motion are derived using Lagrange's equation. For a given constrained substructure this reads

$$\frac{d}{dt} \left( \frac{\partial L}{\partial \dot{y}_k} \right) - \frac{\partial L}{\partial y_k} = Q_{k,l} + Q_{k,c} \quad (\text{A.15})$$

where  $Q_{k,l}$  are the generalized external loads on the substructure and may include as well conservative as non-conservative loads on the substructure.  $Q_{k,c}$  are the generalized reaction forces acting at the constrained degrees of freedom at the interface to adjoint substructures. In chapter 2 the constraint equations are further described.  $y_k$  is the generalized coordinates of the substructure and  $L$  is the Lagrangian of the system defined as the difference between the total kinetic  $T = T(\mathbf{y}, \dot{\mathbf{y}})$  and potential energy  $U = U(\mathbf{y})$

$$L = T - U \quad (\text{A.16})$$

By insertion of the Lagrangian in (A.15) and using the fact that the potential energy do not contain time-derivatives of the generalized coordinates, Lagrange's equation may be written in the following vector form

$$\frac{d}{dt} \left( \frac{\partial T}{\partial \dot{\mathbf{y}}^T} \right) - \frac{\partial T}{\partial \mathbf{y}^T} + \frac{\partial U}{\partial \mathbf{y}^T} = \mathbf{Q}_l + \mathbf{Q}_c \quad (\text{A.17})$$

In the following the kinetic and potential energy will be derived based on the generalized coordinates and inserted in Lagrange's equation to determine the equations of motion.

## A.3 Kinetic Energy

In this section the kinetic energy for a certain substructure is derived which later will be used in Lagrange's equation to obtain the equations of motion. The kinetic energy is determined from the integral of the mass per unit length and the magnitude of the absolute velocity vector  $\mathbf{v}$

squared. The latter will be described in moving frame components and thereby the kinetic energy  $T$  becomes

$$T = \frac{1}{2} \int_L \mathbf{v}^T \mathbf{v} \mu dx_3 \quad (\text{A.18})$$

where  $L$  is the reference length of the substructure and  $\mu$  is the mass per unit length. Previously in (A.9) the velocity vector  $\mathbf{v}$  has been derived. Insertion of the local displacement vector  $\mathbf{u}$  from (A.2) in (A.9) yields the moving frame components of the velocity vector

$$\mathbf{v} = \mathbf{v}_c + \tilde{\omega}(\mathbf{s} + \mathbf{N}\mathbf{y}) + \mathbf{N}\dot{\mathbf{y}} \quad (\text{A.19})$$

By insertion of (A.19) in (A.18) the kinetic energy is obtained as

$$\begin{aligned} T &= \frac{1}{2} \int_L \left( \mathbf{v}_c + \tilde{\omega}(\mathbf{s} + \mathbf{N}\mathbf{y}) + \mathbf{N}\dot{\mathbf{y}} \right)^T \left( \mathbf{v}_c + \tilde{\omega}(\mathbf{s} + \mathbf{N}\mathbf{y}) + \mathbf{N}\dot{\mathbf{y}} \right) \mu dx_3 \\ &= \frac{1}{2} \int_L \left( \mathbf{v}_c^T \mathbf{v}_c + 2\mathbf{v}_c^T \tilde{\omega} \mathbf{s} + 2\mathbf{v}_c^T \tilde{\omega} \mathbf{N}\mathbf{y} + 2\mathbf{v}_c^T \mathbf{N}\dot{\mathbf{y}} + \mathbf{s}^T \tilde{\omega}^T \tilde{\omega} \mathbf{s} + 2\mathbf{s}^T \tilde{\omega}^T \tilde{\omega} \mathbf{N}\mathbf{y} + \right. \\ &\quad \left. 2\mathbf{s}^T \tilde{\omega}^T \mathbf{N}\dot{\mathbf{y}} + \mathbf{y}^T \mathbf{N}^T \tilde{\omega}^T \tilde{\omega} \mathbf{N}\mathbf{y} + 2\dot{\mathbf{y}}^T \mathbf{N}^T \tilde{\omega} \mathbf{N}\mathbf{y} + \dot{\mathbf{y}}^T \mathbf{N}^T \mathbf{N}\dot{\mathbf{y}} \right) \mu dx_3 \end{aligned} \quad (\text{A.20})$$

where the translation velocity  $\mathbf{v}_c$ , the angular velocity  $\omega$ , the generalized coordinates  $\mathbf{y}$  and their time derivatives  $\dot{\mathbf{y}}$  are independent of the spatial coordinates and can be moved outside the integration sign. In so doing the kinetic energy in (A.20) is expressed by

$$T = \frac{1}{2} m \mathbf{v}_c^T \mathbf{v}_c + \mathbf{v}_c^T \mathbf{J}_1 + \mathbf{v}_c^T \mathbf{G}_0 \mathbf{y} + \mathbf{v}_c^T \mathbf{M}_0 \dot{\mathbf{y}} - \frac{1}{2} \mathbf{J} + \mathbf{J}_2 \mathbf{y} + \mathbf{J}_0 \dot{\mathbf{y}} - \frac{1}{2} \mathbf{y}^T \mathbf{D} \mathbf{y} + \dot{\mathbf{y}}^T \mathbf{G} \mathbf{y} + \frac{1}{2} \dot{\mathbf{y}}^T \mathbf{M} \dot{\mathbf{y}} \quad (\text{A.21})$$

where  $m$  is the mass of the substructure given by

$$m = \int_L \mu dx_3 \quad (\text{A.22})$$

$\mathbf{M}$  is the usual symmetric consistent mass matrix of a substructure in a stationary frame of reference

$$\begin{aligned} \mathbf{M} &= \int_L \mathbf{N}^T \mathbf{N} \mu dx_3 \\ M_{IJ} &= \delta_{ij} \int_L N_{iI} N_{jJ} \mu dx_3 \end{aligned} \quad (\text{A.23})$$

where  $M_{IJ}$  denotes the components of  $\mathbf{M}$ . In (A.23) and below upper case indices  $I$  and  $J$  range from 1 to the number of degrees of freedom  $n$  for the substructure. The lower case index  $i, j$  range from 1 to 3. The summation is still presumed over dummy lower case indices.

$\mathbf{M}_0$  is a special mass matrix of dimension  $3 \times n$  representing the effect of uniform translation

$$\begin{aligned} \mathbf{M}_0 &= \int_L \mathbf{N} \mu dx_3 \\ M_{iJ,0} &= \int_L N_{iJ} \mu dx_3 \end{aligned} \quad (\text{A.24})$$

The effect of centrifugal forces are contained in the symmetric matrix  $\mathbf{D}$  given by

$$\begin{aligned}\mathbf{D} &= \int_L \mathbf{N}^T \tilde{\omega} \tilde{\omega} \mathbf{N} \mu dx_3 \\ D_{IJ} &= \tilde{\omega}_{ik} \tilde{\omega}_{jk} \int_L N_{iI} N_{jJ} \mu dx_3\end{aligned}\quad (\text{A.25})$$

The Coriolis forces are represented by the skew-symmetric matrix  $\mathbf{G}$

$$\begin{aligned}\mathbf{G} &= \int_L \mathbf{N}^T \tilde{\omega} \mathbf{N} \mu dx_3 \\ G_{IJ} &= \tilde{\omega}_{ij} \int_L N_{iI} N_{jJ} \mu dx_3\end{aligned}\quad (\text{A.26})$$

Notice, the integrals in the components forms of (A.23), (A.25), and (A.26) are identical. The special form of a uniform translation is defined by the matrix

$$\begin{aligned}\mathbf{G}_0 &= \int_L \tilde{\omega} \mathbf{N} \mu dx_3 = \tilde{\omega} \mathbf{M}_0 \\ G_{IJ,0} &= \tilde{\omega}_{ij} \int_L N_{jJ} \mu dx_3\end{aligned}\quad (\text{A.27})$$

The centrifugal and gyroscopic terms depend on the angular velocity of the moving frame of reference  $\omega$  and therefore are time-dependent for accelerated rotation of the moving frame.

Next, the terms where the motion of the reference position enter are introduced. The matrix  $\mathbf{J}$  is the inertia tensor defining the kinetic energy of the rigid body part of the motion due to the angular rotation.

$$\mathbf{J} = \omega^T \int_L \tilde{\mathbf{s}} \tilde{\mathbf{s}} \mu dx_3 \omega \quad (\text{A.28})$$

$\mathbf{J}_0$  determines the kinetic energy due to couplings between the reference and elastic motion.

$$\mathbf{J}_0 = \omega^T \int_L \tilde{\mathbf{s}} \mathbf{N} \mu dx_3 \quad (\text{A.29})$$

$\mathbf{J}_1$  determines the kinetic energy due to coupling between the angular velocity vector and the reference motion.

$$\mathbf{J}_1 = \tilde{\omega} \int_L \mathbf{s} \mu dx_3 \quad (\text{A.30})$$

Finally, the term  $\mathbf{J}_2$  determines the contribution from reference and local motion.

$$\mathbf{J}_2 = \omega^T \int_L \tilde{\mathbf{s}} \tilde{\omega} \mathbf{N} \mu dx_3 \quad (\text{A.31})$$

It is chosen not to move  $\omega$  out of the above listed terms so the kinetic energy in (A.21) by a first look only depends on the generalized coordinates. This is done because  $\omega$  is assumed to be updated independent of the generalized coordinates.



## A.4 Potential Energy

In this section the potential energy is derived which later will be used in Lagrange's equation to set up the equations of motion of the substructure. The total potential energy  $U$  is determined from

$$U = U_e \quad (\text{A.32})$$

where  $U_e$  is the elastic potential energy from elastic deformations of the substructure. By introducing  $\mathbf{K}_e$  as the stiffness of the substructure, and  $\mathbf{K}_g$  as the geometric stiffness the elastic potential energy becomes

$$U_e = \frac{1}{2} \mathbf{y}^T (\mathbf{K}_e + \mathbf{K}_g) \mathbf{y} \quad (\text{A.33})$$

where  $\mathbf{K}_e$  denotes the elastic stiffness matrix which is positive semi-definite due to no elimination of the rigid body motion.

## A.5 Equations of Motion

When both the kinetic and potential energy are derived the equations of motion can be determined by use of Lagrange's equation.

### A.5.1 Terms from Kinetic Energy

The first term in Lagrange's equation (A.17) is the time derivative of the term

$$\frac{\partial T}{\partial \dot{\mathbf{y}}^T} = \mathbf{M}_0^T \mathbf{v}_c + \mathbf{J}_0^T + \mathbf{G} \mathbf{y} + \mathbf{M} \dot{\mathbf{y}} \quad (\text{A.34})$$

where  $T$  has been derived in (A.21). Both of the mass matrices are time-independent but  $\mathbf{G}$  and  $\mathbf{J}_0$  are not due to the dependency of the angular velocity of the moving frame cf. (A.26) and (A.29), respectively. The time derivative of the moving frame velocity in moving frame components is determined from the fixed frame velocity components  $\bar{\mathbf{v}}_c$  in the following way

$$\dot{\mathbf{v}}_c = \frac{d}{dt} (\mathbf{R}^T \bar{\mathbf{v}}_c) = \mathbf{R}^T \bar{\mathbf{a}}_c + \dot{\mathbf{R}}^T \bar{\mathbf{v}}_c = \mathbf{a}_c - \tilde{\omega} \mathbf{v}_c \quad (\text{A.35})$$

Hereby the time derivative of (A.34) becomes

$$\frac{d}{dt} \left( \frac{\partial T}{\partial \dot{\mathbf{y}}^T} \right) = \mathbf{M}_0^T (\mathbf{a}_c - \tilde{\omega} \mathbf{v}_c) + \dot{\mathbf{J}}_0^T + \dot{\mathbf{G}} \mathbf{y} + \mathbf{G} \dot{\mathbf{y}} + \mathbf{M} \ddot{\mathbf{y}} \quad (\text{A.36})$$

The second term in Lagrange's equation is

$$\frac{\partial T}{\partial \mathbf{y}^T} = \mathbf{G}_0^T \mathbf{v}_c + \mathbf{J}_2^T - \mathbf{D} \mathbf{y} + \mathbf{G}^T \dot{\mathbf{y}} = \mathbf{M}_0^T \tilde{\omega}^T \mathbf{v}_c + \mathbf{J}_2^T - \mathbf{D} \mathbf{y} + \mathbf{G}^T \dot{\mathbf{y}} \quad (\text{A.37})$$

By combining these two contributions to Lagrange's equation the terms containing the velocity  $\mathbf{v}_c$  of the local system cancel, yielding

$$\frac{d}{dt} \left( \frac{\partial T}{\partial \dot{\mathbf{y}}^T} \right) - \frac{\partial T}{\partial \mathbf{y}^T} = \mathbf{M} \ddot{\mathbf{y}} + 2\mathbf{G} \dot{\mathbf{y}} + (\dot{\mathbf{G}} + \mathbf{D}) \mathbf{y} + \mathbf{M}_0^T \mathbf{a}_c + \dot{\mathbf{J}}_0^T - \mathbf{J}_2^T \quad (\text{A.38})$$

In addition to the local acceleration term  $\mathbf{M}\ddot{\mathbf{y}}$  this expression contains three terms generated by the motion of the moving frame.  $\mathbf{M}_0^T \mathbf{a}_c$  is the inertial load due to the acceleration of the moving frame,  $2\mathbf{G}\dot{\mathbf{y}}$  is a skew-symmetric gyroscopic load term and  $(\dot{\mathbf{G}} + \mathbf{D})\mathbf{y}$  represents a stiffness term that combines the effect of angular acceleration and centripetal accelerations from the angular velocity of the moving frame.  $\mathbf{J}_0$  and  $\mathbf{J}_2$  are both couplings between the reference position and the elastic displacements inside the moving frame.

### A.5.2 Terms from Potential Energy

The potential energy from elastic deformations of the substructure (A.33) only contribute to the third term in Lagrange's equation (A.17) due to no terms containing time-derivatives of the generalized coordinates. Hereby, the potential energy in Lagrange's equation from the elastic potential is

$$\frac{\partial U}{\partial \mathbf{y}^T} = (\mathbf{K}_e + \mathbf{K}_g)\mathbf{y} \quad (\text{A.39})$$

### A.5.3 Combined Terms from Kinetic and Potential Energy

By combining the derived terms (A.38) and (A.39) from kinetic and potential energy, respectively, with the right hand terms in (A.17) the equations of motion become

$$\mathbf{M}\ddot{\mathbf{y}} + 2\mathbf{G}\dot{\mathbf{y}} + (\mathbf{K}_e + \dot{\mathbf{G}} + \mathbf{D} + \mathbf{K}_g)\mathbf{y} = -\mathbf{M}_0^T \mathbf{a}_c - \dot{\mathbf{J}}_0^T + \mathbf{J}_2^T + \mathbf{Q}_l + \mathbf{Q}_c \quad (\text{A.40})$$

Here it can be seen that only the generalized coordinates  $\mathbf{y}$  describing the elastic displacements inside the moving frame appear on the left side as unknown degrees-of-freedom. Hereby, it is necessary to know the parameters for the moving frame i.e.  $\mathbf{a}_c$ ,  $\boldsymbol{\omega}$  and  $\boldsymbol{\alpha}$  which also enter the equations of motion. These parameters are assumed known and only updated when the displacements from the moving frame exceed a certain limit whereby the moving frame and these parameters are updated, see chapter 3 for the updating algorithm.

## A.6 Concluding Remarks

In this chapter the equations of motion for a substructure in a moving frame of reference is derived based on Lagrange's equation. In the derivations it is assumed that beam elements are used in the FE discretization of the displacement field for the substructure. The reaction forces necessary to incorporate kinematic constraints of the substructure are included. The motion of the moving frame can be arbitrary, but it is necessary that the belonging substructure is close enough to the moving frame that linear theory is adequate. Therefore, it is necessary to regularly update the motion of the moving frame.

---

## APPENDIX B

# Cross Section Parameters for Wind Turbine Blade and Tower

---

In this chapter the cross section parameters for the wind turbine blade and tower are listed. These data and figures originate from Holm-Jørgensen and Jørgensen [21]. The following nomenclature is used for the cross section parameters.

- ◆  $x_3$ : Position coordinate to the section in the longitudinal direction.
- ◆  $\mu$ : Mass per unit length.
- ◆  $A$ : Area.
- ◆  $E$ : Young's modulus.
- ◆  $G$ : Shear modulus.
- ◆  $I'_1$ : Area moment of inertia around the principal elastic axis  $x'_1$ .
- ◆  $I'_2$ : Area moment of inertia around the principal elastic axis  $x'_2$ .
- ◆  $I_3$ : St. Venant Torsional stiffness.
- ◆  $\theta$ : Angle from the  $(x_1, x_2)$ -coordinate system to the principal  $(x'_1, x'_2)$ -coordinate system including the twist of the blade. Positive around the negative  $x_3$ -direction.

### B.1 Cross Section Parameters for Wind Turbine Blade

The wind turbine blade has a length of 44.8 m and a mass of 9960 kg. The cross section parameters are defined in 22 sections throughout the blade, see Fig. B.1. The data for these sections are listed in Table B.1.

$x_3$ [m]	$\mu$ [kg/m]	$A$ [m <sup>2</sup> ]	$E$ [N/m <sup>2</sup> ]	$G$ [N/m <sup>2</sup> ]	$I_1'$ [m <sup>4</sup> ]	$I_2'$ [m <sup>4</sup> ]	$I_3$ [m <sup>4</sup> ]	$\theta$ [rad]
0.0	637.7	0.319	3.000E+10	1.154E+10	1.644E-01	1.644E-01	3.534E-01	0.000
3.3	637.7	0.319	3.000E+10	1.154E+10	1.644E-01	1.644E-01	3.534E-01	0.000
6.3	307.4	0.154	3.000E+10	1.154E+10	8.294E-02	5.679E-02	1.012E-01	-0.699
7.8	309.4	0.155	3.000E+10	1.154E+10	1.019E-01	4.478E-02	9.259E-02	-0.587
9.4	294.5	0.147	3.000E+10	1.154E+10	9.430E-02	3.392E-02	7.420E-02	-0.500
12.5	266.9	0.133	3.000E+10	1.154E+10	7.700E-02	2.047E-02	4.823E-02	-0.379
15.5	242.0	0.121	3.000E+10	1.154E+10	6.233E-02	1.200E-02	3.021E-02	-0.296
18.6	220.2	0.110	3.000E+10	1.154E+10	5.028E-02	7.000E-03	1.865E-02	-0.234
21.7	201.9	0.101	3.000E+10	1.154E+10	4.042E-02	4.445E-03	1.227E-02	-0.187
24.8	184.5	0.092	3.000E+10	1.154E+10	3.196E-02	2.814E-03	7.999E-03	-0.149
27.9	168.7	0.084	3.000E+10	1.154E+10	2.494E-02	1.893E-03	5.478E-03	-0.118
30.9	91.8	0.046	3.000E+10	1.154E+10	1.137E-02	7.526E-04	2.214E-03	-0.089
34.0	82.7	0.041	3.000E+10	1.154E+10	8.372E-03	5.214E-04	1.544E-03	-0.064
37.1	73.4	0.037	3.000E+10	1.154E+10	5.889E-03	3.486E-04	1.038E-03	-0.039
38.8	68.2	0.034	3.000E+10	1.154E+10	4.730E-03	2.719E-04	8.116E-04	-0.023
40.2	63.6	0.032	3.000E+10	1.154E+10	3.858E-03	2.170E-04	6.492E-04	-0.008
41.7	58.3	0.029	3.000E+10	1.154E+10	2.968E-03	1.635E-04	4.899E-04	0.010
42.5	55.0	0.027	3.000E+10	1.154E+10	2.500E-03	1.351E-04	4.057E-04	0.023
43.3	50.1	0.025	3.000E+10	1.154E+10	1.902E-03	9.769E-05	2.946E-04	0.040
44.1	36.6	0.018	3.000E+10	1.154E+10	7.463E-04	3.616E-05	1.094E-04	0.066
44.6	16.3	0.008	3.000E+10	1.154E+10	6.564E-05	3.218E-06	9.520E-06	0.092
44.8	6.0	0.003	3.000E+10	1.154E+10	3.336E-06	1.931E-07	4.833E-07	-0.056

Table B.1 Cross section parameters for the wind turbine blade in 22 sections.

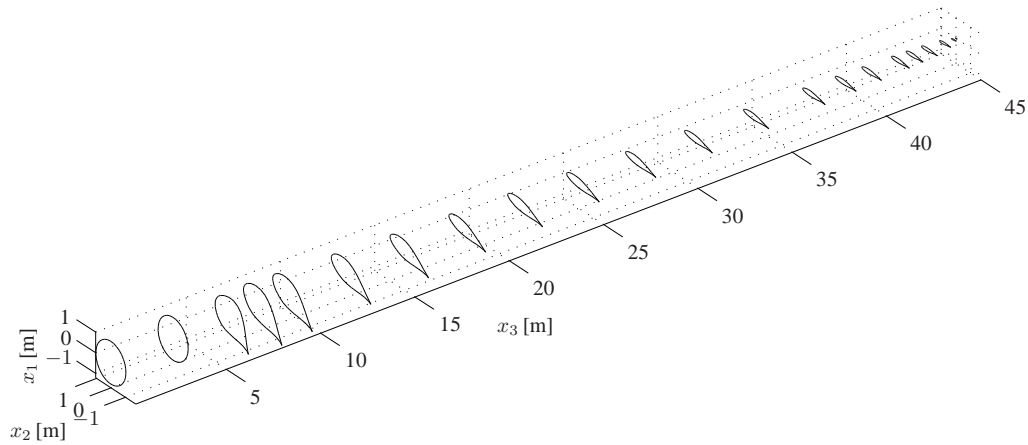


Figure B.1 The outer contour of the 22 sections throughout the blade.

## B.2 Cross Section Parameters for Tower

The tower has a height of 68.0 m and mass of 200000 kg. The tower consists of four sections each with a constant wall thickness, see Fig. B.2. The data for these sections are listed in Table B.2.

$x_3$ [m]	$\mu$ [kg/m]	$A$ [m <sup>2</sup> ]	$E$ [N/m <sup>2</sup> ]	$G$ [N/m <sup>2</sup> ]	$I'_1$ [m <sup>4</sup> ]	$I'_2$ [m <sup>4</sup> ]	$I_3$ [m <sup>4</sup> ]	$\theta$ [rad]
0.0	4099.6	0.522	2.100E+11	8.077E+10	1.023E+00	1.023E+00	2.046E+00	0.000
16.9	3713.5	0.473	2.100E+11	8.077E+10	7.602E-01	7.602E-01	1.520E+00	0.000
17.1	3359.4	0.428	2.100E+11	8.077E+10	6.875E-01	6.875E-01	1.375E+00	0.000
33.9	3012.2	0.384	2.100E+11	8.077E+10	4.956E-01	4.956E-01	9.912E-01	0.000
34.1	2694.7	0.343	2.100E+11	8.077E+10	4.432E-01	4.432E-01	8.865E-01	0.000
50.9	2384.0	0.304	2.100E+11	8.077E+10	3.069E-01	3.069E-01	6.138E-01	0.000
51.1	2103.2	0.268	2.100E+11	8.077E+10	2.707E-01	2.707E-01	5.414E-01	0.000
68.0	1827.4	0.233	2.100E+11	8.077E+10	1.776E-01	1.776E-01	3.551E-01	0.000

Table B.2 Cross section parameters for the tower in 8 sections.

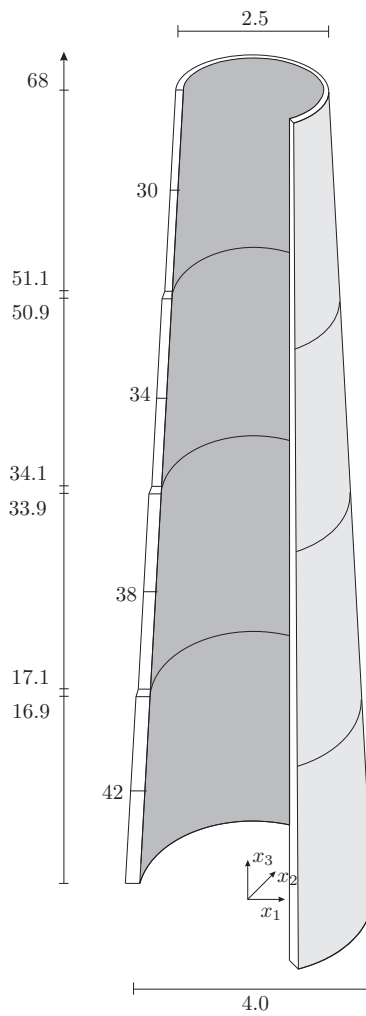


Figure B.2 Sketch of the tower showing the properties. Wall thickness is measured in mm, and the height and diameter are measured in m.



---

**APPENDIX C**  
**Paper: On the Nonlinear**  
**Structural Analysis of Wind**  
**Turbine Blades using Reduced**  
**Degree-of-Freedom Models**

---





## On the nonlinear structural analysis of wind turbine blades using reduced degree-of-freedom models

K. Holm-Jørgensen<sup>†</sup>, J.W. Stærdahl<sup>‡</sup> and S.R.K. Nielsen<sup>‡†</sup>

*Department of Civil Engineering, Aalborg University, Sohngaardsholmsvej 57,  
DK-9000 Aalborg, Denmark*

*(Received October 4, 2006, Accepted August 17, 2007)*

**Abstract.** Wind turbine blades are increasing in magnitude without a proportional increase of stiffness for which reason geometrical and inertial nonlinearities become increasingly important. Often these effects are analysed using a nonlinear truncated expansion in undamped fixed base mode shapes of a blade, modelling geometrical and inertial nonlinear couplings in the fundamental flap and edge direction. The purpose of this article is to examine the applicability of such a reduced-degree-of-freedom model in predicting the nonlinear response and stability of a blade by comparison to a full model based on a nonlinear co-rotating FE formulation. By use of the reduced-degree-of-freedom model it is shown that under strong resonance excitation of the fundamental flap or edge modes, significant energy is transferred to higher modes due to parametric or nonlinear coupling terms, which influence the response and stability conditions. It is demonstrated that the response predicted by such models in some cases becomes unstable or chaotic. However, as a consequence of the energy flow the stability is increased and the tendency of chaotic vibrations is reduced as the number of modes are increased. The FE model representing the case of infinitely many included modes, is shown to predict stable and ordered response for all considered parameters. Further, the analysis shows that the reduced-degree-of-freedom model of relatively low order overestimates the response near resonance peaks, which is a consequence of the small number of included modes. The qualitative erratic response and stability prediction of the reduced order models take place at frequencies slightly above normal operation. However, for normal operation of the wind turbine without resonance excitation 4 modes in the reduced-degree-of-freedom model perform acceptable.

**Keywords:** wind turbine blades; nonlinear vibration; bernoulli-euler beam; co-rotating finite elements; truncated modal expansion.

---

### 1. Introduction

In simulating the behaviour of a wind turbine many load combinations are studied to ensure that the wind turbine is designed to withstand throughout its lifetime. Normally, these life cycle simulations are performed using reduced-degree-of-freedom models because the computation time has to be short. The worst cases are next used in more advanced structural models to verify and optimize the design. During on-line operation of the wind turbine it is also essential with fast working models, in case of active or semi-active vibration control when such mechanisms are

---

<sup>†</sup> Ph.D. Student, Corresponding author, E-mail: khj@civil.aau.dk

<sup>‡</sup> Assistant Professor, Ph.D., E-mail: jws@civil.aau.dk

<sup>‡†</sup> Professor, Ph.D., E-mail: soren.nielsen@civil.aau.dk

installed. In this paper the predictions of response and stability of a wind turbine blade based on such nonlinear reduced-degree-of-freedom model are validated by comparison with those of a full nonlinear co-rotating FE model. Both models are formulated in a moving frame of reference following the stiff body motion of the blade. The considered reduced-order model is based on a spatial discretization using the fixed base undamped eigenmodes as a functional basis. The model incorporates linear and nonlinear coupling terms between the different modes making energy transfer a possibility, contrary to a linear model. This energy transfer is essential for correct stability and response prediction. The geometrical nonlinear terms of the model originate from a nonlinear description of the curvature of the blade and the rotation of internal and external forces during the deformation. The inertial nonlinearities are caused by inertial axial forces induced by the support point motion. The undamped fixed base eigenmodes are determined from an FE model of a beam with pretwist using the Bernoulli-Euler beam theory with St. Venant torsion.

In Larsen and Nielsen (2006a) and Larsen and Nielsen (2006b) the two lowest modes were retained reducing the equations of motion to a nonlinear 2-degree-of-freedom system with the above-mentioned nonlinear coupling terms. The idea was to investigate 2:1 internal resonance, due to the eigenfrequency of the lowest edge mode is approximately two times the eigenfrequency of the fundamental blade mode. Among the many studies was the relative influence of the different parametric and nonparametric coupling terms along with the placement of the resonance peaks. The stability of the 2-degree-of-freedom model was studied by a numerical calculated Lyapunov exponent based on the algorithm of Wolf *et al.* (1984) for different relations between the first two eigenfrequencies and for different relations between the frequency of the support point motion and rotor rotation. At some excitation frequencies the response became both instable and chaotic. During resonance, where the influence of nonlinearities is significant and the modal equations become strongly coupled, it is questionable if only 2 modes are sufficient to get a correct prediction of the response and stability. For this reason a convergence test is performed in this paper increasing the number of modes to 4 and 6. Especially, the primarily nonlinear terms responsible for the energy transfer between the modes are identified. Finally, the response and stability of the model by 2, 4 and 6 modes are compared to a full nonlinear co-rotating FE-beam model. The idea is to investigate to which extent the energy transfer to higher modes than included in the reduced-degree-of-freedom may influence qualitatively on the response and stability predictions.

With emphasis on beam models for a rotor blade Volovoi *et al.* (2001) have reviewed several beam theories considering effects such as transverse shear flexibility, Vlasov's warping etc. The overall conclusions were that for thin-walled box sections the Bernoulli-Euler theory containing extension with St. Venant torsion and bending in two directions behaved adequately in most cases. However, for short-wavelength modes shear effects need to be included using Timoshenko theory as demonstrated by Yu *et al.* (2002). The study of flexible bodies attached to a moving support has continued over seventy years. Baker *et al.* (1993) examined the response and stability of a parametric and chaotic excited beam both experimentally and analytically. The analytical model, derived by a Galerkin reduction of the plane equations of motion, could predict the behaviour from parametric excitation but not for chaotic excitation. The slow convergence of a modal expansion can be overcome by an expansion in nonlinear modes, Nayfeh *et al.* (1995). Based on a nonlinear Bernoulli-Euler FE-beam model of a cantilever rotating beam, Apiwattanalungarn *et al.* (2003) devised a reduced model by use of a nonlinear normal mode expansion. Excellent agreement was achieved by comparison to a full reference model. In creating a reference model the nonlinear co-rotating formulation is ideal for large displacements. In this formulation a local coordinate system

undergoing rigid body motion is assigned to each element. In this local coordinate system the elastic deformations are small whereby regular beam theory is sufficient. This method has existed since the seventies and described and examined in a number of papers and text books, among these Crisfield 1990 and Krenk 2005. The primary deviation between the formulations is the way of incorporating rotations in three dimensions, because finite rotations do not add linearly as vectors. In Sandhu *et al.* (1990) Euler rotations are used and the performance of the formulation is compared to other large deformation formulations by a number of examples using curved 3D-beam elements showing accurate and fast converging results. In the method described in Krenk (2005) quaternions are used to describe the finite rotation of the nodes from which mean rotations are introduced to determine the orientation of the base unit vectors of each element. In Crisfield *et al.* (1997) several time integration algorithms using 3D co-rotational beams with two nodes and six degrees of freedom per node are examined showing good performance by including numerical damping. Other authors observed good experience by use of the Newmark integration with Newton Raphson iteration for a co-rotational finite element formulation, e.g., Hsiao *et al.* (1999) and Behdinan *et al.* (1998).

In a regular three-bladed wind turbine the relation between the excitation frequency and the rotational frequency of the rotor is  $\omega_0/\Omega_0 = 3$  due to changes in wind load when the individual blades are in top and bottom positions of the incoming shear wind field. This is an idealized ratio as turbulence will introduce other ratios. Moreover, the relation between the excitation frequency and the first eigenfrequency of the blade is below 1 i.e.,  $\omega_0/\omega_1 < 1$  during normal operation. In the following simulations the response and stability will be examined for a frequency band of  $\omega_0/\omega_1 \in [0.5; 1.5]$  well knowing that this interval is above the normal operating values of a wind turbine. However, this larger interval will prove if the model produces stable results and examine what happens in case of failure e.g., where the rotor speeds up. The chosen interval will result in rotational frequencies of  $\Omega_0 \in [0.77; 2.31]$  rad/s where the nominal value is  $\Omega_0 = 1.6$  rad/s. In Larsen and Nielsen (2006a) the first fixed base eigenfrequency of the blade at the nominal rotational frequency of the rotor is  $\omega_1 = 5.14$  rad/s resulting in a non-dimensional excitation frequency of  $\omega_0/\omega_1 = 0.93$  for normal operation. A shell model of the blade has been created giving the 10 lowest eigenmodes i.e. up to a eigenfrequency of  $\omega_{10} = 111.31$  rad/s. The eigenfrequency corresponding to the first torsional mode is  $\omega_9 = 100.22$  rad/s, which does not have any significant bending components. Also the remaining considered modes do not show any significant coupling between bending and torsional components. Therefore, the torsional degree-of-freedom and eventually couplings with bending components are not included in the model.

## 2. Reduced degree-of-freedom model

In this section the reduced degrees-of-freedom model is introduced together with the main expressions, ending up with the nonlinear equations of motion for the modal coordinates. The section is based on Larsen and Nielsen (2006a) where a more detailed description of the model and the derived equations of motion can be found.

### 2.1 Coordinate systems and support point motions

In Fig. 1(a) the wind turbine is seen from upwind where the rotor rotates in the clockwise direction. A fixed global  $(x_1, x_2, x_3)$ -coordinate system is placed at the ground level in the centre of

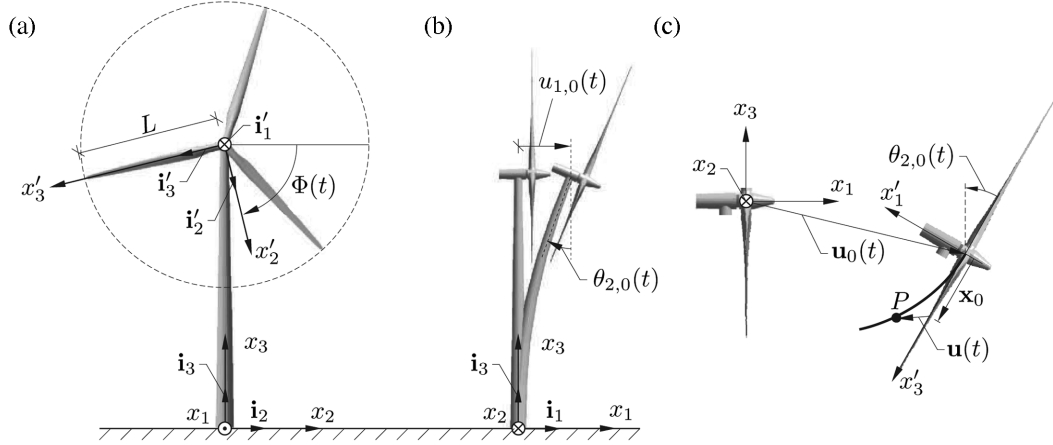


Fig. 1 (a) Wind turbine seen from upwind, (b) Displacement of the nacelle, (c) Displacement of a material point in the blade

the tower. The  $x_1$ -axis is oriented parallel to the rotor axes as shown in Fig. 1. To simplify the matter it is assumed that the nacelle is not tilted and the blades are not coned. The length of a blade is denoted  $L$ . A local  $(x'_1, x'_2, x'_3)$ -coordinate system is fixed to the blade with origin at the hub with the centre of gravity of the sections placed on the  $x'_3$ -axis. The  $x'_1$ - and  $x'_2$ -axis are placed in such a way that they represent the flap- and edge-wise displacement, respectively. The position of the  $x'_2$ -axis is determined by the phase angle  $\Phi(t)$  which is defined clock-wise from the global  $x_2$ -axis. The displacement and rotation of the hub, originating from the motion of the tower and nacelle, are accounted for by introducing a prescribed linear translation and rotation with the global coordinates  $u_{i,0}(t)$  and  $\theta_{i,0}(t)$ , respectively.

In the following it is assumed that the motion of the nacelle and thereby the support point motion only take place in the  $(x_1, x_3)$ -plane, corresponding to the following components, see Fig. 1(b).

$$u_{1,0}(t) = u(t), \quad \theta_{2,0}(t) = \Theta_{2,0}u(t), \quad u_{2,0}(t) = u_{3,0}(t) = \theta_{1,0}(t) = \theta_{3,0}(t) = 0 \quad (1)$$

Here it is assumed that the motion of the tower is controlled by a simple modal coordinate representing the horizontal motion  $u(t)$  of the nacelle.  $\Theta_{2,0}$  is a scaling factor for the corresponding rotation of the nacelle. In the following  $u(t)$  is assumed to vary harmonically with the amplitude  $u_0$  and excitation frequency  $\omega_0$  as

$$u(t) = u_0 \cos \omega_0 t \quad (2)$$

Let  $\underline{v}'$  and  $\underline{v}$  be column matrices storing the moving frame and fixed frame components of a vector  $\mathbf{v}$ . These components are related as

$$\underline{v}' = \underline{A} \underline{v} \quad (3)$$

$\underline{A}$  represents the components of the rotation tensor, rotating the fixed frame base vectors to the moving frame base vectors, i.e.,  $\mathbf{i}'_i = A_{ij} \mathbf{j}_j$ . The transformation matrix  $\underline{A}(t)$  is found as a sequence of rotations. First, a rotation  $\theta_{2,0}$  of the rotor plane around the global  $x_2$ -axis is performed, followed by

a blade rotation  $\Phi(t)$  around the  $x'_1$ -axis of the blade fixed  $(x'_1, x'_2, x'_3)$ -coordinate system.

$$\left. \begin{aligned} \underline{v}_1 &= \underline{A}_1 \underline{v} \\ \underline{v}' &= \underline{A}_2 \underline{v}_1 \end{aligned} \right\} \Rightarrow \underline{v}' = \underline{A}_2 \underline{A}_1 \underline{v}, \quad \underline{A} = \underline{A}_2 \underline{A}_1 \quad (4)$$

where

$$\underline{A}_1(t) = \begin{bmatrix} \cos \theta_{2,0} & 0 & -\sin \theta_{2,0} \\ 0 & 1 & 0 \\ \sin \theta_{2,0} & 0 & \cos \theta_{2,0} \end{bmatrix}, \quad \underline{A}_2(t) = \begin{bmatrix} -1 & 0 & 0 \\ 0 & \cos \Phi & -\sin \Phi \\ 0 & -\sin \Phi & -\cos \Phi \end{bmatrix} \quad (5)$$

The local components of the support point motion are  $u'_{i,0}(t) = A_{i1}(t)u(t)$  and  $\theta'_{i,0}(t) = A_{i2}(t)\Theta_{2,0}u(t)$ , where  $A_{i1}(t)$  and  $A_{i2}(t)$  denote the components in the 1st and 2nd columns of  $\underline{A}(t)$ .

$$\underline{u}'_0(t) = \begin{bmatrix} -\cos \theta_{2,0} \\ -\sin \Phi \sin \theta_{2,0} \\ -\cos \Phi \sin \theta_{2,0} \end{bmatrix} u(t), \quad \underline{\theta}'_0(t) = \begin{bmatrix} 0 \\ \cos \Phi \\ -\sin \Phi \end{bmatrix} \Theta_{2,0} u(t) \quad (6)$$

To simplify matters further, the effects on the hub displacement from the rotation  $\theta_{2,0}$  are disregarded. Hence,  $u'_{1,0}(t) \simeq -u(t)$ ,  $u'_{2,0}(t) = u'_{3,0}(t) \simeq 0$ .

The time-derivative of  $\Phi(t)$  specifies the rotational speed of the rotor

$$\Omega_0(t) = \dot{\Phi}(t) \quad (7)$$

## 2.2 Modal equations of motion

In order to discretize the variational equations obtained from the principles of virtual work, the displacement components  $u'_\alpha(x'_3, t)$  and the variational field  $\delta u'_\alpha(x'_3)$  are represented by the following modal expansions

$$u'_\alpha(x'_3, t) \simeq \sum_{j=1}^N \Phi_\alpha^{(j)}(x'_3) q_j(t), \quad \delta u'_\alpha(x'_3, t) = \sum_{j=1}^N \Phi_\alpha^{(j)}(x'_3) \delta q_j(t) \quad (8)$$

where  $u'_1(x'_3, t)$  is the deformation component in the flap direction, and  $u'_2(x'_3, t)$  is the deformation component in the edgewise direction.  $q_j(t)$  and  $\delta q_j$  denote the modal coordinates and virtual variations of this quantity.  $\Phi_\alpha^{(j)}(x'_3)$  represents the undamped eigenmodes, where the upper index denotes the mode number and the lower index indicates the component. A discretized version of  $\Phi_\alpha^{(j)}(x'_3)$  has been obtained by means of an FE-method, from which all necessary derivatives of the eigenmodes also are obtained as described in Larsen and Nielsen (2006a). Retaining nonlinearities up to 3rd order the ordinary differential equations for the modal coordinates become, Larsen and Nielsen (2006a)

$$\begin{aligned} & \sum_{j=1}^N (m_{ij} \ddot{q}_j + c_{ij}(t) \dot{q}_j + k_{ij}(t) q_j) + \sum_{j=1}^N \sum_{k=1}^N (a_{ijk}(t) q_j q_k + b_{ijk}(t) q_j \dot{q}_k) \\ & + \sum_{j=1}^N \sum_{k=1}^N \sum_{l=1}^N (d_{ijkl} q_j q_k q_l + g_{ijkl} (q_j \dot{q}_k \dot{q}_l + q_j q_k \ddot{q}_l)) = f_i(t) \end{aligned} \quad (9)$$

where

$$\begin{aligned}
 m_{ij} &= M_i \delta_{ij} \\
 c_{ij}(t) &= 2\zeta_i \omega_i M_i \delta_{ij} + \int_0^L \mu \Phi_\alpha^{(i)} E_{\alpha\beta} \Phi_\beta^{(j)} dx'_3 \\
 k_{ij}(t) &= M_i \omega_i^2 \delta_{ij} + \int_0^L \left[ \mu \Phi_\alpha^{(i)} D_{\alpha\beta} \Phi_\beta^{(j)} - \frac{\partial \Phi_\alpha^{(i)}}{\partial x'_3} \frac{\partial \Phi_\alpha^{(j)}}{\partial x'_3} \int_{x'_3}^L \mu D_{33} x'_3 dx'_3 \right] dx'_3
 \end{aligned} \tag{10}$$

In Eq. (10) and below the summation convention is used on the Greek indices which count from 1 to 2, e.g.,  $\frac{\partial \Phi_\alpha^{(i)}}{\partial x'_3} \frac{\partial \Phi_\alpha^{(j)}}{\partial x'_3} = \frac{\partial \Phi_1^{(i)}}{\partial x'_3} \frac{\partial \Phi_1^{(j)}}{\partial x'_3} + \frac{\partial \Phi_2^{(i)}}{\partial x'_3} \frac{\partial \Phi_2^{(j)}}{\partial x'_3}$ .  $M_i$  specifies the modal mass for mode  $i$ ,  $\delta_{ij}$  is the Kronecker's delta.  $\omega_i$  signifies the eigenfrequency of mode  $i$ .  $c_{ij}(t)$  denotes the components of the modal damping matrix. The first term on the right-hand side signifies the structural damping determined by the modal damping ratio  $\zeta_i$  which is specified for each considered mode. As seen, the structural damping has been assumed to decouple in agreement with the well-separated eigenfrequencies and the low structural damping of the system. The last term represents the contribution from the Coriolis forces.  $\mu$  is the mass per unit length, and  $E_{\alpha\beta}$  denotes the components of the upper part of the spin rotational matrix  $\underline{\underline{E}}$  given as

$$\underline{\underline{E}}(t) = 2 \underline{\underline{A}}(t) \dot{\underline{\underline{A}}}^T(t) = 2 \begin{bmatrix} 0 & -\dot{\theta}'_{3,0} & \dot{\theta}'_{2,0} \\ \dot{\theta}'_{3,0} & 0 & -\Omega_0 \\ -\dot{\theta}'_{2,0} & \Omega_0 & 0 \end{bmatrix} \tag{11}$$

$k_{ij}(t)$  represents the components of the modal stiffness matrix. The first term on the right-hand side signifies the modal structural stiffness, whereas the second part indicates the geometrical stiffness due to centrifugal forces.  $D_{\alpha\beta}$  and  $D_{33}$  denote the components in the matrix  $\underline{\underline{D}}$  given as

$$\underline{\underline{D}}(t) = \underline{\underline{A}}(t) \ddot{\underline{\underline{A}}}^T(t) = - \begin{bmatrix} \dot{\theta}'_{3,0}{}^2 + \dot{\theta}'_{2,0}{}^2 & -\dot{\theta}'_{2,0} \Omega_0 + \ddot{\theta}'_{3,0} & -\dot{\theta}'_{3,0} \Omega_0 - \ddot{\theta}'_{2,0} \\ -\dot{\theta}'_{2,0} \Omega_0 - \ddot{\theta}'_{3,0} & \dot{\theta}'_{3,0}{}^2 + \Omega_0^2 & -\dot{\theta}'_{3,0} \dot{\theta}'_{2,0} + \dot{\Omega}_0 \\ -\dot{\theta}'_{3,0} \Omega_0 + \ddot{\theta}'_{2,0} & -\dot{\theta}'_{3,0} \dot{\theta}'_{2,0} - \dot{\Omega}_0 & \dot{\theta}'_{2,0}{}^2 + \Omega_0^2 \end{bmatrix} \tag{12}$$

The position vector of a material point from the origin of the moving frame of reference is denoted  $\mathbf{x}(t) = \mathbf{x}_0(t) + \mathbf{u}(t)$ , where  $\mathbf{x}_0(t)$  is the undeformed or referential position and  $\mathbf{u}(t)$  specifies the local displacement vector of the particle as seen by an observer fixed to the moving frame of reference, see Fig. 1(c). Then, the local components of the acceleration vector are given as, Larsen and Nielsen (2006a)

$$\underline{\underline{a}}'(t) = \underline{\underline{\ddot{u}}}'_0(t) + \underline{\underline{\ddot{x}}}'(t) + \underline{\underline{D}}(t) \underline{\underline{x}}'(t) + \underline{\underline{E}}(t) \dot{\underline{\underline{x}}}'(t) \tag{13}$$

where  $\underline{\underline{\ddot{u}}}'_0(t)$  is the local components of the acceleration vector of the support point, and  $\underline{\underline{x}}'(t)$  stores the moving frame components of  $\mathbf{x}(t)$ .  $\underline{\underline{D}}(t) \underline{\underline{x}}'(t)$  and  $\underline{\underline{E}}(t) \dot{\underline{\underline{x}}}'(t)$  represent the local

components of the centrifugal and Coriolis accelerations, respectively. The nonlinear coupling coefficients in Eq. (9) are defined as follows

$$\begin{aligned}
 a_{ijk}(t) &= \int_0^L \left[ \frac{\partial \Phi_\alpha^{(i)}}{\partial x_3'} \frac{\partial \Phi_\alpha^{(j)}}{\partial x_3'} \int_{x_3'}^L \left[ -p_{\beta,A}'' \frac{\partial \Phi_\beta^{(k)}}{\partial x_3'} - \mu D_{3\beta} \Phi_\beta^{(k)} \right] dx_3' + \frac{1}{2} \Phi_\alpha^{(i)} p_{\beta,A}'' \frac{\partial \Phi_\alpha^{(j)}}{\partial x_3'} \frac{\partial \Phi_\beta^{(k)}}{\partial x_3'} \right] dx_3' \\
 b_{ijk}(t) &= \int_0^L \left[ \frac{\partial \Phi_\alpha^{(i)}}{\partial x_3'} \frac{\partial \Phi_\alpha^{(j)}}{\partial x_3'} \int_{x_3'}^L -\mu E_{3\beta} \Phi_\beta^{(k)} dx_3' \right] dx_3' \\
 d_{ijkl} &= \int_0^L \frac{1}{2} e_{\alpha\eta} E I_{\alpha\beta}'' e_{\beta\xi} \left[ \frac{\partial^2 \Phi_\eta^{(i)}}{\partial x_3'^2} \frac{\partial \Phi_\xi^{(j)}}{\partial x_3'} \frac{\partial \Phi_\gamma^{(k)}}{\partial x_3'} \frac{\partial^2 \Phi_\gamma^{(l)}}{\partial x_3'^2} + \frac{\partial^2 \Phi_\xi^{(l)}}{\partial x_3'^2} \frac{\partial \Phi_\eta^{(i)}}{\partial x_3'} \frac{\partial \Phi_\gamma^{(j)}}{\partial x_3'} \frac{\partial^2 \Phi_\gamma^{(k)}}{\partial x_3'^2} \right. \\
 &\quad \left. + \frac{\partial^2 \Phi_\xi^{(l)}}{\partial x_3'^2} \frac{\partial \Phi_\eta^{(j)}}{\partial x_3'} \frac{\partial \Phi_\gamma^{(i)}}{\partial x_3'} \frac{\partial^2 \Phi_\gamma^{(k)}}{\partial x_3'^2} + \frac{\partial^2 \Phi_\xi^{(l)}}{\partial x_3'^2} \frac{\partial \Phi_\eta^{(i)}}{\partial x_3'} \frac{\partial \Phi_\gamma^{(j)}}{\partial x_3'} \frac{\partial^2 \Phi_\gamma^{(k)}}{\partial x_3'^2} \right] dx_3' \\
 g_{ijkl} &= \int_0^L \left[ \frac{\partial \Phi_\alpha^{(i)}}{\partial x_3'} \frac{\partial \Phi_\alpha^{(j)}}{\partial x_3'} \int_{x_3'}^L \left[ \mu \int_0^{x_3'} \frac{\partial \Phi_\beta^{(k)}}{\partial x_3'} \frac{\partial \Phi_\beta^{(l)}}{\partial x_3'} dx_3' \right] dx_3' \right] dx_3' \quad (14)
 \end{aligned}$$

As seen, the parametric excitation from  $\theta_{2,0}'(t)$  and  $\theta_{3,0}'(t)$  is also present in the quadratic nonlinear coupling terms  $a_{ijk}(t)$  and  $b_{ijk}(t)$ . The quadratic nonlinear coupling coefficient  $a_{ijk}(t)$  includes both contributions from the rotation of the aeroelastic loads orthogonal to the deformed blade and inertial contributions from the support point rotations and the rotational frequency of the rotor.  $b_{ijk}(t)$  is also a quadratic non-linear coupling coefficient originating from inertial nonlinearities from the support point rotation and the rotation of the rotor.  $a_{ijk}(t)$  is influenced by centrifugal terms, whereas Coriolis terms enter in  $b_{ijk}(t)$ . The cubic coupling term  $d_{ijkl}$  is due to the nonlinear description of the curvature.  $E$  is the modulus of elasticity and  $e_{\alpha\beta}$ , is the permutation symbol given as

$$e_{\alpha\beta} = \begin{bmatrix} 0 & 1 \\ -1 & 0 \end{bmatrix} \quad (15)$$

$I_{\alpha\beta}''$  is the inertia tensor given by

$$\begin{aligned}
 I_{\alpha\beta}'' &= I_{\gamma\delta}''' C_{\alpha\gamma} C_{\beta\delta} \\
 \underline{I}''' &= \begin{bmatrix} I_{11}''' & 0 \\ 0 & I_{22}''' \end{bmatrix}, \quad \underline{C} = \begin{bmatrix} \cos \varphi & \sin \varphi \\ -\sin \varphi & \cos \varphi \end{bmatrix} \quad (16)
 \end{aligned}$$

where  $I_{11}'''$  and  $I_{22}'''$  are the principal moments of inertia, and  $\varphi$  is the twist angle cf. Fig. 2(b).  $g_{ijkl}$  is another cubic nonlinear coupling coefficient caused by inertial nonlinearities. These are due to the axial inertial forces which contribute to the geometrical stiffness along with the static axial force.  $f_i(t)$  denotes the modal loads in the  $i$ th mode given as

$$f_i(t) = \int_0^L \Phi_\alpha^{(i)} (p_{\alpha,A}'' - \mu(\ddot{u}_{\alpha,0}' + D_{\alpha 3} x_3')) dx_3' \quad (17)$$

The support point displacement  $u_{1,0}'(t)$  only enters the equations as an additive load term via the

modal loads  $f_i(t)$ .  $p''_{\alpha,A}$  is the aerodynamic load described in Appendix B. The time dependent coefficients are derived in Appendix A.

### 3. Nonlinear co-rotating beam formulation

To determine the accuracy of the reduced-degree-of-freedom model a nonlinear co-rotating beam formulation is implemented. The model is based on Krenk (2005), where a detailed derivation of the tangent stiffness matrix is given.

The idea of a co-rotating formulation is to separate the deformation of each element into a rigid body motion i.e., a translation and rotation of each element with respect to a fixed coordinate system, and an elastic deformation within the local coordinate system fixed to the element. Because the elastic deformations are moderate linear Timoshenko beam theory is adequate. Inside the local coordinate system the beam is able to deform in the longitudinal direction, rotate around the beam axis, and may undergo bending deformations and shear deformations. No coupling between wharping and axial elongation is used i.e., only St. Venant torsion (homogeneous torsion) is used. The orientation of the local coordinate system is defined by the base unit vectors  $\mathbf{i}_1'', \mathbf{i}_2'', \mathbf{i}_3''$  shown in Fig. 2(a). The  $x_3''$ -axis is chosen along the deformed beam through the end points  $A$  and  $B$  of the element, and the  $x_1''$ -and  $x_2''$ -axis are defined by the mean rotation at  $A$  and  $B$ . To get a simple approach for constructing the constitutive relations the principal axes are introduced. This is done by rotating the base unit vectors  $\mathbf{i}_1'', \mathbf{i}_2'', \mathbf{i}_3''$  the angle  $\varphi$  around the  $x_3''$ -axis corresponding to the pretwist of the profile as shown in Fig. 2(b). The inertia of the blade is described by a constant consistent mass matrix for a 3D-beam element. The inertial loads from the support point motion together with the centrifugal and Coriolis contributions are determined from the respective acceleration terms in Eq. (13) multiplied with a lumped mass matrix. Prismatic elements are used when all geometric and material parameters are assigned. In solving the equations of motion Newton-Raphson iteration is used. For time integration a nonlinear Newmark with numerical damping has shown reliable.

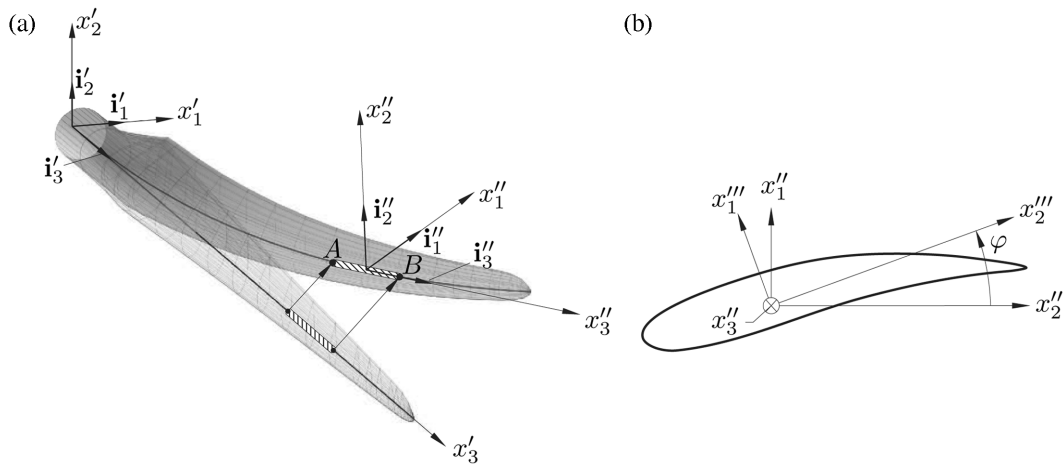


Fig. 2 (a) an element in the co-rotating formulation, (b) rotation into principal axes based on the initial pretwist of the profile and the angle to the principal axes



#### 4. Convergency studies of the reduced-degree-of-freedom model

In this section several simulations of the reduced-degree-of-freedom model are performed with the intention to determine the number of necessary eigenmodes with respect to response and stability. Also the nonlinear couplings and related energy transfer are identified. The stability analysis is based on a numerical calculated Lyapunov exponent using the algorithm by Wolf *et al.* (1984). In the analysis the effect of including two, four and six modes is investigated.

##### 4.1 Input parameters

As mentioned in the introduction it is chosen to fix the ratio between the support frequency and the rotational frequency of the rotor at  $\omega_0/\Omega_0 = 3$ . Moreover, the relation between the support frequency and the first eigenfrequency of the blade is varied in the interval  $\omega_0/\omega_1 \in [0.5; 1.5]$ . Hence, as  $\omega_0$  is varied the rotational speed  $\Omega_0$  must change accordingly. In all the following simulations the amplitude of the horizontal displacement of the nacelle is kept at the value  $u_0 = 0.3$  m. The model parameter of the rotation of the support is held constant at  $\Theta_{2,0} = 0.03$  m<sup>-1</sup> cf. Eq. (1). The time integration is performed by a 4th order Runge Kutta with the time step  $\Delta t = \frac{1}{100}T_0$ , where  $T_0 = \frac{2\pi}{\omega_0}$ . Stabilities such as variances and the Lyapunov exponent are based on time series of the length of 1000 periods. The results will be presented as the root-mean-square (RMS) value of the modal coordinates for the last fifth of the simulated time series in order to have received stationarity of the response. All initial values of the modal coordinates have been chosen to zero.

##### 4.2 Fixed base eigenmodes of the blade

The geometrical and material parameters for the used blade are described in Appendix C. Hereby, an FE Bernoulli-Euler beam model including St. Venant torsion has been devised from which the undamped fixed base eigenmodes are determined. In Fig. 3 the flap component  $\Phi_1^{(i)}$  and the edge-wise component  $\Phi_2^{(i)}$  for the first six fixed base undamped eigenmodes are illustrated with the dominating components normalized to 1 at the blade tip. Modal parameters and information regarding the shape of the eigenmodes are listed in Table 1 for the first six modes. These modes are determined from no rotational speed i.e.,  $\Omega_0 = 0$  whereby no additional stiffness from centrifugal contributions are added in the modes. The damping ratio for all modes is kept constant at  $\zeta_j = 0.01$ . In the fundamental blade mode the aerodynamic damping ratio may vary from about 0.2 in case of fully attached flow to negative values under deep stall conditions. In the used load model no aerodynamic damping is included. The result of varying  $\zeta_1$  has been examined in Larsen and

Table 1 Modal parameters for the first six fixed base eigenmodes

Mode $\Phi^{(j)}$	1	2	3	4	5	6
$\omega_j$ [rad/s]	4.61	9.38	13.65	29.27	34.36	52.57
$M_j$ [kg]	399.1	846.2	367.9	326.6	471.3	232.3
Dominating component	$\Phi_1$	$\Phi_2$	$\Phi_1$	$\Phi_1$	$\Phi_2$	$\Phi_1$
Internal nodes in $\Phi_1^{(i)}$	0	1	1	2	2	3
Internal nodes in $\Phi_2^{(i)}$	0	0	0	1	1	2

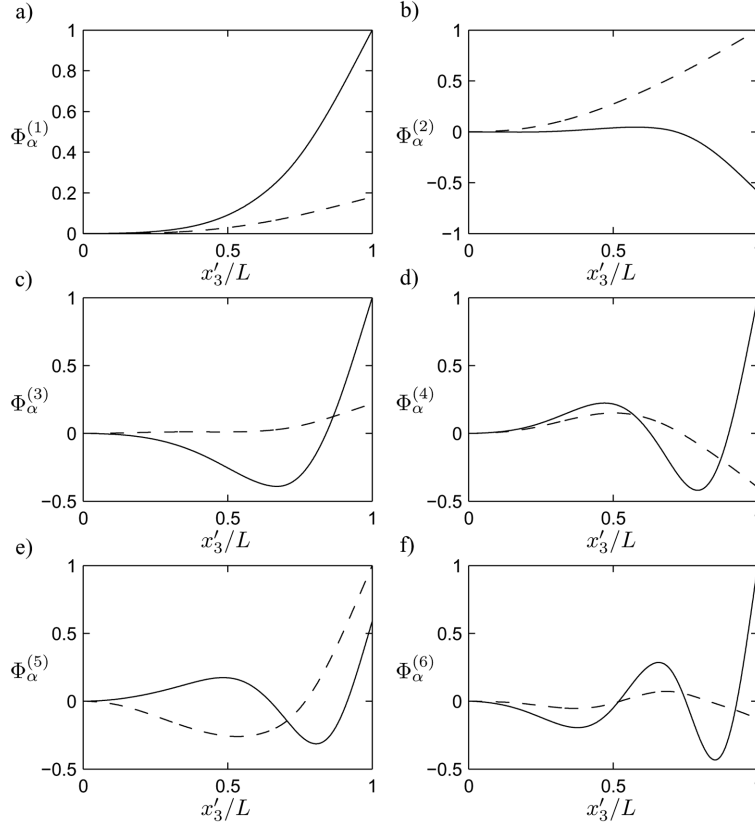


Fig. 3 First six eigenmodes normalised to 1 in the blade tip based on the dominating component. (—) flap component,  $\Phi_1^{(i)}$ . (---) edgewise component,  $\Phi_2^{(i)}$

Nielsen (2006a), where the magnitude of the response at the most dominating resonance peaks approximately became one third by increasing  $\zeta_1$  from  $\zeta_1 = 0.01$  to  $\zeta_1 = 0.05$  and maintaining  $\zeta_2 = 0.01$ .

As seen in Table 1  $\omega_2 \sim 2\omega_1$ , which make internal resonances between these modes possible, either due to nonlinear or parametric linear couplings between the 1st and 2nd modes.

#### 4.3 RMS-values of the modal coordinates for different number of modes

In this section results are presented in terms of the RMS-values of the modal coordinates  $q_j(t)$  as the number of modes is increased in the model. The RMS-value  $Q_j$  is defined by

$$Q_j = \left( \frac{2}{T} \int_0^T (q_j - \mu_{q_j})^2 dt \right)^{1/2}, \quad \mu_{q_j} = \frac{1}{T} \int_0^T q_j(t) dt \quad (18)$$

where  $\mu_{q_j}$  is the mean value and the sampling is performed over the last  $T = 200$  periods of the simulation. In Fig. 4  $Q_j$  is plotted as a function of the nondimensional excitation frequency  $\omega_0/\omega_1$  for  $N = 2, 4, 6$ . Since the modal functions have been normalized to one at the tip in the dominating component,  $Q_j$  may be interpreted physically as the RMS displacement at the tip in that component.

The results for  $Q_1$ ,  $Q_3$ ,  $Q_4$ ,  $Q_6$  and  $Q_2$ ,  $Q_5$  are plotted with different scales with respect to the flap and edge component, respectively. Two conspicuous peaks are visible in almost all modal coordinates at  $\omega_0/\omega_1 \approx 0.85$  and  $\omega_0/\omega_1 \approx 1.22$ . As seen from Eq. (19), the modal loads  $f_1(t)$  and  $f_2(t)$  contain harmonic components with the circular frequencies  $m\Omega_0$ ,  $m = 1, \dots, 4$ . In combination to the frequency ratios  $\omega_2 \approx 2\omega_1$  and  $\omega_0/\Omega_0 = 3$ , it was shown in Larsen and Nielsen (2006b) that resonance from the load terms or internal resonance caused by linear or nonlinear parametric coupling terms may occur in the fundamental blade or edgewise modes at any of the frequency ratios  $\omega_0/\omega_1 = 3/m$  and  $\omega_0/\omega_1 = 6/m$ , respectively, where  $m = 1, \dots, 12$ . The most severe resonance

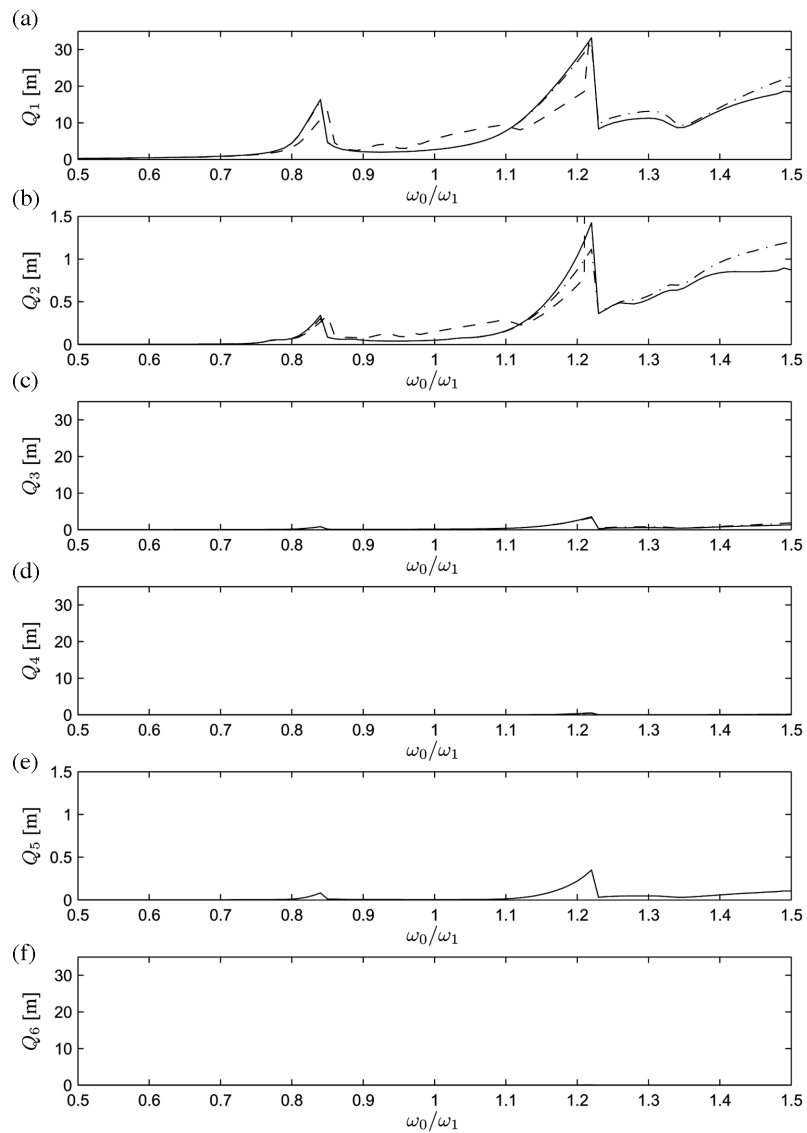


Fig. 4 RMS-values for the modal coordinates with 2, 4 and 6 modes. (---) 2 modes. (-.-.-) 4 modes. (—) 6 modes

peaks occur nearby  $\omega_0/\omega_1 \approx 3/4$  and  $\omega_0/\omega_1 \approx 1.0$  corresponding to  $m = 4, 6$ . In Fig. 4 the corresponding results have been shown for the present system. As seen, the peaks are placed at somewhat higher frequencies due to the geometrical stiffness from the centrifugal force, which is not introduced in the linear eigenvalue problem for finding the eigenmodes and eigenfrequencies i.e. the geometric stiffness is not included in  $\omega_1$ . In Larsen and Nielsen (2006b) this effect was introduced as an additional constant term in the linear eigenvalue problem for finding the eigenmodes and eigenfrequencies. The magnitude of especially  $Q_1$  at the resonance frequency ratio  $\omega_0/\omega_1 \approx 1.22$  shown in Fig. 4(a), is high above any realistic value as the length of the blade is only 46 m. These results should merely be considered as model predictions caused by nearby instability due to loss of damping or stiffness. In reality the wind turbine will be controlled out of this region. For  $N = 2$  the first peak at  $\omega_0/\omega_1 \approx 0.85$  is visible in both Fig. 4(a) and Fig. 4(b). At the second peak the response becomes unstable in both modal coordinates and blows up. For  $N = 4$  the first peak is slightly displaced to the left in both Fig. 4(a) and Fig. 4(b), and the next peak at  $\omega_0/\omega_1 \approx 1.22$  is now visible. For  $\omega_0/\omega_1 > 1.22$  the response stays inside the chosen limits, which is due to energy transfer to especially mode 3. For  $N = 6$  the same characteristics as for  $N = 4$  are observed, but with a slightly higher peak at  $\omega_0/\omega_1 \approx 1.22$  due to resonance in mode 5, see Fig. 4(b). Both mode 4 and mode 6 contribute insignificantly to the response at all frequencies.

#### 4.4 Stability and chaotic behaviour of the reduced-degree-of freedom model

In this section the stability and chaotic behaviour of the response will be further examined by increasing the number of included modes. The stability of the system is investigated by the largest Lyapunov exponent  $\lambda$ .

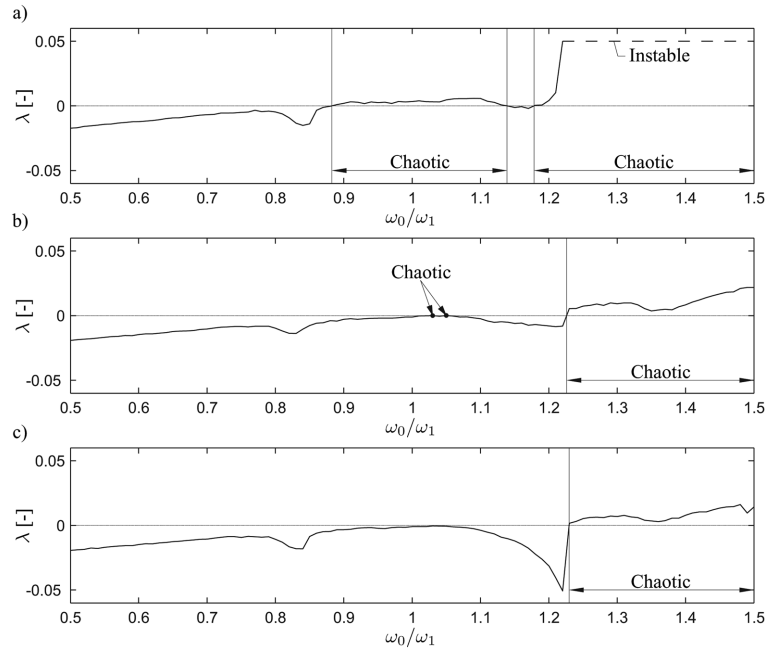


Fig. 5 Largest Lyapunov exponent with a marking of areas with chaotic response. (a)  $N = 2$ , (b)  $N = 4$ , (c)  $N = 6$ . (---) Instable i.e. infinite response

In Fig. 5 the Lyapunov exponent  $\lambda$  has been plotted as a function of the non-dimensional excitation frequency  $\omega_0/\omega_1$  for  $N = 2, 4, 6$ . A positive Lyapunov exponent may either indicate that the response becomes instable or chaotic i.e., that exponential growth takes place of the distance between two neighbouring states of the dynamic system in the phase space. In the following an instable response is defined as a response with infinite magnitude, whereas a chaotic response is finite but not periodic. For  $N = 2$  the response is chaotic in the intervals  $\omega_0/\omega_1 \approx [0.88; 1.14]$ , and for  $\omega_0/\omega_1 > 1.18$ . For  $\omega_0/\omega_1 > 1.22$  the response becomes instable as also shown in Fig. 4(a) and Fig. 4(b). On Fig. 5(b) it is seen that by increasing the number of modes to  $N = 4$  chaotic response is registered in small intervals around the values  $\omega_0/\omega_1 = 1.03$  and  $\omega_0/\omega_1 = 1.05$ . For  $\omega_0/\omega_1 > 1.22$  the response is chaotic but finite, cf. Fig. 4. For  $N = 6$  the value of the Lyapunov exponent is further decreased and the chaotic response only takes place for  $\omega_0/\omega_1 > 1.22$ . Hereby, it can be concluded that the stability overall is increased, and the tendency for chaotic behaviour is reduced, as the number of included modes is increased. Based on the simulations it is evident that more than 2 modes are used. The analyses show that using 4 modes result in a good prediction of the response and stability compared with the situation where 6 modes are included. Hence, the following analyses are restricted to  $N = 4$ .

#### 4.5 Coupling and energy transfer between lower and higher modes

In this section the important coupling coefficients responsible for the energy transfer between the modes are identified. The following analyses are restricted to  $N = 4$  with focus on the energy transfer between the two first modes and the two next modes.

##### 4.5.1 Dominating terms

In the following simulations it is shown that energy transfer between the two lowest modes and two next primarily takes place for  $\omega_0/\omega_1 > 1.0$ , where the quadratic coupling terms i.e.,  $a_{ijk}(t)$  and  $b_{ijk}(t)$  are shown to be the most important. In these coupling terms the gyroscopic components  $D_{3\beta}(t)$  and  $E_{3\beta}(t)$  enter, which consist of the rotational speed of the rotor  $\Omega_0$  together with different rotation components of the support point. As  $\omega_0/\omega_1$  increases so does the rotational speed of the rotor  $\Omega_0$  and the frequency of the support point displacement, whereby the coupling terms including these parameters, quite reasonable become important. The cubic coupling coefficients are both time independent and independent of the gyroscopic components whereby they have little influence on the energy transfer.

##### 4.5.2 Energy transfer by exclusion of coupling terms

In Fig. 6 the response for  $Q_1$  is presented for the reduced model with  $N = 4$ . The idea is to investigate the energy between the two lowest and the two highest modes within the model by excluding in turn linear, quadratic, and cubic coupling terms between the said modes. In Fig. 6(a) the linear coupling term i.e., the coupling coefficients  $m_{ij}$ ,  $c_{ij}$  and  $k_{ij}$ , where  $i = 1, 2$  and  $j = 3, 4$  or  $i = 3, 4, j = 1, 2$  are set to 0. As seen the response has only increased slightly from the full model i.e., only a small part of energy is transferred through these coupling terms and mainly at high values of  $\omega_0/\omega_1$ . In Fig. 6(b) the quadratic coupling coefficients  $a_{ijk}(t)$  between the two lowest and two highest modes are excluded. As seen the response increases heavily at the peak  $\omega_0/\omega_1 \approx 1.22$  from which is concluded that these coefficients carry a substantial flow of energy. For  $\omega_0/\omega_1 > 1.22$  the response corresponds more to the full model. Fig. 6(c) shows the corresponding results where

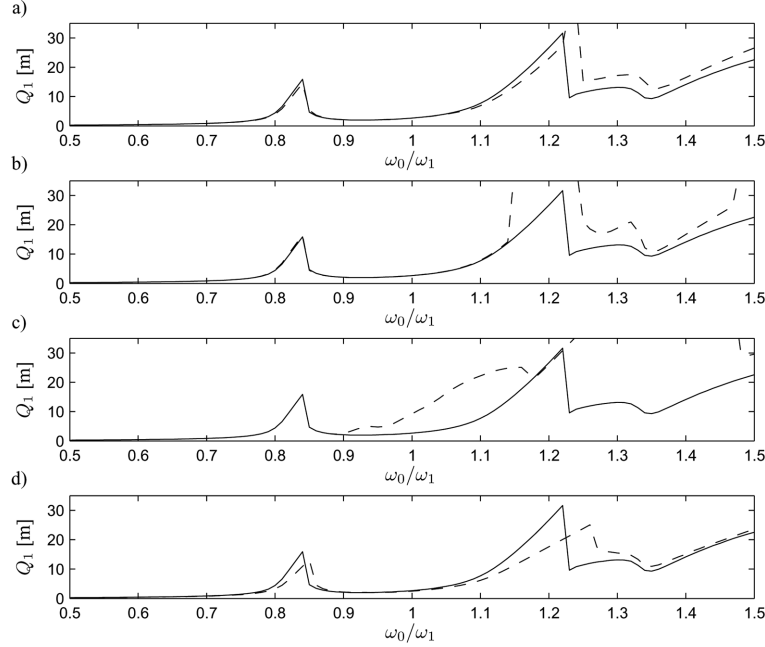


Fig. 6  $Q_1$  for the reduced-order-model with  $N = 4$  where coupling coefficients between the two lowest and two highest modes are excluded, (a) Exclusion of linear coupling terms, (b) Exclusion of quadratic couplings in  $a_{ijk}(t)$ , (c) Exclusion of quadratic couplings in  $b_{ijk}(t)$ , (d) Exclusion of cubic coupling terms. (—) Reduced-order-model. (---) Exclusion of coupling coefficients

the quadratic coupling coefficients  $b_{ijk}(t)$  are excluded. A large deviation relative to the reference model is registered between  $\omega_0/\omega_1 \approx [0.90; 1.18]$ , which to some extent corresponds to the results for  $N = 2$  in Fig. 4(a), but with higher RMS-values. At the peak  $\omega_0/\omega_1 \approx 1.22$  only insignificant deviation is observed. However, for  $\omega_0/\omega_1 > 1.22$  the response increases fast and passes out of the plot, and only enters the limits in the end. Similar, the cubic coupling coefficients only change the response minor cf. Fig. 6(d) and in this case lower the response compared to the full model. Therefore, the cubic coupling coefficients  $d_{ijkl}$  and  $g_{ijkl}$  originating from geometric and inertial nonlinearities are not the primary terms for energy transfer. From the analysis it is concluded that energy transfer primarily takes place through the quadratic coupling coefficients, where the couplings in  $a_{ijk}(t)$  mainly influence the response at the peak  $\omega_0/\omega_1 \approx 1.22$  and the couplings in  $b_{ijk}(t)$  in the remaining part of the frequency band.

## 5. Comparison of the reduced-degree-of-freedom model and the co-rotating model

In this section the reduced-degree-of-freedom model with  $N = 2, 4, 6$  is tested up against the nonlinear co-rotating FE-model for static and dynamic loads. The same input parameters as previous are used except that a time series with a sampling interval of 200 periods is used. A numerical damping parameter of  $\alpha = 0.05$  is used in the nonlinear Newmark time integration scheme. In the co-rotating model 20 beam elements are used corresponding to 126 degrees-of-freedom. The main objectives are to compare the response and stability of the two models.

Table 2 Comparison of tip displacement between the reduced-degree-of-freedom models and the co-rotating FE-model

Model	2 modes	4 modes	6 modes	FE-model
Flap displacement [m]	5.54	5.42	5.42	5.45
Edge displacement [m]	0.86	0.83	0.82	0.80

### 5.1 Static load

In the first comparison a static modal load corresponding to  $f_i = f_{i,00}$  in Eq. (25) is applied, where the support point is fixed and the rotor does not rotate i.e. the test corresponds to a cantilever blade. In the reduced model all included modal coordinates and their belonging mode shapes are used to determine the displacements. In Table 2 the tip displacement in the flap and edge direction for different number of included modes is compared to the corresponding results for the co-rotating FE-model.

As demonstrated previously, only small differences appear between 4 and 6 modes and the results in all cases are close to the predictions of the co-rotating FE-model. Even the results using merely 2 modes are in acceptable agreement with the referential results. It can hereby be concluded that the two models perform almost identical for a static load when 4 modes are used in the reduced-degree-of-freedom model.

### 5.2 Dynamic load

In this section the RMS-value of the tip displacement in the flap and edge direction is compared for the reduced order model with  $N = 4$  and the FE-model. The dynamic excitation is caused by a harmonically varying support point motion in combination with a rotating rotor and aerodynamic load as in the previous investigations. In Fig. 7 the results have been given for the following interval of excitation frequencies  $\omega_0/\omega_1 = [0.5; 1.5]$

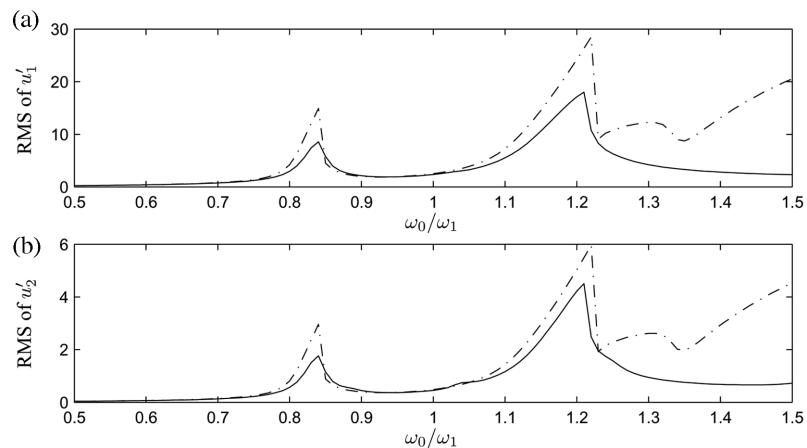


Fig. 7 RMS-values for the tip displacement in the flap and edge direction. (---) 4 modes included in the reduced-degree-of-freedom model. (—) Co-rotating FE-model

As seen, the results are qualitatively in agreement for  $\omega_0/\omega_1 < 1.23$ , although substantial deviations appear at the resonance peaks at  $\omega_0/\omega_1 \approx 0.84$  and  $\omega_0/\omega_1 \approx 1.22$ , where the FE-model produces much smaller response. The characteristics of the to models for  $\omega_0/\omega_1 > 1.23$  are no longer similar which is due to chaotic behaviour of the reduced-degree-of-freedom model as shown in Fig. 5(b). It can hereby be concluded that the reduced-degree-of-freedom model is not valid for  $\omega_0/\omega_1 > 1.23$  and it predicts too high RMS-values at the resonance peaks.

### 5.3 Stability

From Fig. 5 it is seen that  $\omega_0/\omega_1 = 0.5$  results in stable response for all three numbers of modes, and that  $\omega_0/\omega_1 = 0.9$  results in chaotic response, when 2 modes are used, and ordered response for 4 and 6 modes. For  $\omega_0/\omega_1 = 1.3$  a chaotic response is obtained in all cases, and even instability for  $N=2$ . These frequency ratios are used in the following stability analysis. In Fig. 8 a Poincaré map is shown for corresponding values of the tip displacement and velocity in the flap direction at time intervals  $2\pi/\omega_0$  for both the co-rotating FE-model and the reduced-degree-of-freedom model for  $N=4$ . It turns out that the response period is determined from the interference of the response caused by the circular frequencies  $\omega_0 + \Omega_0$  and  $\omega_0 - \Omega_0$ , and for a rational value of  $\omega_0/\Omega_0 = 3$  the response period is in Larsen and Nielsen (2006b) shown to be periodic with the period  $3T_0$ . For the co-rotating FE-model cf. the first row in Fig. 8, the Poincaré map shows as predicted three different points in the phase plane. This is the case for all three values of  $\omega_0/\omega_1$  corresponding to an ordered response. As predicted by the Lyapunov exponent the reduced-degree-of-freedom model is stable at  $\omega_0/\omega_1 = 0.5$ , cf. row two in Fig. 8. For  $\omega_0/\omega_1 = 0.9$  the response is ordered but with slightly more displacements of the points, and at  $\omega_0/\omega_1 = 1.3$  the response is chaotic. The reduced-degree-of-freedom model predicts chaotic response at  $\omega_0/\omega_1 = 1.3$  for  $N = 2, 4, 6$ , which is not the case for a full model. This is due to increased transfer of energy to higher modes for the full model.

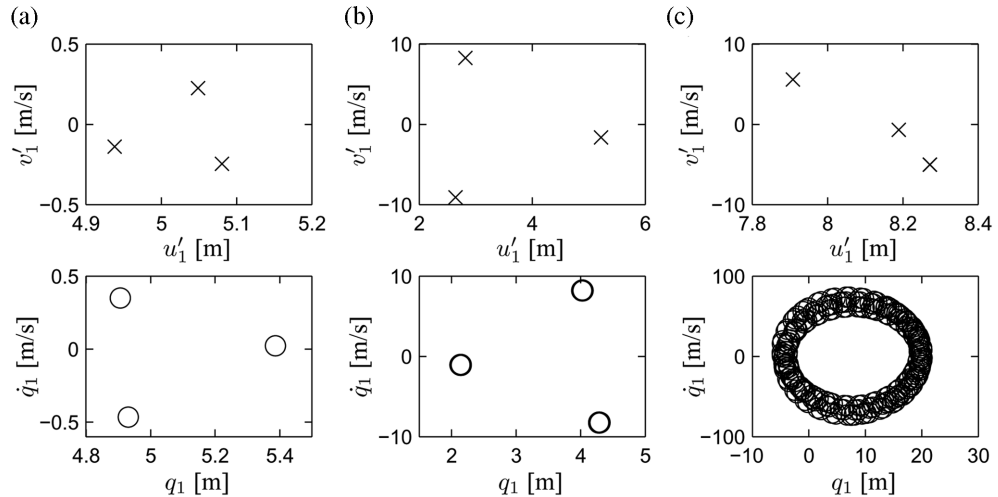


Fig. 8 Poincaré maps for tip motion in flap direction. Column (a)  $\omega_0/\omega_1 = 0.5$ . Column (b)  $\omega_0/\omega_1 = 0.9$ . Column (c)  $\omega_0/\omega_1 = 1.3$



Table 3 Comparison of average computation time per period for the reduced-degree-of-freedom model and the co-rotating model

Model	2 modes	4 modes	6 modes	Co-rotating
Time/period [sek]	0.002	0.008	0.022	2.185

#### 5.4 Time consumption

In this section the computation time of the reduced-degree-of-freedom model and the co-rotating FE-model are compared. Both programs are developed in Fortran and in Table 3 the average simulation time per period is presented.

It is clear that even though the programs could be optimized further a major advantage is gained by using the reduced-degree-of-freedom models over the co-rotating model. From the reduced-degree-of-freedom models the time consumption increases heavily by increasing the number of modes. For large simulations it is therefore necessary to determine the minimum number of modes which produce acceptable results. Based on the previous simulations 4 modes are the best choice among the used number of modes.

### 6. Conclusions

Based on the convergency test of the reduced-degree-of-freedom model it can be concluded that the response by use of two modes does not deviate much from the results by including more modes when looking at a normal operating relation between the frequency of the support point motion and the first blade eigenfrequency. By comparing the results using four modes with the results using six modes almost no difference appears for  $\omega_0/\omega_1 < 1$ . It can also be concluded that the fourth mode contributes very little whereby three modes would result in an efficient and qualitative prediction of the response. If the system by malfunction speeds up the rotor resulting in a relation of  $\omega_0/\omega_1 > 1$  it is shown that the response for two modes becomes instable, which is not the case for four modes. Including six modes do not change the qualitatively and quantitatively behaviour of the system.

From the stability analysis it is shown that by increasing the number of modes the stability of the system is improved. It is also demonstrated that the main terms for energy transfer between the first two modes and the next two are the quadratic terms which describe inertial nonlinearities from the support point motion and the rotor rotation.

In the comparison between the reduced-degree-of-freedom model and the co-rotating FE-model almost identical results under normal operation except at the resonance peaks were produced if the number of modes are four or above. This outcome was repeated both in the static, dynamic and stability tests where four modes produced results close to the co-rotating FE-model. However, for values of  $\omega_0/\omega_1$  outside the normal operating area the reduced-degree-of-freedom model no longer match the co-rotating FE-model in neither response nor stability. A comparison between the time consumption for the two models showed a major gain in using the reduced-degree-of-freedom model.

It can hereby be concluded that the reduced-degree-of-freedom model is not reliable in predicting the response nor the stability for arbitrary relations between the support point motion and the first eigenfrequency of the blade. This way of incorporating couplings between the different modes for energy transfer is therefore not sufficient and other methods where the truncated modes are included

should be investigated e.g. by use of nonlinear normal modes.

However, for normal operation of the wind turbine outside the resonance peaks the two models perform very similar when the number of modes are four but even three modes should produce almost identical results reducing the computational cost.

## Acknowledgements

This work has been supported by the Danish Council for Strategic Research through the project 'Nonlinear Multibody Dynamics of Wind Turbines'.

## References

- Apiwattanalungarn, P., Shaw, S.W., Pierre, C. and Jiang, D. (2003), "Finite-element-based nonlinear modal reduction of a rotation beam with large-amplitude motion", *J. Vib. Control*, **9**, 235-263.
- Baker, C.P., Genaux, M.E. and Burton, T.D. (1993), "Experimental study of chaos in a flexible parametrically excited beam", *Dyn. Vib. Time-Varying Syst. Struct.*, **56**, 195-206.
- Behdinan, K., Stylianou, M.C. and Tabarrok, B. (1998), "Co-rotational dynamic analysis of flexible beams", *Comput. Method. Appl. M.*, **154**, 151-161.
- Crisfield, M.A. (1990), "A consistent co-rotational formulation for non-linear, three-dimensional, beam-elements", *Comput. Method. Appl. M.*, **81**, 131-150.
- Crisfield, M.A., Galvanetto, U. and Jelenić, G. (1997), "Dynamics of 3-D co-rotational beams", *Comput. Mech.*, **20**, 507-519.
- Martin O.L. Hansen (2000), *Aerodynamics of Wind Turbines*, James & James (Science Publishers) Ltd.
- Steen Krenk (2005), "Non-linear modelling and analysis of structures and solids", Lecture notes. Department of Mechanical Engineering, Technical University of Denmark.
- Larsen, J.W. and Nielsen, S.R.K. (2006a), "Non-linear dynamics of wind turbine wings", *J. Non-Linear Mech.*, **41**, 629-643.
- Larsen, J.W. and Nielsen, S.R.K. (2006b), "Nonlinear parametric instability of wind turbine wings", *J. Sound Vib.*, (in press.)
- Hsiao, K.M., Lin, J.Y. and Lin, W.Y. (1999), "A consistent co-rotational finite element formulation for geometrically nonlinear dynamic analysis of 3-D beams", *Comput. Method. Appl. M.*, **169**, 1-18.
- Nayfeh, A.H., Chin, C. and Nayfeh, S.A. (1995), "Nonlinear normal modes of a cantilever beam", *J. Vib. Acoustics*, **117**, 417-481.
- Sandhu, J.S., Stevens, K.A. and Davies, G.A.O. (1990), "A 3-D, co-rotational, curved and twisted beam element", *Comput. Struct.*, **35**(1), 69-79.
- Volovoi, V.V., Hodges, D.H., Cesnik, C.E.S. and Popescu, B. (2001), "Assessment of beam modeling methods for rotor blade applications", *Math. Comput. Model.*, **33**, 1099-1112.
- Wolf, A., Swift, J.B., Swinney, H.L. and Vastano, J.A. (1984), "Determining lyapunov exponents from a time series", *Physica*, **16D**, 285-317.
- Yu, W., Hodges, D.H., Volovoi, V. and Cesnik, C.E.S. (2002), "On timoshenko-like modelling of initially curved and twisted composite beams", *J. Solids Struct.*, **39**, 5101-5121.

## Appendix A. Time dependent coupling coefficients

In this appendix the time dependent coupling coefficients i.e.,  $k_{ij}(t)$ ,  $c_{ij}(t)$ ,  $a_{ijk}(t)$ ,  $b_{ijk}(t)$  and  $f_i(t)$  are rewritten into as many time independent terms as possible to gain a more optimized code. The aerodynamic load is also described.

Inserting the relevant components of  $\underline{D}(t)$  and  $\underline{E}(t)$  as given by Eq. (12) and Eq. (11), respectively, and the local components of the support point motions given by Eq. (6), the time dependent coefficients Eq. (10) and Eq. (14) may be written in the following way

$$\begin{aligned}
 k_{ij}(t) &= -k_{ij,11}\Theta_{2,0}^2\dot{u}^2(t) + k_{ij,12}\Theta_{2,0}(\ddot{u}(t)\sin\Omega_0 t + \dot{u}(t)\Omega_0\cos\Omega_0 t) \\
 &\quad + k_{ij,21}\Theta_{2,0}(-\ddot{u}(t)\sin\Omega_0 t + \dot{u}(t)\Omega_0\cos\Omega_0 t) \\
 &\quad + k_{ij,22}((-\Theta_{2,0}^2\dot{u}^2(t)\sin^2\Omega_0 t - \Omega_0^2) + k_{ij,33}(\Theta_{2,0}^2\dot{u}^2(t)\cos^2\Omega_0 t + \Omega_0^2)), \\
 c_{ij}(t) &= -c_{ij,1}\dot{u}(t)\Theta_{2,0}\sin\Omega_0 t \\
 a_{ijk}(t) &= a_{ijk,0}(t) - a_{ijk,1}\Theta_{2,0}(\ddot{u}(t)\cos\Omega_0 t + \dot{u}(t)\Omega_0\sin\Omega_0 t) - a_{ijk,2}\Theta_{2,0}^2\dot{u}^2(t)\sin\Omega_0 t\cos\Omega_0 t \\
 b_{ijk}(t) &= -b_{ijk,1}\Theta_{2,0}\dot{u}(t)\cos\Omega_0 t + b_{ijk,2}\Omega_0 \\
 f_i(t) &= f_{i,0}(t) + f_{i,1}\Theta_{2,0}(\ddot{u}(t)\cos\Omega_0 t - \Omega_0\dot{u}(t)\sin\Omega_0 t) - f_{i,2}\Theta_{2,0}^2\dot{u}^2(t)\sin\Omega_0 t\cos\Omega_0 t + f_{i,3}\ddot{u}(t) \quad (19)
 \end{aligned}$$

where the time independent coefficients are found to be

$$\begin{aligned}
 c_{ij,1} &= 2 \int_0^L \mu(-\Phi_1^{(i)}\Phi_2^{(j)} + \Phi_2^{(i)}\Phi_1^{(j)})dx_3' \\
 k_{ij,\alpha\beta} &= \int_0^L \mu\Phi_\alpha^{(i)}\Phi_\beta^{(j)}dx_3', \quad k_{ij,33} = \int_0^L \left[ \frac{\partial\Phi_\alpha^{(i)}}{\partial x_3'} \frac{\partial\Phi_\alpha^{(j)}}{\partial x_3'} \int_{x_3'}^L \mu x_3' dx_3' \right] dx_3' \\
 a_{ijk,0} &= \int_0^L \left[ \frac{\partial\Phi_\alpha^{(i)}}{\partial x_3'} \frac{\partial\Phi_\beta^{(j)}}{\partial x_3'} \int_{x_3'}^L -p_{\beta,A}'' \frac{\partial\Phi_\beta^{(k)}}{\partial x_3'} dx_3' + \frac{1}{2}\Phi_\alpha^{(i)}p_{\beta,A}'' \frac{\partial\Phi_\alpha^{(j)}}{\partial x_3'} \frac{\partial\Phi_\beta^{(k)}}{\partial x_3'} \right] dx_3' \\
 a_{ijk,\alpha} &= \int_0^L \left[ \frac{\partial\Phi_\alpha^{(i)}}{\partial x_3'} \frac{\partial\Phi_\beta^{(j)}}{\partial x_3'} \int_{x_3'}^L -\mu\Phi_\alpha^{(k)} dx_3' \right] dx_3', \quad b_{ijk,\alpha} = 2a_{ijk,\alpha} \\
 f_{i,0} &= \int_0^L \Phi_\alpha^{(i)}p_{\alpha,A}'' dx_3', \quad f_{i,\alpha} = -\int_0^L \Phi_\alpha^{(i)}\mu x_3' dx_3', \quad f_{i,3} = \int_0^L \Phi_1^{(i)}\mu dx_3' \quad (20)
 \end{aligned}$$

## Appendix B. Aerodynamic load

The incoming wind velocity  $V_1'(x_3', t)$  as seen from a considered cross section of the blade varies periodically with the rotational speed  $\Omega_0$ .  $V_1'(x_3', t)$  is assumed to vary logarithmic in the following way

$$V_1'(x_3', t) = V_0 \frac{\ln x_3}{\ln h} = V_0 \frac{\ln(h - x_3' \cos\Omega_0 t)}{\ln h} \quad (21)$$

where  $V_0$  is the undisturbed mean wind velocity and  $h$  is the height of the rotor axis. The rotational wind velocity is given as  $V_2'(x_3') = x_3'\Omega_0$ . Then, the resulting wind velocity  $V(x_3', t)$  may be written as

$$V(x_3', t) = \sqrt{V_1'^2(x_3', t) + V_2'^2(x_3')} \quad (22)$$

The following expression for the aerodynamic loads are used

$$\begin{aligned}
 p_{1,A}''(x_3', t) &= \frac{1}{2}\rho V^2(x_3', t)c(x_3')c_L \simeq p_{1,A,0}''(x_3') + \Delta p_{1,A,1}''(x_3')\cos\Omega_0 t \\
 p_{2,A}''(x_3', t) &= \frac{1}{2}\rho V^2(x_3', t)c(x_3')c_D \simeq p_{2,A,0}''(x_3') + \Delta p_{2,A,1}''(x_3')\cos\Omega_0 t \quad (23)
 \end{aligned}$$

where  $\rho$  is the density of air,  $V$  is the resulting wind velocity from the incoming wind velocity and the rotational wind velocity,  $c$  is the chord length, and  $c_L$  and  $c_D$  are the lift and drag coefficients, respectively. In the simulations the following values are used:  $V_0 = 15$  m/s,  $h = 60$  m,  $\rho = 1.2$  kg/m<sup>3</sup>,  $c_L = 1.5$  and  $c_D = 0.05$ .  $p''_{\alpha,A,0}(x'_3)$  denotes the mean value of  $p''_{\alpha,A}(x'_3, t)$ , when the blade is at the top and bottom positions. Correspondingly,  $\Delta p''_{\alpha,A,1}(x'_3)$  denotes half of the difference between these extreme values. The coefficients  $a_{ijk,0}(t)$  and  $f_{i,0}(t)$  in Eq. (20) may then be written in the following way

$$a_{ijk,0}(t) = a_{ijk,00} + \Delta a_{ijk,01} \cos \Omega_0 t, \quad f_{i,0}(t) = f_{i,00} + \Delta f_{i,01} \cos \Omega_0 t \quad (24)$$

with

$$\begin{aligned} a_{ijk,00} &= \int_0^L \left[ \frac{\partial \Phi_\alpha^{(i)}}{\partial x'_3} \frac{\partial \Phi_\alpha^{(j)}}{\partial x'_3} \int_{x'_3}^L \left[ -p''_{\beta,A,0} \frac{\partial \Phi_\beta^{(k)}}{\partial x'_3} \right] dx'_3 + \frac{1}{2} \Phi_\alpha^{(i)} p''_{\beta,A,0} \frac{\partial \Phi_\alpha^{(j)}}{\partial x'_3} \frac{\partial \Phi_\beta^{(k)}}{\partial x'_3} \right] dx'_3 \\ \Delta a_{ijk,01} &= \int_0^L \left[ \frac{\partial \Phi_\alpha^{(i)}}{\partial x'_3} \frac{\partial \Phi_\alpha^{(j)}}{\partial x'_3} \int_{x'_3}^L \left[ -\Delta p''_{\beta,A,1} \frac{\partial \Phi_\beta^{(k)}}{\partial x'_3} \right] dx'_3 + \frac{1}{2} \Phi_\alpha^{(i)} \Delta p''_{\beta,A,1} \frac{\partial \Phi_\alpha^{(j)}}{\partial x'_3} \frac{\partial \Phi_\beta^{(k)}}{\partial x'_3} \right] dx'_3 \\ f_{i,00} &= \int_0^L \Phi_\alpha^{(i)} p''_{\alpha,A,0} dx'_3, \quad \Delta f_{i,01} = \int_0^L \Phi_\alpha^{(i)} \Delta p''_{\alpha,A,1} dx'_3 \end{aligned}$$

### Appendix C. Specifications of blade

The theory is demonstrated using a 46 m pitch regulated blade. The aerodynamic profiles are NACA 63-418 section profiles as illustrated in Fig. 9, scaled with chord and height values indicated in Fig. 11(d). The inner 2.0 m of the blade has a circular cross section with a diameter of 2.0 m. In Fig. 10 the blade is shown based on the geometry of the root and the scaling and pretwisting of the NACA 63-418 profile. The blade has the pretwist angle, the mass, local moments of inertia, chord length and thickness distributions as indicated in Fig. 11. The total weight is 10 t. The stiffness and mass distribution are chosen so that the eigenfrequencies approximately match those given by a manufacture of a corresponding blade size. The modulus of elasticity is  $E = 3 \cdot 10^4$  MPa. The twist throughout the blade is chosen so that the angle of attack of the resulting wind is approximately  $6^\circ$  at a constant rotational speed of 1.6 rad/s, and an incoming wind velocity of 12 m/s. At these nominal values a wind turbine with such three blades should produce approximately 2.75 MW according to the Blade Element Momentum theory described in Hansen 2000.

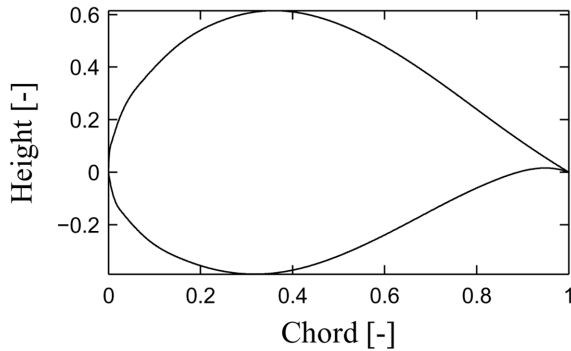


Fig. 9 Normalized profile of a NACA 63-418 blade section

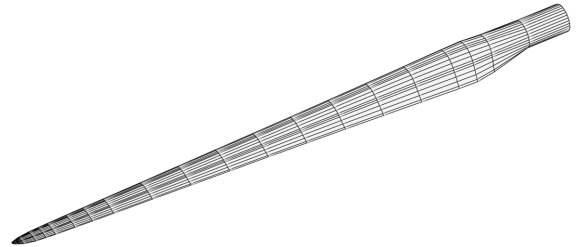


Fig. 10 Illustration of the used blade in the simulations

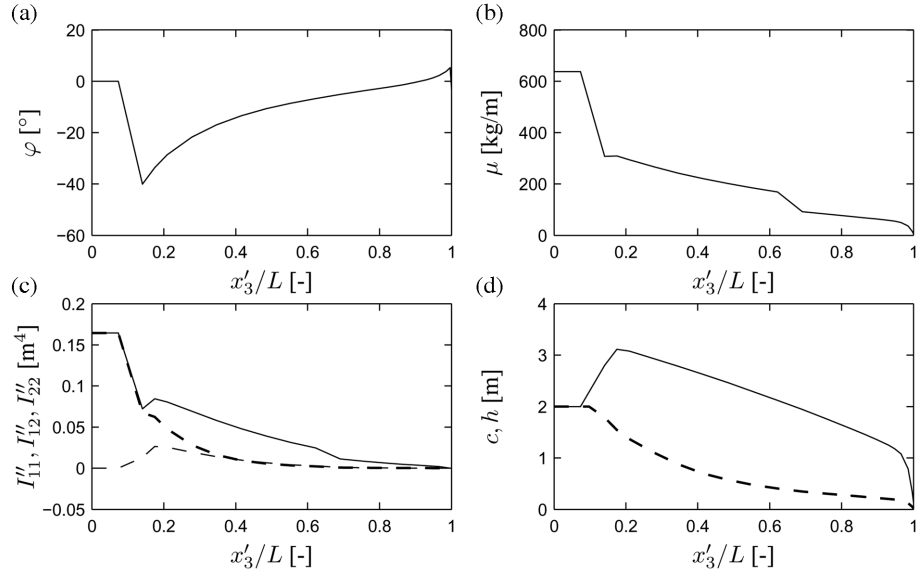


Fig. 11 (a) Pretwist angle throughout the beam, (b) Mass per unit length, (c) Distribution of local moment of inertia. (—)  $I''_{11}$  . (---)  $I''_{12}$  . (- -)  $I''_{22}$  . (d) (—) Chord length  $c$ . (---) Height  $h$  of cross sections



---

**APPENDIX D**  
**Paper: System Reduction in**  
**Multibody Dynamics of Wind**  
**Turbines**

---





# System reduction in multibody dynamics of wind turbines

K. Holm-Jørgensen · S.R.K. Nielsen

Received: 10 December 2007 / Accepted: 24 September 2008 / Published online: 30 October 2008  
© Springer Science+Business Media B.V. 2008

**Abstract** A system reduction scheme is devised related to a multibody formulation from which the dynamic response of a wind turbine is determined. In this formulation, each substructure is described in its own frame of reference, which is moving freely in the vicinity of the moving substructure. The Ritz bases spanning the reduced system comprises of rigid body modes and some dynamic low-frequency elastic eigenmodes compatible to the kinematic constraints of the related substructure. The high-frequency elastic modes are presumed to cause merely quasi-static displacements, and thus are included in the expansion via a quasi-static correction. The results show that by using the derived reduction scheme it is only necessary with 2 dynamical modes for the blade substructure when the remaining modes are treated as quasi-static. Moreover, it is shown that it has little to none effect if the gyroscopic stiffness matrix during a stopped situation or under nominal operational conditions is used to derive the functional basis of the modal expansion.

**Keywords** Multibody dynamics · System reduction · Quasi-static modal model · Wind turbine

## 1 Introduction

The analysis of large structural systems is conveniently carried out by so-called substructure coupling methods, or component mode synthesis (CMS) methods. The basic principle is that each substructure or component is modeled separately. Next, the components are linked together by a coupling scheme complying with the relevant kinematical constraints at the interfaces between the substructures.

The modeling of a component implies a discretization in space. Typically, this is done by an FE method, often involving thousands if not millions of degrees of freedom. In order to reduce the computational efforts, reduced order models of the components need to be implemented, which are usually chosen with emphasis on the low frequency dynamics. The

---

K. Holm-Jørgensen (✉) · S.R.K. Nielsen  
Department of Civil Engineering, Aalborg University, Sohngaardsholmsvej 57, 9000 Aalborg, Denmark  
e-mail: [khj@civil.aau.dk](mailto:khj@civil.aau.dk)

modes included into the reduced Ritz basis of the substructure can be any set of linearly independent vectors capable of modeling the considered frequency range. The modes are taken as rigid body modes whereas the flexible modes are taken as either eigenmodes free or constrained at the boundary degrees of freedom, or as so-called constraint modes and attachment modes. Constraint modes are static deformation modes, where the substructure is free of internal loads, and where each boundary degree of freedom in turn is given a unit displacement with the remaining boundary degrees of freedom fixed, and the interior degrees of freedom are unloaded. Attachment modes are static deformation modes with all boundary degrees of freedom fixed, and where selected internal degrees of freedom in turn are loaded with a unit force, and the remaining degrees of freedom are unloaded, Craig 2000 [1]. Obviously, constraint and attachment modes are unable to describe high frequency elastic deformations. CMS is often split into two methods: the constraint-mode method and the attachment-mode method. The first method was used by Hurty [2] which consists of constraint modes and fixed interface normal modes. The latter method is used by Rubin [3] and MacNeal [4] based on attachment modes and free interface normal modes. In the present paper, the system reduction is performed by a Ritz basis consisting of rigid-body modes and fixed interface normal modes.

Concentrated forces within the substructure, e.g., due to actuator forces from tuned mass dampers or other vibration control devices, contain significant high frequency components, which cannot easily be decomposed into a limited number of modal loads. This is also the case for the aerodynamic load, which although continuous distributed is confined to the outer 30% of the blade. The high-frequency harmonics of these loads do not affect the dynamic response of the substructure, but do induce a quasi-static displacement component, which cannot generally be ruled out. Hence, when using reduced order component models for substructures with substantial concentrated loads, attention should be paid to the quasi-static part of the response from these loads. Reduction schemes based on expansion in a truncated number of normal modes have been indicated by, e.g., Preumont [5].

The basic idea of flexible multibody dynamics is to introduce a moving frame of reference to each substructure. Relative to the moving frame elastic displacements are relatively small rendering linear analysis possible. Hence, nonlinearities are confined to the description of the moving frame. This frame is defined by a position vector and a parameter vector (pseudo-vector) defining the rotation of the moving frame relative to a fixed frame of reference. The standard formulation of the method presumes that the moving frame is fixed to the rigid body motion of the substructure, with the consequence that the coordinates defining position and orientation of the moving frame becomes a part of the degrees of freedom of the multibody system; see, e.g., Nikravesh [6], García and Bayo [7], Géradin and Cardona [8] and Shabana [9]. However, the use of a mixed set of referential and elastic coordinates leads to highly nonlinear inertial couplings between the rigid body motion and elastic deformation.

The basic modeling of the elastic deformations of the substructure in a multibody formulation is performed by an FE-discretization or by eigenmodes Shabana [10]. Lee [11] also used a modal approach where the nonlinear multibody equations of motion are linearized. Because of the linearization of, e.g., the quadratic velocity terms it is necessary to update the linearized equations in each updated time step. Lee also describes the advantages of using modal integration to flexible multibody systems, e.g., to avoid problems caused by inherently stiff systems and the possibility of using larger time steps in the time integration algorithm. Alternatively, an unconditional stable numerical time integration scheme should be applied. By decomposition of terms in the equations of motion into time-dependent and time-independent parts, Pan et al. [12] have reduced the computation time even further.

Khulief et al. [13] have analyzed the dynamic response of rotors using mode truncation in real eigenmodes, but also complex eigenmodes by incorporating the gyroscopic damping term. The two methods showed almost the same level of accuracy. In the present paper, real eigenmodes have been used to create the Ritz basis. Bauchau and Rodriguez [14] and Bauchau et al. [15] used a modal approximation based on Herting's transformation to reduce the computational costs in multibody dynamics. The reduced set of degrees of freedom in this transformation is the boundary degrees of freedom and the modal participation factors for the rigid and elastic modes. This makes a more general selection of modes and boundary conditions.

To circumvent the difficulties with the highly nonlinear system equations, Kawamoto et al. [16–19] suggested to let the moving reference frame float in a controlled way relative to the moving substructure, so these are always sufficiently close to each other that linearization becomes possible. Whenever the substructure has drifted unacceptable far away the position, velocity, and acceleration of the origin together with the rotation, angular velocity, and angular acceleration of the moving frame must be updated. This can even be performed with regular time intervals larger than the time step used for the numerical integration of the equations of motion. In this formulation, the equations of motion for an unconstrained body are linear, but iterations are necessary due to the kinematical constraints and when updating the moving frame. In the present paper, no updating criteria is used so the moving frame is updated in each time step. In Kawamoto et al. [17], the equations of motion in a moving frame are further described and the update of the rotation of the moving frame is performed by a polar decomposition.

The system reduction scheme presented in this paper is based on reducing one or several substructures in a multibody formulation corresponding to Kawamoto et al. [17]. In the original paper, they use a number of rigid body modes together with elastic eigenmodes to describe the displacement field of each substructure. In the present paper, the gyroscopic effects appearing in a rotor dynamic system, e.g., a wind turbine is included in the Ritz basis. This is done by including different stiffness contributions from the equations of motion when determining the elastic mode shapes. Further, the use of various functional bases for the flexible deformation and as explained above the quasi-static contribution from the truncated elastic modes has been included in the system reduction scheme. In contrary to the papers by Kawamoto et al. [16, 17], constraints are described in the present paper and included in the equations of motion. These constraints are solved as they are originally formulated by insertion in the system stiffness matrix, whereby constraint regularization is not necessary.

## 2 Moving frame of reference formulation of multibody dynamics

The idea is to describe the motion of a substructure in a frame of reference which is moving independently in the vicinity of the substructure. All quantities without a bar are defined in the moving frame of reference given by the  $(x_1, x_2, x_3)$ -coordinate system. The  $(\bar{x}_1, \bar{x}_2, \bar{x}_3)$ -coordinate system is fixed and common for all substructures. Fixed frame and moving frame components of vectors and tensors will be indicated with and without a bar, respectively. The moving frame origin is described by a position vector  $\bar{\mathbf{x}}_c$ . The rotation of the moving frame relative to the fixed frame is determined by the parameter vector (or pseudo-vector)  $\boldsymbol{\theta}$ . The angular velocity and angular acceleration vectors are specified by the moving frame components  $\boldsymbol{\omega}$  and  $\boldsymbol{\alpha}$ . Generally, the substructure may drift away from the moving frame, which requires sequential updating of the position, velocity, and acceleration of the origin together with the rotation, angular velocity, and angular acceleration of the referential frame to en-

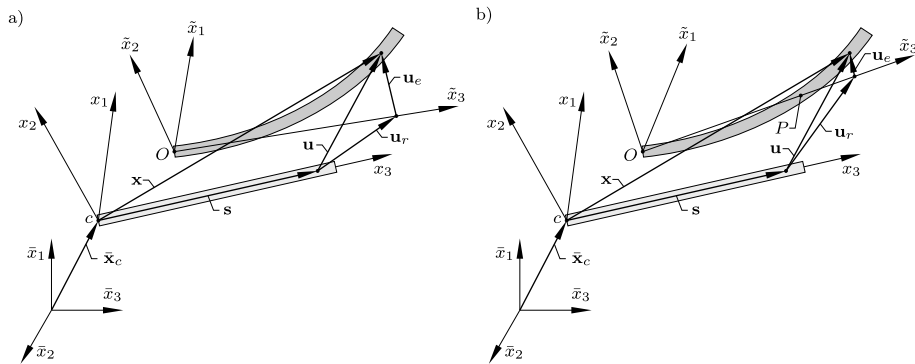


**Fig. 1** Decomposition of the displacement field into rigid body and elastic components

sure small displacement components. In this respect, it is convenient to introduce an auxiliary  $(\bar{x}_1, \bar{x}_2, \bar{x}_3)$ -coordinate system, which is fully constrained to the moving substructure. The total displacement  $\mathbf{u}(\mathbf{s}, t)$  of a certain material point relative to the moving reference frame is given by physics, and thereby fixed. It is, however, arbitrary how this displacement is split up into  $\mathbf{u}_r(\mathbf{s}, t)$  and  $\mathbf{u}_e(\mathbf{s}, t)$  corresponding to the  $(\bar{x}_1, \bar{x}_2, \bar{x}_3)$ -system can be chosen in many ways. The rigid-body displacement  $\mathbf{u}_r(\mathbf{s}, t)$  is spanned by rigid-body modes, and the elastic displacement  $\mathbf{u}_e(\mathbf{s}, t)$  is spanned by the eigenmodes of the substructure constrained to the auxiliary moving frame. Figure 1 shows two possible definitions of the auxiliary coordinate system. In Fig. 1a, the position and rotation of the auxiliary system have been chosen as the position and rotation of the end point O. This results in larger elastic deformations  $\mathbf{u}_e(\mathbf{s}, t)$  than the definition in Fig. 1b where the  $\bar{x}_3$ -axis has been placed along two material points O and P. For the blade substructure, the definition in Fig. 1a complies with the kinematical constraints at the fixed end. However, this definition is not optimal, e.g., a rotor shaft substructure supported by bearings where the definition in Fig. 1b is more optimal and will reduce the number of necessary elastic modes. The eigenmodes of the substructure constrained to the auxiliary moving frame can immediately be determined and will enter in the system reduction algorithm. In the conventional multibody formulation, the  $(\bar{x}_1, \bar{x}_2, \bar{x}_3)$ -system is used as the local frame of reference, and the parameters defining the position and orientation of the coordinate system are introduced as degrees of freedom in the state vector. The position vector to a material point within the substructure has the following moving and fixed frame components

$$\mathbf{x}(\mathbf{s}, t) = \mathbf{s} + \mathbf{u}(\mathbf{s}, t), \quad (1)$$

$$\bar{\mathbf{x}}(\mathbf{s}, t) = \bar{\mathbf{x}}_c + \mathbf{R}(\mathbf{s} + \mathbf{u}(\mathbf{s}, t)), \quad (2)$$

where  $\mathbf{R}$  stores the components of the rotation tensor.  $\mathbf{R}$  is defined by the pseudo-vector  $\boldsymbol{\theta}$  as given by Rodriguez formula, Shabana [9]

$$\mathbf{R} = \cos(\theta)\mathbf{I} + (1 - \cos(\theta))\mathbf{nn}^T + \sin(\theta)\tilde{\mathbf{n}}, \quad (3)$$

where  $\mathbf{n} = \boldsymbol{\theta}/|\boldsymbol{\theta}|$ . The corresponding moving frame components of the velocity and acceleration vector of the point become, Shabana [9]

$$\mathbf{v} = \mathbf{v}_c + \tilde{\boldsymbol{\omega}}(\mathbf{s} + \mathbf{u}) + \dot{\mathbf{u}}, \quad (4)$$

$$\mathbf{a} = \mathbf{a}_c + (\tilde{\boldsymbol{\alpha}} + \tilde{\boldsymbol{\omega}}\tilde{\boldsymbol{\omega}})(\mathbf{s} + \mathbf{u}) + 2\tilde{\boldsymbol{\omega}}\dot{\mathbf{u}} + \ddot{\mathbf{u}}, \quad (5)$$

where  $\alpha = \dot{\omega}$ .  $\tilde{\omega}$  and  $\tilde{\alpha}$  denote the spin matrices related to  $\omega$  and  $\alpha$ .  $\tilde{\omega}$  is given as, Shabana [9]

$$\tilde{\omega} = \begin{bmatrix} 0 & -\omega_3 & \omega_2 \\ \omega_3 & 0 & -\omega_1 \\ -\omega_2 & \omega_1 & 0 \end{bmatrix}. \quad (6)$$

The first term  $\mathbf{v}_c$  in (4) is the translational velocity of the moving frame, the second term  $\tilde{\omega}(\mathbf{s} + \mathbf{u})$  is the rotational velocity, and the last term  $\dot{\mathbf{u}}$  is the velocity from elastic deformations and rigid body motions inside the moving frame. The first term  $\mathbf{a}_c$  in (5) denotes the translational acceleration of the moving frame origin. The term  $\tilde{\alpha}(\mathbf{s} + \mathbf{u})$  is the angular acceleration which is orthogonal on  $\alpha$  and  $(\mathbf{s} + \mathbf{u})$ . The next term  $\tilde{\omega}\tilde{\omega}(\mathbf{s} + \mathbf{u}) = \omega \times (\omega \times (\mathbf{s} + \mathbf{u}))$  describes the centrifugal acceleration. The Coriolis acceleration is described by  $2\tilde{\omega}\dot{\mathbf{u}}$  which is perpendicular to both the direction of the velocity of the moving body and to the rotation axis. Finally, the term  $\ddot{\mathbf{u}}$  describes the moving frame components of the acceleration of the material point as seen by an observer in the moving frame. The equations of motion of the substructure are conveniently derived using analytical mechanics based merely on scalar quantities such as the kinetic  $T = T(\mathbf{y}, \dot{\mathbf{y}})$  and the potential energy  $U = U(\mathbf{y})$  containing contributions from the strain energy and conservative external loads  $\mathbf{Q}_c(\mathbf{y})$  such as gravity, in addition to vectorial quantities as the nonconservative loads  $\mathbf{Q}_{nc}(\mathbf{y})$ . In principle, these loads may be linearized in the applied moving frame of reference. The nonconservative loads are caused by the follower character of the aerodynamic loads. The kinetic energy is most convenient determined by using the moving frame components of the velocity vector  $\mathbf{v}$  from (4). The resulting equations of motion for substructure  $i$  are given by a slightly modified version of Kawamoto et al. [17]

$$\begin{aligned} \mathbf{M}_i \ddot{\mathbf{y}}_i + (\mathbf{C}_{0,i} + 2\mathbf{G}_i) \dot{\mathbf{y}}_i + (\mathbf{K}_{0,i} + \dot{\mathbf{G}}_i + \mathbf{D}_i + \mathbf{K}_{g,i}) \mathbf{y}_i + \mathbf{B}_i(\mathbf{y}_i)^T \tilde{\lambda}_i \\ = -\mathbf{M}_{0,i}^T \mathbf{a}_{c,i} - \mathbf{J}_{0,i}^T + \mathbf{J}_{2,i}^T + \mathbf{Q}_{c,i}(\mathbf{y}_i) + \mathbf{Q}_{nc,i}(\mathbf{y}_i), \end{aligned} \quad (7)$$

where the Lagrange multipliers  $\tilde{\lambda}_i$  contain the reaction forces and moments conjugated to the kinematic constraints and  $\mathbf{B}_i(\mathbf{y}_i)$  is the constraint matrix.  $\mathbf{C}_{0,i}$  and  $\mathbf{K}_{0,i}$  are the structural damping and the elastic stiffness matrix, respectively, and

$$\mathbf{M}_i = \int_V \mathbf{N}_i^T \mathbf{N}_i \rho dV, \quad \mathbf{M}_{0,i} = \int_V \mathbf{N}_i \rho dV, \quad \mathbf{D}_i = \int_V \mathbf{N}_i^T \tilde{\omega}_i \tilde{\omega}_i \mathbf{N}_i \rho dV, \quad (8)$$

$$\mathbf{G}_i = \int_V \mathbf{N}_i^T \tilde{\omega}_i \mathbf{N}_i \rho dV, \quad \mathbf{J}_{0,i} = \omega_i^T \int_V \tilde{\mathbf{s}} \mathbf{N}_i \rho dV, \quad \mathbf{J}_{2,i} = \omega_i^T \int_V \tilde{\mathbf{s}} \tilde{\omega}_i \mathbf{N}_i \rho dV, \quad (9)$$

$$\mathbf{K}_{g,i} = \Omega^2(t) \int_L Q_3(x_3) \frac{d\mathbf{N}_{g,i}^T}{dx_3} \frac{d\mathbf{N}_{g,i}}{dx_3} dx_3. \quad (10)$$

In the geometric stiffness  $\mathbf{K}_{g,i}$ , only the contribution from the centrifugal force,  $\Omega^2(t) Q_3(x_3)$ , is included where the angular velocity of the rotor  $\Omega(t)$ , for the blade substructure, is the only time dependent term.  $\mathbf{M}_i$  is the conventional symmetric mass matrix of the body in the moving reference frame which in the present formulation is independent of the moving frame of reference parameters.  $\mathbf{M}_{0,i}$  is representing the inertial effect of uniform translation. The effect of centrifugal forces are contained in the symmetric matrix  $\mathbf{D}_i$  and the gyroscopic forces are represented by the skew symmetric matrix  $\mathbf{G}_i$ . The remaining  $\mathbf{J}_{0,i}$ - and  $\mathbf{J}_{2,i}$ -terms are couplings between the reference position and the shape functions. Next,

the following damping  $\mathbf{C}_i$  and stiffness matrices  $\mathbf{K}_i$  are introduced together with the load vector  $\mathbf{f}_i$

$$\mathbf{C}_i = \mathbf{C}_{0,i} + 2\mathbf{G}_i, \quad \mathbf{K}_i = \mathbf{K}_{0,i} + \dot{\mathbf{G}}_i + \mathbf{D}_i + \mathbf{K}_{g,i}, \quad (11)$$

$$\mathbf{f}_i = -\mathbf{M}_{0,i}^T \mathbf{a}_{c,i} - \dot{\mathbf{J}}_{0,i}^T + \mathbf{J}_{2,i}^T + \mathbf{Q}_{c,i}(\mathbf{y}_i) + \mathbf{Q}_{nc,i}(\mathbf{y}_i), \quad (12)$$

where by the equations of motion are written as

$$\mathbf{M}_i \ddot{\mathbf{y}}_i + \mathbf{C}_i \dot{\mathbf{y}}_i + \mathbf{K}_i \mathbf{y}_i + \mathbf{B}_i(\mathbf{y}_i)^T \bar{\boldsymbol{\lambda}}_i = \mathbf{f}_i(t). \quad (13)$$

To set up the equations of motion for a multibody system, it is necessary to introduce kinematical constraints in order to incorporate compatibility of the mutual displacements and rotations of the substructures. In relation to a wind turbine, the coupling of two substructures can, e.g., be of the blade and rotor shaft. Additional constraints specify the supports of the rotor shaft via bearings relative to the nacelle. The displacement constraint between two substructures defines that the displacement vector for each of the two substructures at the interface point are identical. The components of this vector need to be defined in a common coordinate system, e.g., a global fixed coordinate system or the moving frame of reference of one of the substructures. In case of modeling, e.g., a cylindrical bearing the relative displacements of the two substructures in this joint are locked in two directions. This restriction is incorporated by scalar multiplication of a unit vector  $\mathbf{n}_c$ , expressing the direction where the relative displacement of the two substructures is locked. In the global fixed frame, the displacement constraint when substructures 1 and 2 are locked in the  $\mathbf{n}_{c1}$ -direction referring to substructure 1, becomes, cf. (2)

$$\begin{aligned} \Phi_{dc} &= \mathbf{n}_{c1}^T \mathbf{R}_1^T (\bar{\mathbf{x}}_{c1} + \mathbf{R}_1(\mathbf{s}_1 + \mathbf{u}_1) - (\bar{\mathbf{x}}_{c2} + \mathbf{R}_2(\mathbf{s}_2 + \mathbf{u}_2))) \\ &= \mathbf{n}_{c1}^T \mathbf{R}_1^T (\bar{\mathbf{x}}_{c1} + \mathbf{R}_1(\mathbf{s}_1 + \mathbf{N}_1 \mathbf{y}_1) - (\bar{\mathbf{x}}_{c2} + \mathbf{R}_2(\mathbf{s}_2 + \mathbf{N}_2 \mathbf{y}_2))) = 0, \end{aligned} \quad (14)$$

where the lower index  $i$  refers to substructure  $i$ , and  $\mathbf{u}_i$  has been interpolated by a set of shape functions  $\mathbf{N}_i(\mathbf{s})$  and generalized coordinates  $\mathbf{y}_i$ .  $\mathbf{R}_1$  and  $\mathbf{R}_2$  represent the rotation tensors of the moving frames relative to the fixed coordinate system. The kinematic rotational constraints between two substructures are determined using the triads to the deformed structures at the interface joint. A total of three orthogonality conditions between these unit vectors are necessary to fix the rotations in the joint. The fixed frame components of the triad to the deformed structure is determined by the following linearization

$$\mathbf{R}_i^* = \mathbf{R}_i \mathbf{R}(\boldsymbol{\varphi}_i) \approx \mathbf{R}_i (\mathbf{I} + \tilde{\boldsymbol{\varphi}}_i), \quad (15)$$

where the rotation  $\boldsymbol{\varphi}_i$  from the moving reference frame is small. In order to fix an angle, e.g.,  $\pi/2$  between two unit vectors in the triads, the orthogonality condition becomes

$$\Phi_{rc} = (\mathbf{R}_1^* \mathbf{i}_1)^T \mathbf{R}_2^* \mathbf{i}_3 = 0, \quad (16)$$

where  $\mathbf{i}_1^T = [1 \ 0 \ 0]$  and  $\mathbf{i}_3^T = [0 \ 0 \ 1]$ . By insertion of (15) in (16), the rotational constraint becomes

$$\Phi_{rc} = \mathbf{i}_3^T \mathbf{R}_2^T \mathbf{R}_1 \tilde{\mathbf{i}}_1 \boldsymbol{\varphi}_1 + (\mathbf{i}_1^T + \boldsymbol{\varphi}_1^T \tilde{\mathbf{i}}_1) \mathbf{R}_1^T \mathbf{R}_2 \tilde{\mathbf{i}}_3 \boldsymbol{\varphi}_2 - \mathbf{i}_1^T \mathbf{R}_1^T \mathbf{R}_2 \mathbf{i}_3 = 0. \quad (17)$$

The rotations are determined by  $\boldsymbol{\varphi}_i = \mathbf{P}_i \mathbf{y}_i$ , where  $\mathbf{P}_i$  represents the compatible rotations derived from the shape functions. Hereby both (14) and (17) become linear in  $\mathbf{y}_i$  but iterations are necessary due to the rotational constraints. Below, an example is given for the assembly of the displacement constraints  $\boldsymbol{\Phi}_{dc}$  from (14)

$$\boldsymbol{\Phi}_{dc} = \mathbf{B}_{d,1} \mathbf{y}_1 - \mathbf{B}_{d,2} \mathbf{y}_2 - \mathbf{b} = \mathbf{0}, \quad (18)$$

$$\mathbf{B}_{d,i} = \mathbf{n}_{c1}^T \mathbf{R}_1^T \mathbf{R}_i \mathbf{N}_i, \quad \mathbf{b} = \mathbf{n}_{c1}^T \mathbf{R}_1^T \left( -(\tilde{\mathbf{x}}_{c1} + \mathbf{R}_1 \mathbf{s}_1) + (\tilde{\mathbf{x}}_{c2} + \mathbf{R}_2 \mathbf{s}_2) \right). \quad (19)$$

Similarly, the rotational constraint  $\boldsymbol{\Phi}_{rc}$  from (17) can be written

$$\boldsymbol{\Phi}_{rc} = \mathbf{B}_{r,1} \mathbf{y}_1 + \mathbf{B}_{r,2} \mathbf{y}_2 - \mathbf{b} = \mathbf{0}, \quad (20)$$

$$\mathbf{B}_{r,1} = \mathbf{i}_3^T \mathbf{R}_2^T \mathbf{R}_1 \tilde{\mathbf{i}}_1 \mathbf{P}_1, \quad \mathbf{B}_{r,2} = (\mathbf{i}_1^T + (\mathbf{P}_1 \mathbf{y}_1)^T \tilde{\mathbf{i}}_1) \mathbf{R}_1^T \mathbf{R}_2 \tilde{\mathbf{i}}_3 \mathbf{P}_2, \quad \mathbf{b} = \mathbf{i}_1^T \mathbf{R}_1^T \mathbf{R}_2 \mathbf{i}_3. \quad (21)$$

From (18) and (20), it can be seen that the constraints can be included in the system stiffness matrix. Often in multibody dynamics, the constraints are differentiated twice with respect to time and inserted in the system mass matrix. Next, constraint regularization is used to ensure that the constraints are satisfied on the displacement and velocity level. In this paper, the constraints are solved as they originally are formulated, and it is therefore not necessary with constraint regularization. By using (13), the structure of the resulting constrained equations of motion for a multibody system consisting of 2 substructures may be written

$$\begin{bmatrix} \mathbf{M}_1 & \mathbf{0} & \mathbf{0} \\ \mathbf{0} & \mathbf{M}_2 & \mathbf{0} \\ \mathbf{0} & \mathbf{0} & \mathbf{0} \end{bmatrix} \begin{bmatrix} \ddot{\mathbf{y}}_1 \\ \ddot{\mathbf{y}}_2 \\ \ddot{\tilde{\lambda}} \end{bmatrix} + \begin{bmatrix} \mathbf{C}_1 & \mathbf{0} & \mathbf{0} \\ \mathbf{0} & \mathbf{C}_2 & \mathbf{0} \\ \mathbf{0} & \mathbf{0} & \mathbf{0} \end{bmatrix} \begin{bmatrix} \dot{\mathbf{y}}_1 \\ \dot{\mathbf{y}}_2 \\ \dot{\tilde{\lambda}} \end{bmatrix} + \begin{bmatrix} \mathbf{K}_1 & \mathbf{0} & \mathbf{B}_1^T \\ \mathbf{0} & \mathbf{K}_2 & \mathbf{B}_2^T \\ \mathbf{B}_1 & \mathbf{B}_2 & \mathbf{0} \end{bmatrix} \begin{bmatrix} \mathbf{y}_1 \\ \mathbf{y}_2 \\ \tilde{\lambda} \end{bmatrix} = \begin{bmatrix} \mathbf{f}_1 \\ \mathbf{f}_2 \\ \mathbf{b} \end{bmatrix}$$

$$\Rightarrow \mathbf{M}\ddot{\mathbf{z}} + \mathbf{C}\dot{\mathbf{z}} + \mathbf{K}\mathbf{z} = \mathbf{f}(t), \quad (22)$$

where  $\tilde{\lambda} = \tilde{\lambda}_1 = -\tilde{\lambda}_2$ . Because the constraints in principle introduce infinite stiffness into the system, it becomes necessary to apply unconditional stable time integrators. In the present case, this is achieved by means of a nonlinear Newmark algorithm.

### 3 Updating of system coordinates

In (22), only the system coordinates, i.e.,  $\mathbf{y}_i$  and  $\tilde{\lambda}$  stored in  $\mathbf{z}$  enter as degrees of freedom which are solved for. However, several terms in  $\mathbf{C}$ ,  $\mathbf{K}$ , and  $\mathbf{f}(t)$  contain parameters related to the motion of the moving frame of reference which are not solved. To determine these parameters, a prediction and correction step need to be introduced. The predicted moving frame parameters are used to setup (22) which next is time integrated to determine the displacements, velocities, and accelerations of the substructure from the predicted moving frame of reference. If the substructure has moved too far away from the moving reference frame, the motion of the moving frame of reference needs to be corrected. This is both to ensure that linear theory is adequate, but also to ensure that, e.g., the gyroscopic terms in (22) are determined precisely enough. The correction is performed by updating the predicted moving frame of reference to the auxiliary  $(\tilde{x}_1, \tilde{x}_2, \tilde{x}_3)$ -coordinate system, shown in Fig. 1. Next, the corrected parameters are inserted in (22) until the substructure is within a chosen tolerance from the moving reference frame.

For clarity, the lower index defining the substructure is left out in this section and the next following sections. Lower index “ $j$ ” refers to the initial or previous time step, lower index “ $j + 1$ ” to the present time step. Upper index “ $*$ ” defines a predicted value and for the corrected value this index has been removed. It is assumed that the accelerations defined by the system coordinates  $\ddot{\mathbf{z}}$  and the moving frame origin  $\bar{\mathbf{a}}_c$  are constant during the time step. Hereby, the belonging velocity and displacement are linear and quadratic varying with the time step, respectively. Then the system coordinates  $\mathbf{z}_{j+1}^*$ , velocities  $\dot{\mathbf{z}}_{j+1}^*$ , and accelerations  $\ddot{\mathbf{z}}_{j+1}^*$  at the time  $t_{j+1}$ , are predicted as

$$\mathbf{z}_{j+1}^* = \mathbf{z}_j + \dot{\mathbf{z}}_j \Delta t + \frac{1}{2} \ddot{\mathbf{z}}_j \Delta t^2, \quad \dot{\mathbf{z}}_{j+1}^* = \dot{\mathbf{z}}_j + \ddot{\mathbf{z}}_j \Delta t, \quad \ddot{\mathbf{z}}_{j+1}^* = \ddot{\mathbf{z}}_j. \quad (23)$$

Similarly, the motion of the moving reference frame origin is defined as

$$\bar{\mathbf{x}}_{c,j+1} = \bar{\mathbf{x}}_{c,j} + \bar{\mathbf{v}}_{c,j} \Delta t + \frac{1}{2} \bar{\mathbf{a}}_{c,j} \Delta t^2, \quad \bar{\mathbf{v}}_{c,j+1} = \bar{\mathbf{v}}_{c,j} + \bar{\mathbf{a}}_{c,j} \Delta t, \quad \bar{\mathbf{a}}_{c,j+1} = \bar{\mathbf{a}}_{c,j}, \quad (24)$$

$\bar{\mathbf{x}}_{c,j+1}$  is used to construct the displacement constraints when assembling substructures in the global fixed frame. Based on a constant angular acceleration of the moving frame of reference during the time step the rotation increment and angular velocity become

$$\Delta \phi = \omega_j \Delta t + \frac{1}{2} \alpha_j \Delta t^2, \quad \omega_{j+1} = \omega_j + \alpha_j \Delta t, \quad \alpha_{j+1} = \alpha_j. \quad (25)$$

The updated rotation tensor  $\mathbf{R}_{j+1}$  is determined by using quaternions. Because the quaternions are referred to the fixed frame, the rotation tensor  $\mathbf{R}_{j+1}$  will transform the components of a vector determined in the present orientation at time  $j + 1$  of the moving frame of reference to the fixed frame. Based on the rotation increment  $\Delta \phi$ , the following quaternion increments are determined, Krenk 2005 [20]:

$$\Delta r = \cos\left(\frac{1}{2} \Delta \bar{\phi}\right), \quad \Delta \mathbf{r} = \sin\left(\frac{1}{2} \Delta \bar{\phi}\right) \mathbf{n}, \quad (26)$$

where  $\Delta \bar{\phi} = \mathbf{R}_j \Delta \phi$ ,  $\Delta \bar{\phi} = |\Delta \bar{\phi}|$ , and  $\mathbf{n} = \Delta \bar{\phi} / \Delta \bar{\phi}$ . The updated quaternions are determined from

$$r_{j+1} = \Delta r r_j - \Delta \mathbf{r} \cdot \mathbf{r}_j, \quad \mathbf{r}_{j+1} = \Delta r \mathbf{r}_j + r_j \Delta \mathbf{r} + \Delta \mathbf{r} \times \mathbf{r}_j. \quad (27)$$

By using  $r = r_{j+1}$  and  $[r_1 \ r_2 \ r_3] = \mathbf{r}_{j+1}^T$ , the updated rotation tensor then becomes

$$\mathbf{R}_{j+1} = \begin{bmatrix} r^2 + r_1^2 - r_2^2 - r_3^2 & 2(r_1 r_2 - r r_3) & 2(r_1 r_3 + r r_2) \\ 2(r_2 r_1 + r r_3) & r^2 - r_1^2 + r_2^2 - r_3^2 & 2(r_2 r_3 - r r_1) \\ 2(r_3 r_1 - r r_2) & 2(r_3 r_2 + r r_1) & r^2 - r_1^2 - r_2^2 + r_3^2 \end{bmatrix}. \quad (28)$$

The acceleration of the moving frame origin  $\bar{\mathbf{a}}_{c,j+1}$  from (24) is transformed to moving frame components for use in (12)

$$\mathbf{a}_{c,j+1} = \mathbf{R}_{j+1}^T \bar{\mathbf{a}}_{c,j+1}. \quad (29)$$

In order to solve (22), the residual  $\mathbf{r}$  and equivalent system stiffness matrix  $\hat{\mathbf{K}}$  are determined by using the nonlinear Newmark algorithm, Géradin and Rixen [21]

$$\mathbf{r} = -\mathbf{M} \ddot{\mathbf{z}}_{j+1}^* - \mathbf{C} \dot{\mathbf{z}}_{j+1}^* - \mathbf{K} \mathbf{z}_{j+1}^* + \mathbf{f}(t), \quad \hat{\mathbf{K}} = \frac{1}{\beta \Delta t^2} \mathbf{M} + \frac{\gamma}{\beta \Delta t} \mathbf{C} + \mathbf{K}, \quad (30)$$



where  $\gamma = \frac{1}{2} + \alpha$ ,  $\beta = \frac{1}{4}(1 + \alpha)^2$ , and  $\alpha$  is used to incorporate numerical damping of high frequency components. In the present case,  $\mathbf{C}$  and  $\mathbf{K}$  are not symmetric. Stability analysis of the Newmark algorithm has originally been performed for symmetric matrices, but it turns out that it also works in the present case. By solving  $\hat{\mathbf{K}}\Delta\mathbf{z} = \mathbf{r}$  for the unknowns  $\Delta\mathbf{z}$ , the following corrected values of the system coordinates are determined

$$\mathbf{z}_{j+1} = \mathbf{z}_{j+1}^* + \Delta\mathbf{z}, \quad \dot{\mathbf{z}}_{j+1} = \dot{\mathbf{z}}_{j+1}^* + \frac{\gamma}{\beta\Delta t}\Delta\mathbf{z}, \quad \ddot{\mathbf{z}}_{j+1} = \ddot{\mathbf{z}}_{j+1}^* + \frac{1}{\beta\Delta t^2}\Delta\mathbf{z}. \quad (31)$$

#### 4 System reduction

The system reduction in this section is primarily intended for the blade substructure but could be used for any substructure. The equations of motion for a substructure (13) are rewritten in the form

$$\mathbf{M}\ddot{\mathbf{y}} + \mathbf{C}\dot{\mathbf{y}} + \mathbf{K}\mathbf{y} = \mathbf{g}(t) = \mathbf{f}(t) - \mathbf{B}^T\tilde{\boldsymbol{\lambda}}, \quad (32)$$

where the displacement dependents of  $\mathbf{f}(t)$  in (12) have been disregarded.  $\mathbf{g}(t)$  is a combined external load vector encompassing wind loads, inertial loads, and reaction forces from the kinematical constraints. The idea of the system reduction algorithm is to decompose the displacement vector  $\mathbf{y}(t)$  into a rigid body component  $\mathbf{y}_r(t)$  and an elastic component  $\mathbf{y}_e(t)$

$$\mathbf{y}(t) = \mathbf{y}_r(t) + \mathbf{y}_e(t). \quad (33)$$

These terms are next described by a Ritz basis and belonging generalized coordinates whereby the decompositions of  $\mathbf{y}_r(t)$  and  $\mathbf{y}_e(t)$  into rigid body  $\Phi_r$  and elastic mode shapes  $\Phi_e$ , respectively, become

$$\mathbf{y}_r(t) = \Phi_r \mathbf{q}_r(t), \quad (34)$$

$$\mathbf{y}_e(t) = \Phi_e \mathbf{q}_e(t), \quad (35)$$

where  $\mathbf{q}_r(t)$  and  $\mathbf{q}_e(t)$  store the rigid body and elastic generalized coordinates. The Ritz basis and generalized coordinates are assembled in the following form

$$\Phi = [\Phi_r \quad \Phi_e], \quad \mathbf{q}(t) = \begin{bmatrix} \mathbf{q}_r(t) \\ \mathbf{q}_e(t) \end{bmatrix}. \quad (36)$$

The rigid body modes are described by the regular 3 translations and 3 rotations to get a total of 6 independent rigid body modes.  $\Phi_r$  is not merely an identity matrix but contains additional components, because a rotation around the  $x_1$ - and  $x_2$ -axis will give a displacement in the  $x_2$ - and  $x_1$ -direction, respectively. The elastic modes  $\Phi_e$  and thereby modal expansion of  $\mathbf{y}_e$  are determined corresponding to the kinematical constraints. This is illustrated in Fig. 1a with a fixed-base and in Fig. 1b where the elastic displacements are supported at the points  $O$  and  $P$ . To incorporate the kinematical constraints on the elastic modes the rows and columns for the corresponding degrees of freedom in  $\mathbf{K}$  and  $\mathbf{M}$  are removed resulting in the following reduced generalized eigenvalue problem

$$(\tilde{\mathbf{K}} - \tilde{\lambda}_j \tilde{\mathbf{M}}) \tilde{\Phi}_e^{(j)} = \mathbf{0}, \quad \tilde{\lambda}_j = \tilde{\omega}_j^2. \quad (37)$$

The vectors entering  $\tilde{\Phi}_e$  are ordered in ascending magnitude of the frequency  $\tilde{\omega}_j$ . Next,  $\tilde{\Phi}_e$  is expanded to full size  $\Phi_e$  by insertion of zeros for the degrees of freedom corresponding

to the removed rows and columns. Insertion of (33)–(36) in (32) and premultiplication with  $\Phi^T$  provides the following reduced equations of motion

$$\mathbf{m}\ddot{\mathbf{q}} + \mathbf{c}\dot{\mathbf{q}} + \mathbf{k}\mathbf{q} = \Phi^T \mathbf{g}(t), \quad (38)$$

where

$$\left. \begin{aligned} \mathbf{m} &= \Phi^T \mathbf{M} \Phi \\ \mathbf{c} &= \Phi^T \mathbf{C} \Phi \\ \mathbf{k} &= \Phi^T \mathbf{K} \Phi \end{aligned} \right\}. \quad (39)$$

Notice that none of the reduced matrices have a diagonal structure. Now, all the elastic modes with frequencies above a certain frequency  $\tilde{\omega}_0$  are assumed to respond quasi-static to the combined external load  $\mathbf{g}(t)$ , whereas the remaining elastic modes respond dynamically. Correspondingly, the partitioning of the elastic modes is subdivided into dynamic and quasi-static components. Then  $\Phi_e$  and  $\mathbf{q}_e(t)$  in (36) are replaced by the following partitionings:

$$\Phi_e = [\Phi_d \quad \Phi_s], \quad \mathbf{q}_e(t) = \begin{bmatrix} \mathbf{q}_d \\ \mathbf{q}_s \end{bmatrix} \quad (40)$$

The indices “ $d$ ” and “ $s$ ” stand for dynamic and static components. Hereby, the displacement vector  $\mathbf{y}(t)$  in (33) is reformulated as

$$\mathbf{y}(t) = \mathbf{y}_r(t) + \mathbf{y}_d(t) + \mathbf{y}_s(t). \quad (41)$$

The static modes are not directly used, instead the quasi-static contribution is determined by the already included dynamical modes as follows, Preumont [5]:

$$\tilde{\mathbf{y}}_s(t) = (\tilde{\mathbf{K}}^{-1} - \tilde{\Phi}_d \tilde{\mathbf{k}}_d^{-1} \tilde{\Phi}_d^T) \tilde{\mathbf{g}}(t) = \tilde{\mathbf{U}} \tilde{\mathbf{g}}(t) \quad (42)$$

where

$$\tilde{\mathbf{k}}_d = \tilde{\Phi}_d^T \tilde{\mathbf{K}} \tilde{\Phi}_d. \quad (43)$$

It is, therefore, necessary that the kinematical supports eliminate any singularity of  $\tilde{\mathbf{K}}$ , which is the case in the numerical example. The full vector  $\mathbf{y}_s(t)$  is obtained by reordering of the degrees of freedom and insertion of zeros corresponding to the kinematical supports. The displacement vector  $\mathbf{y}(t)$  is thereby determined from

$$\mathbf{y}(t) = \mathbf{A}\mathbf{w} + \mathbf{U}\mathbf{g}(t), \quad (44)$$

where

$$\mathbf{A} = [\Phi_r \quad \Phi_d], \quad \mathbf{w} = \begin{bmatrix} \mathbf{q}_r \\ \mathbf{q}_d \end{bmatrix}. \quad (45)$$

Hereby the modal matrices from (39) are redefined as

$$\left. \begin{aligned} \mathbf{m} &= \mathbf{A}^T \mathbf{M} \mathbf{A} \\ \mathbf{c} &= \mathbf{A}^T \mathbf{C} \mathbf{A} \\ \mathbf{k} &= \mathbf{A}^T \mathbf{K} \mathbf{A} \end{aligned} \right\}. \quad (46)$$

Based on the derived system reduction algorithm, a substructure in the original system of (22) can be reduced by insertion of (44) into (32). In the following numerical examples, the

blade substructure has been reduced by using elastic fixed-base eigenmodes. When expanding  $\bar{\mathbf{U}}_1$  to full size  $\mathbf{U}_1$ , zeros are inserted for the originally removed rows and columns corresponding to the fixed boundary.  $\mathbf{B}_1$  only contains values different from zero at the boundary degrees of freedom so  $\mathbf{B}_1 \mathbf{U}_1 = \mathbf{0}$  and  $\mathbf{U}_1 \mathbf{B}_1^T = \mathbf{0}$  which are used below where substructure 1 has been reduced and substructure 2 is left unchanged.

$$\begin{bmatrix} \mathbf{m}_1 & \mathbf{0} & \mathbf{0} \\ \mathbf{0} & \mathbf{M}_2 & \mathbf{0} \\ \mathbf{0} & \mathbf{0} & \mathbf{0} \end{bmatrix} \begin{bmatrix} \ddot{\mathbf{w}}_1 \\ \ddot{\mathbf{y}}_2 \\ \ddot{\boldsymbol{\lambda}} \end{bmatrix} + \begin{bmatrix} \mathbf{c}_1 & \mathbf{0} & \mathbf{0} \\ \mathbf{0} & \mathbf{C}_2 & \mathbf{0} \\ \mathbf{0} & \mathbf{0} & \mathbf{0} \end{bmatrix} \begin{bmatrix} \dot{\mathbf{w}}_1 \\ \dot{\mathbf{y}}_2 \\ \dot{\boldsymbol{\lambda}} \end{bmatrix} + \begin{bmatrix} \mathbf{k}_1 & \mathbf{0} & \mathbf{A}_1^T \mathbf{B}_1^T \\ \mathbf{0} & \mathbf{K}_2 & \mathbf{B}_2^T \\ \mathbf{B}_1 \mathbf{A}_1 & \mathbf{B}_2 & \mathbf{0} \end{bmatrix} \begin{bmatrix} \mathbf{w}_1 \\ \mathbf{y}_2 \\ \boldsymbol{\lambda} \end{bmatrix} \\ = \begin{bmatrix} \mathbf{A}_1^T (\mathbf{I} - \mathbf{K}_1 \mathbf{U}_1) \mathbf{f}_1 \\ \mathbf{f}_2 \\ \mathbf{b} \end{bmatrix}. \quad (47)$$

It should be noted that the structure of the reduced equations of motion is similar to the original full set of (22). Equation (44) is used to determine the original degrees of freedom for substructure 1, i.e.,  $\mathbf{y}_1$ . The velocities  $\dot{\mathbf{y}}_1$  and accelerations  $\ddot{\mathbf{y}}_1$  are determined from the following Newmark scheme:

$$\dot{\mathbf{y}}_1 = \mathbf{A}_1 \dot{\mathbf{w}}_1 + \frac{\gamma}{\beta \Delta t} \mathbf{U}_1 \mathbf{g}_1, \quad \ddot{\mathbf{y}}_1 = \mathbf{A}_1 \ddot{\mathbf{w}}_1 + \frac{1}{\beta \Delta t^2} \mathbf{U}_1 \mathbf{g}_1, \quad \mathbf{g}_1 = \mathbf{f}_1 - \mathbf{B}_1^T \bar{\boldsymbol{\lambda}}. \quad (48)$$

## 5 Numerical example

In this section, the theory is illustrated with a simplified system consisting of four substructures: one blade, rotor shaft, nacelle, and tower, labeled 1, 2, 3, and 4, respectively, as shown in Fig. 2b. The blade and shaft substructures are fixed together and similarly with the nacelle and tower substructures. Moreover, the tower substructure is fixed to the ground. To connect the rotor and nacelle substructures, two main bearings  $B_1$  and  $B_2$  are introduced.  $B_1$  is a so-called cylindrical bearing which allows rotation around the longitudinal axis of the shaft and also displacements in the longitudinal direction relative to the nacelle.  $B_2$  is a so-called stop-bearing which is similar to  $B_1$  except with none relative displacements in the longitudinal direction between the shaft and nacelle. For the formulation of the kinematical constraints at  $B_1$  and  $B_2$ , it is assumed that the shaft and nacelle substructures are overlapping. The length  $L$  of the blade is 44.8 m with a total weight of 10 t and it is constructed by NACA 63-418 section profiles. The cross section parameters and the mass distribution throughout the blade are presented in Larsen and Nielsen [22]. In the following simulations, the blade is not coned, the nacelle is not tilted, and the wind turbine is not yawed from its original position. The numerical FE-model of all substructures is based on prismatic Bernoulli–Euler beam elements with St. Venant torsion and has 6 degrees of freedom for each node. In the numerical tests, only the blade substructure has been reduced because this is the most complex substructure and undergoes the largest deformations which would otherwise require many degrees of freedom. To verify the derived reduction scheme, it is compared to the full FE-model. In the numerical tests, only the moving reference frame for the blade and shaft substructures are rotating. Moreover, the origin of all moving frame of references is not moved during the simulation because these displacements are small. No structural damping is included, i.e.,  $\mathbf{C}_0 = \mathbf{0}$  in (11). A numerical damping of  $\alpha = 0.004$  is used to maintain steady constraints when only a few dynamical modes are used in the reduced model. This numerical damping showed no sign of changes to the response. A time step of  $\Delta t = 1/1000$  s is used to capture all variations.

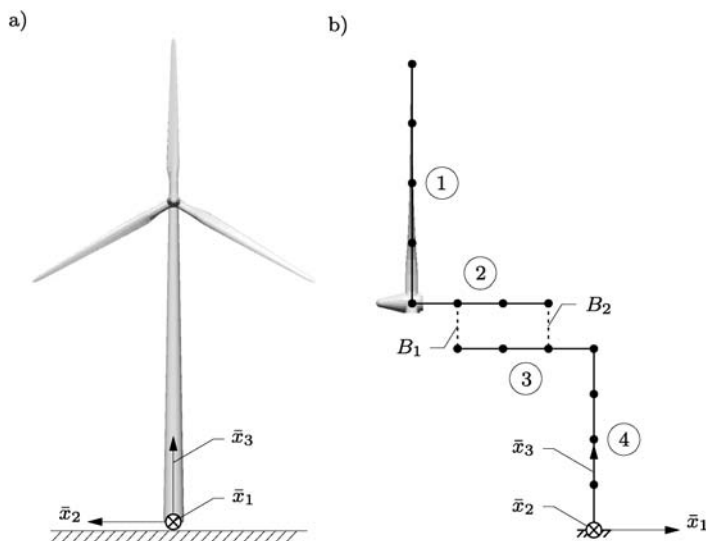


**Fig. 2** (a) Fixed frame of reference in the wind turbine. (b) The numerical model consisting of four substructures

### 5.1 Influence on the fixed-base eigenmodes from the stiffness matrices

Due to the blade and rotor shaft substructures are fixed together, it is reasonable to believe that the most appropriate elastic modes to describe the displacements of the blade are obtained as fixed-base eigenmodes. In this section, the influence of the stiffness terms from (8)–(10) is further investigated when obtaining the fixed base eigenmodes. As seen from (11), the stiffness matrix consists of the elastic stiffness  $\mathbf{K}_0$ , the geometric stiffness  $\mathbf{K}_g$ , and the gyroscopic stiffness terms  $\mathbf{D}$  and  $\dot{\mathbf{G}}$  which depend on the angular velocity of the frame and angular acceleration of the frame, respectively. The following models of the stiffness matrix when obtaining the fixed-base eigenmodes are used:

$$\left. \begin{aligned} \mathbf{K}_a &= \mathbf{K}_0 \\ \mathbf{K}_b &= \mathbf{K}_0 + \mathbf{K}_g \\ \mathbf{K}_c &= \mathbf{K}_0 + \mathbf{K}_g + \mathbf{D} \\ \mathbf{K}_d &= \mathbf{K}_0 + \mathbf{K}_g + \dot{\mathbf{G}} \\ \mathbf{K}_e &= \mathbf{K}_0 + \mathbf{K}_g + \mathbf{D} + \dot{\mathbf{G}} \end{aligned} \right\}. \quad (49)$$

For all situations, the same mass matrix  $\mathbf{M}$  from (8) is used when solving the generalized eigenvalue problem (37). The reason for examining the influence of the different stiffness terms is to determine which are the most important for defining the functional basis for the elastic deformations and to determine if the elastic eigenmodes obtained at one operating situation can be used for a large operating area, i.e., with different angular velocities and angular accelerations of the moving reference frame. The comparisons are based on the three lowest eigenfrequencies and the shapes in the flap and edge direction of the belonging eigenmodes. The nominal angular velocity of the rotor for this particular wind turbine is  $\Omega_n = 1.6$  rad/s. Therefore, an equal size of the angular velocity of the moving frame of

**Table 1** Three lowest fixed-base eigenfrequencies for different models of the stiffness matrix

	$\mathbf{K}_a$	$\mathbf{K}_b$	$\mathbf{K}_c$	$\mathbf{K}_d$	$\mathbf{K}_e$
$\omega_1$ [rad/s]	4.63	5.16	5.15	5.16	5.15
$\omega_2$ [rad/s]	9.41	9.63	9.51	9.63	9.51
$\omega_3$ [rad/s]	13.69	14.24	14.23	14.24	14.23

reference is used. To examine the influence of the  $\dot{\mathbf{G}}$  term, an angular acceleration of the moving reference frame has also been included

$$\boldsymbol{\omega}_1 = \begin{bmatrix} 1.6 \\ 0 \\ 0 \end{bmatrix} \text{ rad/s}, \quad \boldsymbol{\alpha}_1 = \begin{bmatrix} 0.4 \\ 0 \\ 0 \end{bmatrix} \text{ rad/s}^2. \quad (50)$$

When determining the geometric stiffness matrix, the nominal angular velocity of  $\Omega_n = 1.6$  rad/s is used. In Table 1, the three lowest fixed-base eigenfrequencies are given from solving the generalized eigenvalue problem by using the five variations of the stiffness matrix in (49). It appears that the eigenfrequencies for the model described by  $\mathbf{K}_a$  are the smallest of the five models. This model is only based on the elastic stiffness matrix and, therefore, corresponds to a situation where the wind turbine is stopped. In model  $\mathbf{K}_b$ , the geometric stiffness matrix is included and it appears that the eigenfrequencies for all three modes are increased corresponding to an increased stiffness from the centrifugal force in the longitudinal direction of the blade. By inclusion of the gyroscopic term  $\mathbf{D}$  in model  $\mathbf{K}_c$ , the eigenfrequencies are slightly lowered whereby the term  $\mathbf{D}$  reduces the stiffness. From numerical simulations, it has shown that the geometric stiffness term is very important to maintain a stable system, which due to the  $\mathbf{D}$  term would otherwise become unstable. By comparison of  $\mathbf{K}_b$  and  $\mathbf{K}_d$ , it is shown that the angular acceleration of the moving frame of reference has no influence on the eigenfrequencies. It has previously been described that  $\dot{\mathbf{G}}$  is skew-symmetric and the possibility of complex eigenvalues therefore exists. However, when obtaining the fixed-base eigenmodes, all eigenvalues turn out to be real. Because  $\dot{\mathbf{G}}$  has little to no influence on the eigenfrequencies, the results for  $\mathbf{K}_c$  and  $\mathbf{K}_e$  become equal. It is thereby concluded that the variation of the fixed-base eigenfrequencies from the stopped situation to the nominal operation primarily is based on the geometric stiffness matrix. Because  $\dot{\mathbf{G}}$  has none influence on the eigenfrequencies only the components of the mode shapes in the flap  $\Phi_1$  and edge direction  $\Phi_2$  for the models  $\mathbf{K}_a$ ,  $\mathbf{K}_b$ , and  $\mathbf{K}_c$  are examined. In Fig. 3, the mode shapes are normalized with the dominating component in the tip. It appears that  $\Phi^{(1)}$  is dominated by a flap component,  $\Phi^{(2)}$  by an edge component and  $\Phi^{(3)}$  by a flap component. As anticipated from the variation of the eigenfrequencies, almost identical results are presented. It is thereby concluded that even though the eigenfrequencies change from the stopped situation to the nominal operating situation the mode shapes for the displacement components in the flap and edge direction only change very little.

## 5.2 Influence of eigenmodes on the response

In this section, the elastic eigenmodes determined from the previously denoted models  $\mathbf{K}_a$ ,  $\mathbf{K}_b$ , and  $\mathbf{K}_c$  are used to discretize the response of the blade. This is done to determine if it is necessary to use different eigenmodes when the rotor rotates with different angular ve-

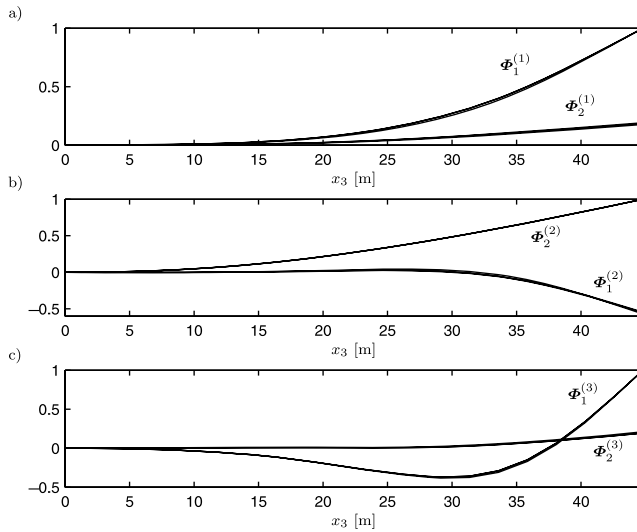


**Fig. 3** Mode shapes in flap  $\Phi_1$  and edge direction  $\Phi_2$  for the three lowest fixed-base eigenmodes: (a)  $\Phi^{(1)}$ ; (b)  $\Phi^{(2)}$ ; (c)  $\Phi^{(3)}$ . The models  $\mathbf{K}_a$ ,  $\mathbf{K}_b$ , and  $\mathbf{K}_c$  are almost identical

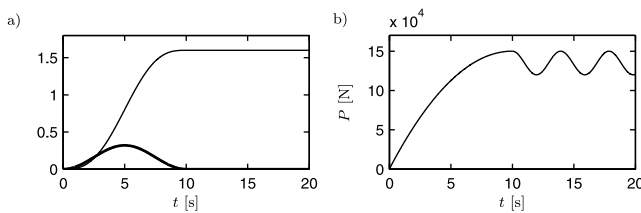


**Fig. 4** Start-up sequence  $t = [0; 10]$  s and operating sequence  $t = ]10; 20]$  s. (a) Angular acceleration (—) and belonging angular velocity (—) of the moving frame of reference. (b) Size of the concentrated load in the flap direction

locity. The numerical example consists of a start-up sequence and an operating sequence. In the start-up sequence, the rotor speeds up from a stopped situation to the nominal angular velocity, and in the operating sequence, the rotor rotates with the nominal angular velocity. Both sequences are modeled by prescribing the angular acceleration of the moving reference frame for the blade and rotor shaft substructure. The related angular velocity is then automatically determined from (25). The following angular acceleration of each moving frame of reference is used during the two sequences where  $t_n$  defines the time where the nominal operating sequence starts

$$\alpha(t) = \begin{cases} \frac{\Omega_n}{t_n} \left( -\cos\left(\frac{2\pi t}{t_n}\right) + 1 \right), & 0 \leq t \leq t_n, \\ 0, & t_n < t. \end{cases} \quad (51)$$

In Fig. 4a, the angular acceleration and angular velocity are plotted for the two sequences where  $t_n = 10$  s and the simulation ends at  $t = 20$  s. To stress the reduction schemes, a concentrated load in the  $u_1$ -direction, i.e., flap-direction is applied to the blade at  $x_3 \approx \frac{2}{3}L$ . The reason for applying the load at this point is because the majority of the wind load is

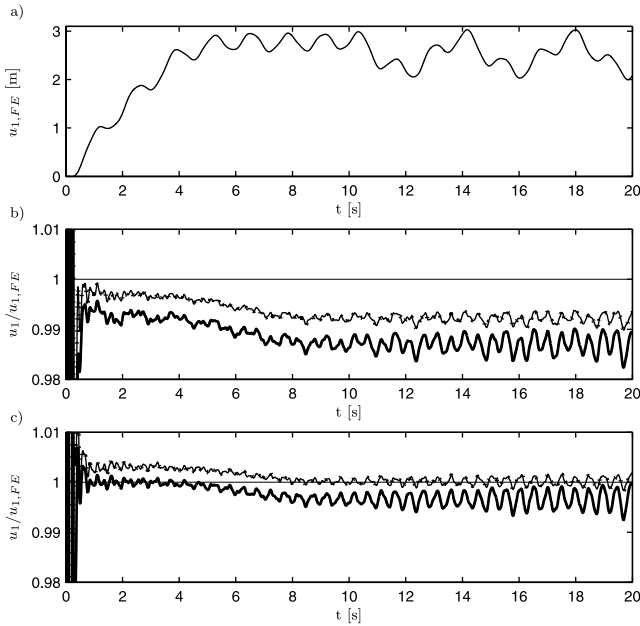


**Fig. 5** Tip response in the flap direction. **(a)** FE-model during the simulated time series. **(b)** Normalized tip response without quasi-static contribution. **(c)** Normalized tip response with quasi-static contribution.  $K_a$  (—),  $K_b$  (.....),  $K_c$  (—)

concentrated around this position. A concentrated load will regularly require a lot of modes to discretize the response, which favors the reduction scheme when the quasi-static contribution from the truncated elastic modes is included. The load has the following characteristics during the start-up sequence and operating sequence

$$P(t) = \begin{cases} P_0 \left( -\left(\frac{t}{t_n}\right)^2 + \frac{2t}{t_n} \right), & 0 \leq t \leq t_n, \\ P_0(1 + p_n \cos(\Omega_n(t - t_n)) - p_n), & t_n < t. \end{cases} \quad (52)$$

In the start-up sequence, the load is stepped up parabolically from  $P = 0$  at  $t = 0$  to a parabolic maximum of  $P = P_0$  at  $t_n$ . In the operating sequence, the applied load is based on a constant load corresponding to a mean wind velocity and a harmonic component with amplitude  $p_n$  due to a variation in the shear wind field. In the simulations, the following values have been used:  $P_0 = 1.5 \times 10^5$  N,  $p_n = 0.1$ ,  $\Omega_n = 1.6$  rad/s, and  $t_n = 10$  s. In Fig. 5a, the tip displacement of the blade in the flap direction  $u_1$  is presented for the full FE-model where the blade is modeled by 20 beam elements, and thereby 126 degrees of freedom. The periods in the response are primarily based on the first eigenfrequency of the blade and for  $t > 10$  s the harmonic frequency of the load. In the following tests, 3 dynamical modes are used with and without the quasi-static contribution. The derived eigenmodes are constant throughout the simulation, i.e., the eigenmodes based on  $K_b$  and  $K_c$  are determined for a situation corresponding to the nominal angular velocity of  $\Omega_n = 1.6$  rad/s. The responses from the models  $K_a$ ,  $K_b$ , and  $K_c$  without the quasi-static correction i.e.  $U_1 = \mathbf{0}$  are shown in Fig. 5b where they are normalized with the response from the FE-model. During the first, approximately 0.5 s large relative differences appear which are not included in the plot. As

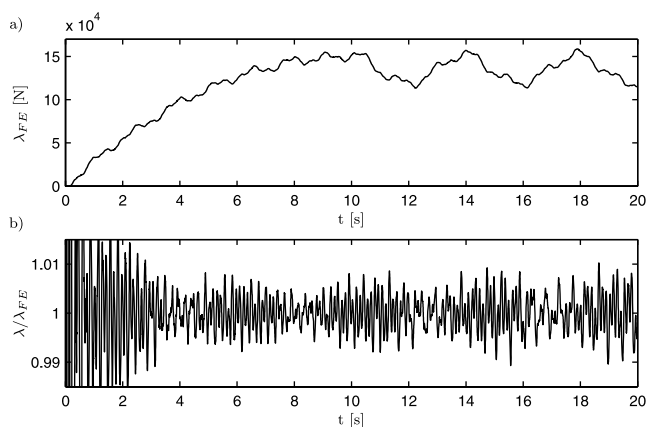


**Fig. 6** Lagrange multiplier for displacement constraint between blade and shaft substructures in the  $\bar{x}_1$ -direction. **(a)** FE-model during the simulated time series. **(b)** Normalized Lagrange multipliers for the  $\mathbf{K}_c$  model with quasi-static contribution

**Table 2** Mean value and standard deviation, denoted by  $\mu$  and  $\sigma$ , respectively, of the normalized response and normalized constraint. In both cases, the data for  $t \geq 2$  s is used

	$\mu_{u_1}$	$\sigma_{u_1}$	$\mu_\lambda$	$\sigma_\lambda$
$\mathbf{K}_a, \mathbf{U}_1 = \mathbf{0}$	0.988	0.002	1.000	0.005
$\mathbf{K}_b, \mathbf{U}_1 = \mathbf{0}$	0.993	0.002	1.000	0.004
$\mathbf{K}_c, \mathbf{U}_1 = \mathbf{0}$	0.993	0.002	1.000	0.004
$\mathbf{K}_a, \mathbf{U}_1 \neq \mathbf{0}$	0.997	0.002	1.000	0.005
$\mathbf{K}_b, \mathbf{U}_1 \neq \mathbf{0}$	1.001	0.001	1.000	0.004
$\mathbf{K}_c, \mathbf{U}_1 \neq \mathbf{0}$	1.001	0.001	1.000	0.004

anticipated, the results from the models  $\mathbf{K}_b$  and  $\mathbf{K}_c$  are almost identical and just slightly better than the results from model  $\mathbf{K}_a$ . In Fig. 5c, the same reduced models are used together with the quasi-static correction, i.e.,  $\mathbf{U}_1 \neq \mathbf{0}$ . Here, it appears that the normalized response from the different models is increased by a constant factor of approximately 0.01. Hereby, the model  $\mathbf{K}_a$  performs best during the first 6 s but overall the models  $\mathbf{K}_b$  and  $\mathbf{K}_c$  perform best. In Table 2, the mean value  $\mu_{u_1}$  and standard deviation  $\sigma_{u_1}$  of the normalized response for  $t \geq 2$  s are shown for the three models with and without the quasi-static contribution. From here, it can be concluded that the best overall results are obtained by using eigenmodes derived from a nominal operating situation and inclusion of the quasi-static contribution. In Fig. 6a, the Lagrange multiplier for the displacement constraint between the blade and shaft substructure in the  $\bar{x}_1$ -direction is shown for the FE-model. Here, it is shown that the constraint ends at approximately  $P_0$  at  $t = 10$  s and has a mean value of approximately  $1.35 \times 10^5$  N for  $t > 10$  s corresponding to the applied load. In Fig. 6b, the normalized constraint by using the  $\mathbf{K}_c$  model is presented with the quasi-static contribution. This variation has a higher frequency than the response and is centered around the results from the FE-model. Almost no difference is visible by using the three models  $\mathbf{K}_a$ ,  $\mathbf{K}_b$ , and  $\mathbf{K}_c$ . This is also presented in Table 2 with the mean and standard deviation of the normalized constraints. The only components entering the constraints are from the rigid body modes which are the same no matter which model is used. Therefore, the only difference is through the quasi-static contribution in the loading term (47) which has very little influence.



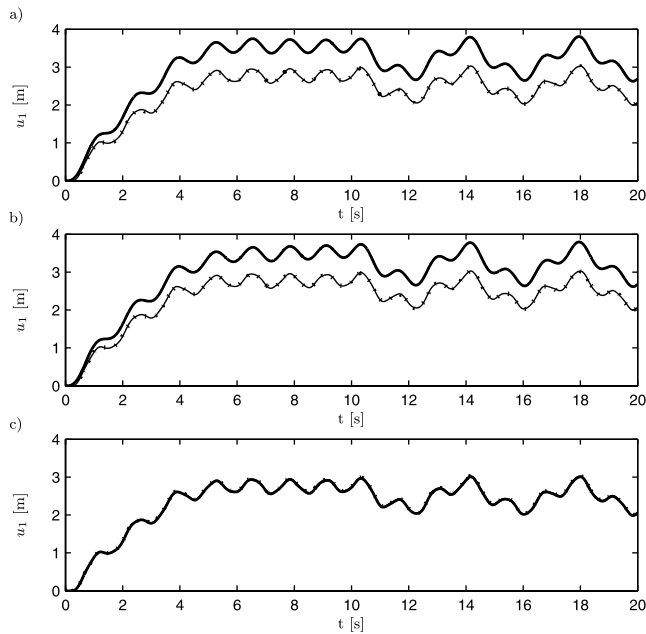


**Fig. 7** Tip response with (.....) and without (—) the quasi-static contribution compared to the FE-model (—). Number of dynamical modes: (a) 1; (b) 2; (c) 3

### 5.3 Quasi-static contribution by using 1, 2, and 3 dynamical modes

In the previous section, it is shown that it has little influence which of the models  $\mathbf{K}_a$ ,  $\mathbf{K}_b$ , and  $\mathbf{K}_c$  are used. In this section, it is examined if fewer than 3 dynamical modes based on the  $\mathbf{K}_c$  eigenmodes can be used to give fair results compared to the FE-model. The importance of the quasi-static contribution is also examined, where all the modes except the rigid body and dynamical modes are assumed to respond quasi-static. In Fig. 7, the tip displacement by using 1, 2, and 3 dynamical modes with and without the quasi-static contribution is compared to the FE-model. Here, it appears that by using 1 or 2 dynamical modes, Fig. 7a and Fig. 7b, respectively, without the quasi-static contribution results in considerably larger deflections compared to the FE-model. However, by inclusion of the quasi-static contribution, the response is very much similar to the FE-model and almost identical by using 2 dynamical modes. The reason for getting these good results by using only 1 dynamical mode is because the load applied is only in the blade direction. By using a detailed load model, the number of necessary dynamical modes will probably rise to at least two. Using 3 dynamical modes, Fig. 7c, it appears that the quasi-static contribution has very little influence which also is shown in Fig. 5. It is previously shown that it has little to none effect on the constraints if the quasi-static contribution is included. By using 1, 2, and 3 dynamical modes, the deviations from the constraint obtained from the FE-model are very small. In Table 3, the mean and standard deviation are shown for the normalized response and normalized constraints by using 1, 2, and 3 dynamical modes. For the constraint, it is shown that the number of dynamical modes only is visible in the standard deviation.

**Table 3** Mean value and standard deviation, denoted by  $\mu$  and  $\sigma$ , respectively, of the normalized response and normalized constraint. In both cases, the data for  $t \geq 2$  s is used and index  $n_d$  denotes the number of dynamical modes

	$\mu_{u_1}$	$\sigma_{u_1}$	$\mu_\lambda$	$\sigma_\lambda$
$n_d = 1, \mathbf{U}_1 = \mathbf{0}$	1.276	0.018	1.000	0.014
$n_d = 2, \mathbf{U}_1 = \mathbf{0}$	1.261	0.026	1.000	0.014
$n_d = 3, \mathbf{U}_1 = \mathbf{0}$	0.993	0.002	1.000	0.004
$n_d = 1, \mathbf{U}_1 \neq \mathbf{0}$	0.999	0.005	1.000	0.014
$n_d = 2, \mathbf{U}_1 \neq \mathbf{0}$	0.999	0.004	1.000	0.014
$n_d = 3, \mathbf{U}_1 \neq \mathbf{0}$	1.001	0.001	1.000	0.004

## 6 Conclusions

In this paper, it is shown how to reduce a blade substructure in a multibody formulation where the body is able to move away from the moving frame of reference. This is done by describing the displacement field by Ritz bases consisting of rigid body and elastic fixed-base eigenmodes. Moreover, the quasi-static contribution from the truncated elastic modes is included in the formulation. Based on the numerical examples during start-up and nominal operation, it is shown that it has little influence if the elastic modes are obtained from a situation where the wind turbine is stopped or from a situation where the wind turbine operates at the nominal angular velocity. Hereby, the same mode shapes can be used for a wide operating area without losing much accuracy. By using a concentrated load, almost an identical response is obtained by only using 2 dynamical modes with the quasi-static contribution compared to the full FE-model. However, for a detailed load model, more dynamical modes will probably be necessary. By inclusion of 3 dynamical elastic modes, the quasi-static contribution has no longer an important effect on the response. The displacement constraint between the blade and rotor shaft substructure is also close to the FE-model by only using 2 dynamical mode. However, the quasi-static contribution has little to no effect on the constraints, so for a higher accuracy, more dynamical modes are necessary.

**Acknowledgements** This work has been supported by the Danish Council for Strategic Research through the project "Nonlinear Multibody Dynamics of Wind Turbines."

## References

1. Craig, R.R. Jr.: Coupling of Substructures for Dynamic Analysis: An Overview. Collection of Technical Papers—AIAA/ASME/ASCE/AHS/ASC Structures, Structural Dynamics and Materials Conference, vol. 5, pp. 3–14 (2000)
2. Hurty, W.C.: Dynamic analysis of structural systems using component modes. *AIAA J.* **3**(4), 678–685 (1965)
3. Rubin, S.: Improved component-mode representation for structural dynamic analysis. *AIAA J.* **13**(8), 995–1006 (1975)
4. MacNeal, R.H.: A hybrid method of component mode synthesis. *Comput. Struct.* **1**(4), 581–601 (1971)
5. Preumont, A.: Vibration Control of Active Structures, an Introduction, 2nd edn. Kluwer Academic, Amsterdam (2002)
6. Nikravesh, P.E.: Computer-Aided Analysis of Mechanical Systems. Prentice-Hall, New York (1988)
7. de Jalón, J.G., Bayo, E.: Kinematic and Dynamic Simulations of Multibody Systems—The Real-Time Challenge. Springer, Berlin (1993)
8. Géradin, M., Cardona, A.: Flexible Multibody Dynamics—A Finite Element Approach. Wiley, New York (2001)
9. Shabana, A.A.: Dynamics of Multibody Systems, 3rd edn. Cambridge University Press, Cambridge (2005)

10. Shabana, A.A.: Substructure synthesis methods for dynamic analysis of multi-body systems. *Comput. Struct.* **20**(4), 737–744 (1985)
11. Lee, J.-H.: On the application of the modal integration method to flexible multibody systems. *Comput. Struct.* **59**(3), 553–559 (1996)
12. Pan, W., Mao, S., Haug, E.J., Solis, D.: Efficient modal approach for flexible multibody dynamic simulation. *Mech. Based Des. Struct. Mach.* **31**(1), 1–23 (2003)
13. Khulief, Y.A., Mohiuddin, M.A.: On the dynamic analysis of rotors using modal reduction. *Finite Elements Anal. Des.* **26**(1), 41–55 (1997)
14. Bauchau, O.A., Rodriguez, J.: Formulation of modal-based elements in nonlinear, flexible multibody dynamics. *J. Multiscale Comput. Eng.* **1**(2), 161–179 (2003)
15. Bauchau, O.A., Rodriguez, J., Chen, S.-Y.: Coupled rotor-fuselage analysis with finite motions using component mode synthesis. *J. Am. Helicopter Soc.* **49**(2), 201–211 (2004)
16. Kawamoto, A., Inagaki, M., Aoyama, T., Yasuda, K.: Vibration of Moving Flexible Bodies (Formulation of Dynamics by using Normal Modes and a Local Observer Frame). *Proceeding of DETC99/VIB-8232* (1999)
17. Kawamoto, A., Krenk, S., Suzuki, A.: Flexible body dynamics in a freely floating local frame. In: *EC-COMAS Conference on Multibody Dynamics*, Milan, 25–28 June (2007)
18. Kawamoto, A., Suzuki, A., Inagaki, M., Krenk, S.: Flexible-body dynamics in a floating frame with extraction of rigid body motion. In: *4th Asian Conference on Multibody Dynamics*, ACMD 2008, Jeju, Korea, August 20–23 (2008)
19. Kawamoto, A., Krenk, S., Suzuki, A., Inagaki, M.: Flexible body dynamics in a local frame of reference with explicitly predicted motion. *Int. J. Numer. Meth. Eng.* (2008)
20. Krenk, S.: Non-linear modelling and analysis of structures and solids. Lecture notes. Department of Mechanical Engineering, Technical University of Denmark (2005)
21. Géradin, M., Rixen, D.: *Mechanical Vibrations: Theory and Application to Structural Dynamics*, 2nd edn. Wiley, New York (1997)
22. Larsen, J.W., Nielsen, S.R.K.: Non-linear dynamics of wind turbine wings. *J. Non-Linear Mech.* **41**(5), 629–643 (2006)



---

**APPENDIX E**  
**Paper: A Component Mode**  
**Synthesis Algorithm for**  
**Multibody Dynamics of Wind**  
**Turbines**

---





Contents lists available at ScienceDirect

## Journal of Sound and Vibration

journal homepage: [www.elsevier.com/locate/jsv](http://www.elsevier.com/locate/jsv)

# A component mode synthesis algorithm for multibody dynamics of wind turbines

K. Holm-Jørgensen\*, S.R.K. Nielsen<sup>1</sup>

Department of Civil Engineering, Aalborg University, Sohngaardsholmsvej 57, DK-9000 Aalborg, Denmark

## ARTICLE INFO

### Article history:

Received 29 September 2008

Received in revised form

4 May 2009

Accepted 6 May 2009

Handling Editor: M.P. Cartmell

## ABSTRACT

A system reduction scheme related to a multibody formulation of wind turbine dynamics is devised. Each substructure is described in its own frame of reference, which is moving freely in the vicinity of the moving substructure, in principle without any constraints to the rigid body part of the motion of the substructure. The system reduction is based on a component mode synthesis method, where the response of the internal degrees of freedom of the substructure is described as the quasi-static response induced by the boundary degrees of freedom via the constraint modes superimposed in combination to a dynamic component induced by inertial effects and internal loads. The latter component is modelled by a truncated modal expansion in fixed interface undamped eigenmodes. The selected modal vector base for the internal dynamics ensures that the boundary degrees of freedom account for the rigid-body dynamics of the substructure, and explicitly represent the coupling degrees of freedom at the interface to the adjacent substructures. The method has been demonstrated for a blade structure, which has been modelled as two substructures. Two modelling methods have been examined where the first is by use of fixed–fixed eigenmodes for the innermost substructure and fixed–free eigenmodes for the outermost substructure. The other approach is by use of fixed–free eigenmodes for both substructures. The fixed–fixed method shows good correspondence with the full FE model which is not the case for the fixed–free method due to incompatible displacements and rotations at the interface between the two substructures. Moreover, the results from the reduced model by use of constant constraint modes and constant fixed interface modes over a large operating area for the wind turbine blade are almost identical to the full FE model.

© 2009 Elsevier Ltd. All rights reserved.

## 1. Introduction

Flexible multibody based simulations of the dynamic behaviour of a wind turbine requires a discretization in space for each substructure of the system. Typically, this is done by an FE method, often involving many degrees of freedom for each substructure. In order to reduce the computational effort, reduced order models of the substructures need to be implemented. Especially, this is necessary in stochastic analyses based on Monte Carlo simulations, or during the design phase of a wind turbine, where multiple load cases need to be analysed. A reduced order model is also necessary in some active vibration control algorithms, where the structural model must be processed in real time. Due to the geometric

\* Corresponding author.

E-mail addresses: [khj@civil.aau.dk](mailto:khj@civil.aau.dk) (K. Holm-Jørgensen), [soren.nielsen@civil.aau.dk](mailto:soren.nielsen@civil.aau.dk) (S.R.K. Nielsen).

<sup>1</sup> Tel.: +45 99 40 84 51; fax: +45 98 14 25 55.

complexity of the blades, which otherwise requires many elements to model, the system reduction in this paper is focused on the blades.

The basic idea of flexible multibody dynamics is to introduce a moving frame of reference to each substructure. Relative to the moving frame elastic displacements are relatively small, rendering linear analysis possible. Hence, nonlinearities are confined to the description of the moving frame. This is defined by a position vector and a parameter vector, also known as a pseudovector, defining the origin and rotation of the moving frame relative to a fixed frame of reference. The standard formulation of multibody methods requires that there is no rigid-body motion between the substructure and its moving frame. In Agrawal and Shabana [1] an automated method is derived to eliminate the rigid-body motion of the body relative to the moving frame. This is done by imposing reference conditions by use of a boolean matrix on the shape functions whereby the deformation modes become consistent with the boundary conditions. In Shabana [2] it is demonstrated that two sets of deformation modes associated with two different sets of boundary conditions e.g. simply supported and free-free can be used to obtain the same solution provided that the moving frame is properly selected. The position and orientation of the moving frame is defined by a set of Lagrangian coordinates that describe the rigid-body translation and rotation. Hereby, these coordinates become a part of the degrees of freedom of the multibody system, see e.g. Nikravesh [3], García and Bayo [4], G  radin and Cardona [5] and Shabana [6]. The use of such a mixed set of referential and elastic coordinates leads to highly nonlinear system equations. Further, as a result of the inertial coupling between the said degrees of freedom the mass matrix depends on the referential coordinates, even when formulated in the moving frame. To circumvent these difficulties Kawamoto et al. [7–10] suggested to let the moving frame of reference float in a controlled way relative to the moving substructure, so these are always sufficiently close to each other, in order for the small displacement assumption to be fulfilled. Hereby, the system matrices do not depend on the generalized coordinates by explicitly predicting the rigid-body motion. To reduce or eliminate the gap between the predicted and actual motion, it is necessary to regularly update the motion of the moving frame of reference as demonstrated in Kawamoto et al. [10]. The main difference to the multibody formulation described in Agrawal and Shabana [1] and Shabana [2] is that the parameters for the moving frame do not enter as degrees of freedom in the system state vector and that it is possible for the body to have a small rigid-body displacement relative to the moving frame. In Kawamoto et al. [7] the updating scheme is originally described, where the orientation, angular velocity, and angular acceleration of the moving frame are updated based on a local triad linked to four nodes in the body. In Kawamoto et al. [8] the local triad is updated based on a polar decomposition. In Kawamoto et al. [9,10] rigid-body modes are used to update the motion of the moving frame. In a previous paper by the present authors [11] the same approach as described in Kawamoto et al. [8] by using a freely moving frame in a multibody formulation is adopted. Here, the wind turbine blade is modelled by only one multibody and reduced by a Ritz bases consisting of rigid-body and elastic fixed-base eigenmodes. Moreover, the quasi-static contribution from the truncated elastic modes is included in the formulation. In order to get a better description of the large nonlinear displacements of a wind turbine blade it is necessary to include more than one multibody in the blade. The purpose of the present paper is to demonstrate a general approach for including an arbitrary number of reduced multibodies to model e.g. a wind turbine blade. The updating scheme of the moving frame of reference in the present paper follows the same principles as described in Kawamoto et al. [8]. A small change when updating the moving frame is presented, where the orientation of the moving frame is updated based on the motion of two boundary nodes. It is possible to use other nodes than the boundary nodes in the updating procedure. The selected updating nodes may even be shifted during a numerical simulation, if this is considered favourable in reducing the displacements of the substructure relative to the moving frame. It should be noticed that possible geometrical nonlinear elastic deformations may be further reduced or removed by subdividing the considered substructure.

The following outline presumes a partitioning of the degrees of freedom of the substructure in the boundary degrees at the interface to the adjacent substructures and the remaining interior degrees of freedom. Static condensation proposed by Guyan [12] completely ignores dynamics of the interior degrees of freedom, which are described as a linear function of the boundary degrees of freedom. Hence, the substructure is completely described by the boundary degrees of freedom. It is well-known that this method in principle is a Ritz method, and hence leads to an overestimation of the natural frequencies, see e.g. Bathe [13]. The so-called dynamic condensation method, proposed by Leung [14–16], Petersmann [17] and others, is an extension of the static condensation method in the sense that a few boundary degrees of freedom are kept and the remaining interior degrees of freedom are eliminated in terms of these. Contrary to static condensation, the condensation matrix contains inertial and damping terms for the interior degrees of freedom and thereby time derivatives of these, which make iterations necessary. Often the Guyan reduction is used in the first iteration. Variants of the iterative methods have been given in [18–21]. In the present paper no iterations are performed in the condensation matrix. The method resembles the specific realization of the component mode synthesis (CMS) method known as the constraint-mode method, which consists of rigid-body modes, constraint modes and fixed interface normal modes to describe the interior dynamics, Hurty [22,23]. Constraint modes are defined as static deformation modes, where the substructure is free of internal loads, and where each boundary degree of freedom in turn is given a unit displacement with the remaining boundary degrees of freedom fixed. Hence, these modes represent the modes available in static condensation. The fixed interface normal modes representing the interior dynamics are determined from the generalized eigenvalue problem of the internal degrees of freedom. Craig and Bampton [24] simplified the approach considerably by treating rigid-body modes as a special case of constraint modes. The method in the present paper is based on this Craig–Bampton method.



Ambrósio and Gonçalves [25] used a traditional multibody formulation with a mixed set of reference and elastic coordinates. The elastic coordinates were later described by a reduced number of fixed interface modal coordinates. Shanmugan and Padmanabhan [26] have described a hybrid fixed-free CMS method for rotordynamic analysis which showed better accuracy than the traditional fixed-fixed and free-free methods. The reason for this is that the boundary displacements in this case represent the exact coupling degrees of freedom, unaffected by the interior dynamics. This compatibility is also achieved by the method in the present paper, and its importance is demonstrated by modelling the blade by two substructures both by use of fixed-free eigenmodes. Hereby, compatibility at the assembling point between the two substructures is not fulfilled, except for a large number of included eigenmodes. Moreover, the purpose in this paper is to demonstrate that constant constraint modes and constant fixed interface normal modes can be used over a wide operating area, where the wind turbine blade speeds up from a stopped situation to its nominal operating situation.

## 2. Moving frame of reference formulation of multibody dynamics

The idea is to describe the motion of a substructure in a  $(x_1, x_2, x_3)$ -coordinate system, which is freely moving in the vicinity of the substructure. Further, a fixed  $(\bar{x}_1, \bar{x}_2, \bar{x}_3)$ -coordinate system is introduced common for all substructures. Accordingly, fixed frame and moving frame components of vectors and tensors will be indicated with and without a bar, respectively. The origin of the moving coordinate system is described by a position vector with the global components  $\bar{\mathbf{x}}_c$ , and its rotation is determined by the parameter vector (or pseudovector)  $\boldsymbol{\theta}$ . The angular velocity and angular acceleration vectors of the moving frame are specified by their moving frame components  $\boldsymbol{\omega}$  and  $\boldsymbol{\alpha}$ , respectively. Generally, the substructure may drift away from the moving frame, which requires sequential updating of the position, velocity and acceleration of the origin together with the rotation, angular velocity and angular acceleration vectors to ensure small displacement components of the substructure relative to the moving frame, but also for the gyroscopic loads on the substructure to be determined with a satisfying accuracy. The essential point is that the degrees of freedom for the substructure and the parameters defining the moving frame are independently specified. Therefore, it is possible to have rigid-body displacements of the body relative to the moving frame. This gap should be sufficiently small in order for the small displacement assumption to be fulfilled. The gap can be reduced or eliminated by updating the motion of the moving frame iteratively. At time  $t = t_j$  the position of a substructure and its belonging moving frame of reference are illustrated in Fig. 1a.  $\mathbf{s}$  is a position vector along the moving  $x_3$ -axis, identifying a given cross-section of the beam, and  $\mathbf{u}(\mathbf{s}, t)$  is the moving coordinates of the displacement field for the centroid of the cross-section.  $\mathbf{u}(\mathbf{s}, t)$  is determined by shape functions in the FE model and mode shapes in the reduced model, both with corresponding generalized coordinates  $\mathbf{y}(t)$  and  $\mathbf{w}(t)$ , respectively. Figs. 1b and c display various possibilities for updating the position of the moving frame of reference relative to the moving beam-like substructure at the time  $t_{j+1} = t_j + \Delta t$  where  $\Delta t$  denotes the elapsed time step. Figs. 1b and c show the cases, where the motion at one and two boundary nodes, respectively, will be used to update the parameters for the moving frame. The latter will in most cases reduce the displacements of the substructure from the moving frame compared to only using one boundary node in the update. Because the moving frame of reference parameters enter the equations of motion it is necessary to iteratively update these parameters together with the motion of the substructure, which will be described in a later section.

First, the equations of motion for a constrained multibody system are described. The position vector to a material point within the substructure has the following moving and fixed frame components:

$$\mathbf{x}(\mathbf{s}, t) = \mathbf{s} + \mathbf{u}(\mathbf{s}, t) \quad (1)$$

$$\bar{\mathbf{x}}(\mathbf{s}, t) = \bar{\mathbf{x}}_c + \mathbf{R}(\mathbf{s} + \mathbf{u}(\mathbf{s}, t)) \quad (2)$$

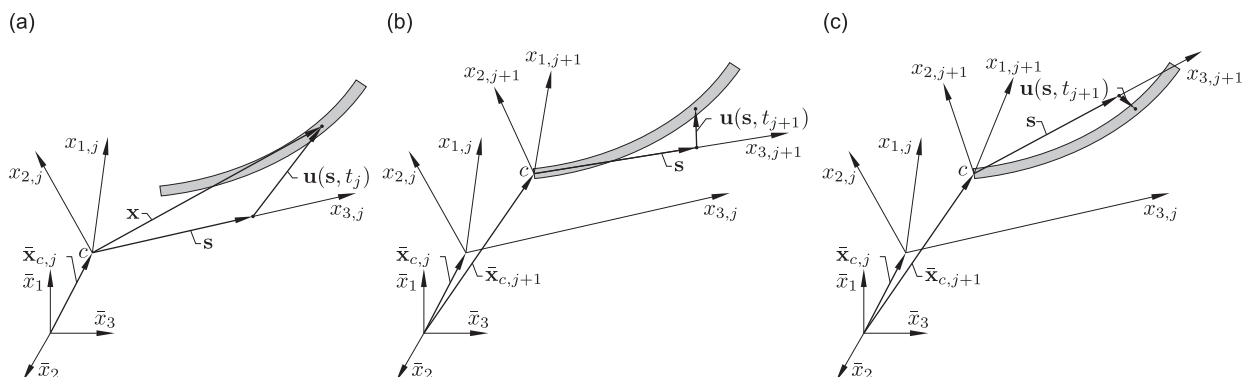


**Fig. 1.** (a) A substructure and the belonging moving frame of reference at time  $t = t_j$ . At time  $t_{j+1} = t_j + \Delta t$  the moving frame of reference has been updated based on: (b) the motion of one boundary node; (c) the motion of both boundary nodes.

where  $\mathbf{R}$  stores the components of the rotation tensor related to the moving frame.  $\mathbf{R}$  is defined by the pseudovector  $\boldsymbol{\theta}$  as given by the Rodriguez formula, see e.g. Shabana [6]

$$\mathbf{R} = \cos \theta \mathbf{I} + (1 - \cos \theta) \mathbf{n} \mathbf{n}^T + \sin \theta \hat{\mathbf{n}} \quad (3)$$

where  $\mathbf{n} = \boldsymbol{\theta}/|\boldsymbol{\theta}|$  is the rotation unit vector.  $\mathbf{n} \mathbf{n}^T$  is the outer product of this vector with itself, and  $\hat{\mathbf{n}}$  is the spin matrix related to  $\mathbf{n}$ .  $\hat{\mathbf{n}}$  is given as

$$\hat{\mathbf{n}} = \begin{bmatrix} 0 & -n_3 & n_2 \\ n_3 & 0 & -n_1 \\ -n_2 & n_1 & 0 \end{bmatrix} \quad (4)$$

$[n_1, n_2, n_3]$  specify the components of  $\mathbf{n}$ . These are the same in the fixed and the moving coordinate systems. The corresponding moving frame components of the velocity and acceleration vector of the material point become

$$\mathbf{v} = \mathbf{v}_c + \tilde{\omega}(\mathbf{s} + \mathbf{u}) + \dot{\mathbf{u}} \quad (5)$$

$$\mathbf{a} = \mathbf{a}_c + (\tilde{\alpha} + \tilde{\omega}\tilde{\omega})(\mathbf{s} + \mathbf{u}) + 2\tilde{\omega}\dot{\mathbf{u}} + \ddot{\mathbf{u}} \quad (6)$$

where  $\boldsymbol{\alpha} = \dot{\boldsymbol{\omega}}$ .  $\tilde{\omega}$  and  $\tilde{\alpha}$  denote the spin matrices in moving coordinates related to  $\boldsymbol{\omega}$  and  $\boldsymbol{\alpha}$ . The first term  $\mathbf{v}_c$  in Eq. (5) is the translational velocity of the moving frame, the second term  $\tilde{\omega}(\mathbf{s} + \mathbf{u})$  is the rotational velocity, and the last term  $\dot{\mathbf{u}}$  stores the moving coordinates of the velocity from elastic deformations and rigid-body motions inside the moving frame. The first term  $\mathbf{a}_c$  in Eq. (6) denotes the translational acceleration of the moving frame origin. The term  $\tilde{\alpha}(\mathbf{s} + \mathbf{u})$  is the angular acceleration which is orthogonal on  $\boldsymbol{\alpha}$  and  $(\mathbf{s} + \mathbf{u})$ . The next term  $\tilde{\omega}\tilde{\omega}(\mathbf{s} + \mathbf{u}) = \boldsymbol{\omega} \times (\boldsymbol{\omega} \times (\mathbf{s} + \mathbf{u}))$  describes the centrifugal acceleration. The Coriolis acceleration in moving coordinates is described by  $2\tilde{\omega}\dot{\mathbf{u}}$  which is perpendicular to both the direction of the velocity of the moving body and to the rotation axis. Finally, the term  $\ddot{\mathbf{u}}$  describes the moving frame components of the acceleration of the material point as seen by an observer in the moving frame. Based on an FE discretization the local displacement field for a beam element is interpolated in the form

$$\begin{aligned} \mathbf{u}_{el}(\mathbf{s}_{el}, t) &= \mathbf{N}_{el}(\mathbf{s}_{el}) \mathbf{y}_{el}(t) \\ \mathbf{N}_{el}(\mathbf{s}_{el}) &= \begin{bmatrix} N_2 & 0 & 0 & 0 & N_3 & 0 & N_5 & 0 & 0 & 0 & N_6 & 0 \\ 0 & N_2 & 0 & -N_3 & 0 & 0 & 0 & N_5 & 0 & -N_6 & 0 & 0 \\ 0 & 0 & N_1 & 0 & 0 & 0 & 0 & 0 & N_4 & 0 & 0 & 0 \end{bmatrix} \\ N_1 &= 1 - \xi, \quad N_2 = 2\xi^3 - 3\xi^2 + 1, \quad N_3 = (\xi^3 - 2\xi^2 + \xi)L_{el} \\ N_4 &= \xi, \quad N_5 = -2\xi^3 + 3\xi^2, \quad N_6 = (\xi^3 - \xi^2)L_{el} \end{aligned} \quad (7)$$

$\xi = s_{el}/L_{el}$  is a dimensionless interpolation parameter where  $s_{el}$  is a local reference length from the beginning  $s_{el} = 0$  to the end  $s_{el} = L_{el}$  of the element and  $L_{el}$  is the reference length of the beam element.  $\mathbf{y}_i(t)$  is the degrees of freedom of the FE model of the substructure  $i$ . In a beam model they represent the moving coordinates of the nodal displacements and rotations relative to the moving frame of reference and  $\mathbf{N}_i(\mathbf{s})$  is an interpolation matrix. The equations of motion of the substructure  $i$  are conveniently derived using analytical mechanics using an extended Lagrangian to account for the kinematic constraints, in combination with the kinetic energy  $T = T(\mathbf{y}_i, \dot{\mathbf{y}}_i)$  and the potential energy  $U = U(\mathbf{y}_i)$  from all substructures. The latter contains contributions from the strain energy and conservative external loads  $\mathbf{Q}_{c,i}(\mathbf{y}_i)$  such as gravity, in addition to vectorial quantities as the non-conservative loads  $\mathbf{Q}_{nc,i}(\mathbf{y}_i)$ . In principle, these loads may be linearized in the applied moving frame of reference. The non-conservative loads are caused by the follower character of the aerodynamic loads. The kinetic energy is most convenient determined by use of the moving frame components of the velocity vector  $\mathbf{v}$  from Eq. (5). In a slightly modified version of those given by Kawamoto et al. [8] the resulting equations become

$$\begin{aligned} \mathbf{M}_i \ddot{\mathbf{y}}_i + (\mathbf{C}_{0,i} + 2\mathbf{G}_i) \dot{\mathbf{y}}_i + (\mathbf{K}_{e,i} + \dot{\mathbf{G}}_i + \mathbf{D}_i + \mathbf{K}_{g,i}) \mathbf{y}_i + \mathbf{B}_i^T(\mathbf{y}_i) \tilde{\boldsymbol{\lambda}}_i \\ = -\mathbf{M}_{0,i}^T \mathbf{a}_{c,i} - \mathbf{J}_{0,i}^T + \mathbf{J}_{2,i}^T + \mathbf{Q}_{c,i}(\mathbf{y}_i) + \mathbf{Q}_{nc,i}(\mathbf{y}_i) \end{aligned} \quad (8)$$

where the Lagrange multipliers  $\tilde{\boldsymbol{\lambda}}_i$  contain the global components of the reaction forces and moments conjugated to the kinematic constraints and  $\mathbf{B}_i^T(\mathbf{y}_i)$  is the constraint matrix. Because the constraints have been formulated in the fixed frame of reference the components of  $\tilde{\boldsymbol{\lambda}}$  are also in the fixed frame. The symmetric matrices  $\mathbf{C}_{0,i}$  and  $\mathbf{K}_{e,i}$  denote the structural damping and elastic stiffness matrix, respectively. The latter includes bending, torsional, and axial stiffnesses.  $\mathbf{K}_{g,i}$  denotes the geometrical stiffness matrix. For a beam-like substructure of the length  $L$  this may be written as

$$\mathbf{K}_{g,i} = \Omega^2(t) \int_L Q_3(x_3, t) \frac{d\mathbf{N}_{g,i}^T}{dx_3} \frac{d\mathbf{N}_{g,i}}{dx_3} dx_3 \quad (9)$$

where  $Q_3(x_3, t)$  represents the distribution of the centrifugal axial force for  $\Omega = 1$ , so  $\Omega^2(t)Q_3(x_3, t)$  denotes the axial force at the position  $x_3$ .  $\mathbf{N}_{g,i}$  includes the two first rows in  $\mathbf{N}_i$  which represent the two displacement components orthogonal to the beam axis. For a wind turbine blade the axial load is caused by the centrifugal and gravity forces. During operation the

geometric stiffness from the centrifugal axial force will assist to stretch out the blade corresponding to an increased stiffness and thereby reduce the displacements in the flap direction. Moreover, this term has shown to increase the stability of the numerical model. The other matrices and vectors are defined as

$$\mathbf{M}_i = \int_L \mathbf{N}_i^T \mathbf{N}_i \mu \, dx_3, \quad \mathbf{M}_{0,i} = \int_L \mathbf{N}_i \mu \, dx_3, \quad \mathbf{D}_i = \int_L \mathbf{N}_i^T \tilde{\omega}_i \tilde{\omega}_i \mathbf{N}_i \mu \, dx_3 \quad (10)$$

$$\mathbf{G}_i = \int_L \mathbf{N}_i^T \tilde{\omega}_i \mathbf{N}_i \mu \, dx_3, \quad \mathbf{J}_{0,i} = \omega_i^T \int_L \mathbf{s} \mathbf{N}_i \mu \, dx_3, \quad \mathbf{J}_{2,i} = \omega_i^T \int_L \mathbf{s} \tilde{\omega}_i \mathbf{N}_i \mu \, dx_3 \quad (11)$$

$$\dot{\mathbf{G}}_i = \int_L \mathbf{N}_i^T \dot{\tilde{\omega}}_i \mathbf{N}_i \mu \, dx_3, \quad \dot{\mathbf{J}}_{0,i} = \dot{\omega}_i^T \int_L \mathbf{s} \mathbf{N}_i \mu \, dx_3 \quad (12)$$

$\mathbf{M}_i$  is the conventional symmetric mass matrix of the body in the moving frame of reference, which in the present formulation is independent of the moving frame of reference parameters.  $\mu = \mu(\mathbf{s})$  denotes the mass per unit length.  $\mathbf{M}_{0,i}$  is a matrix representing the inertial effect of uniform translation. The effect of centrifugal forces due to elastic deformations is contained in the symmetric matrix  $\mathbf{D}_i$  and the gyroscopic forces are represented by the skew symmetric matrix  $\mathbf{G}_i$ . The remaining  $\mathbf{J}_{0,i}$  and  $\mathbf{J}_{2,i}$  terms are couplings between the reference position and the shape functions. In Kawamoto et al. [10] it is shown how  $\mathbf{D}_i$ ,  $\mathbf{G}_i$ , and  $\dot{\mathbf{G}}_i$  can be simplified by extracting  $\tilde{\omega}_i$  and  $\dot{\tilde{\omega}}_i$  outside the integration for isoparametric volume elements. For ease the nonlinearity displayed by the dependency of  $\mathbf{y}_i$  in the load vector is neglected, whereby the equations of motion conveniently are written in the form

$$\mathbf{M}_i \ddot{\mathbf{y}}_i + \mathbf{C}_i \dot{\mathbf{y}}_i + \mathbf{K}_i \mathbf{y}_i + \mathbf{B}_i^T(\mathbf{y}_i) \bar{\lambda}_i = \mathbf{f}_i(t) \quad (13)$$

where

$$\mathbf{C}_i = \mathbf{C}_{0,i} + 2\mathbf{G}_i, \quad \mathbf{K}_i = \mathbf{K}_{e,i} + \dot{\mathbf{G}}_i + \mathbf{D}_i + \mathbf{K}_{g,i} \quad (14)$$

$$\mathbf{f}_i(t) = -\mathbf{M}_{0,i}^T \mathbf{a}_{c,i} - \dot{\mathbf{J}}_{0,i}^T + \mathbf{J}_{2,i}^T + \mathbf{Q}_{c,i} + \mathbf{Q}_{nc,i} \quad (15)$$

$\mathbf{C}_i$  and  $\mathbf{K}_i$  may be interpreted as resulting non-symmetric damping and stiffness matrices for the unconstrained substructure.

To set up the equations of motion for a multibody system it is necessary to introduce kinematical constraints in order to incorporate compatibility of the mutual displacements and rotations of the substructures. In relation to wind turbines, displacement constraints between the rotor shaft and the nacelle are specified at the bearings of the nacelle. Rotational constraints are e.g. prescribed between the rotor shaft and the blade substructure in terms of a controlled pitch angle. The kinematic constraints are vector relations with components, which need to be defined in a common coordinate system e.g. a global fixed coordinate system or the moving frame of reference of one of the substructures. The following constraint equations can be generalized to an arbitrary number of constraints and substructures, but are here shown for two adjacent substructures. Below,  $\mathbf{s}_{1,0}$  and  $\mathbf{s}_{2,0}$  denote the referential position vectors in the respective moving frames, defining a point in substructures 1 and 2 at which a kinematical displacement constraint is specified, and  $\mathbf{u}_{1,0}$  and  $\mathbf{u}_{2,0}$  are the corresponding displacement vectors. A displacement constraint which fixes the position of two arbitrary points in the substructures 1 and 2 becomes, cf. Eq. (2)

$$\begin{aligned} \Phi_{dc} &= \bar{\mathbf{x}}_{c1} + \mathbf{R}_1(\mathbf{s}_{1,0} + \mathbf{u}_{1,0}) - (\bar{\mathbf{x}}_{c2} + \mathbf{R}_2(\mathbf{s}_{2,0} + \mathbf{u}_{2,0})) \\ &= \bar{\mathbf{x}}_{c1} + \mathbf{R}_1(\mathbf{s}_{1,0} + \mathbf{N}_{1,0} \mathbf{y}_1) - (\bar{\mathbf{x}}_{c2} + \mathbf{R}_2(\mathbf{s}_{2,0} + \mathbf{N}_{2,0} \mathbf{y}_2)) \\ &= \mathbf{B}_{d,1} \mathbf{y}_1 - \mathbf{B}_{d,2} \mathbf{y}_2 - \mathbf{b} = \mathbf{0} \end{aligned} \quad (16)$$

$$\mathbf{B}_{d,i} = \mathbf{R}_i \mathbf{N}_{i,0}, \quad \mathbf{b} = -(\bar{\mathbf{x}}_{c1} + \mathbf{R}_1 \mathbf{s}_{1,0}) + (\bar{\mathbf{x}}_{c2} + \mathbf{R}_2 \mathbf{s}_{2,0})$$

In an FE formulation, where  $\mathbf{u}_i(\mathbf{s}_i, t)$  is interpolated by a set of shape functions  $\mathbf{N}_i(\mathbf{s}_i)$  and degrees of freedom  $\mathbf{y}_i(t)$ ,  $\mathbf{u}_{i,0}(t) = \mathbf{N}_{i,0} \mathbf{y}_i(t)$ , where  $\mathbf{N}_{i,0} = \mathbf{N}_i(\mathbf{s}_{i,0})$ . Further,  $\mathbf{R}_1$  and  $\mathbf{R}_2$  represent the rotation tensors of the moving frames relative to the global coordinate system. Let  $\phi_{i,0}$  denote the local rotation components of the interface node relative to the moving frame of substructure  $i$ . The rotation tensor of the said node is then given by

$$\mathbf{R}_i^* = \mathbf{R}_i \mathbf{R}(\phi_{i,0}) \simeq \mathbf{R}_i (\mathbf{I} + \hat{\phi}_{i,0}) \quad (17)$$

where the indicated linearization presumes  $|\phi_{0,i}| \ll 1$ . Let  $\mathbf{n}_1$  and  $\mathbf{n}_2$  be the local components in the moving coordinate systems of unit vectors attached to the interface nodes in substructures 1 and 2. The rotation of these vectors is given as  $\mathbf{R}_1^* \mathbf{n}_1$  and  $\mathbf{R}_2^* \mathbf{n}_2$ , respectively. Assume that the vectors before and during the elastic deformation of the interface nodes remain orthogonal. Then the rotational constraint can be specified as

$$\Phi_{rc} = (\mathbf{R}_1^* \mathbf{n}_1)^T \mathbf{R}_2^* \mathbf{n}_2 = 0 \quad (18)$$

A total of three scalar products are necessary to fix the rotations in the joint. In the following derivations, focus is on a fixed interface where the unit vectors are orthogonal throughout the simulations. By insertion of Eq. (17) in Eq. (18) the

rotational constraint becomes

$$\begin{aligned}\Phi_{rc} &= \mathbf{n}_2^T \mathbf{R}_2^T \mathbf{R}_1 \tilde{\mathbf{n}}_1 \boldsymbol{\varphi}_{1,0} + \mathbf{n}_1^T \mathbf{R}_1^T \mathbf{R}_2 \tilde{\mathbf{n}}_2 \boldsymbol{\varphi}_{2,0} - \mathbf{n}_1^T \mathbf{R}_1^T \mathbf{R}_2 \mathbf{n}_2 + \boldsymbol{\varphi}_{1,0}^T \tilde{\mathbf{n}}_1 \mathbf{R}_1^T \mathbf{R}_2 \tilde{\mathbf{n}}_2 \boldsymbol{\varphi}_{2,0} \\ &= \mathbf{n}_2^T \mathbf{R}_2^T \mathbf{R}_1 \tilde{\mathbf{n}}_1 \mathbf{P}_{1,0} \mathbf{y}_1 + \mathbf{n}_1^T \mathbf{R}_1^T \mathbf{R}_2 \tilde{\mathbf{n}}_2 \mathbf{P}_{2,0} \mathbf{y}_2 - \mathbf{n}_1^T \mathbf{R}_1^T \mathbf{R}_2 \mathbf{n}_2 + (\mathbf{P}_{1,0} \mathbf{y}_1)^T \tilde{\mathbf{n}}_1 \mathbf{R}_1^T \mathbf{R}_2 \tilde{\mathbf{n}}_2 \mathbf{P}_{2,0} \mathbf{y}_2 \\ &= \mathbf{B}_{r,1} \mathbf{y}_1 + \mathbf{B}_{r,2} \mathbf{y}_2 - \mathbf{b} = 0\end{aligned}\quad (19)$$

$$\mathbf{B}_{r,1} = \mathbf{n}_2^T \mathbf{R}_2^T \mathbf{R}_1 \tilde{\mathbf{n}}_1 \mathbf{P}_{1,0}, \quad \mathbf{B}_{r,2} = \mathbf{n}_1^T \mathbf{R}_1^T \mathbf{R}_2 \tilde{\mathbf{n}}_2 \mathbf{P}_{2,0}, \quad \mathbf{b} = \mathbf{n}_1^T \mathbf{R}_1^T \mathbf{R}_2 \mathbf{n}_2 - (\mathbf{P}_{1,0} \mathbf{y}_1)^T \tilde{\mathbf{n}}_1 \mathbf{R}_1^T \mathbf{R}_2 \tilde{\mathbf{n}}_2 \mathbf{P}_{2,0} \mathbf{y}_2, \quad (20)$$

The rotations are determined by  $\boldsymbol{\varphi}_{i,0} = \mathbf{P}_{i,0} \mathbf{y}_i$ , where  $\mathbf{P}_i(\mathbf{s}_i)$  represents the compatible rotations derived from the shape functions. Hereby, both Eqs. (16) and (19) become linear in  $\mathbf{y}_i$  but iterations are necessary due to the rotational constraints. This can be seen in b in Eq. (20), where it is necessary to insert predicted values of  $\mathbf{y}_1$  and  $\mathbf{y}_2$  until it has converged.

Next, the global equations of motion are formulated by combining the equation of motion Eq. (13) for each substructure with the kinematical constraints Eqs. (16) and (19). For ease this is only demonstrated for a multibody system consisting of two substructures where the equations attain the form

$$\begin{bmatrix} \mathbf{M}_1 & \mathbf{0} & \mathbf{0} \\ \mathbf{0} & \mathbf{M}_2 & \mathbf{0} \\ \mathbf{0} & \mathbf{0} & \mathbf{0} \end{bmatrix} \begin{bmatrix} \ddot{\mathbf{y}}_1 \\ \ddot{\mathbf{y}}_2 \\ \ddot{\tilde{\lambda}} \end{bmatrix} + \begin{bmatrix} \mathbf{C}_1 & \mathbf{0} & \mathbf{0} \\ \mathbf{0} & \mathbf{C}_2 & \mathbf{0} \\ \mathbf{0} & \mathbf{0} & \mathbf{0} \end{bmatrix} \begin{bmatrix} \dot{\mathbf{y}}_1 \\ \dot{\mathbf{y}}_2 \\ \dot{\tilde{\lambda}} \end{bmatrix} + \begin{bmatrix} \mathbf{K}_1 & \mathbf{0} & \mathbf{B}_1^T \\ \mathbf{0} & \mathbf{K}_2 & \mathbf{B}_2^T \\ \mathbf{B}_1 & \mathbf{B}_2 & \mathbf{0} \end{bmatrix} \begin{bmatrix} \mathbf{y}_1 \\ \mathbf{y}_2 \\ \tilde{\lambda} \end{bmatrix} = \begin{bmatrix} \mathbf{f}_1 \\ \mathbf{f}_2 \\ \mathbf{b} \end{bmatrix} \quad (21)$$

$$\Rightarrow \mathbf{M}\ddot{\mathbf{z}} + \mathbf{C}\dot{\mathbf{z}} + \mathbf{K}\mathbf{z} = \mathbf{f}(t)$$

where  $\tilde{\lambda} = \tilde{\lambda}_1 = -\tilde{\lambda}_2$ . Because the constraints in principle introduce infinite stiffness into the global system it becomes necessary to apply unconditional stable time integrators. In the present case this is achieved by means of a nonlinear Newmark algorithm.

### 3. System reduction

The following reduction scheme deals with a specific substructure for which reason the index  $i$  is omitted for ease. Hereby, the equations of motion for the substructure equation (13) are rewritten in the form

$$\mathbf{M}\ddot{\mathbf{y}} + \mathbf{C}\dot{\mathbf{y}} + \mathbf{K}\mathbf{y} = \mathbf{g}(t) = \mathbf{f}(t) - \mathbf{B}^T \tilde{\lambda} \quad (22)$$

$\mathbf{g}(t)$  is a combined load vector encompassing wind loads, inertial loads, and reaction forces from the kinematical constraints.

#### 3.1. System reduction by use of fixed-fixed and fixed-free eigenmodes

At first, the vector  $\mathbf{y}$  of dimension  $n$  is partitioned into boundary  $\mathbf{y}_b$  and interior  $\mathbf{y}_e$  degrees of freedom i.e.  $\mathbf{y}^T = [\mathbf{y}_b^T \mathbf{y}_e^T]$ . The dimensions of  $\mathbf{y}_b$  and  $\mathbf{y}_e$  are  $n_b$  and  $n_e = n - n_b$ , respectively. The method will be illustrated with beam elements with 6 degrees of freedom for each node. Hereby  $n_b$  takes either the value 6 or 12 depending on the substructure has a free end or not. The two different sets of boundary conditions are sketched in Figs. 2a and b. When a blade is modelled by two or more substructures the boundary conditions in Figs. 2a and b are used for the innermost and outermost substructures, respectively. In Figs. 2c and d constraint modes from a unit displacement for the two types of boundary conditions are sketched. Similarly, in Figs. 2e and f constraint modes from a unit rotation are sketched. Obviously, the constraint modes account for the rigid-body motion of the substructure. Eq. (22) takes the following form by use of the partitioning of  $\mathbf{y}$ :

$$\begin{bmatrix} \mathbf{M}_{bb} & \mathbf{M}_{be} \\ \mathbf{M}_{eb} & \mathbf{M}_{ee} \end{bmatrix} \begin{bmatrix} \ddot{\mathbf{y}}_b \\ \ddot{\mathbf{y}}_e \end{bmatrix} + \begin{bmatrix} \mathbf{C}_{bb} & \mathbf{C}_{be} \\ \mathbf{C}_{eb} & \mathbf{C}_{ee} \end{bmatrix} \begin{bmatrix} \dot{\mathbf{y}}_b \\ \dot{\mathbf{y}}_e \end{bmatrix} + \begin{bmatrix} \mathbf{K}_{bb} & \mathbf{K}_{be} \\ \mathbf{K}_{eb} & \mathbf{K}_{ee} \end{bmatrix} \begin{bmatrix} \mathbf{y}_b \\ \mathbf{y}_e \end{bmatrix} = \begin{bmatrix} \mathbf{g}_b \\ \mathbf{g}_e \end{bmatrix} \quad (23)$$

Next, the interior degrees of freedom  $\mathbf{y}_e$  are written as a combination of the quasi-static response from the boundary degrees of freedom  $\mathbf{y}_b$  superposed with a modal representation of the remaining part of the internal response as follows:

$$\mathbf{y}_e = -\mathbf{K}_{ee}^{-1} \mathbf{K}_{eb} \mathbf{y}_b + \boldsymbol{\Phi} \mathbf{q} \quad (24)$$

$$\mathbf{q} = \begin{bmatrix} q_1(t) \\ \vdots \\ q_{n_e}(t) \end{bmatrix}, \quad \boldsymbol{\Phi} = [\boldsymbol{\Phi}_1 \cdots \boldsymbol{\Phi}_{n_e}] \quad (25)$$

$\boldsymbol{\Phi}_j$  is the  $j$ th fixed interface normal mode and  $q_j$  is the related generalized coordinate. In Figs. 2g and h an example of a fixed interface normal mode is sketched by use of the two types of boundary conditions. These eigenmodes are determined from the following generalized eigenvalue problem

$$(\mathbf{K}_{ee}(\omega, \boldsymbol{\alpha}, \Omega) - \omega_j^2 \mathbf{M}_{ee}) \boldsymbol{\Phi}_j = \mathbf{0} \quad (26)$$

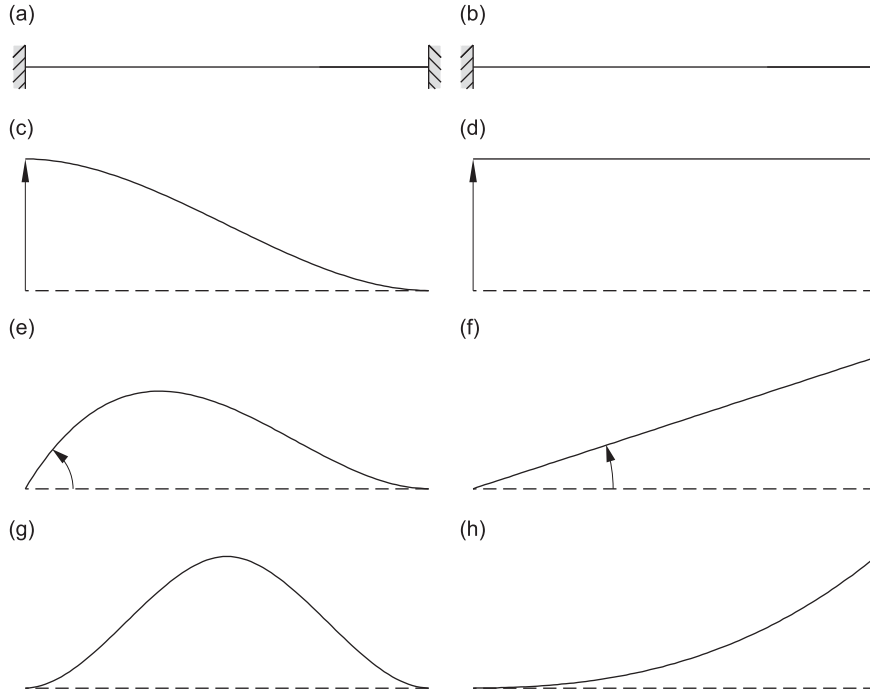


**Fig. 2.** (a) Boundary conditions for interior substructures. (b) Boundary conditions for substructure with a free end. (c)–(f) Constraint modes based on a unit displacement and unit rotation of the interface nodes. (g)–(h) Fixed interface normal modes.

It is intended that the eigenmodes are constant in time, whereby it is necessary to select the components of the angular velocity vector, angular acceleration vector, and the operating angular frequency, which all are used to set up the stiffness matrix in Eq. (14).  $\omega_j$  denotes the undamped angular eigenfrequencies of the substructure with fixed boundary degrees of freedom  $\mathbf{y}_b = \mathbf{0}$ . The eigenmodes are ordered in ascending magnitude of the frequency  $\omega_j$  and those with frequencies above a certain threshold frequency  $\omega_0$  are truncated, whereas the remaining eigenmodes respond dynamically. Then, the dynamic degrees of freedom  $\mathbf{q}_d$  and dynamic eigenmodes  $\Phi_d$  become

$$\mathbf{q}_d = \begin{bmatrix} q_1(t) \\ \vdots \\ q_{n_d}(t) \end{bmatrix}, \quad \Phi_d = [\Phi_1 \cdots \Phi_{n_d}] \quad (27)$$

where  $\mathbf{q}_d$  has the dimensions  $n_d < n_e$ . The degrees of freedom  $\mathbf{y}(t)$  and their time derivatives defining the substructure can hereby be presented in the following reduced form:

$$\mathbf{y}(t) = \mathbf{A}\mathbf{w}(t), \quad \dot{\mathbf{y}}(t) = \mathbf{A}\dot{\mathbf{w}}(t), \quad \ddot{\mathbf{y}}(t) = \mathbf{A}\ddot{\mathbf{w}}(t) \quad (28)$$

where

$$\mathbf{A} = \begin{bmatrix} \mathbf{I} & \mathbf{0} \\ \mathbf{V} & \Phi_d \end{bmatrix}, \quad \mathbf{V} = -\mathbf{K}_{ee}^{-1}\mathbf{K}_{eb}, \quad \mathbf{w} = \begin{bmatrix} \mathbf{y}_b \\ \mathbf{q}_d \end{bmatrix} \quad (29)$$

Insertion of Eq. (28) in Eq. (22) and premultiplication with  $\mathbf{A}^T$  provide the following reduced equations of motion:

$$\mathbf{m}\ddot{\mathbf{w}} + \mathbf{c}\dot{\mathbf{w}} + \mathbf{k}\mathbf{w} = \mathbf{A}^T\mathbf{g}(t) \quad (30)$$

where

$$\left. \begin{aligned} \mathbf{m} &= \mathbf{A}^T\mathbf{M}\mathbf{A} \\ \mathbf{c} &= \mathbf{A}^T\mathbf{C}\mathbf{A} \\ \mathbf{k} &= \mathbf{A}^T\mathbf{K}\mathbf{A} \end{aligned} \right\} \quad (31)$$

Notice that none of the reduced matrices have a diagonal structure. To set up the system equations of motion it is necessary to partition  $\mathbf{B}^T$  and  $\mathbf{f}$  in Eq. (22) consistently with the partition of  $\mathbf{y}$ .

### 3.2. System reduction by use of fixed-free eigenmodes

To be used for later comparison an alternative variant is used to model the innermost substructures of the blade. This is done by use of the procedure described above for the outermost substructure. Hereby, the innermost substructures are described by use of fixed-free eigenmodes and the dimension of the boundary degrees of freedom is  $n_b = 6$  corresponding to the fixed end. Hereby, the first six columns in  $\mathbf{A}$  correspond to rigid-body modes.

### 3.3. Reduced system of equations

Based on the derived system reduction algorithm a substructure in the system can be reduced by use of Eq. (30) together with Eq. (28) for the constraints. For the illustrative example described by Eq. (21) substructure 1 will be reduced, whereas substructure 2 is left unchanged

$$\begin{bmatrix} \mathbf{m}_1 & \mathbf{0} & \mathbf{0} \\ \mathbf{0} & \mathbf{M}_2 & \mathbf{0} \\ \mathbf{0} & \mathbf{0} & \mathbf{0} \end{bmatrix} \begin{bmatrix} \dot{\mathbf{w}}_1 \\ \dot{\mathbf{y}}_2 \\ \dot{\lambda} \end{bmatrix} + \begin{bmatrix} \mathbf{c}_1 & \mathbf{0} & \mathbf{0} \\ \mathbf{0} & \mathbf{C}_2 & \mathbf{0} \\ \mathbf{0} & \mathbf{0} & \mathbf{0} \end{bmatrix} \begin{bmatrix} \dot{\mathbf{w}}_1 \\ \dot{\mathbf{y}}_2 \\ \dot{\lambda} \end{bmatrix} + \begin{bmatrix} \mathbf{k}_1 & \mathbf{0} & \mathbf{A}_1^T \mathbf{B}_1^T \\ \mathbf{0} & \mathbf{K}_2 & \mathbf{B}_2^T \\ \mathbf{B}_1 \mathbf{A}_1 & \mathbf{B}_2 & \mathbf{0} \end{bmatrix} \begin{bmatrix} \mathbf{w}_1 \\ \mathbf{y}_2 \\ \lambda \end{bmatrix} = \begin{bmatrix} \mathbf{A}_1^T \mathbf{f}_1 \\ \mathbf{f}_2 \\ \mathbf{b} \end{bmatrix} \quad (32)$$

The state vector related to the reduced system is now defined as

$$\mathbf{z}(t) = \begin{bmatrix} \mathbf{w}_1 \\ \mathbf{y}_2 \\ \lambda \end{bmatrix} \quad (33)$$

## 4. Updating of system state vector and moving frame of reference

At first an introductory overview of the following updating algorithm will be given based on a number of 2D illustrations depicted in Fig. 3. The updating scheme of the moving frame of reference follows the same principles as described in Kawamoto et al. [8]. The orientation of the moving frame of reference with the related rotation tensor  $\mathbf{R}(t)$  has been indicated at various levels of the updating procedure. The corresponding degrees of freedom vector  $\mathbf{y}(t)$  is symbolically indicated by the position vector of the interface node, describing the position and rotation of the substructure from the moving frame, see Fig. 3a. At the time  $t = t_j$  the system state vector  $\mathbf{z}_j = \mathbf{z}(t_j)$  along with its time derivatives  $\dot{\mathbf{z}}_j = \dot{\mathbf{z}}(t_j)$  and  $\ddot{\mathbf{z}}_j = \ddot{\mathbf{z}}(t_j)$  are known. Additionally, several parameters describing the motion of the moving frame of reference for each substructure are known. These are the global components of the position vector of the origin  $\bar{\mathbf{x}}_{c,j} = \bar{\mathbf{x}}_c(t_j)$ , the related velocity vector  $\bar{\mathbf{v}}_{c,j} = \bar{\mathbf{v}}_c(t_j)$ , and acceleration vector  $\bar{\mathbf{a}}_{c,j} = \bar{\mathbf{a}}_c(t_j)$ , as well as the components of the rotation tensor  $\mathbf{R}_j = \mathbf{R}(t_j)$  and the moving frame components of the angular velocity and angular acceleration vectors  $\boldsymbol{\omega}_j = \boldsymbol{\omega}(t_j)$ , and  $\boldsymbol{\alpha}_j = \boldsymbol{\alpha}(t_j)$ , respectively. All these known parameters and system vectors make the starting point at the determination of the

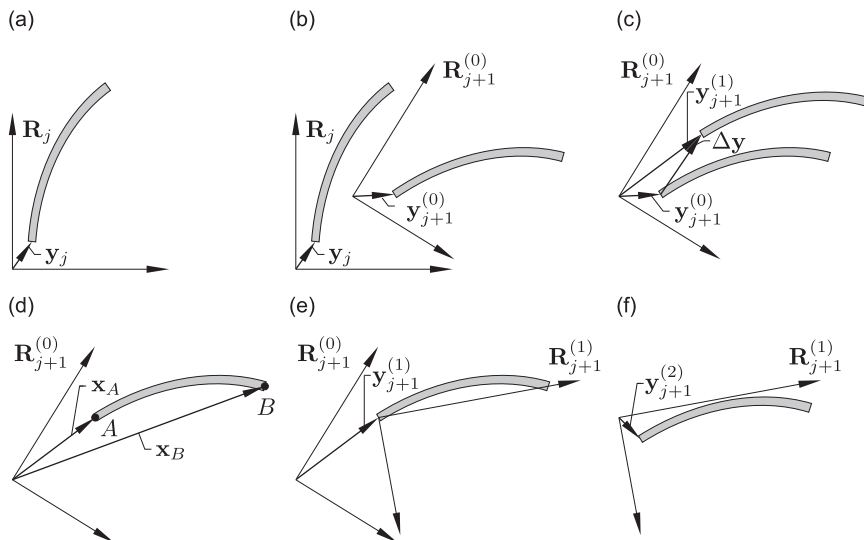


**Fig. 3.** (a) Moving frame and substructure at the initial situation at time  $t = t_j$ . (b) Prediction of moving frame and system state vector at time  $t_{j+1} = t_j + \Delta t$ . (c) Determination of the system state vector for the first iteration step. (d) Updating of the moving frame based on the motion of two boundary nodes. (e) Updated position and orientation of the moving frame. (f) Determination of the system state vector for the second iteration referring the motion of the substructure to the updated moving frame of reference.

corresponding quantities at the new time  $t_{j+1} = t_j + \Delta t$ , on condition that the new load vector  $\mathbf{f}_{j+1} = \mathbf{f}(t_{j+1})$  can be calculated. In what follows an upper index ( $k$ ) is used to specify the iteration step during the considered time step. Initially, predicted values based on simple Taylor expansions for the vectors related to the moving frame and the moving substructure at the time  $t_{j+1}$  are determined from the corresponding values at time  $t_j$ . Predicted values are denoted with an upper index  $k = 0$ , and the prediction step has been sketched in Fig. 3b. Next, the equations of motion Eq. (32) are solved with the predicted values entering the system matrices and vectors. Hereby, the nodal displacement vector for the first iteration  $\mathbf{y}_{j+1}^{(1)}$  together with its time derivatives are determined, see Fig. 3c.  $\Delta \mathbf{y}$  indicates the displacement difference between predicted and corrected estimates, which should be zero when the displacements of the substructure from the moving frame are converged. Based on the displacements of the substructure from the moving frame of reference another convergency criterion is set up. If these displacements are above a chosen tolerance the moving frame of reference is updated. The position of the origin together with its time derivatives is updated based on the motion of the belonging boundary node of the substructure. The orientation together with angular velocity and angular acceleration is updated by use of the motion of two boundary nodes, as sketched in Fig. 1c. In Fig. 3d both nodes are sketched, where they have been labelled A and B and the position vector in Eq. (1) from the origin of the moving frame to these nodes is denoted  $\mathbf{x}_A$  and  $\mathbf{x}_B$ , respectively. In Fig. 3e the updated position and orientation of the moving frame of reference are illustrated. If convergence has not been achieved the updated system equations are solved again with updated system matrices and vectors. Hereby, a new nodal displacement vector  $\mathbf{y}_{j+1}^{(2)}$  is determined referring the motion of the substructure to the updated moving frame of reference given by the rotation tensor  $\mathbf{R}_{j+1}^{(1)}$ , see Fig. 3f. This iteration continues until convergency is obtained.

Next, the indicated updating algorithm is described in a formal way. At the instant of time  $t = t_{j+1}$  the vectors related to the origin of the moving frame of reference are predicted by the truncated Taylor expansions of the solution from the previous time step

$$\bar{\mathbf{x}}_{cj+1}^{(0)} = \bar{\mathbf{x}}_{cj} + \bar{\mathbf{v}}_{cj}\Delta t + \frac{1}{2}\bar{\mathbf{a}}_{cj}\Delta t^2, \quad \bar{\mathbf{v}}_{cj+1}^{(0)} = \bar{\mathbf{v}}_{cj} + \bar{\mathbf{a}}_{cj}\Delta t, \quad \bar{\mathbf{a}}_{cj+1}^{(0)} = \bar{\mathbf{a}}_{cj} \quad (34)$$

$\bar{\mathbf{x}}_{cj+1}^{(0)}$  is used in the displacement constraints Eq. (16). The moving frame components of the vectors defining the rotation of the moving frame of reference are similarly predicted by the Taylor expansions

$$\Delta\psi_{j+1}^{(0)} = \omega_j\Delta t + \frac{1}{2}\alpha_j\Delta t^2, \quad \omega_{j+1}^{(0)} = \omega_j + \alpha_j\Delta t, \quad \alpha_{j+1}^{(0)} = \alpha_j \quad (35)$$

$\Delta\psi_{j+1}^{(0)}$  denotes the moving frame components of the predicted rotation vector of the moving frame during the interval  $\Delta t$ . The rotation tensor  $\mathbf{R}_{j+1}^{(0)}$ , corresponding to the moving frame orientation after the rotation  $\Delta\psi_{j+1}^{(0)}$ , is next determined by use of Rodriguez formula Eq. (3)

$$\mathbf{R}_{j+1}^{(0)} = \mathbf{R}_j\mathbf{R}(\Delta\psi_{j+1}^{(0)}) \quad (36)$$

In Eq. (15) the moving frame components of the acceleration of the origin are needed. These are determined from the corresponding global components via the transformation

$$\mathbf{a}_{cj+1}^{(0)} = \mathbf{R}_{j+1}^{(0)T} \bar{\mathbf{a}}_{cj+1}^{(0)} \quad (37)$$

Next, the system coordinates are predicted based on the truncated Taylor expansions

$$\mathbf{z}_{j+1}^{(0)} = \mathbf{z}_j + \dot{\mathbf{z}}_j\Delta t + \frac{1}{2}\ddot{\mathbf{z}}_j\Delta t^2, \quad \dot{\mathbf{z}}_{j+1}^{(0)} = \dot{\mathbf{z}}_j + \ddot{\mathbf{z}}_j\Delta t, \quad \ddot{\mathbf{z}}_{j+1}^{(0)} = \ddot{\mathbf{z}}_j \quad (38)$$

Hereby, all predicted parameters for the moving frame of reference together with the predicted system coordinates are determined. The damping matrix  $\mathbf{C}^{(0)}$ , stiffness matrix  $\mathbf{K}^{(0)}$ , and mass matrix  $\mathbf{M}$  from Eq. (32) are determined next. Here, it should be noted that the mass matrix is independent of the moving frame parameters and thereby constant. In order to solve Eq. (32) the residual  $\mathbf{r}$  and equivalent system stiffness matrix  $\hat{\mathbf{K}}$  are determined by use of the nonlinear Newmark algorithm, G eradin and Rixen [27]

$$\mathbf{r} = -\mathbf{M}\ddot{\mathbf{z}}_{j+1}^{(0)} - \mathbf{C}^{(0)}\dot{\mathbf{z}}_{j+1}^{(0)} - \mathbf{K}^{(0)}\mathbf{z}_{j+1}^{(0)} + \mathbf{f}_{j+1}^{(0)}, \quad \hat{\mathbf{K}} = \frac{1}{\beta\Delta t^2}\mathbf{M} + \frac{\gamma}{\beta\Delta t}\mathbf{C}^{(0)} + \mathbf{K}^{(0)} \quad (39)$$

where  $\gamma = \frac{1}{2} + \alpha$ ,  $\beta = \frac{1}{4}(1 + \alpha)^2$ , and  $\alpha$  is used to incorporate numerical damping. By solving  $\hat{\mathbf{K}}\Delta\mathbf{z} = \mathbf{r}$  for the unknowns  $\Delta\mathbf{z}$ , the following corrected values of the system coordinates are determined:

$$\mathbf{z}_{j+1}^{(1)} = \mathbf{z}_{j+1}^{(0)} + \Delta\mathbf{z}, \quad \dot{\mathbf{z}}_{j+1}^{(1)} = \dot{\mathbf{z}}_{j+1}^{(0)} + \frac{\gamma}{\beta\Delta t}\Delta\mathbf{z}, \quad \ddot{\mathbf{z}}_{j+1}^{(1)} = \ddot{\mathbf{z}}_{j+1}^{(0)} + \frac{1}{\beta\Delta t^2}\Delta\mathbf{z} \quad (40)$$

Hereby the displacement and rotation degrees of freedom of the substructure referred to the moving frame of reference can be determined together with their time derivatives. In case of using the reduced models the transformations to the full set of degrees of freedom are performed by use of Eq. (28). The displacements and rotations at the boundaries are referred to as  $\mathbf{u}_A$ ,  $\varphi_A$ , and  $\mathbf{u}_B$ ,  $\varphi_B$ . The same notation follows for the time derivatives of the displacements and rotations. The used convergency criterion is based on the position of the moving frame of reference. Therefore, the Euclidian norms of  $\mathbf{u}_A$  and  $\mathbf{u}_B$  are used. If these norms are within a chosen tolerance there is no need to update the moving frame of reference and the



present solution is used as input in the new time step. If this is not the case, the moving frame of reference parameters are updated.

The position, velocity and acceleration of the origin of the moving frame of reference are updated by use of Eqs. (2), (5) and (6)

$$\bar{\mathbf{x}}_{cj+1}^{(k+1)} = \bar{\mathbf{x}}_{cj+1}^{(k)} + \mathbf{R}_{j+1}^{(k)} \mathbf{u}_A \quad (41)$$

$$\bar{\mathbf{v}}_{cj+1}^{(k+1)} = \bar{\mathbf{v}}_{cj+1}^{(k)} + \mathbf{R}_{j+1}^{(k)} (\tilde{\omega}_{j+1}^{(k)} (\mathbf{s} + \mathbf{u}_A) + \dot{\mathbf{u}}_A) \quad (42)$$

$$\bar{\mathbf{a}}_{cj+1}^{(k+1)} = \bar{\mathbf{a}}_{cj+1}^{(k)} + \mathbf{R}_{j+1}^{(k)} ((\tilde{\alpha}_{j+1}^{(k)} + \tilde{\omega}_{j+1}^{(k)} \tilde{\omega}_{j+1}^{(k)}) (\mathbf{s} + \mathbf{u}_A) + 2\tilde{\omega}_{j+1}^{(k)} \dot{\mathbf{u}}_A + \ddot{\mathbf{u}}_A) \quad (43)$$

In the following, the update of the orientation, angular velocity and angular acceleration of the moving frame of reference is described, which is based on the motion of both boundary nodes *A* and *B*. The purpose of the present update is to align the beam axis and thereby the  $x_3$ -axis so it passes through both nodes. In order to determine the orientation of the remaining  $x_1$ - and  $x_2$ -axes the average rotation  $\varphi_3$  around the beam axis is used, which is given by the third rotation component at the two nodes

$$\varphi_3 = \frac{1}{2}(\varphi_{B,3} + \varphi_{A,3}) \quad (44)$$

Then, the two basis vectors  $\mathbf{n}_1$  and  $\mathbf{n}_2$  for the  $x_1$ - and  $x_2$ -axis are given as

$$[\mathbf{n}_1 \ \mathbf{n}_2 \ \mathbf{n}_3] = \begin{bmatrix} \cos \varphi_3 & -\sin \varphi_3 & 0 \\ \sin \varphi_3 & \cos \varphi_3 & 0 \\ 0 & 0 & 1 \end{bmatrix} \quad (45)$$

The purpose is to rotate the full basis through the minimum angle bringing one of the vectors into a given new direction. In the present case the vector  $\mathbf{n}_3$  is to be rotated into the direction of the beam axis defined by the unit vector  $(\mathbf{x}_B - \mathbf{x}_A)/|\mathbf{x}_B - \mathbf{x}_A|$ , where  $\mathbf{x}_A$  and  $\mathbf{x}_B$  are the position vectors of the end nodes relative to the moving frame origin cf. Fig. 3d. First, the mean direction is defined by the unit vector  $\mathbf{n}$

$$\mathbf{n} = \mathbf{n}_3 + \frac{\mathbf{x}_B - \mathbf{x}_A}{|\mathbf{x}_B - \mathbf{x}_A|}, \quad \mathbf{n} := \mathbf{n}/|\mathbf{n}| \quad (46)$$

Next, a Householder transformation is used, which corresponds to a reflection in the plane orthogonal to the unit vector  $\mathbf{n}$ , Krenk [28]

$$\Delta \mathbf{R} = (\mathbf{I} - 2\mathbf{n}\mathbf{n}^T)[\mathbf{n}_1 \ \mathbf{n}_2 \ -\mathbf{n}_3] \quad (47)$$

Hereby, a new set of unit vectors contained in  $\Delta \mathbf{R}$  are determined, which describe the updated orientation seen from the present orientation of the moving frame of reference. The updated rotation tensor is given by, cf. Fig. 3e

$$\mathbf{R}_{j+1}^{(k+1)} = \mathbf{R}_{j+1}^{(k)} \Delta \mathbf{R} \quad (48)$$

In order to update the angular velocity it is used that the global components of the velocity at node *B* should be the same in the present known configuration of the moving frame and in the updated one. The global components of the velocity at node *B* are determined by use of Eq. (5)

$$\bar{\mathbf{v}}_B = \bar{\mathbf{v}}_{cj+1}^{(k)} + \mathbf{R}_{j+1}^{(k)} (\tilde{\omega}_{j+1}^{(k)} (\mathbf{s}_B + \mathbf{u}_B) + \dot{\mathbf{u}}_B) \quad (49)$$

where  $\mathbf{s}_B$  given in the updated moving frame of reference marks the node *B*. The updating strategy presumes that the local displacement and velocity at *B* vanish, cf. Fig. 3e. Hereby, by use of Eq. (5) and the results from Eq. (49) the following relation is obtained for the updated angular velocity

$$\mathbf{R}_{j+1}^{(k+1)T} (\bar{\mathbf{v}}_B - \bar{\mathbf{v}}_{cj+1}^{(k+1)}) = \tilde{\omega}_{j+1}^{(k+1)} \mathbf{s}_B \quad (50)$$

The two first rows give a solution for the two first components of the angular velocity  $\omega_{1,j+1}^{(k+1)}$  and  $\omega_{2,j+1}^{(k+1)}$ . The third component is determined from the previous known value and the average of the belonging angular velocity component of the two nodes

$$\omega_{3,j+1}^{(k+1)} = \omega_{3,j+1}^{(k)} + \frac{1}{2}(\dot{\varphi}_{B,3} + \dot{\varphi}_{A,3}) \quad (51)$$

Similarly, the angular acceleration is determined by use of Eq. (6)

$$\bar{\mathbf{a}}_B = \bar{\mathbf{a}}_{cj+1}^{(k)} + \mathbf{R}_{j+1}^{(k)} ((\tilde{\alpha}_{j+1}^{(k)} + \tilde{\omega}_{j+1}^{(k)} \tilde{\omega}_{j+1}^{(k)}) (\mathbf{s}_B + \mathbf{u}_B) + 2\tilde{\omega}_{j+1}^{(k)} \dot{\mathbf{u}}_B + \ddot{\mathbf{u}}_B) \quad (52)$$



$$\mathbf{R}_{j+1}^{(k+1)\top} (\bar{\mathbf{a}}_B - \bar{\mathbf{a}}_{c_{j+1}}^{(k+1)}) - \bar{\omega}_{j+1}^{(k+1)} \bar{\omega}_{j+1}^{(k+1)} \mathbf{s}_B = \bar{\alpha}_{j+1}^{(k+1)} \mathbf{s}_B \quad (53)$$

$$\alpha_{3,j+1}^{(k+1)} = \alpha_{3,j+1}^{(k)} + \frac{1}{2}(\ddot{\varphi}_{B,3} + \ddot{\varphi}_{A,3}) \quad (54)$$

## 5. Numerical example

In this section the theory is illustrated with a simplified system consisting of a wind turbine blade divided into two substructures labelled 1 and 2. The fixed frame of reference is shown in Fig. 4a and the two substructures are shown in Fig. 4b. The origin of the initial moving frame of reference  $(x_{1,1}, x_{2,1}, x_{3,1})$  belonging to substructure 1 is identical to the fixed frame of reference  $(\bar{x}_1, \bar{x}_2, \bar{x}_3)$  whereas the origin of the initial moving frame of reference  $(x_{1,2}, x_{2,2}, x_{3,2})$  belonging to substructure 2 is displaced half the blade length in the  $\bar{x}_3$ -direction. In total 11 constraints are introduced where six fix displacements and rotations at the assembling point of the two substructures. The remaining five constraints are used at the origin of substructure 1. Here, three constraints fix the displacements and two constraints fix the rotation around the  $\bar{x}_2$ - and  $\bar{x}_3$ -axes. I.e. at the root it is only possible for the blade to rotate around the  $\bar{x}_1$ -axis. The moving frame of reference for both substructures is updated based on the motion of the two end points in each substructure. The updating algorithm is described in Section 4 and the  $x_3$ -axis for the two moving frames are sketched in Fig. 4c. The length of the blade is 44.8 m with a total weight of 10 t and it is constructed by NACA 63-418 section profiles. The cross section parameters throughout the blade are presented in Fig. 5. A Young's modulus of  $E = 3 \times 10^{10}$  Pa, shear modulus of  $G = E/2.6$ , and density  $\rho = 2 \times 10^3 \text{ kg m}^{-3}$  are used for all sections. The element stiffness matrix is setup in principal directions and rotated the angle  $\phi$  to align with the  $(x_1, x_2)$ -coordinate system, see Fig. 5f. The FE model of both substructures is based on prismatic Bernoulli–Euler beam elements with St. Venant torsion and has 6 degrees of freedom for each node. Both substructures have equal reference length of 22.4 m and both are discretized by use of 10 prismatic elements of equal length. This FE model constitutes the full model while the reduced models are compared to. No structural damping is included i.e.  $\mathbf{C}_0 = \mathbf{0}$  in Eq. (14) and  $\alpha = 0.08$  is used to incorporate numerical damping in the nonlinear Newmark algorithm with constant time steps of  $\Delta t = 0.02$  s. The moving frames are updated in each time step. In Holm-Jørgensen and Nielsen [11] the three lowest undamped fixed-base circular eigenfrequencies of the blade are  $\omega_1 = 5.15$ ,  $\omega_2 = 9.51$ , and  $\omega_3 = 14.23$ . In determining these a constant angular velocity of the moving frame corresponding to the operating frequency of the rotor is used to set up the stiffness matrix.

The purpose of the numerical simulation is to verify that the results from the reduced model based on fixed–fixed interface normal modes for substructure 1 are almost identical to the full FE model. Moreover, the importance of using compatible interface normal modes at the assembling point to substructure 2 is illustrated by use of fixed–free interface normal modes for substructure 1, with the free end at the assembling points. For both reduced models, substructure 2 is modelled by use of fixed–free interface normal modes. For comparison of the two reduced models it is chosen to keep the same number of degrees of freedom. When referring to the number of fixed–fixed and fixed–free interface normal modes, it is only the modes with the lowest eigenfrequencies cf. Eq. (26) which are used and the remaining modes are truncated. In one case substructure 1 has 12 boundary degrees of freedom and three fixed–fixed interface normal modes. In the other case substructure 1 is modelled by 6 boundary degrees of freedom and nine fixed–free interface normal modes. In both

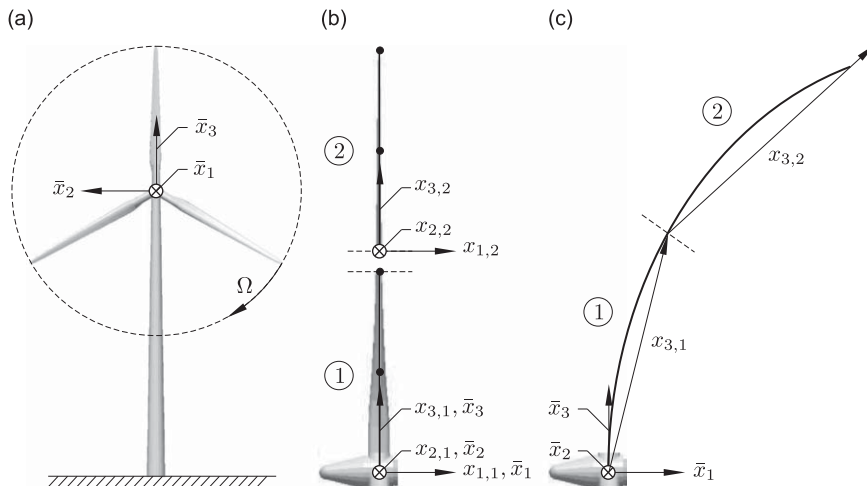


**Fig. 4.** (a) Fixed frame of reference in the wind turbine. (b) In the numerical model the blade is divided into two substructures labelled 1 and 2. (c) Illustration of the  $x_3$ -axis for the moving frame of reference belonging to substructure 1 and 2 denoted by  $x_{3,1}$  and  $x_{3,2}$ , respectively.

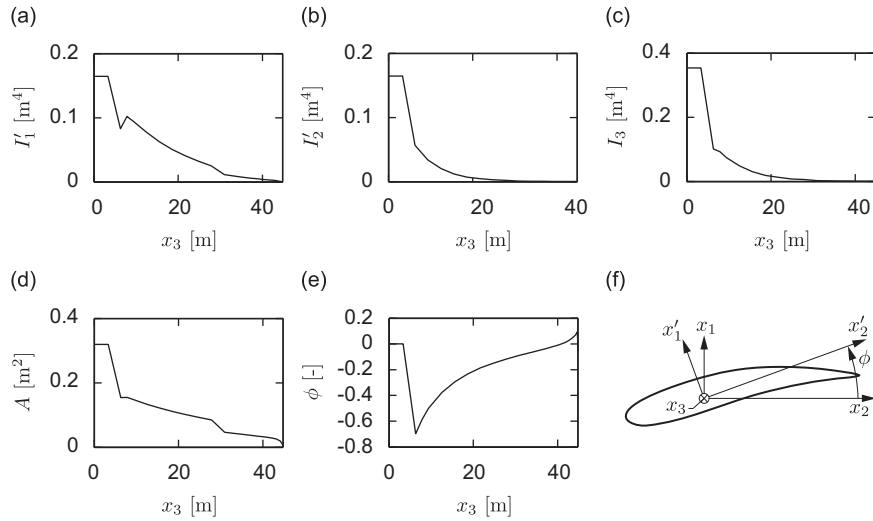


**Fig. 5.** (a) Principal moment of inertia around  $x'_1$ . (b) Principal moment of inertia around  $x'_2$ . (c) St. Venant torsional constant. (d) Areal of cross section. (e) Pretwist angle defined as the angle between the tangential  $x_2$ -axis and principal  $x'_2$ -axis. (f) Sign definition of  $\phi$ .

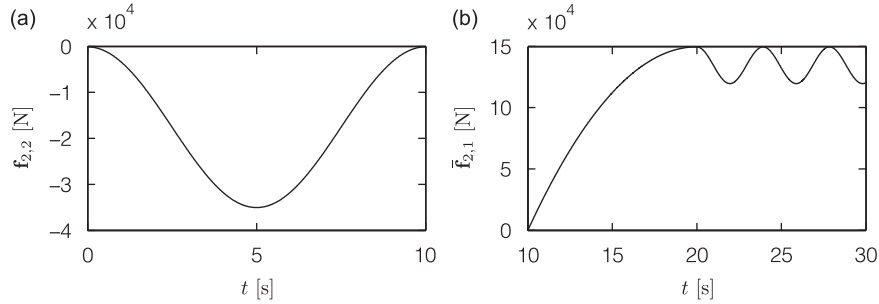


**Fig. 6.** (a) Load component in the  $x_2$ -direction. (b) Load component in the  $\bar{x}_1$ -direction.

cases substructure 2 is modelled as fixed–free with a total of 6 boundary degrees of freedom and 12 fixed–free interface normal modes. Hereby, the FE model has 132 degrees of freedom and the reduced models have 33 degrees of freedom.

### 5.1. Exterior load and fixed interface normal modes

The numerical simulation consists of a start-up sequence and an operating sequence. The start-up sequence is split in two where the first sequence  $0 \leq t \leq t_1$  speeds up the blade from a stopped situation at  $t = 0$  to the nominal angular velocity  $\Omega_n = 1.6 \text{ rad s}^{-1}$  of the rotor at  $t = t_1$ . In the second sequence  $t_1 < t \leq t_2$  an exterior load in the global  $\bar{x}_1$ -direction is stepped up. In the operating sequence  $t > t_2$  the exterior load is based on a constant load corresponding to a mean wind velocity and a harmonic component due to a variation in the shear wind field. The sequences are modelled by applying concentrated loads at a node in the beam model placed at the moving coordinate  $x_{3,2} = 6.72 \text{ m}$ . The reason for applying the load at this point is because the maximum intensity of the wind load is concentrated around this position. The components of the applied exterior load at substructure 2 are shown in Fig. 6 and defined as

$$\mathbf{f}_2(t) = \begin{cases} [0 \ 1 \ 0]^T \frac{1}{2} P_0 \left( 1 - \cos\left(\frac{2\pi}{t_1} t\right) \right), & 0 \leq t \leq t_1 \\ \mathbf{R}_2^T [1 \ 0 \ 0]^T P_1 \left( -\left(\frac{t-t_1}{t_2-t_1}\right)^2 + 2\frac{t-t_1}{t_2-t_1} \right), & t_1 < t \leq t_2 \\ \mathbf{R}_2^T [1 \ 0 \ 0]^T P_1 (1 + p \cos(\Omega_n(t-t_2)) - p), & t > t_2 \end{cases} \quad (55)$$

Here, it is seen that the applied load in the sequence  $0 \leq t \leq t_1$  is oriented in the edge direction in order to speed-up the blade. In the other two sequences the load is oriented in the  $\bar{x}_1$ -direction i.e. primarily in the flap direction. In the simulations the following values have been used:  $P_0 = -3.5 \times 10^4 \text{ N}$ ,  $P_1 = 1.5 \times 10^5 \text{ N}$ ,  $p = 0.1$ ,  $\Omega_n = 1.6 \text{ rad s}^{-1}$ ,  $t_1 = 10 \text{ s}$ , and  $t_2 = 20 \text{ s}$ . Based on the applied load the components of the angular velocity and angular acceleration of the

moving frames during the time series are determined by use of the FE model. The orientation of the moving frames given by the parameter vector  $\theta$  is determined by use of Spurriers algorithm, see e.g. Crisfield [29]. All three components of the parameter vector, angular velocity, and angular acceleration for the two moving frames are plotted in Fig. 7. Here, it is shown that for both substructures 1 and 2 the first component of the angular velocity of the belonging moving frame of reference is almost constant at  $\omega_{1,1} \simeq \omega_{1,2} \simeq 1.6 \text{ rad s}^{-1}$  in the operating sequence  $t > t_2$  and considerably larger than the second and third components. The reason for not being constant is because no generator is applied to control the angular velocity. Another reason is that the blade is twisted resulting in both flap and edge wise displacements when a load in the flap direction is applied. It can also be seen that all second and third components for substructure 1 are considerably smaller than for substructure 2. This is due to the small displacement in the  $\bar{x}_{1,1}$ -direction at the end node of this substructure which leaves the  $x_{3,1}$ -axis almost orthogonal to the  $\bar{x}_1$ -axis. Moreover, in the operating situation the angular acceleration is close to zero. When creating the fixed interface normal modes Eq. (26) for the reduced models it is computational advantageous if these are constant throughout the simulated time series. Similarly with the constraint modes listed in Eq. (29). As seen from Eq. (14), the stiffness matrix consists of the elastic stiffness  $\mathbf{K}_e$ , the geometric stiffness  $\mathbf{K}_g$  and the gyroscopic stiffness terms  $\mathbf{D}$  and  $\mathbf{G}$  which depend on the angular velocity and angular acceleration of the moving frame, respectively. In a previous paper by the authors [11] three different stiffness matrices were used to extract the eigenmodes for a blade modelled by fixed-free eigenmodes, depending on different values of the angular velocity and angular acceleration vectors and different terms of the included stiffness matrices from Eq. (14). Small differences were observed but the overall best results were obtained by use of

$$\mathbf{K} = \mathbf{K}_e + \mathbf{K}_g(\Omega_n) + \mathbf{D}(\omega_n), \quad \omega_n = \begin{bmatrix} \Omega_n \\ 0 \\ 0 \end{bmatrix} \quad (56)$$

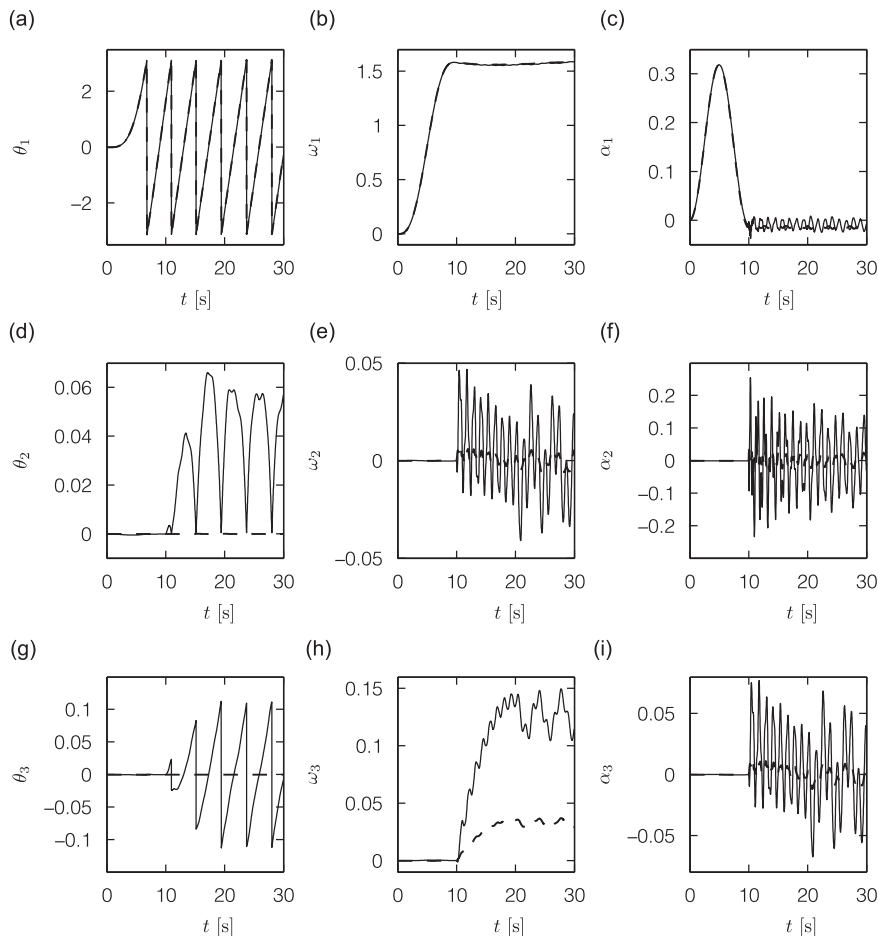


**Fig. 7.** Moving frame components of the parameter vector  $\theta$ , angular velocity  $\omega$ , and angular acceleration  $\alpha$  for the two moving frames. (a)–(c) First component. (d)–(f) Second component. (g)–(i) Third component. (---) Substructure 1. (—) Substructure 2.

which is used for both substructures in the present simulations. For all situations the same mass matrix  $\mathbf{M}$  from Eq. (10) is used when solving the generalized eigenvalue problem Eq. (26).

## 5.2. Results for response and constraint

Results for the tip position of the blade in  $\bar{x}_1$  during the time series  $10 \leq t \leq 30$  s are shown in Fig. 8a for the FE model, and the two reduced models with fixed-fixed and fixed-free interface normal modes for substructure 1. The results from the FE model are used to normalize the results from the reduced models shown in Fig. 8b. The reason for not displaying the first 10 s is because these displacements in  $\bar{x}_1$  are small, and the normalized response of the reduced models is outside the area of interest. In Fig. 8b the results by use of the fixed-fixed modes are very close to the full FE model, even though these modes are constant throughout the time series. Moreover, these modes are based on a constant angular velocity around just one axis, where it is shown in Fig. 7 that this is not the actual case, especially for substructure 2. By use of the fixed-free modes the size of the response is notably changed. The importance of using compatible interface normal modes at the assembling point between the substructures is hereby demonstrated.

In Fig. 9a the Lagrange multiplier for the displacement constraint in the  $\bar{x}_1$ -direction at the root of the blade is shown. Here, the reaction force is approximately  $P_1$  at  $t = 20$  s and has a mean value of approximately  $1.35 \times 10^5$  N for  $t > 20$  s corresponding to the applied load component. In Fig. 9b the normalized Lagrange multiplier by use of fixed-fixed and fixed-free interface normal modes for substructure 1 is presented. Again, the best results are obtained by use of fixed-fixed modes, but the results by use of fixed-free modes are at least centred around the results from the FE model.

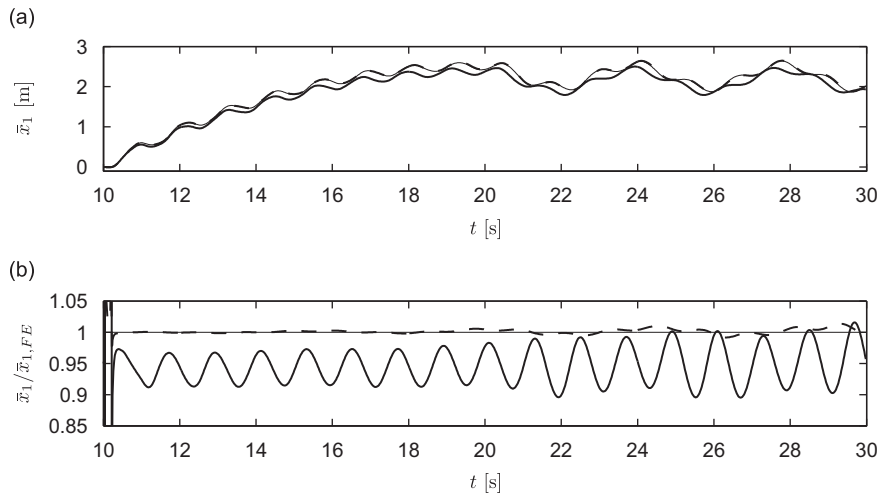


**Fig. 8.** (a) Tip position in  $\bar{x}_1$ . (b) Normalized tip position in  $\bar{x}_1$ . (—) FE model. (--) Fixed-fixed modes. (—) Fixed-free modes.

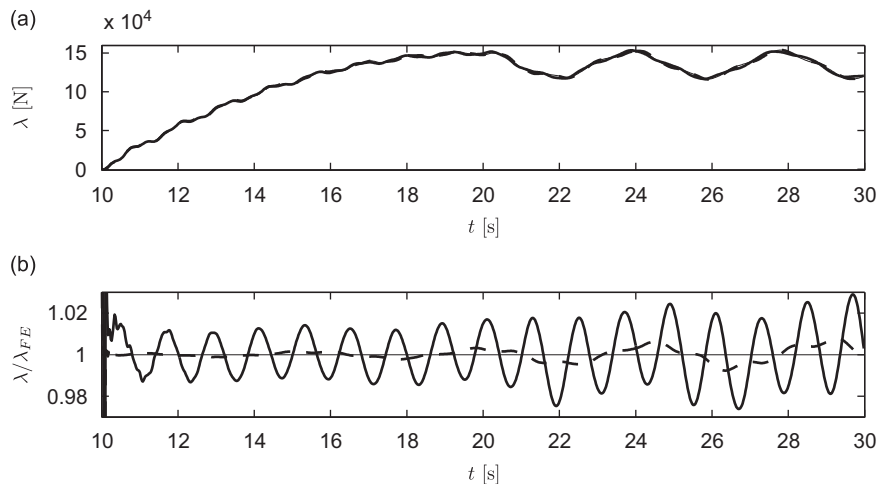


**Fig. 9.** (a) Lagrange multiplier for displacement constraint in the  $\bar{x}_1$ -direction at the hub of the blade. (b) Normalized Lagrange multiplier. (—) FE model. (--) Fixed-fixed modes. (—) Fixed-free modes.

## 6. Conclusions

In this paper it is demonstrated that an FE model of a wind turbine blade divided into two substructures in the used multibody formulation with completely freely moving local frames of reference efficiently can be reduced by use of constraint modes and fixed interface normal modes. Even by keeping these modes constant throughout the numerical simulations, where the blade goes from a stopped situation to the nominal operating situation, the results are almost identical to the full FE model. The importance of using compatible modes at the assembling point between the substructures of the blade is demonstrated. Further, an updating algorithm for the freely moving frame based on the motion of two arbitrary nodes in the substructure has been devised and its applicability has been demonstrated by use of the end nodes in the belonging substructures. For smaller displacements of the substructure from the moving frame of reference and to get a better nonlinear description of the displacements the reference length of the two multibodies should be further examined instead of splitting the blade into two multibodies of equal reference length.

## Acknowledgements

This work has been supported by the Danish Council for Strategic Research through the project 'Nonlinear Multibody Dynamics of Wind Turbines'.

## References

- [1] O.P. Agrawal, A.A. Shabana, Dynamic analysis of multibody systems using component modes, *Computers & Structures* 21 (6) (1985) 1303–1312.
- [2] A.A. Shabana, Resonance conditions and deformable body co-ordinate systems, *Journal of Sound and Vibration* 192 (1) (1996) 389–398.
- [3] P.E. Nikravesh, *Computer-aided Analysis of Mechanical Systems*, Prentice-Hall, Englewood Cliffs, NJ, 1988.
- [4] J.G. de Jalón, E. Bayo, *Kinematic and Dynamic Simulations of Multibody Systems—The Real-Time Challenge*, Springer, Berlin, 1993.
- [5] M. Géradin, A. Cardona, *Flexible Multibody Dynamics — A Finite Element Approach*, Wiley, New York, 2001.
- [6] A.A. Shabana, *Dynamics of Multibody Systems*, third ed., Cambridge University Press, Cambridge, 2005.
- [7] A. Kawamoto, M. Inagaki, T. Aoyama, K. Yasuda, Vibration of moving flexible bodies (formulation of dynamics by using normal modes and a local observer frame), *Proceeding of DETC99/VIB-8232*, 1999.
- [8] A. Kawamoto, S. Krenk, A. Suzuki, Flexible body dynamics in a freely floating local frame, *ECCOMAS Conference on Multibody Dynamics 2007*, Milan, Italy, 25–28 June 2007.
- [9] A. Kawamoto, A. Suzuki, M. Inagaki, S. Krenk, Flexible-body dynamics in a floating frame with extraction of rigid body motion, *4th Asian Conference on Multibody Dynamics 2008*, ACMD, Jeju, Korea, August 20–23, 2008.
- [10] A. Kawamoto, S. Krenk, A. Suzuki, M. Inagaki, Flexible body dynamics in a local frame of reference with explicitly predicted motion, *International Journal for Numerical Methods in Engineering* 2009, to appear.
- [11] K. Holm-Jørgensen, S.R.K. Nielsen, System reduction in multibody dynamics of wind turbines, *Journal of Multibody System Dynamics* 21 (2009) 147–165.
- [12] R.J. Guyan, Reduction of stiffness and mass matrices, *AIAA Journal* 3 (1965) 380.
- [13] K.-J. Bathe, *Finite Element Procedures*, Prentice-Hall, Englewood Cliffs, NJ, 1988.
- [14] A.Y.T. Leung, An accurate method of dynamic substructuring with simplified computation, *International Journal of Numerical Methods in Engineering* 14 (1979) 1241–1256.
- [15] A.Y.T. Leung, A simplified dynamic substructure method, *Earthquake Engineering and Structural Dynamics* 14 (1988) 827–837.
- [16] A.Y.T. Leung, *Dynamic Stiffness and Substructures*, Springer, Berlin, 1993.
- [17] N. Petersmann, Calculation of eigenvalues using substructures and dynamic condensation, *Proceedings of the 2nd International Conference on Recent Advances in Structural Dynamics 1984*, Southampton, April 1984, pp. 211–219.
- [18] N. Bouhaddi, R. Fillod, Model reduction by a simplified variant of dynamic condensation, *Journal of Sound and Vibration* 191 (2) (1996) 233–250.
- [19] Z.-Q. Qu, Z.-F. Fu, An iterative method for dynamic condensation of structural matrices, *Mechanical Systems and Signal Processing* 14 (4) (2000) 667–678.
- [20] Z.-Q. Qu, W. Chang, Dynamic condensation method for viscously damped vibration systems in engineering, *Engineering Structures* 23 (2000) 1426–1432.
- [21] Z.-Q. Qu, R.P. Selvam, Insight into the dynamic condensation technique of non-classically damped models, *Journal of Sound and Vibrations* 272 (2004) 581–606.
- [22] W.C. Hurty, Dynamic analysis of structural systems using component modes, *AIAA Journal* 3 (4) (1965) 678–685.
- [23] W.C. Hurty, J.D. Collins, G.C. Hart, Dynamic analysis of large structures by modal synthesis techniques, *Computers & Structures* 1 (1971) 535–563.
- [24] R.R. Craig Jr., M.C.C. Bampton, Coupling of substructures for dynamic analysis, *AIAA Journal* 6 (7) (1968) 1313–1319.
- [25] J.A.C. Ambrósio, J.P.C. Gonçalves, Complex flexible multibody systems with application to vehicle dynamics, *Multibody System Dynamics* 6 (2001) 163–182.
- [26] A. Shanmugam, C. Padmanabhan, A fixed-free interface component mode synthesis method for rotordynamic analysis, *Journal of Sound and Vibration* 297 (2006) 664–679.
- [27] M. Géradin, D. Rixen, *Mechanical Vibrations: Theory and Application to Structural Dynamics*, second ed., Wiley, New York, 1997.
- [28] S. Krenk, *Non-Linear Modeling and Analysis of Solids and Structures*, Cambridge University Press, Cambridge, 2009.
- [29] M.A. Crisfield, *Non-Linear Finite Element Analysis of Solids and Structures, Advanced Topics*, vol. 2, Wiley, New York, 1997.





# Nonlinear Multibody Dynamics of Wind Turbines

**Kristian Holm-Jørgensen**

*Thesis submitted for the degree of Doctor of Philosophy at the  
Faculty of Engineering, Science and Medicine, Aalborg University, Denmark.*

The present thesis deals with nonlinear multibody dynamic aspects of wind turbines. The covered topics include:

- ◆ A flexible multibody formulation based on a Local Observer Frame formulation, where Bernoulli-Euler beam elements with St. Venant torsion are used to model the substructures,
- ◆ Update algorithms of the parameters describing the motion of the moving frames.
- ◆ Large nonlinear geometric displacements of a wind turbine blade by use of the different update algorithms,
- ◆ Undamped eigenfrequencies and eigenmodes of a multibody system,
- ◆ System reduction of a substructure in the multibody formulation. In one method a Ritz basis is used consisting of rigid body modes and elastic eigenmodes compatible to the kinematical interface. In another method a Component Mode Synthesis method is used consisting of constraint modes and fixed interface normal modes.
- ◆ An FE-model is implemented to determine the cross section parameters for a blade section for use in beam elements.